Advances in Materials Science and Engineering

Synthesis and Application of Novel Hybrid Nanomaterials in Catalysis, Adsorption, and Electrochemistry

Lead Guest Editor: Dinh Quang Khieu
Guest Editors: Nguyen Thanh Dinh, Tran Xuan Mau, and Hien Duy Mai

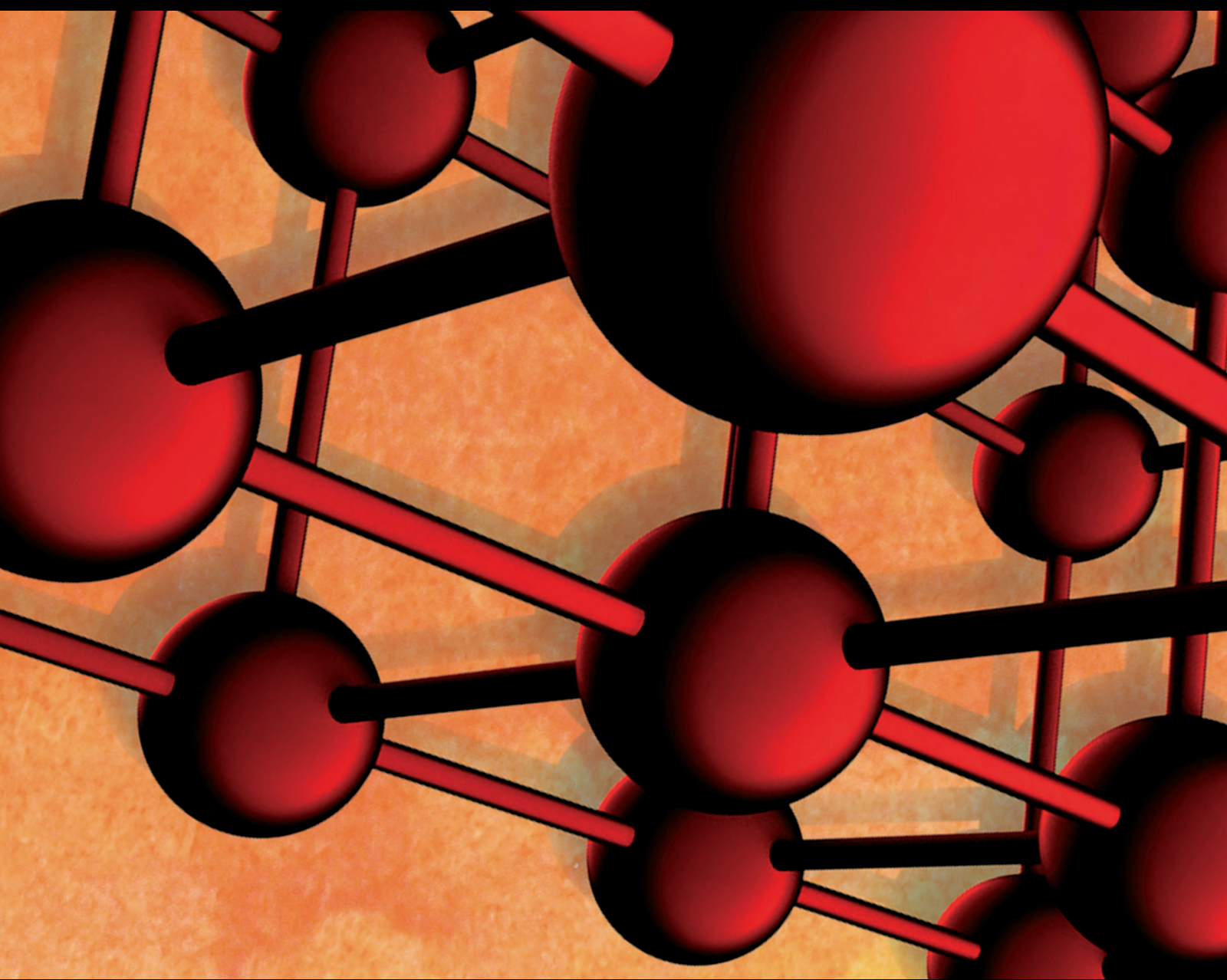

Synthesis and Application of Novel Hybrid Nanomaterials in Catalysis, Adsorption, and Electrochemistry

Advances in Materials Science and Engineering

Synthesis and Application of Novel Hybrid Nanomaterials in Catalysis, Adsorption, and Electrochemistry

Lead Guest Editor: Dinh Quang Khieu
Guest Editors: Nguyen Thanh Dinh, Tran Xuan Mau, and Hien Duy Mai

Editorial Board

Contents

Hindawi
Advances in Materials Science and Engineering
Volume 2019, Article ID 6182374, 1 page
https://doi.org/10.1155/2019/6182374

Editorial

Synthesis and Application of Novel Hybrid Nanomaterials in Catalysis, Adsorption, and Electrochemistry

Dinh Quang Khieu,[1] **Nguyen Thanh Dinh**,[2] **Tran Xuan Mau**,[1] **and Hien Duy Mai**[3]

[1]*University of Sciences, Hue University, Hue, Vietnam*
[2]*Department of Chemistry, University of British Columbia, Vancouver, Canada*
[3]*Department of Chemistry, Hallym University, Chuncheon, Republic of Korea*

Correspondence should be addressed to Dinh Quang Khieu; dqkhieu@hueuni.edu.vn

Received 19 August 2019; Accepted 22 August 2019; Published 9 September 2019

Porous materials with nanostructures are receiving great attention in the scientific community as well as in industry, thanks to their high performance and multifunctionality for various applications. Important requirements of the novel materials include high specific surface area, particularly well-controlled size, homogeneous distribution, and strong attachment to the interfacial surfaces. In addition, the ability to tailor the structure and properties of these materials over a broad length scale suggests that research on hybrid nanomaterials will have a tremendous impact in the fields of environmental adsorption, catalysis, and electrochemistry.

This special issue concentrates on the recent advances in the synthesis, processing, functionalization, application, and challenges of novel hybrid materials. Among ten papers published, three deal with nano-organic materials for bioapplication; two endeavor to the development of novel adsorbents for removing toxic metals in the aqueous solution; two focus on catalytic materials for dye degradation and organic synthesis; one concentrates on nanoparticle synthesis; and the last two develop analytical methods.

The papers deal with a wide range of research from natural porous materials such as bentonite and hydroxyapatite to synthetic materials, e.g., highly ordered mesoporous materials like MCM-41, zeolitic imidazolate framework-8, or platinum nanoparticles. I hope that these special issues will be able to provide readers some typical and exciting snapshots regarding the synthesis of nanoparticles of metal oxides, ordered mesoporous materials, and metal-organic frameworks; functionalization of hybrid nanomaterials; environmental treatment application of novel hybrid materials; catalysis application in organic synthesis; and environmental treatment. Due to the highly dynamic nature of the field, it is impossible to cover every aspect of hybrid nanomaterials, particularly, those achieved recently by the research groups that do not involve in the preparation of this issue. It is clear that this field will develop significantly with the contribution of scientists in different fields.

Conflicts of Interest

The authors declare that there are no conflicts of interest regarding the publication of this paper.

Dinh Quang Khieu
Nguyen Thanh Dinh
Tran Xuan Mau
Hien Duy Mai

Hindawi
Advances in Materials Science and Engineering
Volume 2019, Article ID 2857282, 14 pages
https://doi.org/10.1155/2019/2857282

Research Article

Application and Analysis of an Ionic Liquid Gel in a Soft Robot

Chenghong Zhang,[1] Bin He,[1] Zhipeng Wang,[1] Yanmin Zhou,[1] and Aiguo Ming[2]

[1]*College of Electronics and Information Engineering, Tongji University, Shanghai 201804, China*
[2]*Department of Mechanical Engineering and Intelligent Systems, The University of Electro-Communications, Tokyo 182-8585, Japan*

Correspondence should be addressed to Bin He; hebin@tongji.edu.cn

Received 24 January 2019; Revised 25 March 2019; Accepted 4 April 2019; Published 2 May 2019

Guest Editor: Nguyen Thanh Dinh

Due to their light weight, flexibility, and low energy consumption, ionic electroactive polymers have become a hotspot for bionic soft robotics and are ideal materials for the preparation of soft actuators. Because the traditional ionic electroactive polymers, such as ionic polymer-metal composites (IPMCs), contain water ions, a soft actuator does not work properly upon the evaporation of water ions. An ionic liquid polymer gel is a new type of ionic electroactive polymer that does not contain water ions, and ionic liquids are more thermally and electrochemically stable than water. These liquids, with a low melting point and a high ionic conductivity, can be used in ionic electroactive polymer soft actuators. An ionic liquid gel (ILG), a new type of soft actuator material, was obtained by mixing 1-butyl-3-methylimidazolium tetrafluoroborate ($BMIMBF_4$), hydroxyethyl methacrylate (HEMA), diethoxyacetophenone (DEAP) and ZrO_2 and then polymerizing this mixture into a gel state under ultraviolet (UV) light irradiation. An ILG soft actuator was designed, the material preparation principle was expounded, and the design method of the soft robot mechanism was discussed. Based on nonlinear finite element theory, the deformation mechanism of the ILG actuator was deeply analyzed and the deformation of the soft robot when grabbing an object was also analyzed. A soft robot was designed with the soft actuator as the basic module. The experimental results show that the ILG soft robot has good driving performance, and the soft robot can grab a 105 mg object at an input voltage of 3.5 V.

1. Introduction

Traditional robots are typically constructed of rigid motion joints based on hard materials and can perform tasks quickly and accurately. However, such robots have limited movement flexibility and low environmental adaptability and cannot work under space-constrained conditions. These factors limit the application of rigid robots in unstructured and complex environments [1–3].

In nature, mollusks are widely distributed in oceans, rivers, and lakes and on land. After hundreds of millions of years of evolution, this animal has gradually developed the characteristics of a large deformation ability, a light weight, and a high power density ratio and can achieve efficient movement under complex natural environment conditions by changing its body shape. In recent years, researchers have attempted to apply the biological principles of mollusks to the research and design of robotics. A soft robot is composed of a soft material that can withstand large strains, has the capabilities for continuous deformation and drive-structure integration and can arbitrarily change its shape and size over a wide range. Such a robot has strong adaptability to unstructured environments and broad application prospects in military reconnaissance, rescue, and medical surgery [4–6].

A flexible actuator based on an ionic electroactive polymer (EAP) has the advantages of a low driving voltage, a large displacement ability, a light weight, etc. Such actuators have become a research hotspot in the field of bionic robots. In the past few decades, electrochemical actuators, which are substitutes for air- and fluid-derived devices, have been further developed due to their ideal mechanical properties for use in intelligent robots. However, traditional ionic EAP actuators, such as those based on IPMCs, have the characteristics of a short working time in nonwater media, a

complex manufacturing process, and a high cost. An ILG is a new type of ionic EAP that can work in air for a long time. Because an ILG offers chemical stability, thermal stability, and simpler ion transport, it is more suitable for the production of soft robot actuators than other EAPs.

In this paper, a soft robot actuator based on an ILG material is proposed and its preparation, driving mechanism, and design method are deeply analyzed. Finally, the validity and rationality of the soft robot are verified by driving performance and grabbing experiments.

2. Design of the ILG Soft Robot

The ILG soft actuator consists of a 5-layer structure, as shown in Figure 1. The middle layer is an electroactive layer composed of the ILG material, which functions to store ionic liquids. The outer two layers that wrap the middle layer are electrode layers, which consist of activated carbon. Activated carbon has a high specific surface area, a high electrical conductivity, a high density, a strong adsorption force, etc., making it very suitable for use as an electrode material [7]. In addition, gold foil is selected as a current collector to cover the surface of the activated carbon layers. When the actuator is working, one end is attached to an external metal electrode, and a wire is led from the external electrode to connect to a power supply.

The soft robot consists of three ILG actuators, a common copper electrode, and three independent copper electrodes, as shown in Figure 2. The input unit consists of a common electrode and an independent electrode. The common electrode is a copper column, with the upper end fixed with a fixture, and the copper electrode is connected to a power source. The soft robot consists of three ILG actuators evenly distributed around the common electrode at 120°. Two copper electrodes sandwich one ILG actuator.

Figure 3 shows the motion cycle of the soft robot to grab an object, which can be described as follows. First, the ILG actuator is naturally stretched, and by applying an input voltage of 3.5 V to the electrodes, the actuator quickly bends outward. Second, when the actuator is close to the target object, the input voltage direction is changed, and the actuator bends inward to clamp the object. Finally, the input signal is changed, and the actuator bends outward to release the object.

2.1. Preparation of the Soft Actuator. The preparation process of an ILG is a process of ionic liquid loading. Ionic liquid loading refers to the immobilization of an ionic liquid to form a solid carrier by physical or chemical means [8]. $BMIMBF_4$ was selected as the ionic liquid. The carriers of ionic liquids need to have interconnected porous structures, large specific surface area and porosity, and good mechanical strength and electrochemical stability. Therefore, HEMA was selected to prepare the carrier. This material is a colorless and transparent liquid that is soluble in water and has low toxicity. HEMA was polymerized under ultraviolet light to form polyhydroxyethyl methacrylate (PHEMA) with a porous structure.

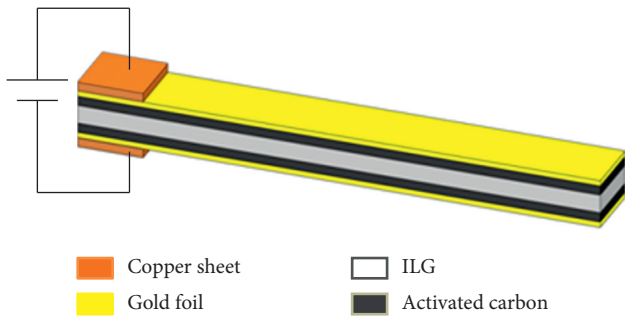

Figure 1: Five-layer structure of the soft actuator.

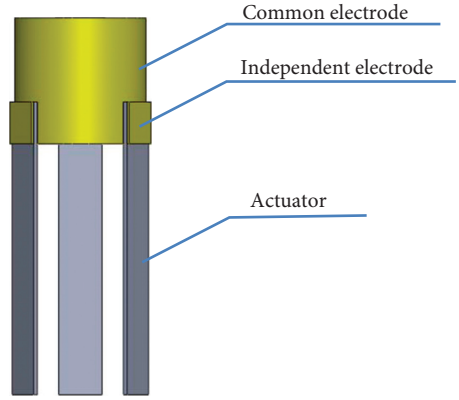

Figure 2: Configuration of the soft robot.

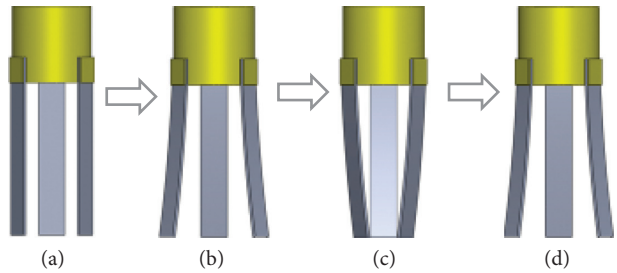

Figure 3: Motion cycle of the soft robot manipulator to grab an object.

The mixed solution consists of $BMIMBF_4$, HEMA, and ZrO_2. Under UV light, the ILG is generated by the polymerization reaction induced by DEAP. The polymer matrix is cross-linked into a porous network structure. ZrO_2 enhances the mechanical strength of the gel, and as the ZrO_2 content increases, the tensile strength of the ILG increases [9, 10]. Figure 4 shows the soft actuator fabrication process. Figure 4(a) shows the ILG sample, which is covered with a layer of $BMIMBF_4$ due to osmosis. Because the ionic liquid has a certain viscosity, the activated carbon electrode can be directly affixed to both sides of the gel, as shown in Figure 4(b). Finally, the gold foil is evenly affixed to the surface of the activated carbon layers to obtain an ILG soft actuator, as shown in Figure 4(c).

2.2. Soft Actuator Deformation Mechanism. For the ILG actuator, the application of a voltage on the electrode can

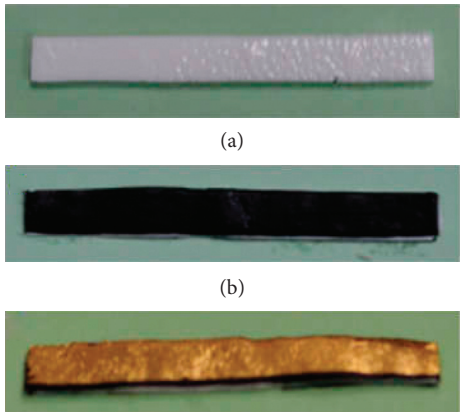

(a)

(b)

(c)

Figure 4: Fabrication process of the soft actuator: (a) ILG; (b) the activated carbon layer is affixed; (c) the gold foil layer is affixed.

cause bending deformation, which is the result of the coupling of the electric field, chemical field, flow field, and field force. The average pore diameter of the structure is greater than 10 microns, which is much larger than the diameter of free ions in the ionic liquids (nanoscale). Therefore, $BMIM^+$ and BF_4^- can move freely inside the carrier. Under the action of the electric field, positive and negative ions accumulate in the electrode layers on both sides of the ILG. Because the cation volume is much larger than the anion volume, the volume of the ILG cathode side expands and the volume of the ILG anode side shrinks [11, 12]. The entire actuator therefore bends toward the anode side, as shown in Figure 5.

When an electric field is applied, the movement of the internal ions of the ILG actuator in the porous medium can be described by the Nernst–Planck equation [13]:

$$j_i = -d_i\left(\nabla\varpi_i + \frac{F}{RT}\varpi_i z_i \nabla\Theta\right), \tag{1}$$

where i is the ion type ($i = 1$ represents the cation, and $i = 2$ represents the anion), j_i is the flow of ions in the PHEMA pores, d_i is the diffusion coefficient of the ions, ϖ_i is the ion concentration, $\nabla\varpi_i$ is the ion concentration gradient, Θ is the potential, $\nabla\Theta$ is the potential gradient, F is the Faraday constant, R is the gas constant, T is the absolute temperature, and z_i is the number of ionic charges. The first term on the right-hand side of the formula indicates the contribution of the cation or anion concentration diffusion; the second term indicates the contribution of electromigration.

The continuous equation of concentration changing with time is

$$\frac{\partial\varpi_i}{\partial t} = -\nabla j_i, \tag{2}$$

where ∇j_i is the flow change of the i-th ion in the PHEMA pores and t is the time.

The internal electric field balance equation of the ILG actuator can be expressed as follows:

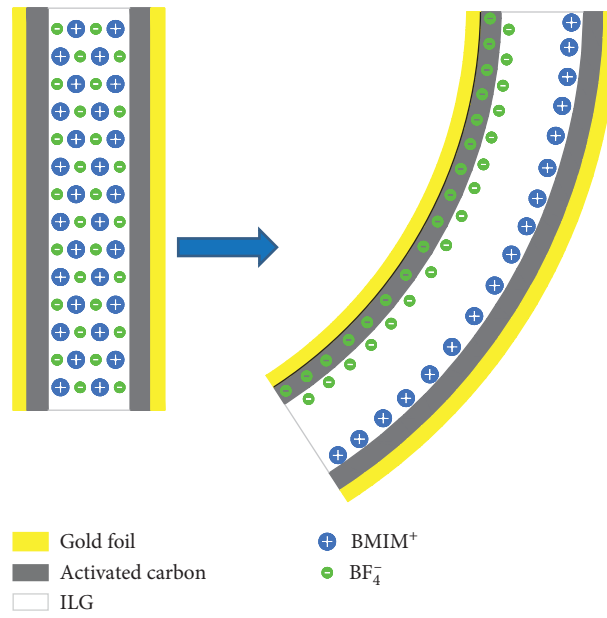

Figure 5: Working principle of the actuator.

$$E = \frac{D}{k_e} = -\nabla\Theta,$$
$$\nabla D = \rho = F(\varpi_1 - \varpi_2), \tag{3}$$

where D is the electric displacement, E is the electric field, ρ is the net charge density, and k_e is the effective dielectric constant of the ILG.

The effect of the electrode layer on the bending deformation of the actuator along the width and the thickness is ignored. Considering only the relationship between the axial deformation of the electrode layer and the net charge density, the axial induced strain can be expressed as follows:

$$\varepsilon_c(s) = \rho(s)\alpha(s), \tag{4}$$

where ε_c is the induced strain, $\alpha(s)$ is the induced strain coupling coefficient, and s is the Laplace domain.

Therefore, the axial induced stress is

$$\sigma_c(s) = \varepsilon_c E_t = \rho(s)d(s),$$
$$d(s) = \alpha(s)E_t, \tag{5}$$

where E_t is the elastic modulus of the electrode layer and $d(s)$ is the axial-induced stress coupling coefficient.

The bending moment of the actuator is

$$M(s) = 2\int_{b_1}^{b} \sigma_c(s)xw\,dx = 2\int_{b_1}^{b} \rho(s)d(s)xw\,dx, \tag{6}$$

where b and b_1 are half the thickness of the actuator and ILG layer, respectively, and w is the width of the actuator.

The ILG actuator is the basic unit of a soft robot and is the source of its deformation. For flexible mechanisms, the degrees of freedom and constraints are determined by the flexibility matrix. The cantilever beam flexibility matrix is as follows [14]:

$$R = \operatorname{diag}\left(R_{\theta x}, R_{\theta y}, R_{\theta z}, R_x, R_y, R_z\right) = \operatorname{diag}\left(\frac{l}{E_a I_x}, \frac{l}{E_a I_y}, \frac{l}{G_a J}, \frac{l^3}{12 E_a I_y}, \frac{l^3}{12 E_a I_x}, \frac{l}{E_a A}\right), \tag{7}$$

where $R_{\theta x}$, $R_{\theta y}$, and $R_{\theta z}$ represent rotational flexibility around the x, y, and z axes, respectively, and R_x, R_y, and R_z represent translational flexibility along the x, y,and z axes, respectively. If the order of magnitude of an element in one direction is significantly greater than that of the element in the other directions, then the mechanism has a degree of freedom in this direction. Using this method, the equivalent constraints or degrees of freedom of the soft robot can be established.

3. Hyperelastic Arruda–Boyce Model

Material nonlinearity is caused by the nonlinearity of the constitutive relationship of the material. The constitutive relationship of a material includes the stress, strain, strain rate, load duration, temperature, etc. After a load is unloaded, residual strain will appear in a nonlinear material, as shown in Figure 6.

The hyperelastic Arruda–Boyce model, typically used for relatively largely deformed materials, is used to simulate ILGs. Hyperelastic materials can be described by the strain energy function W, which is used to define the strain energy density in the material. The Arruda–Boyce strain energy function W is as follows [15–17]:

$$W = G\sum_{k=1}^{5}\frac{c_k}{\lambda_m^{2(k-1)}}\left(I_1^k - 3^k\right) + \frac{1}{D}\left(\frac{J_{el}^2 - 1}{2} - \ln J_{el}\right), \tag{8}$$

with $c_1 = (1/2)$, $c_2 = (1/20)$, $c_3 = (11/1050)$, $c_4 = (19/7000)$, and $c_5 = (519/673750)$, where W is the strain energy density, G is the initial shear modulus, λ_m is the deformation rate, J_{el} is the elastic volume ratio, and D is the temperature-dependent material parameter associated with the bulk modulus. A material is completely incompressible when $J_{el} = 1$.

I_1 is the first strain invariant of the deviatoric strain, and the relationship between I_1 and the main tensile strain rates λ_1, λ_2, and λ_3 is as follows:

$$I_1 = \lambda_1^2 + \lambda_2^2 + \lambda_3^2,$$
$$I_2 = \frac{1}{\lambda_1^2} + \frac{1}{\lambda_2^2} + \frac{1}{\lambda_3^2}, \tag{9}$$
$$I_3 = \lambda_1^2 \times \lambda_2^2 \times \lambda_3^2,$$

where λ_1, λ_2, and λ_3 are the main (extension) deformation rates along the x, y, and z directions, respectively. I_1, I_2, and I_3 are the relative changes of the length, the surface area, and the volume of the elastomer, respectively.

The material stress is obtained by differentiating the stretching:

$$\sigma_n = \frac{\partial W}{\partial \lambda_n}, \tag{10}$$

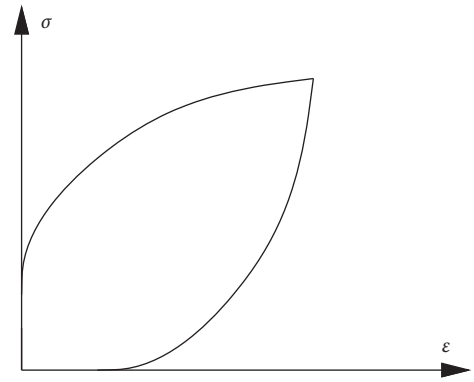

Figure 6: Stress-strain curve of nonlinear materials.

where σ_n is the normal stress and λ_n is the stretching in the loading direction.

The isotropic and incompressible deformation process of an ILG is given by

$$\sqrt{I_3} = \lambda_1\lambda_2\lambda_3 = 1. \tag{11}$$

When the ILG is uniformly stretched, $\lambda_2 = \lambda_3$; equation (11) can be used to calculate

$$\lambda_2 = \lambda_3 = \frac{1}{\sqrt{\lambda_1}}. \tag{12}$$

The true stress is obtained by

$$\sigma_0 = \sigma_n\lambda_n. \tag{13}$$

Differentiating equation (8), we obtain

$$\sigma_0 = G\left[\left(\lambda_n^2 - \lambda_n^{-1}\right) + \frac{1}{5\lambda_m^2}\left(\lambda_n^4 - \lambda_n^{-2}\right) + \frac{11}{175\lambda_m^4}\left(\lambda_n^6 - \lambda_n^{-3}\right) + \frac{19}{875\lambda_m^6}\left(\lambda_n^8 - \lambda_n^{-4}\right) + \frac{519}{67375\lambda_m^8}\left(\lambda_n^{10} - \lambda_n^{-5}\right)\right]. \tag{14}$$

4. Model for the Soft Robot. To establish a gripping model scheme as shown in Figure 7, assume that the soft robot is an inextensible, fully flexible elastic rod. Assume that l is the length of the evenly distributed rod, EI is the flexural rigidity, ρ is the mass per unit length, and k_g is the curvature profile when the object is gripped [18, 19].

4.1. Deformation Analysis for Soft Actuators. At $s = s^*$, the position of any material point can be represented by the following formula [20], as shown in Figure 8.

$$\vec{r}\left(s = s^*\right) = X\left(s = s^*\right)\vec{E}_1 + Y\left(s = s^*\right)\vec{E}_2, \tag{15}$$

where, in Cartesian coordinates, X and Y are represented as follows:

$$\begin{cases} X\left(s = s^*\right) = X\left(s = 0\right) + \int_0^{s^*}\cos\left(\theta(\eta)\right)d\eta, \\ Y\left(s = s^*\right) = Y\left(s = 0\right) + \int_0^{s^*}\sin\left(\theta(\eta)\right)d\eta, \end{cases} \tag{16}$$

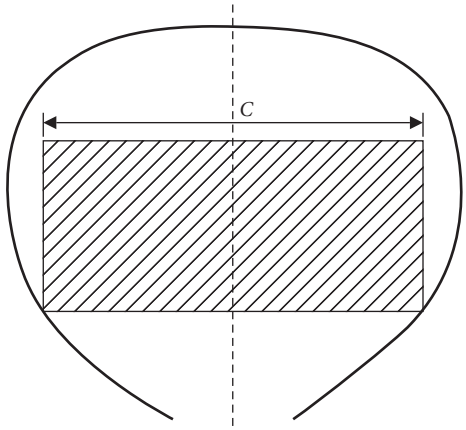

Figure 7: Lifting of an object, considering the normal force and the static friction force at the contact point of the soft actuator.

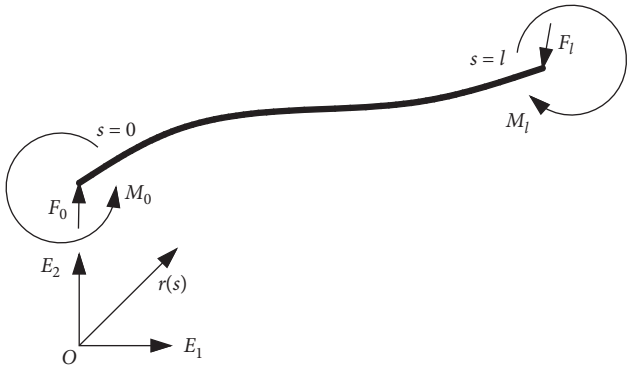

Figure 8: At $s = 0$, F_0 and M_0 are the terminal force and terminal moment, respectively; at $s = l$, F_l and M_l are the terminal force and terminal moment; and at point $s = \xi$, F_ξ is the force.

where η is a dummy variable and θ is the angle between the unit tangent vector and the horizontal direction.

$$\vec{r}' = \cos(\theta(s))\vec{E}_1 + \sin(\theta(s))\vec{E}_2, \tag{17}$$

where the prime ($'$) represents the partial derivative with respect to s. Assuming that $\vec{r}$ is continuous, θ and $\vec{r}'$ are also continuous.

At point $s = \varsigma$, the jump in any function $\chi = \chi(s, \theta(s), \theta'(s))$ is expressed by a compact notation:

$$[\![\chi]\!]_\varsigma = \chi(\varsigma^+) - \chi(\varsigma^-), \tag{18}$$

where

$$\begin{cases} \chi(\varsigma^-) = \lim\limits_{s \nearrow \varsigma} \chi(s, \theta(s), \theta'(s)), \\ \chi(\varsigma^+) = \lim\limits_{s \searrow \varsigma} \chi(s, \theta(s), \theta'(s)). \end{cases} \tag{19}$$

The jump will be associated with the force applied at the discrete point.

The bending moment M is described by a constitutive equation:

$$\vec{M} = EI(\theta' - k_0)\vec{E}_3, \tag{20}$$

where k_0 represents the curvature. In addition to the gravity per unit length and end load of the rod, the singular force $\vec{F}_\xi$ at $s = \xi$ must be considered. Figure 7 shows the force that simulates the contact of an object with the soft robot. The governing equation can be derived from the equilibrium of the linear and angular momentum [21–23]:

$$\begin{cases} \vec{m}' - \rho g \vec{E}_2 = 0, \\ \dfrac{\partial}{\partial s}\left(EI(\theta' - k_0) + m_2\cos(\theta) - m_1\sin(\theta)\right) = 0, \\ [\![\vec{m}]\!]_\xi + \vec{F}_\xi = 0, \end{cases} \tag{21}$$

where $\vec{m} = m_1\vec{E}_1 + m_2\vec{E}_2$.

4.2. Deformation Analysis Governing Formula for the Soft Robot. The corner of the object is assumed to be in contact with the soft robot at $s = \xi$. Two new unit vectors are defined as follows, as shown in Figure 9:

$$\begin{cases} \vec{H}_1 = \cos(\theta(\xi))\vec{E}_1 + \sin(\theta(\xi))\vec{E}_2, \\ \vec{H}_1 = -\sin(\theta(\xi))\vec{E}_1 + \cos(\theta(\xi))\vec{E}_2, \end{cases} \tag{22}$$

where $\vec{H}_1$ is the tangent to the centerline of the soft robot and $\vec{H}_2$ is perpendicular to the centerline of the soft robot.

$$\vec{F}_\xi = f_1\vec{H}_1 + f_2\vec{H}_2 = N_1\vec{E}_1 + N_2\vec{E}_2, \tag{23}$$

where f_1 is the normal force and f_2 is the corresponding friction force.

Equation (21) is applied to segment $s \in (\xi, l)$, and we obtain the following equation:

$$\begin{cases} \vec{m}(\xi^+) = -\rho g(l - \xi)\vec{E}_2, \\ \vec{m}(\xi^-) = N_1\vec{E}_1 + N_2\vec{E}_2 - \rho g(l - \xi)\vec{E}_2. \end{cases} \tag{24}$$

The expression of the potential energy W of the soft robot is established:

$$\begin{aligned} W = &\int_0^\xi \left\{\frac{EI}{2}(\theta' - k_0)^2 + \rho g Y(s) - \vec{m}(\xi^-)\cdot\vec{r}'\right\} ds \\ &+ \int_\xi^l \left\{\frac{EI}{2}(\theta' - k_0)^2 + \rho g Y(s)\right\} ds, \end{aligned} \tag{25}$$

where

$$Y(s) = \int_0^s \sin(\theta(\xi))d\xi. \tag{26}$$

Equation (21) can be used to establish boundary value problems.

$$\begin{cases} EI(\theta'' - k_0') - \rho g(l - s)\cos(\theta) = 0, & s \in (0, \xi), \\ EI(\theta'' - k_0') - \rho g(l - s)\cos(\theta) + N_2\cos(\theta) & \\ \quad - N_1\sin(\theta) = 0, & s \in (\xi, l), \end{cases} \tag{27}$$

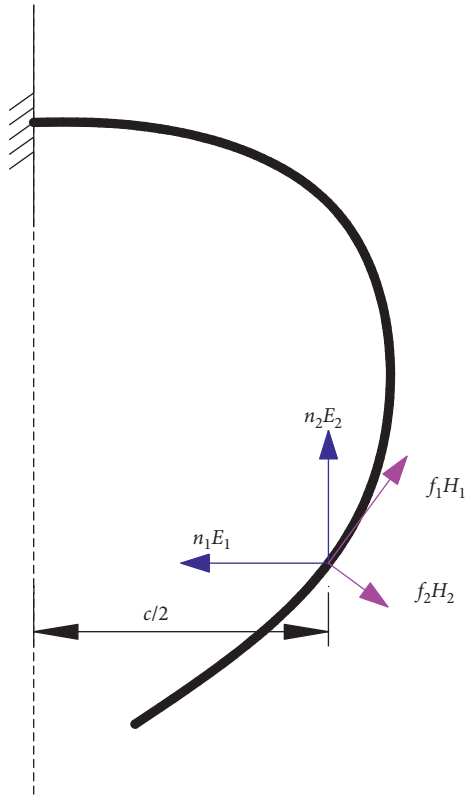

Figure 9: At point $s = \xi$, the object is in contact with the soft robot. The object is assumed to remain stationary due to the static friction force $f_1\bar{H}_1$ and the normal force $f_2\bar{H}_2$.

where the solution $\theta = \theta^*$ satisfies the conditions

$$\begin{aligned} \theta(0) &= 0, \\ \theta'(l) &= k_0(l), \\ [\![\theta]\!]_\xi &= 0, \\ [\![\theta']\!]_\xi &= 0, \\ \int_0^\xi \cos(\theta(s))ds &= \frac{c}{2}. \end{aligned} \tag{28}$$

The soft robot is divided into K segments. The total potential energy expression is approximated as follows:

$$\begin{aligned} W_d = {} & \frac{EI}{2}\sum_{i=1}^{K}\left(\frac{\theta_i - \theta_{i-1}}{ds} - k_0\right)^2 ds + \rho g(l - s_0)\sin(\theta_0)\frac{ds}{2} \\ & + \sum_{i=1}^{K-1}\rho g(l - s_i)\sin(\theta_i)ds + \rho g(l - s_K)\sin(\theta_n)\frac{ds}{2} \\ & - N_1\cos(\theta_0)\frac{ds}{2} - N_1\sum_{i=1}^{I-1}\cos(\theta_i)ds - N_1\cos(\theta_I)\frac{ds}{2} \\ & - N_2\sin(\theta_0)\frac{ds}{2} - N_2\sum_{i=1}^{I-1}\sin(\theta_i)ds - N_2\sin(\theta_I)\frac{ds}{2}, \end{aligned} \tag{29}$$

where the constraint function W_c is

$$W_c = \frac{ds}{2} + \sum_{i=1}^{I-1}\cos(\theta_i)ds + \cos(\theta_I)\frac{ds}{2} - \frac{c}{2}. \tag{30}$$

5. Nonlinear Finite Element Method

Geometric nonlinearity arises from the nonlinear relationship between the strain and displacement. Currently, research on geometric nonlinearity mainly focuses on three types of problems: (1) a large displacement with a small strain, (2) a small displacement with a large strain, and (3) a large displacement with a large strain. A geometric nonlinear problem has two main characteristics. First, due to the large deformation of the structure, the strain and displacement of the structure are nonlinear. Second, a balance equation is established at the position after deformation. In the analysis of large deformation, the displacement of the structure changes continuously and appropriate strain, stress, and constitutive relationships should be adopted.

To capture the nonlinear behavior of the structure, the full nonlinear finite element formulas of the truss elements and beam elements are studied.

5.1. Nonlinear FEM for Truss Elements. In the Cartesian coordinate system, the object is displaced to a certain position under the action of external forces, as shown in Figure 10. (x_1, y_1, z_1) and (x_2, y_2, z_2) are the position co-

ordinates of points P_1 and P_2 before deformation, respectively. The object is deformed to a new position under the action of external forces. (u_1, v_1, w_1) and (u_2, v_2, w_2) are the deformation coordinates of points P_1 and P_2 after deformation, respectively.

The formula for the undeformed length of a truss element is as follows:

$$l = \sqrt{(x_2 - x_1)^2 + (y_2 - y_1)^2 + (z_2 - z_1)^2}. \tag{31}$$

The expression of the total Lagrangian strain ε along the deformation axis is

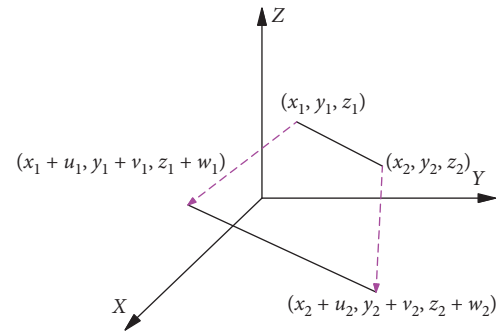

Figure 10: Nondeformed and deformed geometry of a truss element.

$$\varepsilon = \frac{\sqrt{(u_2 + x_2 - u_1 - x_1) + (v_2 + y_2 - v_1 - y_1) + (w_2 + z_2 - w_1 - z_1)} - l}{l}. \tag{32}$$

According to the change of the elastic energy, the product of the stiffness matrix and the displacement vector is expressed as follows [2, 24]:

$$\begin{cases} [k]\{u\} = AlE\varepsilon\{\varphi\}, \\ \{\varphi\} = \left\{\dfrac{\partial\varepsilon}{\partial u_1}, \dfrac{\partial\varepsilon}{\partial v_1}, \dfrac{\partial\varepsilon}{\partial w_1}, \dfrac{\partial\varepsilon}{\partial u_2}, \dfrac{\partial\varepsilon}{\partial v_2}, \dfrac{\partial\varepsilon}{\partial w_2}\right\}^T, \end{cases} \tag{33}$$

where E is Young's modulus, A is the cross sectional area, and l is the length of the truss element.

The tangent stiffness matrix is obtained by differentiating equation (33) with respect to the displacement vector:

$$\begin{aligned} [\breve{k}] &= \frac{\partial([k]\{u\})}{\partial\{u\}} = EAl\{\varphi\}\frac{\partial\varepsilon}{\partial\{u\}} + EAl\varepsilon\frac{\partial\{\varphi\}}{\partial\{u\}} \\ &= EAl\{\varphi\}\{\varphi\}^T + EAl\varepsilon\frac{\partial^2\{\varphi\}}{\partial\{u\}^2}. \end{aligned} \tag{34}$$

The mass matrix is the same as that for a linear truss element [25, 26]:

$$[m] = \frac{\rho Al}{6}\begin{bmatrix} 2 & 0 & 0 & 1 & 0 & 0 \\ 0 & 2 & 0 & 0 & 1 & 0 \\ 0 & 0 & 2 & 0 & 0 & 1 \\ 1 & 0 & 0 & 2 & 0 & 0 \\ 0 & 1 & 0 & 0 & 2 & 0 \\ 0 & 0 & 1 & 0 & 0 & 2 \end{bmatrix}. \tag{35}$$

5.2. Nonlinear FEM for Beam Elements. The two famous beam theories are the Euler–Bernoulli and Timoshenko beam theories. The Euler–Bernoulli beam theory assumes that the cross section remains planar and normal to the reference line after bending and its stiffness is higher than the actual stiffness. Timoshenko's beam theory overcomes this problem by introducing shear deformation into the model, which obtains accurate results for thick beam calculations. Because the soft actuators are slender, the shear deformation is negligible. Therefore, nonlinear Euler–Bernoulli beams with von Karman nonlinearity can be used for modeling and analysis of the soft actuators.

In addition to the bending effect, the finite element formula should also include the torsion and tensile effects to reflect the large deformation effect [27, 28]:

$$\begin{cases} \varepsilon_{11} = e + z\rho_2 - y\rho_3, \\ \varepsilon_{12} = -z\rho_1, \\ \varepsilon_{13} = y\rho_1, \\ e = u' + \dfrac{(v')^2}{2} + \dfrac{(w')^2}{2}, \\ \rho_1 = \varphi', \\ \rho_2 = -w''\left(1 - (w')^2\right), \\ \rho_3 = -v\left(1 - (v)^2\right), \end{cases} \tag{36}$$

where ε_{ij} is the engineering strain tensor, e is the axial strain, y and z are the coordinates on the cross section, and ρ_i is the deformation curvature. u, v, and w are the displacements on the cross section.

When a change of energy is applied, the product of the stiffness matrix and the displacement vector is expressed as follows:

$$[k]\{h\} = \int_l [B]^T[\Psi]^T[\Phi]\{\phi\}dx, \tag{37}$$

where

$$[B] = \frac{\partial [N]}{\partial s},$$

$$[\Psi] = \begin{bmatrix} 1 & v' & w' & 0 & 0 & 0 \\ 0 & 0 & 0 & 1 & 0 & 0 \\ 0 & 0 & 2w'w'' & 0 & 0 & -\left(1-(w')^2\right) \\ 0 & -2v'v'' & 0 & 0 & 1-(v')^2 & 0 \end{bmatrix},$$

$$[\Phi] = \begin{bmatrix} EA & 0 & 0 & 0 \\ 0 & GI_{11} & 0 & 0 \\ 0 & 0 & EI_{22} & 0 \\ 0 & 0 & 0 & EI_{33} \end{bmatrix},$$

$$\{\phi\} = \begin{Bmatrix} e \\ \rho_1 \\ \rho_2 \\ \rho_3 \end{Bmatrix}. \tag{38}$$

Assume that

$$\left\{h^{(i)}\right\} = \left\{\overline{h}\right\} + \left\{\Delta h^{(i)}\right\}. \tag{39}$$

The mass matrix is the same as that of a linear beam element.

5.3. Nonlinear Convergence Algorithms. Although the Newton–Raphson algorithm is used for nonlinear static analysis, the tangent stiffness matrix becomes singular at some points, which makes a global equilibrium solution impossible. Riks proposed a process to track the intersection of the normal to the tangent line with the equilibrium path to solve this problem [29], as shown in Figure 11. The Crisfield method uses arcs instead of vertical lines to search for solutions. The increment of the load factor becomes an unknown problem to be solved in the iterative process.

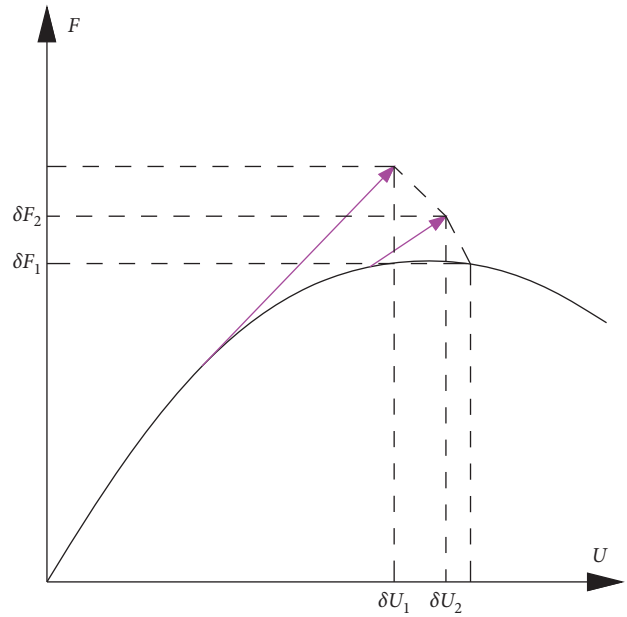

Figure 11: Scheme of the Crisfield method.

By applying Taylor expansion without higher order terms, the tangential stiffness matrix is expressed as follows:

$$[\breve{k}] = \int_l [B]^T \left([\overline{\Psi}]^T [\Phi] \{\Psi\} + [\Gamma] \right) [B] dx, \tag{40}$$

where

$$[\Gamma] = \begin{bmatrix} 0 & 0 & 0 & 0 & 0 & 0 \\ 0 & EAe - 2EI_{33}v''\rho_3 & 0 & 0 & -2EI_{33}v'\rho_3 & 0 \\ 0 & 0 & EAe + 2EI_{22}w''\rho_2 & 0 & 0 & 2EI_{33}w'\rho_2 \\ 0 & 0 & 0 & 0 & 0 & 0 \\ 0 & 0 & 0 & 0 & 0 & 0 \\ 0 & 0 & 0 & 0 & 0 & 0 \end{bmatrix}. \tag{41}$$

Assume that

$$\{F\} = \lambda \left\{\vec{F}\right\}, \tag{42}$$

where λ is the load parameter and $\vec{F}$ is the preselected load vector.

The residual force vector of the i-th step is expressed as follows:

$$R\left(\left\{\vec{U}\right\}^i, \lambda^i\right) = R\left(\left\{\vec{U}\right\}^{i-1}, \lambda^{i-1}\right) + \left.\frac{\partial R}{\partial \left\{\vec{U}\right\}}\right|_{\left\{\vec{U}\right\}^{i-1}, \lambda^{i-1}} \cdot \delta\left\{\vec{U}\right\}^i + \left.\frac{\partial R}{\partial \{\lambda\}}\right|_{\left\{\vec{U}\right\}^{i-1}, \lambda^{i-1}} \delta\lambda_1^i, \tag{43}$$

where $\vec{U}$ is the displacement vector.

$$[k]\{\vec{U}\}\Big|_{\{\vec{U}\}^{i-1},\lambda^{i-1}} - \lambda^{i-1}\{\vec{F}\} + [k_T]\Big|_{\{\vec{U}\}^{i-1},\lambda^{i-1}}\delta\{\vec{U}\}_1^i + \{\vec{F}\}\delta\lambda_1^i = \{0\}, \tag{44}$$

where $\delta\{\vec{U}\}_1^i$ is the first increment of the load parameter in the i-th step and $\delta\lambda_1^i$ is the first increment of the displacement vector in the i-th step.

$$\{\vec{U}\}_1^i = \{\vec{U}\}^{i-1} + \delta\{\vec{U}\}_1^i, \tag{45}$$

$$\lambda_1^i = \lambda^{i-1} + \delta\lambda_1^i. \tag{46}$$

Substituting (45) and (46) into equation (44), we obtain

$$[k]\{\vec{U}\}\Big|_{\{\vec{U}\}_1^i,\lambda_1^i} - \lambda_1^i\{\vec{F}\} + [k_T]\Big|_{\{\vec{U}\}_1^i,\lambda_1^i}\delta\{\vec{U}\}_2^i + \{\vec{F}\}\delta\lambda_2^i = \{0\}. \tag{47}$$

When the second step incremental search path is perpendicular to the normal of the first step incremental path, we obtain

$$\delta\{\vec{U}\}_1^i \cdot \delta\{\vec{U}\}_2^i + \{\vec{F}\}\delta\lambda_1^i \cdot \{\vec{F}\}\delta\lambda_2^i = \{0\}. \tag{48}$$

When solving nonlinear finite element equations by an iterative method, choosing the appropriate convergence criterion is necessary to ensure that the iteration can be terminated. The convergence criterion will directly affect the speed and accuracy of the solution. If the convergence criterion is not appropriately chosen, the calculation will fail.

From equations (47) and (48), we obtain

$$\delta\{\vec{U}\}_2^i = -\left([k_T]\big|_{\{\vec{U}\}_1^i,\lambda_1^i}\right)^{-1}\left([k]\{\vec{U}\}\Big|_{\{\vec{U}\}_1^i,\lambda_1^i} - \lambda_1^i\{\vec{F}\} + \{\vec{F}\}\delta\lambda_2^i\right),$$

$$\delta\lambda_2^i = \frac{\delta\{\vec{U}\}_1^i\left([k_T]\big|_{\{\vec{U}\}_1^i,\lambda_1^i}\right)^{-1}\left([k]\{\vec{U}\}\Big|_{\{\vec{U}\}_1^i,\lambda_1^i} - \lambda_1^i\{\vec{F}\}\right)}{\left(\{\vec{F}\}\delta\lambda_1^i\{\vec{F}\}\right) - \delta\vec{U}_1^i\left([k_T]\big|_{\{\vec{U}\}_1^i,\lambda_1^i}\right)^{-1}\{\vec{F}\}}. \tag{49}$$

The convergent load parameters and displacement vectors are as follows:

$$\lambda^i = \lambda^{i-1} + \delta\lambda_1^i + \delta\lambda_2^i + \delta\lambda_3^i + \cdots,$$
$$\{\vec{U}\}^i = \{\vec{U}\}^{i-1} + \delta\{\vec{U}\}_1^i + \delta\{\vec{U}\}_2^i + \delta\{\vec{U}\}_3^i + \cdots. \tag{50}$$

6. Experimental Analysis

6.1. Stress Calculation of the ILG. To verify the accuracy and practicability of the induced stress expression of the ILG, the deformation rate of each point in the uniaxial tensile test is substituted into the stress expression to calculate the stress.

For the Arruda–Boyce model, the parameters G and λ_m are as follows:

$$G = 4.10736,$$
$$\lambda_m = 4.62529. \tag{51}$$

A comparison of the uniaxial tensile stress calculation data with the experimental data is given in Table 1.

Table 1, which presents comparisons of the tensile stress calculation data with experimental data, shows that the minimum relative error of the Arruda–Boyce model is 3.72 and the maximum relative error is 8.51. This result shows that the calculation accuracy of the Arruda–Boyce model is high and satisfies the requirement of material performance analysis in soft robot design.

Figure 12 shows that the first half of the stress-strain curve calculated by the Arruda–Boyce model almost coincides with the experimental curve, while for the second half, the relative error between the calculated and experimental stress-strain curves becomes increasingly larger but remains small. The above analyses indicate that the calculation formula of the ILG stress is feasible and reliable.

6.2. Experiment on the Soft Actuator. The square wave of the input signal has a magnitude of 4 V, a period of 30 s, and a duty cycle of 50%. The actuator size is 30 mm × 5 mm × 0.5 mm, the free segment length is 25 mm, and the average thickness of the ILG layer is approximately 0.4 mm.

The interval of the displacement reading is 3 s. Figure 13 shows that the maximum amplitude of the positive axis of the actuator is 4.8 mm, and the maximum amplitude of the negative axis is 5 mm. The positive and negative displacements of the actuator are basically symmetrical and stable, and the attenuation of the long-term working drive performance is very small.

In Figure 14, the simulation results are analyzed: when the input voltage is 3.0 V, the maximum displacement of the soft actuator is 3.7 mm; when the input voltage is 3.5 V, the maximum displacement is 4.3 mm; and when the input voltage is 4.0 V, the maximum displacement is 5.0 mm. The displacement calculation results for the different input voltages are shown in Table 2.

According to Figure 15, the simulation value curve is almost consistent with the experimental value curve, and the change trends of the displacement curves from the simulation and experiment are almost identical. The relative error between the calculated and experimental displacement curves is small. Therefore, the calculation formula of the soft actuator is feasible and credible.

6.3. Working Performance Test of the Soft Actuator. The long-term stable working performance is an important factor in ionic EAP soft actuators. Since the traditional IPMC actuator contains a water-based electrolyte, maintaining a stable driving performance after operation in air for dozens of seconds is difficult due to the evaporation of water and electrolysis [30]. The ILG soft robot does not contain a water-based electrolyte, which avoids the problem of water molecule loss, and can work stably in air for a long time.

Table 1: Comparison of the tensile stress calculation data with experimental data obtained in the uniaxial tensile test.

Measurement data		Experimental results		Arruda–Boyce model	
Force (mN)	Deformation (mm)	Strain (%)	Stress (kPa)	Calculated stress (σ_E) (kPa)	Error (%)
4.97	2.0	5.7	0.50	0.54	7.42
8.21	3.5	10	0.86	0.92	6.64
14.88	7.0	20	1.70	1.78	4.70
20.52	10.5	30	2.54	2.64	4.08
25.35	14.0	40	3.38	3.53	4.38
29.47	17.5	50	4.21	4.43	5.21
33.06	21.0	60	5.04	5.34	6.02
36.22	24.5	70	5.86	6.26	6.69
38.94	28.0	80	6.68	7.16	7.31
41.48	31.5	90	7.50	8.06	7.40
43.58	35.0	100	8.30	8.94	7.70
45.50	38.5	110	9.10	9.80	7.65
47.13	42.0	120	9.88	10.63	7.64
48.67	45.5	130	10.65	11.44	7.26
49.98	49.0	140	11.41	12.21	6.93
51.03	52.5	150	12.15	12.96	6.71
51.95	56.0	160	12.86	13.69	6.39
52.75	59.5	170	13.56	14.38	6.02
53.40	63.0	180	14.24	15.05	5.66
53.90	66.5	190	14.89	15.69	5.36
54.32	70.0	200	15.52	16.30	5.01
54.65	73.5	210	16.12	16.88	4.65
54.78	77.0	220	16.70	17.44	4.50
54.86	80.5	230	17.25	17.98	4.31
54.94	84.0	240	17.78	18.50	3.97
54.84	87.5	250	18.28	18.99	3.88
54.72	91.0	260	18.74	19.46	3.72
54.47	94.5	270	19.18	19.91	3.73
54.01	98.0	280	19.57	20.34	4.06
53.61	101.5	290	19.93	20.75	4.22
53.23	105.0	300	20.24	21.15	4.29
52.48	108.5	310	20.50	21.53	5.05
51.83	112.0	320	20.73	21.89	5.59
51.02	115.5	330	20.91	22.23	6.42
50.29	119.0	340	21.04	22.57	7.09
49.21	122.5	350	21.12	22.88	8.51

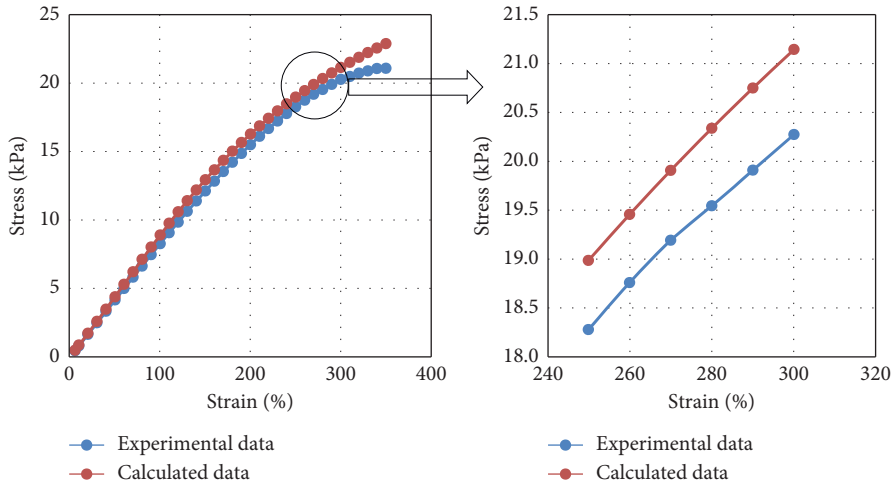

Figure 12: Comparison of the tensile stress calculation data with experimental data obtained in the uniaxial tensile test.

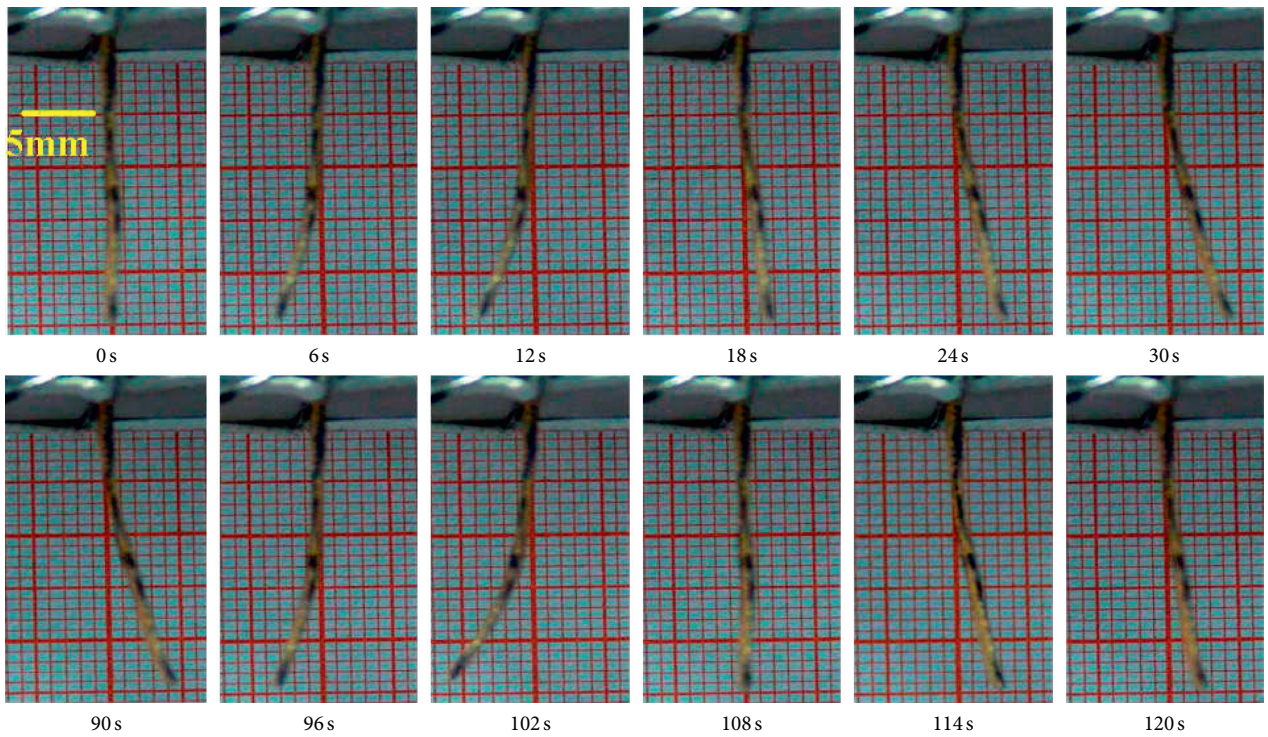

Figure 13: Soft actuator motion screenshots when the input voltage is 4 V.

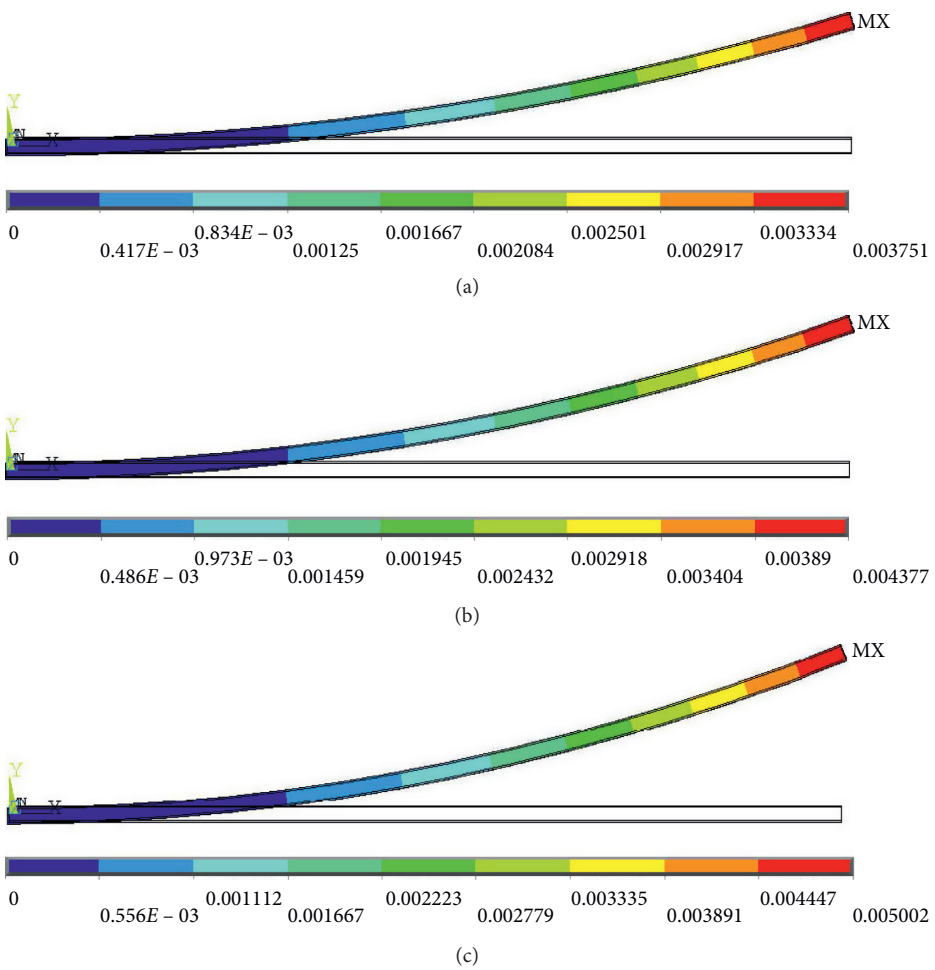

Figure 14: (a–c) Displacement calculation results for the input voltages of 3 V, 3.5 V, and 4 V, respectively.

Table 2: Displacement calculation results for the different input voltages.

Force (V)	3.0	3.5	4.0
Deformation (mm)	3.7	4.3	5.0

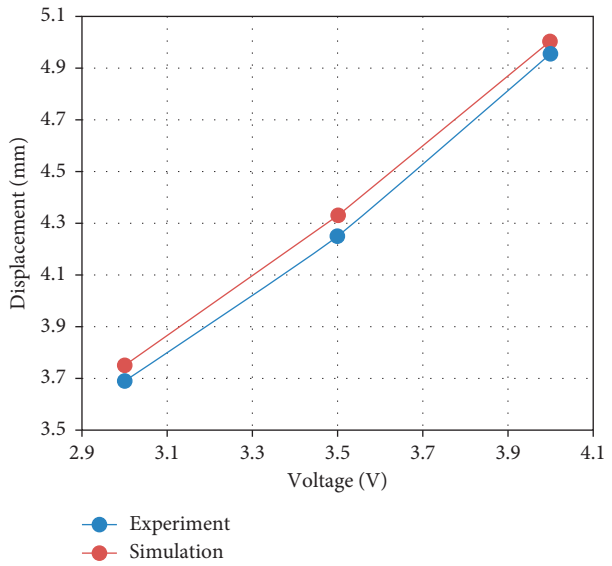

Figure 15: Comparison of the displacement calculation data with experimental data.

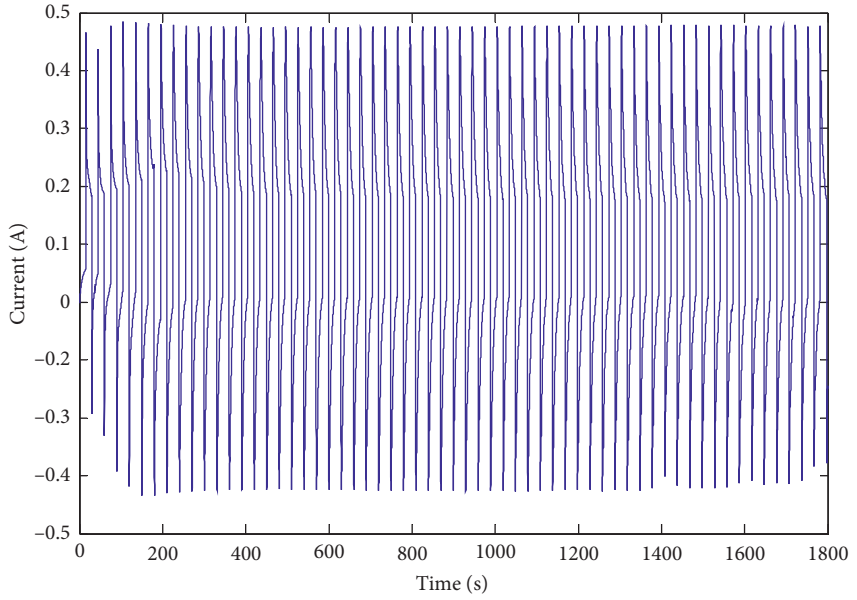

Figure 16: Current response curve of the soft actuator.

The current response stability of the soft actuator is tested by applying a square wave signal with a magnitude of 4 V, a period of 30 s, and a duty cycle of 50%, and the current response curve is shown in Figure 16. The experimental results show that the current peaks remain unchanged over 30 minutes, and the current response of the ILG actuator is stable. Therefore, the internal electrolyte is not substantially decomposed.

From the above experiments, the ILG actuator can maintain stable current response and bending displacement in air. These results show that the ILG actuator can effectively avoid the defects of traditional EAP actuators and has excellent driving performance.

6.4. Experiment of the Soft Robot Grabbing an Object. First, an input voltage of 3.5 V is applied across the electrodes, and the soft robot gradually opens outward. Next, the operating platform is moved close to the target object. Finally, by changing the direction of the supply voltage, the soft robot reversely bends to clamp the object.

Table 3: Parameters of the soft manipulator.

Number	Total length (mm)	Mass (g)	Free segment length (mm)	Width (mm)	Total thickness (mm)	ILG layer thickness (mm)
1	35	0.068	30	5	0.5	0.4
2	35	0.070	30	5	0.5	0.4
3	35	0.073	30	5	0.5	0.4

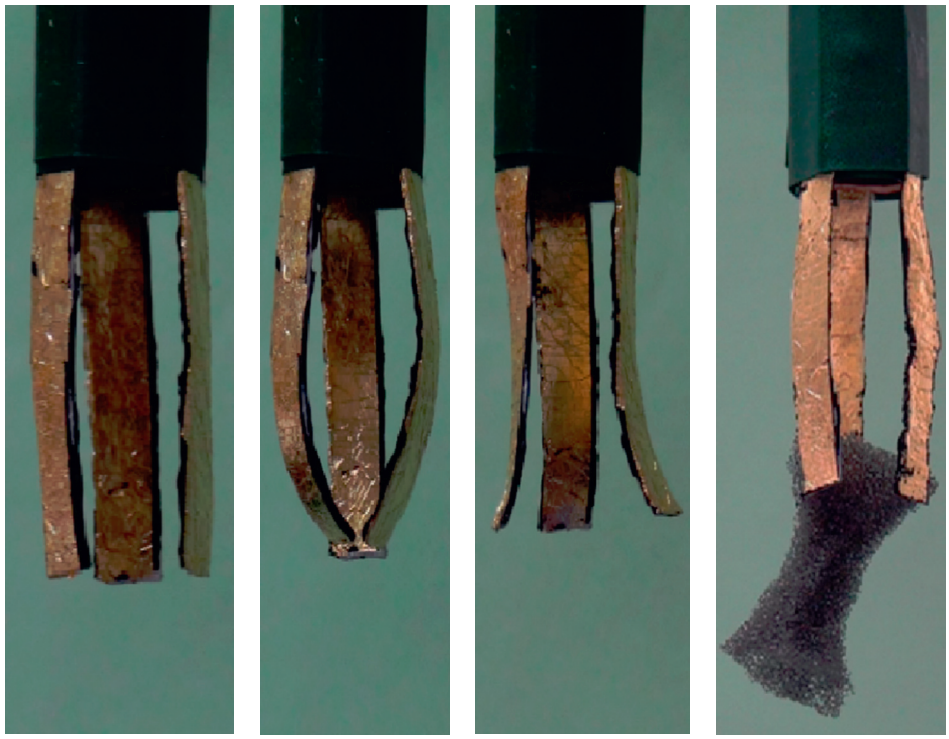

(a) (b) (c) (d)

Figure 17: Screenshots of the soft robot grabbing an object. (a) Natural stretching. (b) Bending inward. (c) Bending outward. (d) Grabbing an object.

The parameters of the soft robot are shown in Table 3. The values 1~3 in the first column are the ILG actuator number, corresponding the three sets of execution components on the manipulator, with a total mass of 211 mg.

A set of screenshots of the soft robot manipulator's experimental process is shown in Figure 17. The process of the soft robot grabbing an object is shown in Figure 3. From Figures 17(a) and 17(b), when no object is grabbed, the deformation of the soft actuator is larger, and the deformation is similar to that in Figure 13. In this case, the mass of the object clamped by the soft robot at an input voltage of 3.5 V is approximately 105 mg. The experiments verify the effectiveness of ILG soft robots.

Compared with the soft robot designed by Saito et al., which has a load capacity of approximately 3 mg, the ILG soft robot designed in this paper has a greatly increased load capacity. Since the soft robot consists of three actuators, this ILG soft robot has better adaptability for grabbing complex shape objects than Saito's soft robot, which consists of two actuators [31].

In addition, the service life is an important performance indicator for EAP robots. The ILG material avoids the defects of IPMCs, and the soft robot proposed in this paper can theoretically work in air for a long time.

7. Conclusions

A soft robot is a new flexible structure, and the materials and mechanism design methods of a soft robot are quite different from those of traditional robots. To avoid the shortcomings of traditional rigid manipulators, such as large energy consumption and complex mechanisms, a soft robot based on a new ILG material is proposed in this paper.

A high-performance ILG actuator based on the principle of light curing was developed, and a modular design method based on motion and constraints was discussed. An ion transport model of porous media based on the Nernst–Planck equation was established, and the deformation mechanism of the ILG actuator was deeply analyzed in combination with the theory of cantilever beam deformation. Based on nonlinear finite element theory, the deformation of the soft robot when grabbing an object was analyzed. A three-finger type soft robot was designed, and the maximum displacement was 5 mm at a 4 V square wave voltage. The soft robot can grab a 105 mg object under a 3.5 V voltage. The results prove that the ILG bionic soft robot has good development prospects.

Data Availability

The data used to support the findings of this study are included within the article.

Conflicts of Interest

The authors declare that there are no conflicts of interest regarding the publication of this paper.

Acknowledgments

This work was supported by the National Natural Science Foundation of China (Grant nos. 51605334, 51705368, 61825303, and U1713215), Natural Science Foundation of Shanghai (Grant no. 17ZR1441800), Shanghai Sailing Program (Grant no. 17YF1420200), and International Exchange Program for Graduate Students, Tongji University (No. 2018020018).

References

[1] M. A. McEvoy and N. Correll, "Materials that couple sensing, actuation, computation, and communication," *Science*, vol. 347, no. 6228, article 1261689, 2015.

[2] B. He, C. Zhang, Y. Zhou, and Z. Wang, "A computing method to determine the performance of an ionic liquid gel soft actuator," *Applied Bionics and Biomechanics*, vol. 2018, Article ID 8327867, 11 pages, 2018.

[3] B. He, Z. Wang, M. Li, K. Wang, R. Shen, and S. Hu, "Wet adhesion inspired bionic climbing robot," *IEEE/ASME Transactions on Mechatronics*, vol. 19, no. 1, pp. 312–320, 2014.

[4] D. Trivedi, C. D. Rahn, W. M. Kier, and I. D. Walker, "Soft robotics: biological inspiration, state of the art, and future research," *Applied Bionics and Biomechanics*, vol. 5, no. 3, pp. 99–117, 2008.

[5] D. Rus and M. T. Tolley, "Design, fabrication and control of soft robots," *Nature*, vol. 521, no. 7553, pp. 467–475, 2015.

[6] W. Zhao, A. Ming, and M. Shimojo, "Development of high-performance soft robotic fish by numerical coupling analysis," *Applied Bionics and Biomechanics*, vol. 2018, Article ID 5697408, 12 pages, 2018.

[7] X. H. Liu, B. He, Z. P. Wang et al., "Tough nanocomposite ionogel-based actuator exhibits robust performance," *Scientific Reports*, vol. 3, p. 6673, 2014.

[8] S. J. Zhang, C. M. Xu, X. M. Lü et al., *Ionic Liquid and Green Chemistry*, Science Press, Beijing, China, 2009, in Chinese.

[9] B. He, C.-H. Zhang, and A. Ding, "Finite element analysis of ionic liquid gel soft actuator," *Chinese Physics B*, vol. 26, no. 12, article 126102, 2017.

[10] S. J. Chang and J. Chen, "Design and fabrication of the large thrust force piezoelectric actuator," *Advances in Materials Science and Engineering*, vol. 2013, Article ID 912587, 2013.

[11] Z. P. Wang, B. He, X. H. Liu, and Q. G. Wang, "Development of soft manipulator based on ionogel," *Chinese Science Bulletin*, vol. 61, no. 23, pp. 2637–2647, 2016, in Chinese.

[12] C. Zhang, B. He, A. Ding, S. Xu, Z. Wang, and Y. Zhou, "Motion simulation of ionic liquid gel soft actuators based on CPG control," *Computational Intelligence and Neuroscience*, vol. 2019, Article ID 8256723, 11 pages, 2019.

[13] J. Newman and K. E. Thomas-Alyea, *Electrochemical Systems*, John Wiley & Sons, Hoboken, NY, USA, 2012.

[14] X. L. Ding and J. M. Selig, "Screw theoretic view on dynamics of spatially compliant beam (in Chinese)," *Applied Mathematics and Mechanics*, vol. 31, no. 9, pp. 1118–1132, 2010.

[15] Y. C. Fung, *Biomechanics: Mechanical Properties of Living Tissues*, Springer-Verlag, New York, NY, USA, 1993.

[16] A. Avanzini and D. Battini, "Integrated experimental and numerical comparison of different approaches for planar biaxial testing of a hyperelastic material," *Advances in Materials Science and Engineering*, vol. 2016, Article ID 6014129, 12 pages, 2016.

[17] J. Bergstrom and M. C. Boyce, "Constitutive modeling of the large strain time-dependent behavior of elastomers," *Journal of the Mechanics and Physics of Solids*, vol. 46, no. 5, pp. 931–954, 1998.

[18] C. Majidi, R. F. Shepherd, R. K. Kramer, G. M. Whitesides, and R. J. Wood, "Influence of surface traction on soft robot undulation," *The International Journal of Robotics Research*, vol. 32, no. 13, pp. 1577–1584, 2013.

[19] C. Majidi, O. M. O'Reilly, and J. A. Williams, "On the stability of a rod adhering to a rigid surface: shear-induced stable adhesion and the instability of peeling," *Journal of the Mechanics and Physics of Solids*, vol. 60, no. 5, pp. 827–843, 2012.

[20] X. Zhou, C. Majidi, and O. M. O'Reilly, "Soft hands: an analysis of some gripping mechanisms in soft robot design," *International Journal of Solids and Structures*, vol. 64-65, pp. 155–165, 2015.

[21] K. Suzumori, S. Endo, T. Kanda, and N. Kato, "A bending pneumatic rubber actuator realizing soft-bodied manta swimming robot," in *Proceedings 2007 IEEE International Conference on Robotics and Automation*, pp. 4975–4980, Rome, Italy, April 2007.

[22] N. Faruksenan, O. Oreilly, and T. Tresierras, "Modeling the growth and branching of plants: a simple rod-based model," *Journal of the Mechanics and Physics of Solids*, vol. 56, no. 10, pp. 3021–3036, 2008.

[23] X. Zhou, C. Majidi, and O. M. O'Reilly, "Flexing into motion: a locomotion mechanism for soft robots," *International Journal of Non-Linear Mechanics*, vol. 74, pp. 7–17, 2015.

[24] P. F. Pai, *Highly Flexible Structures: Modeling, Computation, and Experimentation*, American Institute of Aeronautics and Astronautics, Reston, VA, USA, 2007.

[25] K. J. Bathe, *Finite Element Procedures*, Prentice Hall, Upper Saddle River, NJ, USA, 1996.

[26] H. Shi, H. Salim, Y. Shi, and F. Wei, "Geometric and material nonlinear static and dynamic analysis of space truss structures," *Mechanics Based Design of Structures and Machines*, vol. 43, no. 1, pp. 38–56, 2014.

[27] H. Shi and H. Salim, "Geometric nonlinear static and dynamic analysis of guyed towers using fully nonlinear element formulations," *Engineering Structures*, vol. 99, pp. 492–501, 2015.

[28] X. Guo, D. Liu, W. Zhang, L. Sun, and S. Chen, "Nonlinear dynamic analysis of macrofiber composites laminated shells," *Advances in Materials Science and Engineering*, vol. 2017, Article ID 4073591, 17 pages, 2017.

[29] J. N. Reddy, *An Introduction to Nonlinear Finite Element Analysis*, Oxford University Press, New York, NY, USA, 2004.

[30] T. Fukushima, K. Asaka, A. Kosaka, and T. Aida, "Fully plastic actuator through layer-by-layer casting with ionic-liquid-based bucky gel," *Angewandte Chemie International Edition*, vol. 44, no. 16, pp. 2410–2413, 2005.

[31] S. Saito, Y. Katoh, H. Kokubo, M. Watanabe, and S. Maruo, "Development of a soft actuator using a photocurable ionic gel," *Journal of Micromechanics and Microengineering*, vol. 19, no. 3, article 035005, 2009.

Hindawi
Advances in Materials Science and Engineering
Volume 2019, Article ID 3534807, 8 pages
https://doi.org/10.1155/2019/3534807

Research Article

Nanoliposomal L-Asparaginase and Its Antitumor Activities in Lewis Lung Carcinoma Tumor-Induced BALB/c Mice

Thi Thao Do,[1,2] **Thi Phuong Do**,[1] **Thi Nga Nguyen**,[1] **Thi Cuc Nguyen**,[1] **Thi Thu Phuong Vu**,[1] **and Thi Giang An Nguyen**[3]

[1]*Institute of Biotechnology, Vietnam Academy of Science and Technology, 18 Hoang Quoc Viet Road, Nghia Do, Cau Giay, Ha Noi, Vietnam*
[2]*Graduate University of Science and Technology, Vietnam Academy of Science and Technology, 18 Hoang Quoc Viet Road, Nghia Do, Cau Giay, Ha Noi, Vietnam*
[3]*School of Natural Sciences Education, Vinh University, 182 Le Duan Str, Vinh, Nghe An Province, Vietnam*

Correspondence should be addressed to Thi Thao Do; thaodo74@yahoo.com

Received 14 January 2019; Revised 15 March 2019; Accepted 18 March 2019; Published 2 May 2019

Guest Editor: Dinh Quang Khieu

Although L-Asparaginase (L-ASP) is an effective chemotherapeutic agent, it has side effects such as fever, skin rashes, chills, anaphylaxis, and severe allergic reactions. Moreover, the short half-life of L-ASP reduces its antitumor activity. To reduce its side effects and broaden its pharmaceutical applications, L-ASP obtained from *Pectobacterium carotovorum* was subjected to liposomal conjugation. The enzyme was then loaded into liposomes using the hydrated thin-film method. The *in vitro* cytotoxic activity of liposomal L-ASP was evaluated with the MTT assay using cancerous cell lines, and its antitumor effects were examined in Lewis lung carcinoma (LLC) tumorized mice. The average size of the liposomes containing purified L-asparagine was 93.03 ± 0.49 nm. They had a zeta potential of -15.45 ± 6.72 mV, polydispersity index of 0.22 ± 0.02, and encapsulation efficiency of $53.99 \pm 5.44\%$. The *in vitro* cytotoxic activity of liposomal L-ASP was less effective against LLC, MCF-7 (human breast carcinoma), HepG2 (human hepatocellular carcinoma), SK-LU-1 (human lung carcinoma), and NTERA-2 (pluripotent human embryonic carcinoma) cells than that of free L-ASP. However, the antitumor activity of liposomal L-ASP was significantly greater than that of untrapped L-ASP at the same doses (6 UI/mouse) in terms of tumor size ($6309.11 \pm 414.06\ mm^3$) and life span (35.00 ± 1.12 days). This is the first time the antitumor activities of PEGylated nanoliposomal L-ASP have been assessed in LLC carcinoma tumor-induced BALB/c mice and showed significantly improved pharmacological properties compared to those of free L-ASP ($P < 0.05$). Thus, nanoliposomal L-ASP should be considered for its widening applications against carcinoma tumors.

1. Introduction

L-Asparaginase (L-ASP) hydrolyzes L-asparagine into L-aspartate and ammonia and is used to treat acute lymphoblastic leukemia (ALL) and non-Hodgkin lymphoma [1]. Although the enzyme has been a mainstay in the treatment of ALL [2–4], it can induce fever, skin rashes, chills, anaphylaxis, and severe allergic reactions [5, 6]. Continued treatment leads to frequent hypersensitivity reactions in the enzyme as a foreign protein [7, 8]. To minimize the incidence of systemic immunological reactions and other limitations of L-ASP, liposomal encapsulation of the enzyme using different techniques has been adopted. The main components of liposomes are phospholipids, which are similar to cell membranes [9]. The phospholipids form a bilayer membrane, which allows drugs with different physicochemical properties to be loaded into the liposome or conjugated into the biolayers and then delivered to a lesion [10]. When liposomes are loaded with enzymes, they can be targeted to organs such as the spleen, liver, and bone marrow [11], prolonging the circulation time without inhibiting enzymatic activities [12]. L-ASP was clarified for its antitumor activities in breast tumor bearing mice by Shiromizu et al. [13]. However, liposomal L-ASP has been

only reported for its improvement *in vivo* anticancer activities in lymphomatic mice [11]. Therefore, we developed PEGylated nanoliposomal L-ASP and first time evaluated its antitumor efficacy in Lewis lung carcinoma (LLC) tumorized BALB/c mice for broadening its pharmaceutical applications.

2. Materials and Methods

2.1. Materials. The bacterial strain *Pectobacterium carotovorum* was provided by Prof. Gilles Truan (Axe Biocatalyse/Ingénieries Métabolique et Moléculaire, LISBP, INSA, Toulouse, France). The strain was used for the production of L-ASP enzyme. 1,2-Distearoyl-*sn*-glycero-3-phosphoethanolamine-N-[amino(polyethylene glycol)-2000] (DSPE-PEG-2000) was purchased from Avanti polar lipids Inc. (Alabaster, Alabama, USA). Cholesterol, soybean lecithin, fetal bovine serum (FBS), and gentamicin was obtained from Sigma Chemical Co. (St. Louis, MO., USA). Dulbecco's modified Eagle's medium and nonessential amino acid (NAA) and L-glutamine was purchased from Invitrogen (Carlsbad, CA, USA).

2.2. Animals. Male and female albino BALB/c mice (8–10 weeks old) were obtained from the Institute of Biotechnology, Vietnam Academy of Science and Technology (VAST, Hanoi, Vietnam). All mice were housed in a temperature-controlled room on a 12-hour light/12-hour dark cycle with food and water ad libitum. Experiments were performed in accordance with Vietnamese Ethical Laws and European Communities Council Directives of November 24, 1986 (86/609/EEC) guidelines for the care and use of laboratory animals.

2.3. Isolation, Extraction, and Purification of L-Asparaginase. The bacterium was cultivated in the optimal medium to produce L-asparaginase as reported by Gulati et al. [14]. In details, the inoculum was prepared by adding a loop full of 250 ml cultivated medium in a 1 L flask and incubated at 30°C, 180 rpm in a shaking incubator for 12 h (to reach the culture OD at 600 nm = 0.6 to 0.8). The continued 2% of the inoculum was continuously incubated in a shaking incubator at 30°C, 180 rpm for additional 24 h. Cells were harvested by centrifugation at 10,000 g for 10 min at 4°C. Cells were washed with 50 mM Tris-HCl buffer (pH 8, 6) and resuspended in the same buffer. The cells were cooled on ice and ultrasonicated at 20 MHz, 35% amplitude, 20 min. The lysate was centrifuged at 20,000 g for 10 min at 4°C. The clear supernatant was loaded on DEAE cellulose and Sephadex G-100 chromatography for purification. The obtained eluted fractions were protein-quantitated using Pierce BCA Protein Assay Kit (Thermo Scientific) and qualified using SDS-PAGE [15].

2.4. Determination of L-Asparaginase Activity. L-ASP activity was measured by the modified method of Wriston [16] in which the rate of ammonia formation will be detected by Nessler' reagent at 37°C. One unit of L-ASP activity was defined that liberates the amount of enzyme that released 1 μM of ammonia (with 10 μM–10 mM ammonium sulfate as the standard) per minute under the assay conditions.

2.5. Procedure for the Preparation of L-ASP Nanoliposomes. L-ASP was entrapped into liposomes by thin film dehydration-rehydration method, as Cruz et al. [17] with slight modification. Briefly, soybean lecithin (40 μmol), cholesterol (4 μmol), and DSPE-PEG-2000 (8 μmol) were dissolved in chloroform : methanol (9 : 1 v/v) and stirred mechanically to form homogeneous mixture in round bottom flask. The solvent was removed using a rotary evaporator under an aspirate vacuum (25 mmHg) and a water bath with the temperature maintained at 25°C. The thin film which formed on the walls of the flask was dispersed in 2 ml of 5 mM potassium phosphate buffer (pH 7.5) containing L-ASP (150 I.U.) and rotated without vacuum at 100 rpm, 25°C. Then, the multilamellar vesicles were sonicated three times at 30 seconds intervals for resizing before filtered through 0.22 μm membrane to receive the L-ASP liposomal mixture. Finally, the liposomal mixture was washed twice with normal saline.

The particle size, zeta potentials, and size distribution of liposomes were determined using a Zetasizer Nano-Z (Malvern Instruments, UK). The conjugates were also observed by high-solution transmission electronic microscopy (TEM) (Jeol 1200EX TEM, Jeol Company, Tokyo, Japan). The liposomal samples were mounted on metal stands and coated with gold to thickness of 200–500 A°. Then, the plates were magnified 200x to capture the morphology of the prepared liposomes.

2.6. Determination of Encapsulation Efficiency (EE). After preparation, liposomal solution was loaded to Vivaspin column and centrifuged at 3000 RCF for 20 min, 25°C to remove the free L-ASP. The liposome pellet was lysed with 10% Triton X-100 to disrupt the liposomal bilayer and to release L-ASP. The Bradford assay was used to determine the amount of released L-ASP. Encapsulation efficiency of L-ASP into liposomes is determined as the following formula [18]:

$$\text{EE\%} = \frac{C_f}{C_i} \times 100, \quad (1)$$

where C_f is the encapsulated amount of L-ASP into liposomes measured after lysing with 10% Triton-X 100 and C_i is the L-ASP amount added to the lipid mixture.

2.7. Antiproliferative Activities of L-ASP Encapsulated Nanoliposomes. The antiproliferative assays were carried out in triplicate in 96-well microtiter plates against LLC (Lewis lung carcinoma), MCF-7 (human breast carcinoma), HepG2 (human hepatocellular carcinoma), SK-LU-1 (human lung carcinoma), and NTERA-2 (pluripotent human embryonic carcinoma) cells. Those cells were maintained in Dulbecco's modified Eagle's medium supplemented with 10% FBS (Sigma-Aldrich, St. Louis, MO),

1% antibiotic-antimycotic (Thermo Fisher), 1% nonessential amino acid, and 2 mM of L-glutamine. For MCF-7, insulin was added to the growth medium at 10 μg/ml concentration. All cells were incubated in a humidifier with 5% CO_2 at 37°C and subcultured every 2-3 days. The cancer cells were seeded into a 96-well plate at a density of 1×10^4 cells/well. Then nanoliposomal conjugates were added to reach the final concentration ranging from 0.01–2.5 UI/mL and incubated for further 72 h. To assess effect of liposomes on cell viability, the MTT assay was performed as previously described [19].

2.8. Antitumor Efficiency of L-ASP Encapsulated Liposomes. The experiment was carried out using BALB/c mice at 20–25 gr weight. Mice were inoculated by subcutaneously injection with 1×10^6 LLC cells to induce tumor. On the day 7th of LLC cell injection, mice were randomly divided into 4 groups (6 mice per group) including a control group, two treated groups of liposomal L-ASP (6 UI/mouse and 3 UI/mouse), and the free L-ASP treated group (6 UI/mouse). The drugs were administrated intravenously every 2 days. Growth of tumor was determined by caliper measurements in two dimensions, length (L) and width (W), every 7 days. The tumor volume (V) was calculated using the formula $V = 1/2 \times L \times W^2$ [20].

The survival time of mice in all experimental groups were recorded. It was calculated from the day of LLC cell inoculation to the day of death, and percentage increase in average life span (ILS) was calculated by the formula % $\text{ILS} = (A/B - 1) \times 100$ in which A means survival time of treated, B is mean survival time of control group, and ILS is increase in average life span group.

2.9. Statistical Analysis. Statistical analyses and significance, as measured by two-way analysis of variance (ANOVA), were performed using GraphPad PRISM 5.0 software (GraphPad Software, USA). In all comparisons, $P < 0.05$ was considered statistically significance.

3. Results and Discussion

3.1. Isolation, Purification, and Determination of L-ASP Activity. First, L-ASP crude extract was purified in three steps with a final yield of 23.5% and a purification fold of 9.38 (Table 1). The estimated molecular weight of the obtained enzyme was 36 kDa (Figure 1). This purified enzyme was used for further liposomal conjugation.

3.2. Physicochemical Characteristics of Liposomal L-ASP. Generally, the components of a bilayer have strong effects on the rigidity, fluidity, and toxicity of the phospholipid bilayer [21]. Nontoxic phospholipids are usually selected to reduce toxicity and to strengthen drug-liposomal conjugates, including natural and synthetic phospholipids such as soybean lecithin and DSPE-PEG-2000 [10]. Soybean lecithin is a natural phospholipid that is often used for large-scale industrial applications to reduce production costs [22]. DSPE-PEG-2000 is reported elsewhere as important breakthrough in the liposomal development pertaining stealth behavior [23]. Cholesterol is often used in liposomal formulation because it facilitates complex interactions with phospholipids and other lipids in cellular membranes [24]. Therefore, we used soybean lecithin, DSPE-PEG-2000, and cholesterol to make liposomal L-ASP, encapsulating the purified L-ASP using the rehydrated thin film method. The resulting liposomes were 93.03 ± 0.49 nm in size with a polydispersity index of 0.22 ± 0.02, indicating that the size distribution was quite homogeneous. The zeta potential is a measure of the magnitude of electrostatic or charge repulsion between particles, which affects liposome stability [25–27]. The liposomes harboring L-ASP had a zeta potential of -15.45 ± 6.72 mV, the opposite of liposomes reported by Bahreini et al. that were made from chitosan and tripolyphosphate using ionotropic gelation [28]. The entrapment efficiency was determined as the ratio of encapsulated L-ASP to the amount used to prepare the liposomes. The encapsulation efficiency was 53.99%, demonstrating that L-ASP was effectively loaded into the liposomes (Table 2).

3.3. High-Resolution Transmission Electron Microscopic Analysis. High-resolution transmission electron microscope (TEM) was used to evaluate the size, shape, and morphology of the L-ASP liposomes [26]. On TEM, the L-ASP liposomal particles were spherical and evenly dispersed (Figure 2). The obtained liposomes were nanometers in size (Figure 2).

3.4. Cytotoxicity Activities. The effects of free and liposomal L-ASP on the survival of LLC (Lewis lung carcinoma), MCF-7 (human breast carcinoma), HepG2 (human hepatocellular carcinoma), SK-LU-1 (human lung carcinoma), and NTERA-2 (pluripotent human embryonic carcinoma) cell lines were evaluated using the MTT assay. The cytotoxic activity of the liposomal L-ASP was dependent on the cancer cell line and concentrations tested (Table 3 and Figure 3). SK-LU-1 cells were the most sensitive to liposomal L-ASP and to the unloaded enzyme. The conjugates had similar activity on SK-LU-1 and LLC cells, with IC_{50} values of 0.21 ± 0.03 and 0.23 ± 0.02 UI/mL, respectively. MCF-7 cells were the least sensitive to both free and liposomal L-ASP. A decrease in the L-ASP concentration led to reduced cell death in all cell lines tested. Generally, malignant cells have a high division rate and need more nutrients than normal cells. Asparagine is important in cell growth and function, as it coordinates protein and nucleotide synthesis [29]. L-ASP induces cytotoxicity by breaking asparagine into L-aspartate and ammonia. According to Moharib, the cytotoxic activity of L-ASP is closely related to asparagine, and the asparagine level differed among various cell lines [30]. Therefore, L-ASP induced cancer cell death to varying degrees. However, the cytotoxic activity of the liposomal L-ASP was 3.00–5.68 times lower than that of free L-ASP after 72 h of treatment. In general, and with L-ASP, liposomal formulations are significantly less toxic than the unconjugated forms because of slow uptake. In our study, the L-ASP liposomes were less active against all cancer cells, in agreement with other studies

Table 1: Purification profile of isolated L-ASP.

Steps	Total activity (IU)	Total protein (mg)	Specific activity (IU/mg)	Purification fold	Yield (%)
Crude extract	5972	276.5	21.6	0	100
Ammonium sulfate precipitation	2204	65.4	33.7	1.56	36.9
Sephadex G-100 chromatography	1403	6.9	202.6	9.38	23.5

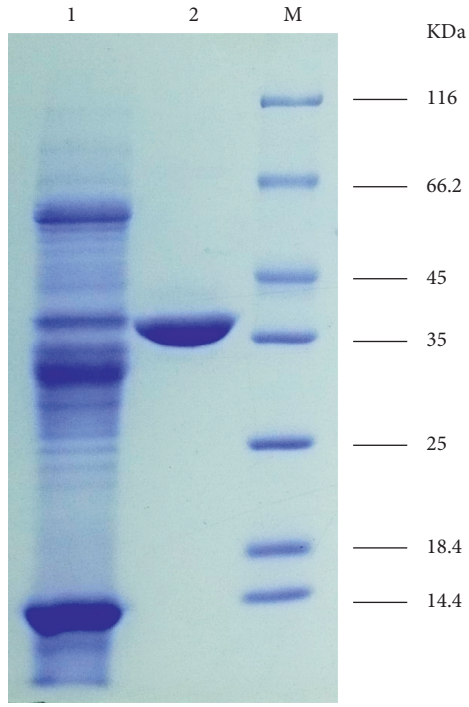

Figure 1: Molecular weight analysis of purified L-ASP obtained from *P. carotovorum* using SDS-PAGE on 12.5% gel of stained with coomassie blue; M-Fermentas ladder; 1-crude extract of L-ASP; 2-purified L-ASP.

Table 2: Determined physiochemical characteristics of liposomes loaded L-ASP.

Samples	Size (nm)	PDI	Zeta potential (mV)	EE (%)
Blank liposome*	97.53 ± 22.17	0.24 ± 0.02	−22.80 ± 0.00	—
L-ASP-liposome	93.03 ± 0.49	0.22 ± 0.02	−15.45 ± 6.72	53.99 ± 5.44

*Blank liposome containing soy lecithin, cholesterol, and DSPE-PEG2000.

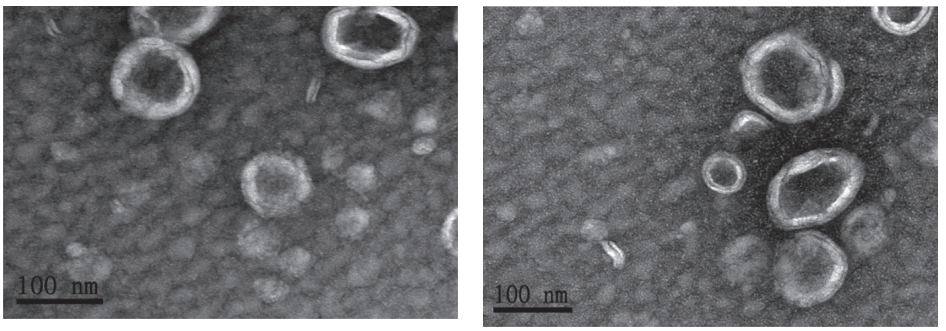

(a) (b)

Figure 2: The TEM images of nanoliposomes (Jeol 1200EX TEM system, Japan) (a) DSPE-PEG2000-soy lecithin-cholesterol-loaded L-ASP nanoliposomes; (b) blank liposomal nanospheres.

Table 3: Cytotoxic activities of L-ASP-encapsulated liposomes and free L-ASP on different cell lines.

Samples	Values of IC_{50} (UI/ml)				
	LLC	HepG2	SK-LU-1	MCF-7	NTERA-2
Loaded L-ASP liposomes	0.23 ± 0.02	0.28 ± 0.01	0.21 ± 0.03	0.36 ± 0.05	0.23 ± 0.02
Free L-ASP	0.079 ± 0.001	0.044 ± 0.004	0.037 ± 0.001	0.12 ± 0.01	0.038 ± 0.003

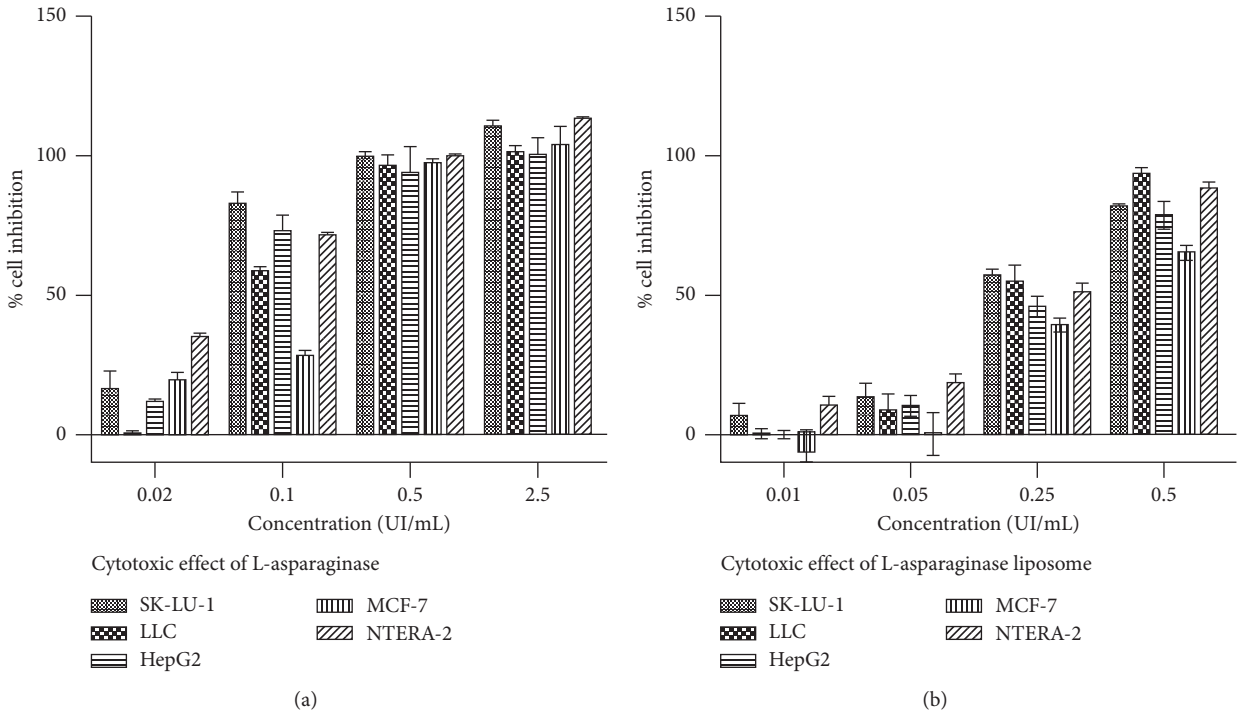

Figure 3: Effectiveness of free L-ASP (a) and L-ASP-encapsulated liposomes (b) on different cell lines. Cultured cells (1×10^4 cells/well) were treated with different concentrations of either liposomal (a) or free L-ASP (b). Normal saline was served as the negative control. Each value represents the mean ± SD.

[17]. The reduction in L-ASP cytotoxicity with liposomal encapsulation might be due to the slower release rate and slower substrate depletion, allowing cells to adapt and synthesize asparagine themselves.

3.5. In Vivo Antitumor Activity of Liposomal L-ASP. The antitumor activity of liposome-L-ASP was examined in BALB/c mice harboring tumors induced by LLC cells (Figure 4). Groups of mice were treated with two doses of liposomal L-ASP (6 or 3 UI/mouse) or free L-ASP (6 UI/mouse) intravenously. The tumor volumes of the mice were analyzed at different time points. Dose-dependent antitumor activity of liposomal L-ASP was observed. Twenty-eight days after LLC inoculation, the tumors of the group treated with 6 UI liposomal L-ASP measured $6309.11 \pm 414.06\ mm^3$, which was significantly smaller than in the negative control ($9{,}319.35 \pm 469.58\ mm^3$, $P < 0.01$). Liposomal L-ASP suppressed tumor growth more strongly and significantly at a dose of 6 UI than at a dose of 3 UI ($7{,}885.80 \pm 824.36\ mm^3$) ($P < 0.05$). The tumors in the group treated with free L-ASP ($7{,}544.94 \pm 284.05\ mm^3$) were larger than those in the group treated with liposomal L-ASP at the same dose (6 UI/mouse), and this difference was significant ($P < 0.05$) (Figure 4). The mice treated with 6 UI/mouse untrapped L-ASP showed smaller volumes of tumors in comparison with the 3 UI/mouse liposomal treated group but no significance was observed ($P > 0.05$). The mean body weight of the mice in the liposomal L-ASP groups was similar to that of the negative controls at the end of the experiment, indicating that the encapsulation did not induce toxicity (data not shown).

Furthermore, the administration of liposomal L-ASP prolonged the lives of the mice (Table 4). The median survival of mice treated with 6 UI liposomal L-ASP was 35.00 ± 1.13 days, which was 12.30% longer than that of control mice ($P < 0.05$). The life span also increased slightly in the free L-ASP group, but not significantly.

Since the early 1970s, L-ASP has been used to treat ALL. Currently, L-ASP is also used to treat ovarian cancer, hepatocellular carcinoma, and gastric carcinoma [31]. However, L-ASP can induce fever, thrombosis, and impaired liver, kidney, and central nervous system function, which may be related to the glutaminase activity of L-ASP [32].

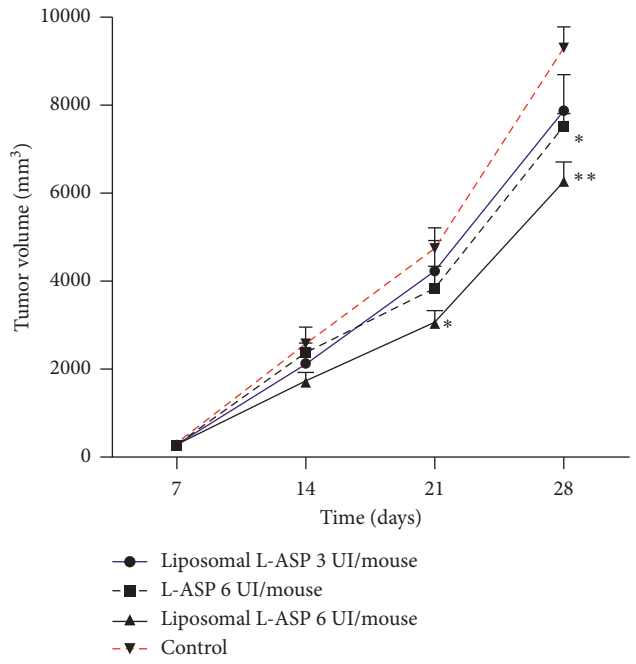

Figure 4: Tumor growth after treatment with free L-ASP or liposomal L-ASP. BALB/c mice harboring tumors induced by LLC cells were treated with either free L-ASP (6 UI/mouse) or encapsulated L-ASP liposomes at either 6 UI/mouse or 3 UI/mouse ($n = 6$). Liposome-entrapped L-ASP at both doses 6 UI/mouse and 3 UI/mouse significantly inhibited tumor growth after 28 days compared with the negative control (blank liposome) ($^{**}P < 0.01$ and $^{*}P < 0.05$, respectively). Error bars represent standard error (SE).

Table 4: Effects of liposome-L-ASP and free L-ASP on survival time of LLC cells bearing mice from different experimented groups (mean ± SE) ($n = 6$).

Groups	Mean survival time (days)	% ILS
Control group (blank lipsosome)	31.17 ± 1.28	—
Liposomal-L-ASP (3 UI/mouse)	33.33 ± 0.92	6.95
Liposomal-L-ASP (6 UI/mouse)	35.00 ± 1.13*	12.30
Free L-ASP (6 UI/mouse)	32.17 ± 0.79	3.21

*$P < 0.05$ in comparison with the control group (blank liposome).

According to Kumar et al. [15], L-ASP from *Pectobacterium carotovorum* is free of glutaminase activity, which might avoid the disadvantages of L-ASP isolated from bacteria such as *Escherichia coli* and *Erwinia chrysanthemi*. In our study, both free and liposomal L-ASP isolated from *P. carotovorum* showed strong activity against various solid cancer cell lines, including lung, liver, and breast carcinomas and pluripotent human embryonic carcinoma cells. Shiromizu et al. reported similar activity of L-ASP in colon cancer (C-26), a murine sarcoma cell line (S-180), and murine breast cancer (4T1) [13].

Other limitations of L-ASP treatment include its short biological half-life ($T_{50} = 2.88$ h), which necessitates increasing the dosage and intervals of L-ASP treatment [33]. Liposomes are considered an effective solution to these obstacles. Since their discovery in the 1960s, liposomes have been used as drug carriers to enhance the potency and to reduce the toxicity of therapeutic agents. Liposomes also improve the delivery of therapeutic agents to specific sites in the body [18, 34]. As reported elsewhere, solid tumors show enhanced permeability by and retention of lipids and macromolecules [35, 36]. Some effects in some solid tumors are not observed in normal tissues or organs, such as extensive angiogenesis and impaired lymphatic drainage/recovery [37]. These effects lead to higher delivery of a liposome-encapsulated drug to tumors compared with other sites. However, the size of liposomes affects the circulation of drug-loaded liposomes, especially liposomal L-ASP. Larger liposomes are easily opsonized and then rapidly removed from the blood by the mononuclear phagocytic system [38], whereas small liposomes (range 50–200 nm) increase the circulation time of loaded molecules, such as enzymes [39]. With the thin film method, simplified dehydration-rehydration vesicles produce large liposomes. However, our use of bath sonication produced liposomes smaller than 200 nm. This suitable average size helps to prolong the retention time of circulating liposomal L-ASP *in vivo* and its accumulation in tumors.

Additionally, the PEGylation of the liposomes helped them to avoid recognition by the mononuclear phagocytic system. Other outstanding features of PEG-coated liposomes include avoiding aggregation between liposomal particles and reduced clearance and immunogenicity [40]. These result in higher antitumor efficacy of liposomal L-ASP *in vivo*. However, the drug release rates of PEGylated formulations were lower than those with no PEGylation [41, 42], which may be an additional explanation for the lower *in vitro* cytotoxic activity of liposomal L-ASP.

4. Conclusion

Using the dehydrate-rehydrate thin film method, L-ASP was effectively encapsulated into liposome carriers at an efficiency of 53.99 ± 5.44%. PEGylated nanoliposomal L-ASP first showed significantly improved antitumor activities compared to those of free L-ASP ($P < 0.05$) in LLC induced BALB/c mice but showed lower activity in an *in vitro* assay. Our PEGylated nanoliposomal L-ASP exhibited improved pharmacological properties and bioavailability and should be considered for further clinical applications against carcinoma tumors.

Data Availability

The physicochemical data of blank and liposomal L-ASP used to support the findings of this study are included within the supplementary information files.

Conflicts of Interest

The authors report no conflicts of interest.

Acknowledgments

The authors acknowledge the financial support from Vietnam Academy of Science and Technology [1] under the

grants VAST04.10/18–19 and VAST.HTQT.PHAP.02/17-18.

Supplementary Materials

Supplementary Table 1: concentration of L-ASP in nanoliposomes. Supplementary Table 2: relative concentration of L-ASP with concentration of liposomes in Figure 3(B). Supplementary Figure 1: normalized tumor volume change to body weight after treatment with free L-ASP or liposomal L-ASP at different times. BALB/c mice harboring tumors induced by LLC cells were treated with either free L-ASP (6 UI/mouse) or encapsulated L-ASP liposomes at either 6 UI/mouse or 3 UI/mouse ($n = 6$). Liposome-entrapped L-ASP at both doses 6 UI/mouse and 3 UI/mouse significantly inhibited tumor growth after 28 days compared with the negative control (blank liposome) ($^{**}P < 0.01$ and $^{*}P < 0.05$, respectively). Error bars represent standard error (SE). (*Supplementary Materials*)

References

[1] A. Shrivastava, A. A. Khan, M. Khurshid, M. A. Kalam, S. K. Jain, and P. K. Singhal, "Recent developments in L-Asparaginase discovery and its potential as anticancer agent," *Critical Reviews in Oncology/Hematology*, vol. 100, pp. 1–10, 2016.

[2] M. Amylon, J. Shuster, J. Pullen et al., "Intensive high-dose asparaginase consolidation improves survival for pediatric patients with T cell acute lymphoblastic leukemia and advanced stage lymphoblastic lymphoma: a pediatric oncology group study," *Leukemia*, vol. 13, no. 3, pp. 335–342, 1999.

[3] I. Hann, S. Richards, A. Vora et al., "Benefit of intensified treatment for all children with acute lymphoblastic leukaemia: results from MRC UKALL XI and MRC ALL97 randomised trials," *Leukemia*, vol. 14, no. 3, pp. 356–363, 2000.

[4] M. Schrappe, A. Reiter, W. D. Ludwig et al., "Improved outcome in childhood acute lymphoblastic leukemia despite reduced use of anthracyclines and cranial radiotherapy: results of trial ALL-BFM 90. German-Austrian-Swiss ALL-BFM Study Group," *Blood*, vol. 95, no. 11, pp. 3310–3322, 2000.

[5] V. J. Land, W. W. Sutow, D. J. Fernbach, D. M. Lane, and T. E. Williams, "Toxicity of L-Asparaginase in children with advanced leukemia," *Cancer*, vol. 30, no. 2, pp. 339–347, 1972.

[6] H. F. Oettgen, P. A. Stephenson, M. K. Schwartz et al., "Toxicity of *E. coli* L-Asparaginase in man," *Cancer*, vol. 25, no. 2, pp. 253–278, 1970.

[7] R. W. Baldwin, "Experimental and clinical effects of L-Asparaginase," *Immunology*, vol. 21, no. 4, p. 727, 1971.

[8] R. G. Peterson, R. E. Handschumacher, and M. S. Mitchell, "Immunological responses to L-Asparaginase," *Journal of Clinical Investigation*, vol. 50, no. 5, pp. 1080–1090, 1971.

[9] H. Daraee, A. Etemadi, M. Kouhi, S. Alimirzalu, and A. Akbarzadeh, "Application of liposomes in medicine and drug delivery," *Artificial Cells, Nanomedicine, and Biotechnology*, vol. 44, no. 1, pp. 381–391, 2016.

[10] J. Li, X. Wang, T. Zhang et al., "A review on phospholipids and their main applications in drug delivery systems," *Asian Journal of Pharmaceutical Sciences*, vol. 10, no. 2, pp. 81–98, 2015.

[11] J. O. C. S. Jorge, R. Perez-Soler, J. G. Morais, and M. E. N. M. Cruz, "Liposomal palmitoyl-L-Asparaginase: characterization and biological activity," *Cancer Chemotherapy and Pharmacology*, vol. 34, no. 3, pp. 230–234, 1994.

[12] M. Jahadi and K. Khosravi-Darani, "Liposomal encapsulation enzymes: from medical applications to kinetic characteristics," *Mini-Reviews in Medicinal Chemistry*, vol. 17, no. 4, pp. 366–370, 2017.

[13] S. Shiromizu, N. Kusunose, N. Matsunaga, S. Koyanagi, and S. Ohdo, "Optimizing the dosing schedule of L-Asparaginase improves its anti-tumor activity in breast tumor-bearing mice," *Journal of Pharmacological Sciences*, vol. 136, no. 4, pp. 228–233, 2018.

[14] R. Gulati, R. K. Saxena, and R. Gupta, "A rapid plate assay for screening L-Asparaginase producing micro-organisms," *Letters in Applied Microbiology*, vol. 24, no. 1, pp. 23–26, 1997.

[15] S. Kumar, V. Venkata Dasu, and K. Pakshirajan, "Purification and characterization of glutaminase-free L-Asparaginase from *Pectobacterium carotovorum* MTCC 1428," *Bioresource Technology*, vol. 102, no. 2, pp. 2077–2082, 2011.

[16] J. C. Wriston Jr., "[79] asparaginase," *Glutamate, Glutamine, Glutathione, and Related Compounds*, vol. 113, pp. 608–618, 1985.

[17] M. E. M. Cruz, M. M. Gaspar, F. Lopes, J. S. Jorge, and R. Perez-Soler, "Liposomal L-Asparaginase: in vitro evaluation," *International Journal of Pharmaceutics*, vol. 96, no. 1–3, pp. 67–77, 1993.

[18] P. R. Kulkarni, J. D. Yadav, and K. A. Vaidya, "Liposomes: a novel drug delivery system," *International Journal of Current Pharmaceutical Research*, vol. 3, no. 2, pp. 10–18, 2011.

[19] D. A. Scudiero, R. H. Shoemaker, K. D. Paull et al., "Evaluation of a soluble tetrazolium/formazan assay for cell growth and drug sensitivity in culture using human and other tumor cell lines," *Cancer Research*, vol. 48, no. 17, pp. 4827–4833, 1988.

[20] M. M. Jensen, J. T. Jørgensen, T. Binderup, and A. Kjaer, "Tumor volume in subcutaneous mouse xenografts measured by microCT is more accurate and reproducible than determined by 18F-FDG-microPET or external caliper," *BMC Medical Imaging*, vol. 8, no. 1, 2008.

[21] A. Akbarzadeh, R. Rezaei-Sadabady, S. Davaran et al., "Liposome: classification, preparation, and applications," *Nanoscale Research Letters*, vol. 8, no. 1, p. 102, 2013.

[22] P. van Hoogevest and A. Wendel, "The use of natural and synthetic phospholipids as pharmaceutical excipients," *European Journal of Lipid Science and Technology*, vol. 116, no. 9, pp. 1088–1107, 2014.

[23] O. Nag and V. Awasthi, "Surface engineering of liposomes for stealth behavior," *Pharmaceutics*, vol. 5, no. 4, pp. 542–569, 2013.

[24] M.-L. Briuglia, C. Rotella, A. McFarlane, and D. A. Lamprou, "Influence of cholesterol on liposome stability and on in vitro drug release," *Drug Delivery and Translational Research*, vol. 5, no. 3, pp. 231–242, 2015.

[25] S. Honary and F. Zahir, "Effect of zeta potential on the properties of nano-drug delivery systems-a review (part 2)," *Tropical Journal of Pharmaceutical Research*, vol. 12, no. 2, pp. 265–273, 2013.

[26] S. Salgin, U. Salgin, and S. Bahadir, "Zeta potentials and isoelectric points of biomolecules: the effects of ion types and ionic strengths," *International Journal of Electrochemical Science*, vol. 7, no. 12, pp. 12404–12414, 2012.

[27] Y. Zhang, M. Yang, N. G. Portney et al., "Zeta potential: a surface electrical characteristic to probe the interaction of nanoparticles with normal and cancer human breast epithelial

cells," *Biomedical Microdevices*, vol. 10, no. 2, pp. 321–328, 2008.

[28] E. Bahreini, K. Aghaiypour, R. Abbasalipourkabir, A. Mokarram, M. Goodarzi, and M. Saidijam, "Preparation and nanoencapsulation of L-Asparaginase II in chitosan-tripolyphosphate nanoparticles and in vitro release study," *Nanoscale Research Letters*, vol. 9, no. 1, p. 340, 2014.

[29] A. S. Krall, S. Xu, T. G. Graeber, D. Braas, and H. R. Christofk, "Asparagine promotes cancer cell proliferation through use as an amino acid exchange factor," *Nature Communications*, vol. 7, no. 1, p. 11457, 2016.

[30] S. A. Moharib, "Anticancer activity of L-Asparaginase produced from vigna unguiculata," *World Scientific Research*, vol. 5, no. 1, pp. 1–12, 2018.

[31] D. Covini, S. Tardito, O. Bussolati et al., "Expanding targets for a metabolic therapy of cancer: L-Asparaginase," *Recent Patents on Anti-Cancer Drug Discovery*, vol. 7, no. 1, pp. 4–13, 2012.

[32] L. Huang, Y. Liu, Y. Sun, Q. Yan, and Z. Jiang, "Biochemical characterization of a novel L-Asparaginase with low glutaminase activity from *Rhizomucor miehei* and its application in food safety and leukemia treatment," *Applied and Environmental Microbiology*, vol. 80, no. 5, pp. 1561–1569, 2014.

[33] A. De and D. N. Venkatesh, "Design and evaluation of liposomal delivery system for L-Asparaginese," *Journal of Applied Pharmaceutical Science*, vol. 2, no. 8, p. 112, 2012.

[34] A. Babu, A. K. Templeton, A. Munshi, and R. Ramesh, "Nanodrug delivery systems: a promising technology for detection, diagnosis, and treatment of cancer," *AAPS PharmSciTech*, vol. 15, no. 3, pp. 709–721, 2014.

[35] H. Kobayashi, R. Watanabe, and P. L. Choyke, "Improving conventional enhanced permeability and retention (EPR) effects; what is the appropriate target," *Theranostics*, vol. 4, no. 1, pp. 81–89, 2013.

[36] A. D. Wong, M. Ye, M. B. Ulmschneider, and P. C. Searson, "Quantitative analysis of the enhanced permeation and retention (EPR) effect," *PloS One*, vol. 10, no. 5, Article ID e0123461, 2015.

[37] S. Stapleton, M. Milosevic, C. Allen et al., "A mathematical model of the enhanced permeability and retention effect for liposome transport in solid tumors," *PloS One*, vol. 8, no. 12, Article ID e81157, 2013.

[38] A. C. Anselmo, V. Gupta, B. J. Zern et al., "Delivering nanoparticles to lungs while avoiding liver and spleen through adsorption on red blood cells," *ACS Nano*, vol. 7, no. 12, pp. 11129–11137, 2013.

[39] M. M. Gaspar, R. Perez-Soler, and M. E. M. Cruz, "Biological characterization of L-Asparaginase liposomal formulations," *Cancer Chemotherapy and Pharmacology*, vol. 38, no. 4, pp. 373–377, 1996.

[40] M. L. Immordino, F. Dosio, and L. Cattel, "Stealth liposomes: review of the basic science, rationale, and clinical applications, existing and potential," *International Journal of Nanomedicine*, vol. 1, no. 3, pp. 297–315, 2006.

[41] F. Atyabi, A. Farkhondehfai, F. Esmaeili, and R. Dinarvand, "Preparation of pegylated nano-liposomal formulation containing SN-38: in vitro characterization and in vivo biodistribution in mice," *Acta Pharmaceutica*, vol. 59, no. 2, pp. 133–144, 2009.

[42] L. Cai, X. Wang, W. Wang et al., "Peptide ligand and PEG-mediated long-circulating liposome targeted to FGFR overexpressing tumor in vivo," *International Journal of Nanomedicine*, vol. 7, pp. 4499–4510, 2012.

Hindawi
Advances in Materials Science and Engineering
Volume 2019, Article ID 5978149, 9 pages
https://doi.org/10.1155/2019/5978149

Research Article

Nanosized Zincated Hydroxyapatite as a Promising Heterogeneous Photo-Fenton-Like Catalyst for Methylene Blue Degradation

Van Dat Doan,[1] Van Thuan Le,[2] Thi Thanh Nhi Le,[2] and Hoai Thuong Nguyen[3,4]

[1]*Faculty of Chemical Engineering, Industrial University of Ho Chi Minh City, Ho Chi Minh City, Vietnam*
[2]*Center for Advanced Chemistry, Institute of Research & Development, Duy Tan University, Danang, Vietnam*
[3]*Division of Computational Physics, Institute for Computational Science, Ton Duc Thang University, Ho Chi Minh City, Vietnam*
[4]*Faculty of Electrical & Electronics Engineering, Ton Duc Thang University, Ho Chi Minh City, Vietnam*

Correspondence should be addressed to Hoai Thuong Nguyen; nguyenhoaithuong@tdtu.edu.vn

Received 21 January 2019; Accepted 28 March 2019; Published 24 April 2019

Guest Editor: Dinh Quang Khieu

This study is devoted to synthesis of nanosized zincated hydroxyapatite (Zn-HA) and its utilization as a heterogeneous photo-Fenton-like catalyst for degradation of methylene blue (MB) in aqueous solution. The prepared catalyst was characterized by various techniques such as X-ray diffraction, scanning electron microscopy, transmission electron microscopy, energy-dispersive X-ray, and Fourier transform infrared spectroscopy. The catalytic activity of Zn-HA towards MB and the effects of various experimental factors such as pH, zinc substitution degrees, initial MB concentration, and H_2O_2 dosage were studied in detail. The results showed that the zinc substitution degree of 0.4 is optimal to get the highest degradation efficiency under conditions of pH = 10, H_2O_2 dosage of 0.05 M, and MB concentration of 30 mg/L for a contact time of 120 min. The degradation mechanism was proposed and discussed thoroughly. Besides, the ability of long-term use for the synthesized catalyst was also evaluated.

1. Introduction

The rapid industrialization with developing various kinds of chemical-based industries leads to several major environmental issues caused by a huge amount of toxic substances discharged into ecosystems. In this context, persistent organic pollutants as dyes must be taken into account due to their high toxicity and nonbiodegradability under normal conditions [1–4]. Recently, an examination conducted in Singapore in 2017 reported that essential everyday foods such as vegetables, canned meat, fruits, and cheese in local supermarkets contained at least one type of azo dyes which might cause several health problems as lethal, genotoxic, mutagenic, and carcinogenic effects [5]. Thus, removal of toxic dyes from contaminated sources is extremely important and attracts a great attention from the global scientific community.

Up to now, there have been several methods used for removal of organic pollutants such as flocculation, ion-exchange, reverse osmosis, adsorption, etc. [6–8]. A major drawback of these methods is related to the secondary polluted compounds that can be generated since the separated pollutants are not destroyed after detoxification [9, 10]. To overcome this barrier, heterogeneous Fenton-photocatalysis has been utilized to remove organic pollutants by degrading them into eco-friendly biodegradable substances [11, 12]. In this photocatalysis, properties of photocatalysts play a leading role in ensuring success of a treatment process. In this regard, many kinds of Fenton-photocatalysts have been developed. Among them, heterogeneous photocatalysts containing transition metals such as Fe, Cu, Zn, Mn, Co, Mn, and Ti are widely used due to their high photocatalytic activity and low cost [11, 13]. However, these materials exhibit a good performance mostly in UV region, but not under a wide spectrum of visible light due to the limits of their band gaps [14–16]. Moreover, most of the methods used to modify band gaps for improving

photocatalytic activity of catalysts are quite expensive and complicated [17–20].

Recently, several studies have been made on using hydroxyapatite ($Ca_{10}(PO_4)_6(OH)_2$-HA), a main mineral constituent of mammalian hard tissues, as a supporting material for improving photocatalytic activity of catalysts because of its biocompatibility and excellent adsorption capacity and photocatalytic activity for removal of both organic compounds and toxic heavy metals [21–24]. With regards to photocatalytic activity, Valizadeh et al. have successfully synthesized magnetite-hydroxyapatite for photocatalytic degradation of acid blue 25 [24]. Besides, another research group [25] used waste mussel shells to develop HA as a greener and renewable photocatalyst for the degradation of methylene blue (MB) [25]. Although the photocatalytic capacity of HA is not higher than those of metal-oxide photocatalysts, cost benefits, eco-friendliness, simple preparation, and reusability are huge advantages of this material. Especially, the structure of HA can be modified because its cations Ca^{2+} and functional groups of PO_4^{3-} and OH^- are easily replaced by other ions, and therefore, its photocatalytic potential can be intervened. For example, Fe_3O_4-hydroxyapatite modified by Mn, Fe, Co, Ni, Cu, and Zn as reported in [26] exhibited very high photocatalytic capability towards dyes in water under UV irradiation. However, there have been several drawbacks that are needed to overcome. Firstly, the Fe_3O_4 and hydroxyapatite components were physically linked to each other, leading to the low stability of material structure during a long-term treatment process. Secondly, the used metals were distributed mainly inside Fe_3O_4-hydroxyapatite structure, but not on its surface due to the substitution of Ca^{2+} by metals ions took place mainly at lattice points [26, 27]. As a result, Fe_3O_4-hydroxyapatite could not be able to exhibit its full photocatalytic potential.

Based on the above arguments, this study is devoted to using chemical precipitation method to develop a single-phase Zn-HA as a heterogenous photo-Fenton-like catalyst for MB degradation. For this material, Zn is integrated into HA via anion substitution of PO_4^{3-} by $Zn(OH)_4^{2-}$. Crystalline structure, morphology, features of functional groups, and element analysis of Zn-HA were carefully characterized using XRD, SEM, TEM, FTIR, and EDX techniques. Besides, the optimal conditions for degradation of MB were also determined. Finally, the reusability was also evaluated for the long-term of the catalyst.

2. Materials and Methods

2.1. Reagents and Materials. Calcium hydroxide ($Ca(OH)_2$, ≥96%), phosphoric acid (H_3PO_4, 85%), sodium hydroxide (NaOH, 99%), zinc oxide (ZnO, 99%), MB ($C_{16}H_{18}ClN_3S$, ≥82%), hydrogen peroxide (H_2O_2, 30%), and ammonium hydroxide (NH_4OH, 30%) were reagent-grade, supplied by Merck chemical company (Germany), and used without further purification. Distilled water was used to prepare all necessary solutions for the synthesis of Zn-HA.

2.2. Preparation of Zn-HA Catalyst. The Zn-HA samples were synthesized by the chemical precipitation method from solutions of $Na_2Zn(OH)_4$, $Ca(OH)_2$, and H_3PO_4. The solution of $Na_2Zn(OH)_4$ was prepared by adding gradually 0.2 M NaOH solution into a suspension of 0.05 M ZnO until a clear solution was obtained. The solutions of 0.02 M $Ca(OH)_2$ and H_3PO_4 10% were prepared from pure solid of $Ca(OH)_2$ and concentrated solution of H_3PO_4 85%, respectively. For the synthesis of Zn-HA, the solution of H_3PO_4 10% was slowly added drop by drop into a reactor containing $Na_2Zn(OH)_4$ and $Ca(OH)_2$ with vigorous stirring for 1 h. The solutions were taken out at different Ca : P : Zn ratios of 9 : 6 : 0; 9 : 5.9 : 0.1; 9 : 5.75 : 0.25; 9 : 5.6 : 0.4; 9 : 5.4 : 0.55; and 9 : 5.3 : 0.65 named as HA, Zn-HA-0.1, Zn-HA-0.25, Zn-HA-0.4, Zn-HA-0.55, and Zn-HA-0.65, respectively. The pH of obtained solutions was kept at pH ≥ 10 using NH_4OH. After the reactions finished, the mixtures were left for aging at room temperature for 24 h and then filtered, washed, dried, crushed, and pulverized through a 100-mesh sieve.

2.3. Characterization of Catalysts. X-ray powder diffraction (XRD) on a Shimadzu 6100 diffractometer (Japan) with Cu target ($\lambda = 1.5406$ Å), accelerating voltage of 40 kV, and current stream of 30 mA in a scanning range from 5 to 90° at a speed of 0.05°/s with a step size of 0.02° was used to explore structural properties of materials. The features of functional groups were analyzed by Fourier transform infrared spectroscopy (FTIR) technique on a Tensor 27 spectrophotometer (Germany) in a scanning range from 500–4000 cm^{-1} using KBr pellet method. The morphology of materials was tested by the methods of scanning electron microscopy (SEM) and transmission electron microscopy (TEM) on Jeol JSM-6480 LV and Jeol 1400 (Japan) microscopes, respectively. Finally, energy-dispersive X-ray (EDX) and element mapping techniques were utilized on a Horiba 7593 dispersive X-ray microanalyzer (Japan) to analyze the chemical elemental characteristics of the obtained materials.

2.4. Experiments for MB Degradation. The photo-Fenton catalytic potential of the as-prepared Zn-HA composite was evaluated through the degradation of MB as a model azo dye. A certain amount of catalyst was dispersed into 100 mL of MB solution (20, 30, 50, 80, 100 mg/L) and stirred in the dark for 30 min to reach adsorption-desorption equilibrium between MB and catalyst. Then, a calculated amount of H_2O_2 was added into the suspension to initiate the reaction under light irradiation turned on at the same time from 250 W halogen lamp (HLX 64653; Osram, Germany, wavelength range of 300–800 nm) equipped with a 420 nm cut-off filter. Besides, a thermostatic water-bath was employed to keep the reaction temperature at a desired value. In addition, the initial pH of MB solutions was adjusted to a desired value using 0.1 M NaOH or 0.1 M HCl solutions. After each 10-minute contact time, 2 mL of the mixture was taken out, the catalyst was then eliminated by centrifugation, and the remaining MB concentration was analyzed using an Evolution 600 UV-visible spectrophotometer at $\lambda_{max} = 664$ nm. The influence of factors as initial pH, catalyst dosage, initial

hydrogen peroxide dosage, MB concentration, and zinc content on the MB degradation was carefully examined. The efficiency for degradation of MB using Zn-HA is calculated by the following formula:

$$R_e = \frac{C_0 - C_f}{C_0} \cdot 100, \quad (1)$$

where R_e (%) is the removal efficiency and C_0(mg/L) and C_f(mg/L) are the initial and final concentrations of MB solution before and after degradation, respectively.

Photocatalytic stability and reusability of the catalysts were evaluated by testing the photocatalytic degradation efficiency of MB in five consecutive cycles, each cycle lasted 60 min. After each cycle, the photocatalyst was centrifuged and then added again into fresh MB solution (100 mL, 50 mg/L, pH of 10, H_2O_2 dosage of 0.05 M) for the next round.

3. Results and Discussion

3.1. Characterization of the Catalyst. The results for study on crystalline structures of HA and Zn-HA with different Zn content are shown in Figure 1.

It is obviously seen that the XRD patterns of Zn-HA samples contain all characteristic peaks for HA at 2θ of 10.8, 25.7, 28.2, 29.1, 31.7, 32.8, 39.7, 46.9, 48, 49.5, and 53.1° (ICD PDF 00-024-0033). In other words, the zinc doping did not affect crystalline structure of HA. Similar results were also reported in previous studies [28–30]. However, as compared to the HA, the peaks obtained for Zn-HA are broadened. This might be due to the decrease in the crystallinity and particle size of the Zn-HA sample [30]. Besides, the XRD patterns also indicated that there were additional phases of $Ca(OH)_2$ and $CaCO_3$ detected in Zn-HA samples at a zinc substitution degree higher than 0.4 (Figure 1). This anomaly can be explained as follows. The increase in the amount of $Zn(OH)_4^{2-}$ (which was made by the dissolution of ZnO in NaOH as described above) in the reaction mixture of $Ca(OH)_2$ and H_3PO_4 led to the shortage of H_3PO_4 due to its neutralization by NaOH and therefore resulting in the superabundance of $Ca(OH)_2$. At the same time, a part of extra $Ca(OH)_2$ could react with CO_2 in atmosphere to form $CaCO_3$.

The morphology of HA and Zn-HA at Zn-substitution degree of 0.4 is presented in Figure 2. It can be seen that the crystals of HA were grown in needle shape with 150–200 nm length and 30–50 nm width (Figure 2(a)) while Zn-HA crystals have a spherical shape with a diameter of about 20 nm (Figure 2(b)). The difference of size and shape between HA and Zn-HA might be associated with the increased number of crystallization centers when $Zn(OH)_4^{2-}$ was added into the reaction mixture of $Ca(OH)_2$ and H_3PO_4. Consequently, more crystals might be formed, leading to the decrease in their size. This is also in good agreement with the above XRD patterns. It should be noticed that the smaller the size of crystals, the larger the specific surface area obtained. This feature is an advantage of Zn-HA over HA towards photocatalytic ability. On a larger-scale view as shown in SEM images (Figures 2(c) and 2(d)), both HA and Zn-HA show a similar morphology.

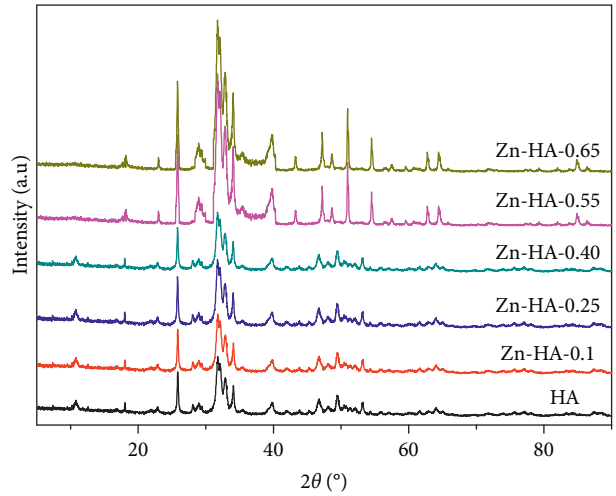

Figure 1: XRD patterns of HA and Zn-HA samples with different Zn content.

The doping of Zn into HA was also confirmed by EDX spectra and element mapping as shown in Figure 3. According to the EDX spectrum for Zn-HA (Figure 3(b)), along with the main elements characteristic for HA such as Ca, P, and O (Figure 3(a)), Zn was detected. Besides, the contents of Ca, P, and O elements in HA and Zn-HA are different. Comparing with HA, the content of P and O in Zn-HA was found to decrease from 13.77 to 2.41 w% and 59.97 to 50.01 w%, respectively. Meanwhile, the Ca content increased from 23.81 to 44% equal to the Ca content in stoichiometric HA. It obviously indicated that PO_4^{3-} groups in HA were partially replaced by $Zn(OH)_4^{2-}$. Moreover, the element mapping shows also the appearance of 4 elements of Ca, Zn, O and P on Zn-HA (Figures 3(c)–3(f)). In addition, the even distribution of Zn ions on Zn-HA surface (Figure 3(d)) is expected to improve photocatalytic activity of the synthesized catalyst as compared to those of HA.

The results for study on features of functional groups for HA and Zn-HA with different Zn content are shown in Figure 4. It is obviously seen that FTIR spectra obtained for HA and Zn-HA have a similar shape and most of characteristic peaks as 1030, 1085, 956, and 874 cm^{-1} referred to OH^- were detected at the same positions. Besides, the presence of CO_3^{2-} as mentioned above was also detected at 1650 and 1423 cm^{-1}. However, a difference of intensity between some peaks in HA and Zn-HA was observed. Specifically, for Zn-HA samples, the intensity of a peak at 3640 cm^{-1} (OH^- groups) was found to be increased and at 1030 cm^{-1} (PO_4^{3-} groups) decreased in comparison with those for HA, confirming the successful integration of $Zn(OH)_4^{2-}$ into HA structure.

3.2. Photo-Fenton Catalytic Activity of the Catalysts. In order to evaluate the photocatalytic advantage of Zn-HA over HA, a comparative study was conducted under the same experimental conditions of light irradiation, pH = 10, and catalyst loading of 0.1 g added into 100 mL of 50 mg·L^{-1} MB solution at room temperature. The Fenton-photocatalytic activity of catalysts was tested by adding 0.05 M H_2O_2 into

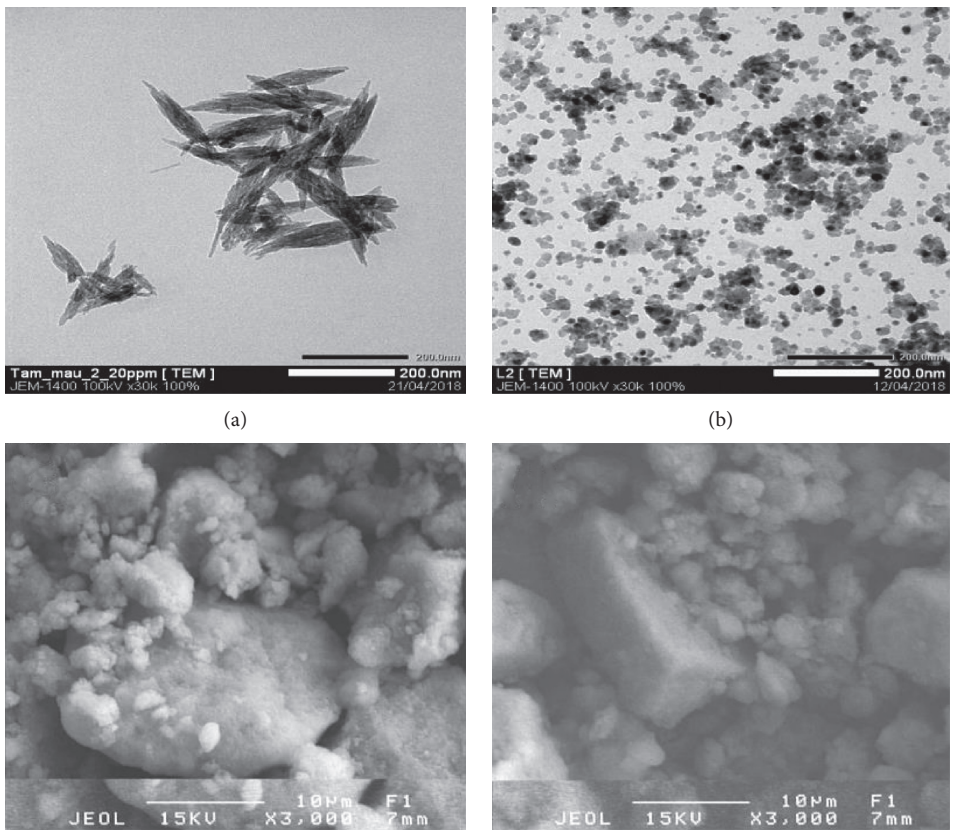

(a) (b)

(c) (d)

Figure 2: TEM and SEM images for HA (a, c) and Zn-HA (b, d).

the MB solution. As seen in Figure 5, when H_2O_2 was absent, the removal efficiencies obtained for both Zn-HA and HA were quite low as compared to those with the participation of H_2O_2. Besides, the maximum degradation efficiency of Zn-HA was much higher than that of HA for both cases with presence of H_2O_2 and absence of H_2O_2 (Figure 5). Obviously, the removal process in the absence of H_2O_2 was controlled mainly by adsorption mechanism, and therefore, the smaller size of Zn-HA helps it to take advantage over HA. In the presence of H_2O_2, along with adsorption mechanism, the Fenton-photocatalytic reactions could be activated and improved the degradation process. In this regard, the higher degradation efficiency of Zn-HA than that of HA indicated its stronger Fenton-photocatalytic potential. In other words, the presence of Zn could significantly improve the Fenton-photocatalytic ability of HA.

The photodegradation mechanism can be formulated as follows. Under visible light irradiation, electron/hole pairs were photogenerated in the catalyst (equation (2)). Then, photogenerated electrons could be trapped by H_2O_2, leading to the formation of $^{\cdot}OH$ (equation (3)) [31]. At the same time, Zn^{2+} ions after occupying electrons (equations (4)) were transformed into Zn which reacted with H_2O_2 to form ZnO, a strong photocatalyst (equation (5)) [32]. During light irradiation, ZnO was capable of creating more electrons and holes (equation (6)), and therefore, the decomposition process of H_2O_2 to release $^{\cdot}OH$ will be accelerated due to the support of electrons (equation (8)). In addition, the generated electrons could also stimulate the formation of superoxide radicals through reactions with dissolved oxygen in the solution (equation (7)). Meanwhile, the holes could also contribute to the formation of $^{\cdot}OH$ when reacting with H_2O and OH^- (equations (8) and (9)). Finally, $^{\cdot}OH$ and $^{\cdot}O_2^-$ will degrade MB molecules according to equations (10) and (11) [33].

$$\mathrm{Zn-HA} + h\nu \longrightarrow \mathrm{Zn-HA} + e^- + h^+ \quad (2)$$

$$\mathrm{H_2O_2} + e^- \longrightarrow {}^{\cdot}\mathrm{OH} + \mathrm{OH^-} \quad (3)$$

$$\mathrm{Zn^{2+}} + 2e^- \longrightarrow \mathrm{Zn} \quad (4)$$

$$\mathrm{Zn} + \mathrm{H_2O_2} \longrightarrow \mathrm{ZnO} + \mathrm{H_2O} \quad (5)$$

$$\mathrm{ZnO} + h\nu \longrightarrow e^- + h^+ \quad (6)$$

$$e^- + \mathrm{O_2} \longrightarrow {}^{\cdot}\mathrm{O_2^-} \quad (7)$$

$$h^+ + \mathrm{H_2O} \longrightarrow \mathrm{H^+} + {}^{\cdot}\mathrm{OH} \quad (8)$$

$$h^+ + \mathrm{OH^-} \longrightarrow {}^{\cdot}\mathrm{OH} \quad (9)$$

$$^{\cdot}\mathrm{OH} + \mathrm{MB} \longrightarrow \text{degradation products} \quad (10)$$

$$^{\cdot}\mathrm{O_2^-} + \mathrm{MB} \longrightarrow \text{degradation products} \quad (11)$$

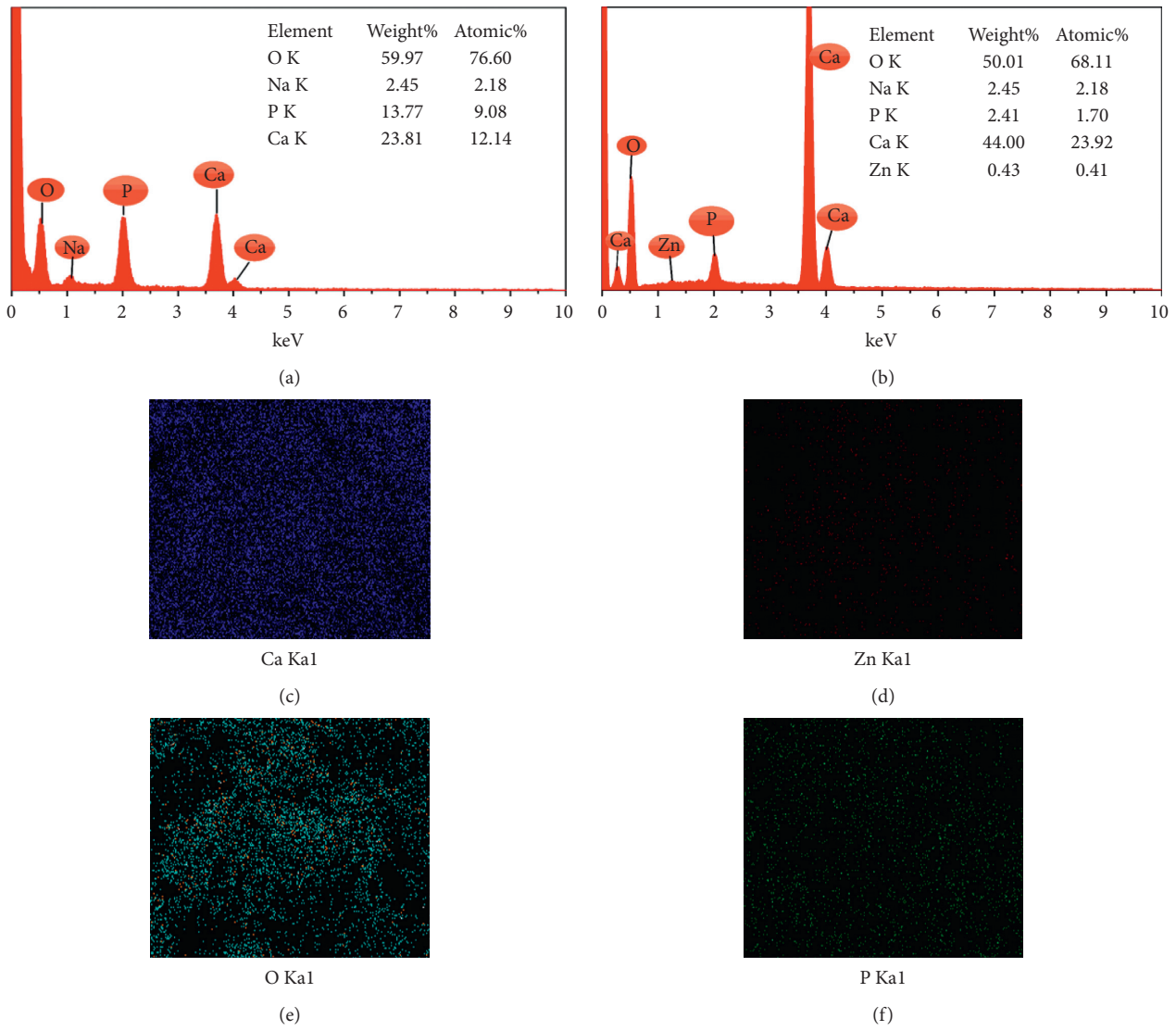

Figure 3: EDX patterns of HA (a) and Zn-HA (b), and element distribution on Zn-HA surface for calcium (c), zinc (d), oxygen (e), and phosphorus (f).

Although the above results indicated the advantage of Zn in enhancing Fenton-photocatalytic activity of Zn-HA over HA, the optimum content of Zn is needed to be determined. For this purpose, a comparative study on catalytic activity of Zn-HA samples with different zinc substitution degrees under the same degradation conditions as mentioned. The results showed that the zinc substitution degree of 0.4 gave the highest degradation efficiency of 95% after a contact time of 30 min as shown in Figure 6. In this regard, the obtained value of 0.4 is reasonable and was chosen for further experiments.

3.3. Influence of Experimental Conditions on MB Degradation

3.3.1. Effect of pH. Effect of pH on degradation efficiency of Zn-HA was studied in pH range from 4 to 10 using 0.1 g of Zn-HA added into 100 mL solution of 50 mg/L MB and 0.05 M H_2O_2. The obtained results are presented in Figure 7(a). It is obviously seen that the degradation efficiency significantly increased with increasing solution pH. This can be explained by the increased amount of OH^- groups, leading to rise in the amount of $^{\cdot}OH$ radicals generated through Fenton-oxidation mechanism, and therefore the degradation process was improved [13]. The fact that increasing pH greater than 10 does not make sense for practical applications since there is no economic benefit and the secondary pollutants could be generated at high pH. In this regard, pH = 10 was chosen as an optimal pH for all catalytic experiments in this work.

3.3.2. Effect of Initial MB Concentrations. Different initial MB concentrations of 20, 30, 50, 80, and 100 mg/L were used to evaluate their effect on degradation efficiency of Zn-HA catalyst under pH of 10, catalyst dosage of 0.1 g, and

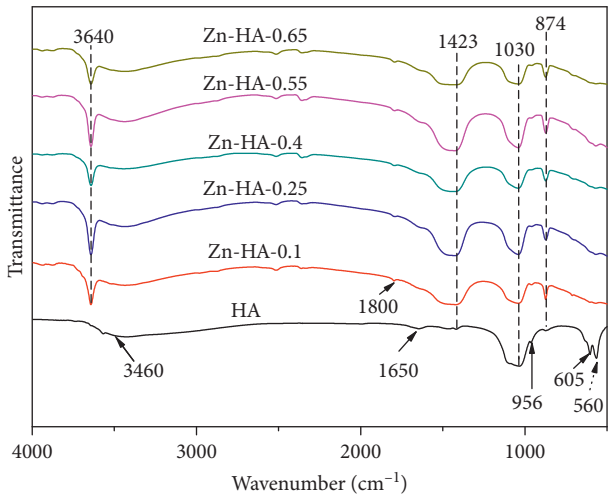

Figure 4: FTIR spectra for HA and Zn-HA samples with different Zn content.

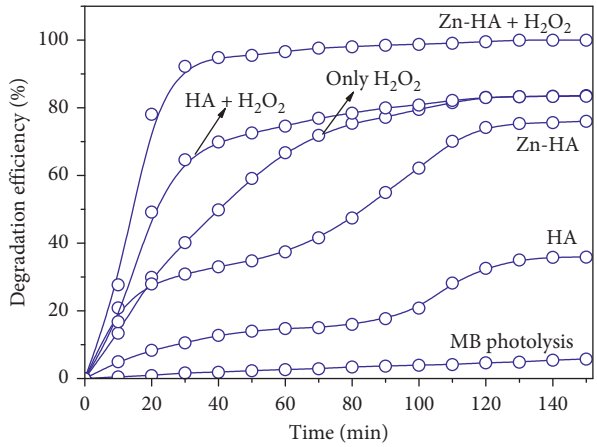

Figure 5: Comparative study on catalytic activity of the HA and Zn-HA for degradation of MB.

H_2O_2 dosage of 0.05 M at room temperature. Based on the obtained results, the optimal initial MB concentration was determined as 30 mg/L (Figure 7(b)). At concentrations higher than 30 mg/L, the reduction of degradation efficiency was observed. The anomaly could be related to the formation of a layer of MB molecules accumulated on Zn-HA surface at high MB concentrations, inhibiting light from entering Zn sites and therefore holding back the decolorization process [34].

3.3.3. Effect of H_2O_2 Concentration. The study was carried out using different initial H_2O_2 concentrations of 0.01, 0.03, 0.05, and 0.10 M under the established above optimal conditions. According to the results shown in Figure 7(c), the initial H_2O_2 concentration of 0.05 M is optimal for degradation of MB using Zn-HA. The deviation of initial H_2O_2 concentration from 0.05 M did not improve degradation process. It is obviously seen that at H_2O_2 concentrations lower 0.05 M, the reduction of

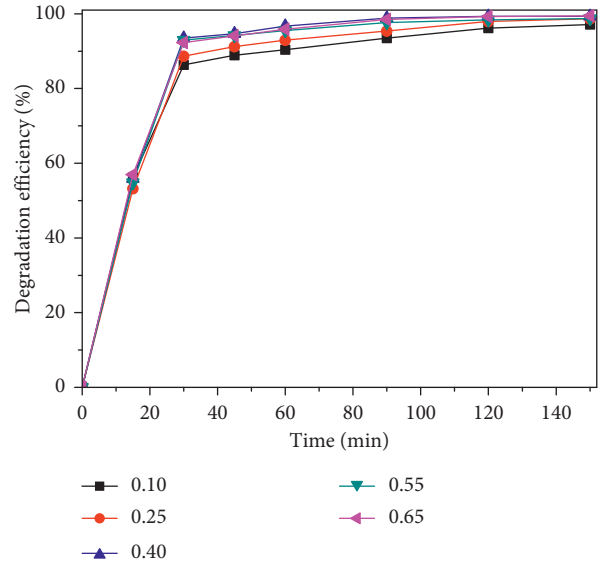

Figure 6: Comparative study on catalytic activity of Zn-HA samples with different zinc substitution degrees.

degradation efficiency could be associated with the decrease in the number of generated $^{\cdot}OH$ radicals. Meanwhile, at H_2O_2 concentrations greater than 0.05 M, the degradation efficiency did not increase (Figure 7(c)), probably, due to the generation of perhydroxyl radicals caused by the combination of extra H_2O_2 dosage with hydroxyl radicals [35].

3.4. Stability and Reusability of Catalyst. The stability and reusability of a catalyst are essential for its practical applications. For Zn-HA catalyst, the recycling tests were carried out under optimal conditions in five continuous cycles. The results shown in Figure 8(a) indicated that the catalytic potential of Zn-HA towards MB was well maintained with a slight reduction of degradation efficiency from 100% to 96.5% after five continuous cycles. Besides, the XRD pattern of Zn-HA after the fifth degradation cycle contained almost all characteristic peaks (Figure 8(b)), demonstrating high stability of composite structure during degradation process.

4. Conclusions

In this study, the nanosized Zn-HA was successfully synthesized and applied as a heterogeneous photo-Fenton-like catalyst for MB degradation under optimal conditions of pH = 10, H_2O_2 dosage of 0.05 M, and MB concentration of 30 mg/L for a contact time of 120 min. Besides, the zinc substitution degree of 0.4 is optimal to improve the photocatalytic activity of the catalyst. The recycling study demonstrated a good maintenance of degradation ability and high stability of catalyst structure in a long-term degradation process. Overall, the positive results suggested that the synthesized catalyst can be expected as a promising heterogeneous photocatalyst for degradation of MB in industrial wastewater.

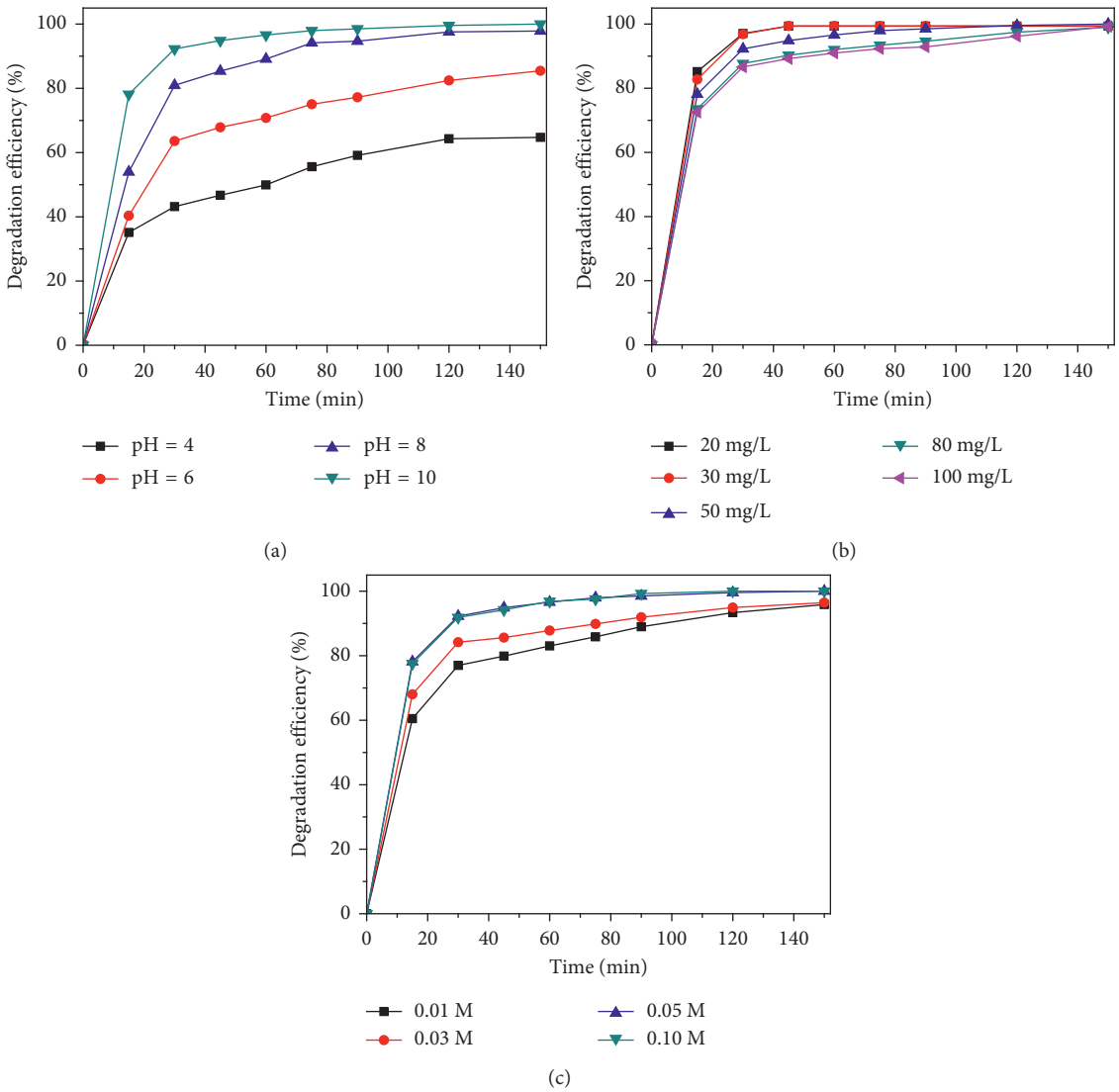

Figure 7: Effects of degradation conditions on degradation efficiency of Zn-HA sample. (a) pH. (b) Initial MB concentration. (c) Initial H_2O_2 concentration.

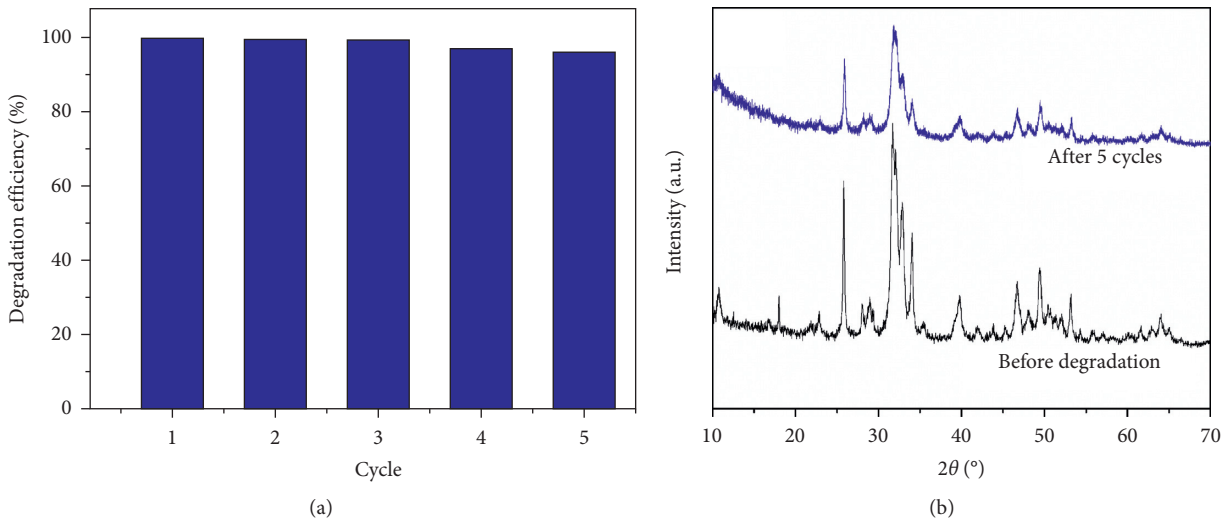

Figure 8: Degradation efficiency reduction (a) and the change of XRD pattern (b) of Zn-HA after for continuous cycles.

Data Availability

The all data used to support the findings of this study are included within the article.

Conflicts of Interest

The authors declare that they have no conflicts of interest.

Acknowledgments

The authors acknowledge the Industrial University of Ho Chi Minh City, Vietnam, for supporting this work (Funding No. 184.HHO5).

References

[1] V. Katheresan, J. Kansedo, and S. Y. Lau, "Efficiency of various recent wastewater dye removal methods: a review," *Journal of Environmental Chemical Engineering*, vol. 6, no. 4, pp. 4676–4697, 2018.

[2] H. Mittal, S. M. Alhassan, and S. S. Ray, "Efficient organic dye removal from wastewater by magnetic carbonaceous adsorbent prepared from corn starch," *Journal of Environmental Chemical Engineering*, vol. 6, no. 6, pp. 7119–7131, 2018.

[3] T. T. T. Tran, V. D. Doan, T. T. T. Ho, V. T. Le, and H. T. Nguyen, "Novel of TiO_2/Ag_3PO_4/bentonite composite photocatalyst: preparation, characterization, and application for degradation of methylene blue in aqueous solution," *Environmental Engineering Science*, vol. 36, no. 1, pp. 71–80, 2019.

[4] K.-T. Chung, "Azo dyes and human health: a review," *Journal of Environmental Science and Health, Part C*, vol. 34, no. 4, pp. 233–261, 2016.

[5] L. Leo, C. Loong, X. L. Ho, M. F. B. Raman, M. Y. T. Suan, and W. M. Loke, "Occurrence of azo food dyes and their effects on cellular inflammatory responses," *Nutrition*, vol. 46, pp. 36–40, 2018.

[6] L. Tang, J. Yu, Y. Pang et al., "Sustainable efficient adsorbent: alkali-acid modified magnetic biochar derived from sewage sludge for aqueous organic contaminant removal," *Chemical Engineering Journal*, vol. 336, pp. 160–169, 2018.

[7] M. Wawrzkiewicz and Z. Hubicki, "Anion exchange resins as effective sorbents for removal of acid, reactive, and direct dyes from textile wastewaters," in *Ion Exchange-Studies and Applications*, IntechOpen, London, UK, 2015.

[8] M. T. Yagub, T. K. Sen, S. Afroze, and H. M. Ang, "Dye and its removal from aqueous solution by adsorption: a review," *Advances in Colloid and Interface Science*, vol. 209, pp. 172–184, 2014.

[9] P. Zhao, S. Li, J. Zhao, C. M. Gaspar, and X. Weng, "Training by visual identification and writing leads to different visual word expertise N170 effects in preliterate Chinese children," *Developmental Cognitive Neuroscience*, vol. 15, pp. 106–116, 2015.

[10] S. De Gisi, G. Lofrano, M. Grassi, and M. Notarnicola, "Characteristics and adsorption capacities of low-cost sorbents for wastewater treatment: a review," *Sustainable Materials and Technologies*, vol. 9, pp. 10–40, 2016.

[11] R. Ameta, A. K. Chohadia, A. Jain, and P. B. Punjabi, "Fenton and photo-fenton processes," in *Advanced Oxidation Processes for Waste Water Treatment*, S. C. Ameta and R. Ameta, Eds., pp. 49–87, Academic Press, Cambridge, MA, USA, 2018, ISBN 9780128104996.

[12] A. Mirzaei, Z. Chen, F. Haghighat, and L. Yerushalmi, "Removal of pharmaceuticals from water by homo/heterogonous Fenton-type processes—a review," *Chemosphere*, vol. 174, pp. 665–688, 2017.

[13] S. Kalal, A. Pandey, R. Ameta, and P. B. Punjabi, "Heterogeneous photo-Fenton-like catalysts $Cu_2V_2O_7$ and $Cr_2V_4O_{13}$ for an efficient removal of azo dye in water," *Cogent Chemistry*, vol. 2, no. 1, article 1143344, 2016.

[14] B. Palas, G. Ersöz, and S. Atalay, "Photo Fenton-like oxidation of Tartrazine under visible and UV light irradiation in the presence of $LaCuO_3$ perovskite catalyst," *Process Safety and Environmental Protection*, vol. 111, pp. 270–282, 2017.

[15] Y. He, D. B. Jiang, D. Y. Jiang, J. Chen, and Y. X. Zhang, "Evaluation of MnO_2-templated iron oxide-coated diatomites for their catalytic performance in heterogeneous photo Fenton-like system," *Journal of Hazardous Materials*, vol. 344, pp. 230–240, 2018.

[16] M. S. Vasilyeva, V. S. Rudnev, A. A. Zvereva et al., "FeOx,SiO_2,TiO_2/Ti composites prepared using plasma electrolytic oxidation as photo-Fenton-like catalysts for phenol degradation," *Journal of Photochemistry and Photobiology A: Chemistry*, vol. 356, pp. 38–45, 2018.

[17] Y. Zhu, R. Zhu, L. Yan et al., "Visible-light Ag/AgBr/ferrihydrite catalyst with enhanced heterogeneous photo-Fenton reactivity via electron transfer from Ag/AgBr to ferrihydrite," *Applied Catalysis B: Environmental*, vol. 239, pp. 280–289, 2018.

[18] A. Zhang, L. Zhu, and Z. Nan, "Ni-doped Fe_3O_4 nanoparticles coupled with SnS_2 nanosheets as 0D/2D heterogeneous catalyst for photo-Fenton reaction," *Materials Chemistry and Physics*, vol. 224, pp. 156–168, 2019.

[19] L. Yu, J. Chen, Z. Liang, W. Xu, L. Chen, and D. Ye, "Degradation of phenol using Fe_3O_4-GO nanocomposite as a heterogeneous photo-Fenton catalyst," *Separation and Purification Technology*, vol. 171, pp. 80–87, 2016.

[20] C. Liang, Y. Liu, K. Li et al., "Heterogeneous photo-Fenton degradation of organic pollutants with amorphous Fe-Zn-oxide/hydrochar under visible light irradiation," *Separation and Purification Technology*, vol. 188, pp. 105–111, 2017.

[21] V. T. Le, V. D. Doan, D. D. Nguyen et al., "A novel cross-linked magnetic hydroxyapatite/chitosan composite: preparation, characterization, and application for Ni(II) ion removal from aqueous solution," *Water, Air, & Soil Pollution*, vol. 229, no. 3, p. 101, 2018.

[22] L. V. Thuan, D. V. Dat, P. C. Nguyen, and M. A. Trubitsyn, "Synthesis of calcium-deficient carbonated hydroxyapatite as promising sorbent for removal of lead ions," *Journal of Nano Research*, vol. 45, pp. 124–133, 2017.

[23] W. Liu, G. Qian, B. Zhang, L. Liu, and H. Liu, "Facile synthesis of spherical nano hydroxyapatite and its application in photocatalytic degradation of methyl orange dye under UV irradiation," *Materials Letters*, vol. 178, pp. 15–17, 2016.

[24] S. Valizadeh, M. H. Rasoulifard, and M. S. S. Dorraji, "Modified Fe_3O_4-hydroxyapatite nanocomposites as heterogeneous catalysts in three UV, Vis and Fenton like degradation systems," *Applied Surface Science*, vol. 319, pp. 358–366, 2014.

[25] J. H. Shariffuddin, M. I. Jones, and D. A. Patterson, "Greener photocatalysts: hydroxyapatite derived from waste mussel shells for the photocatalytic degradation of a model azo dye wastewater," *Chemical Engineering Research and Design*, vol. 91, no. 9, pp. 1693–1704, 2013.

[26] A. Fihri, C. Len, R. S. Varma, and A. Solhy, "Hydroxyapatite: a review of syntheses, structure and applications in

heterogeneous catalysis," *Coordination Chemistry Reviews*, vol. 347, pp. 48–76, 2017.

[27] M. Ferri, S. Campisi, M. Scavini, C. Evangelisti, P. Carniti, and A. Gervasini, "In-depth study of the mechanism of heavy metal trapping on the surface of hydroxyapatite," *Applied Surface Science*, vol. 475, pp. 397–409, 2019.

[28] E. S. Thian, T. Konishi, Y. Kawanobe et al., "Zinc-substituted hydroxyapatite: a biomaterial with enhanced bioactivity and antibacterial properties," *Journal of Materials Science: Materials in Medicine*, vol. 24, no. 2, pp. 437–445, 2013.

[29] T. G. Peñaflor Galindo, T. Kataoka, S. Fujii, M. Okuda, and M. Tagaya, "Preparation of nanocrystalline zinc-substituted hydroxyapatite films and their biological properties," *Colloid and Interface Science Communications*, vol. 10-11, pp. 15–19, 2016.

[30] I. Karacan, D. Senturk, F. N. Oktar et al., "Structural and characterisation analysis of zinc-substituted hydroxyapatite with wet chemical precipitation method," *International Journal of Nano and Biomaterials*, vol. 6, no. 3-4, pp. 188–204, 2016.

[31] X. S. Nguyen, G. Zhang, and X. Yang, "Mesocrystalline Zn-doped Fe_3O_4 hollow submicrospheres: formation mechanism and enhanced photo-fenton catalytic performance," *ACS Applied Materials & Interfaces*, vol. 9, no. 10, pp. 8900–8909, 2017.

[32] K. M. Lee, C. W. Lai, K. S. Ngai, and J. C. Juan, "Recent developments of zinc oxide based photocatalyst in water treatment technology: a review," *Water Research*, vol. 88, pp. 428–448, 2016.

[33] W. Li, G. Wang, C. Chen, J. Liao, and Z. Li, "Enhanced visible light photocatalytic activity of ZnO nanowires doped with Mn^{2+} and Co^{2+} ions," *Nanomaterials*, vol. 7, no. 1, p. 20, 2017.

[34] F. Ji, C. Li, J. Zhang, and L. Deng, "Efficient decolorization of dye pollutants with $LiFe(WO_4)^2$ as a reusable heterogeneous Fenton-like catalyst," *Desalination*, vol. 269, no. 1–3, pp. 284–290, 2011.

[35] S. Xavier, R. Gandhimathi, P. V. Nidheesh, and S. T. Ramesh, "Comparison of homogeneous and heterogeneous Fenton processes for the removal of reactive dye Magenta MB from aqueous solution," *Desalination and Water Treatment*, vol. 53, no. 1, pp. 109–118, 2015.

Hindawi
Advances in Materials Science and Engineering
Volume 2019, Article ID 9624374, 5 pages
https://doi.org/10.1155/2019/9624374

Research Article

Synthesis of Platinum Nanoparticles by Gamma Co-60 Ray Irradiation Method Using Chitosan as Stabilizer

Thi Kim Lan Nguyen,[1] Ngoc Duy Nguyen,[1] Van Phu Dang,[1] Dinh Tuan Phan,[2] Thai Hoa Tran,[3] and Quoc Hien Nguyen[1]

[1]*Research and Development Center for Radiation Technology, Vietnam Atomic Energy Institute, 202A Street 11, Linh Xuan Ward, Thu Duc District, Ho Chi Minh City 700000, Vietnam*
[2]*Hochiminh City University of Natural Resources and Environment, 263B Le Van Sy Street, Ho Chi Minh City 700000, Vietnam*
[3]*College of Sciences, Hue University, Hue 530000, Vietnam*

Correspondence should be addressed to Thai Hoa Tran; trthaihoa@yahoo.com and Quoc Hien Nguyen; hien7240238@yahoo.com

Received 4 January 2019; Accepted 24 March 2019; Published 18 April 2019

Guest Editor: Hien Duy Mai

Platinum nanoparticles were synthesized using the gamma-ray irradiation as a reducing factor and chitosan as a stabilizer. The prepared platinum nanoparticles were characterized using ultraviolet-visible spectroscopy (UV-Vis), transmission electron microscopy (TEM), and Fourier-transform infrared spectroscopy (FT-IR). The saturated conversion dose to reduce the Pt^{4+} to Pt^0 was found to be about 14 kGy for initial Pt^{4+} concentration of 1 mM. The size of the platinum nanoparticles (1.4–1.6 nm) did almost not change with the increase of chitosan concentration from 0.5 to 2.0%. Thus, gamma Co-60 ray irradiation method is favorable for synthesizing PtNPs with the small sizes.

1. Introduction

Platinum nanoparticles (PtNPs) have attracted great attention in many fields due to their applications in catalysis [1–7], such as in fuel cell technology [1], exhaust purification [2], automobile [3], and energy storage and sensors [8]. However, the possible applications are related to the size and morphology of PtNPs [1, 3, 8, 9]. PtNPs with small sizes possess a large number of surface atoms that affect its surface activity [8]. So, it is essential to prepare small size of PtNPs. The synthesis of PtNPs has already been studied using different methods such as chemical reduction [8–13], electrochemical deposition [1, 8], hydrothermal reduction [1, 3], biological synthesis [14], gamma Co-60 ray irradiation [4, 6], and polyol method [1]. In comparison with other methods, the gamma Co-60 ray irradiation is considered as an effective method for the synthesis of metal nanoparticles due to several advantages such as (1) the reduction reaction of metal ions performed at ambient condition; (2) the rate of reduction reaction can be properly controlled; (3) the reducing agents uniformly distributed in the solution; and (4) large-scale production can be favorably set up and satisfied with requirements of the clean production process [6]. Stabilizers, such as dextran [3], polyvinyalcohol, polyacrylic acid, and polyacrylate [4], and chitosan [5], and others must be used for the protection of PtNPs from agglomeration. Among stabilizers studied, chitosan (CTS) is widely used in the synthesis of metallic nanoparticles such as gold, platinum, silver, and palladium [10]. The CTS is one of the environmentally friendly polymers that is particularly interesting in the synthesis of metal nanoparticles due to its interactions with metal nanoparticles through both steric and electrostatic effect. The polymer molecules bind with the nanoparticles to prevent leaching from the catalysts. These characteristics make CTS an ideal material as catalystic support [1, 5, 11]. To the best of our knowledge, there has been no research on the synthesis of PtNPs with small size (1-2 nm) and narrow particle size distribution by the

radiolytic method. In this study, the synthesis of PtNPs by the gamma Co-60 ray irradiation using CTS as a stabilizer was carried out, and the effect of CTS concentration on the size of PtNPs was also investigated.

2. Materials and Methods

2.1. Materials and Chemicals. Potassium hexachloroplatinate (IV) (K_2PtCl_6) was purchased from Merck. CTS with the molecular weight of ~95,000 g/mol and deacetylation degree of ~90% were supplied by a factory in Vung Tau Province, Vietnam. Lactic acid was purchased from Shanghai Chemical Reagent Co., China. Distilled water was used in all experiments.

2.2. Preparation of Pt^{4+}/CTS Solution and Gamma-Ray Irradiation. Three-gram CTS was dissolved in 100 ml lactic acid 1.5% (v/v) to prepare a 3% (w/v) CTS solution. K_2PtCl_6 was then dissolved in CTS solutions to prepare Pt^{4+}/CTS solutions with 1 mM Pt^{4+} and different CTS concentrations of 0.5, 1.0, and 2.0% (w/v). Then, the solutions of Pt^{4+}/CTS were poured into glass bottles with caper and irradiated on the gamma Co-60 irradiator, STSV Co-60/B (Hungary), at VINAGAMMA Center, Ho Chi Minh City, with doses up to 17.5 kGy (dose rate of 1.25 kGy/h) measured by the dichromate dosimetry system [15].

2.3. Characterization of Colloidal PtNPs/CTS Solution. The UV-Vis absorption spectra of PtNPs/CTS solutions were measured on a UV-Vis spectrophotometer model Jasco-V630, Japan. The size and size distribution of the PtNPs were determined from TEM images on a transmission electron microscope model JEM 1010, JEOL, Japan, operating at 80 kV and statistically calculated using Photoshop software [16]. The FT-IR spectra of samples were measured on a FT-IR spectrometer 8400S, Shimadzu, Japan. For FT-IR measurement, the PtNPs/CTS solutions were dried at 60°C in a forced air oven. The dried PtNPs/CTS samples were ground into fine powder. After that, the powder samples of PtNPs/CTS were mixed with KBr and compressed into pellets with a thickness of 0.5 mm.

3. Results and Discussion

The 1 mM Pt^{4+}/1% CTS solution was irradiated with the different doses of 3.5, 7.0, 10.5, 14.0, and 17.5 kGy did almost not have clearly maximum absorption peak (λ_{max}) in the wavelength range of the measured UV-Vis spectrum, but the absorbance was increased with the increase of dose up to 14 kGy (Figure 1). After irradiation, the color of the initial colorless Pt^{4+}/CTS solutions was converted to brown color, and the higher the absorption dose, the darker the color of PtNPs/CTS solutions obtained. The same pattern of UV-Vis spectrum of PtNPs with no λ_{max} was also reported by Yang et al. [3] using the chemical reduction, and by Remita et al. [4] and Choi et al. [6] using the gamma Co-60 ray irradiation method. However, Gharibshahi et al. [17] recently have reported that the PtNPs (2.8–4.4 nm) synthesized by the

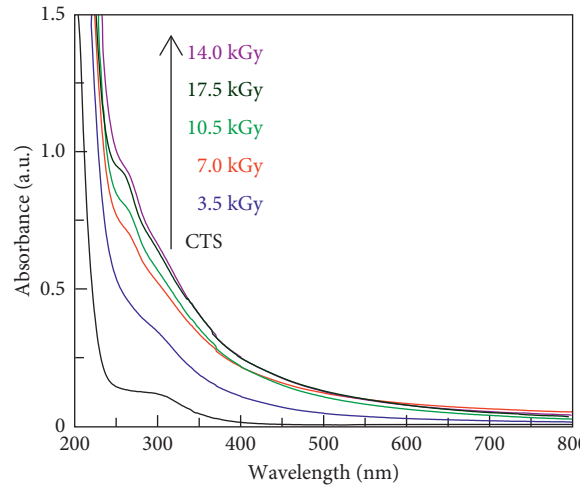

Figure 1: UV-Vis spectra of CTS and Pt^{4+}/CTS solutions irradiated with different doses.

gamma-ray irradiation of 3.4 mM Pt^{4+} solution appeared two λ_{max} in the UV-Vis spectrum, particularly the first peak in the range of 209–214 nm and the second one in the range of 257–262 nm. Furthermore, Cele et al. [18] reported that the PtNPs solutions prepared by the gamma-ray radiolytic method with the concentrations from 1 to 10 mM also had two λ_{max} as in the study of Gharibshahi et al. [17] except for the sample of 1 mM PtNPs without λ_{max} in the UV region due to less Pt atoms interacting with the light.

Figure 1 shows that the CTS solution has a weak peak at ~300 nm. All spectra of PtNPs/CTS solutions also manifested a weak peak at 260–300 nm with increased absorbance corresponding to the increase of the absorbed dose. This may be due to the formation of carbonyl groups from CTS by chain scission during irradiation [19]. Besides, the absorbance was increased with the increase of dose and reached a stable level at 14 kGy. So, it could be inferred that the absorbed dose of 14 kGy could be selected as the saturated conversion dose to completely reduce Pt^{4+} with the concentration of 1 mM to Pt^0. The mechanism of PtNPs formation from Pt^{4+} ion solution by the gamma Co-60 ray irradiation was described in detail by Choi et al. [6] and Cele et al. [18]. Briefly, Pt^{4+} ions were reduced to Pt^0 mainly by hydrated electrons (e^-_{aq}), hydrogen radicals (H˙), and hydroxyl radicals (˙OH). For ˙OH radicals, they were converted into secondary radicals by hydrogen abstraction from free radical scavengers (alcohol, polysaccharides, etc.) for reducing Pt^{4+} ions.

The effect of CTS concentration was studied for the initial Pt^{4+} concentration of 1 mM. Figure 2 indicates that there was almost no difference among UV-Vis spectra of PtNPs/CTS samples with different CTS concentrations. In addition, the size of the radiolytic synthesized PtNPs in Figure 3 was virtually not affected by the CTS concentrations from 0.5 to 2.0%.

The synthesized PtNPs have a rather small size and narrow size distribution in the range of 1.4–1.6 nm (Figure 3). The size of resultant PtNPs with the concentration of 1 mM in this study was smaller than the size of 4.4 and

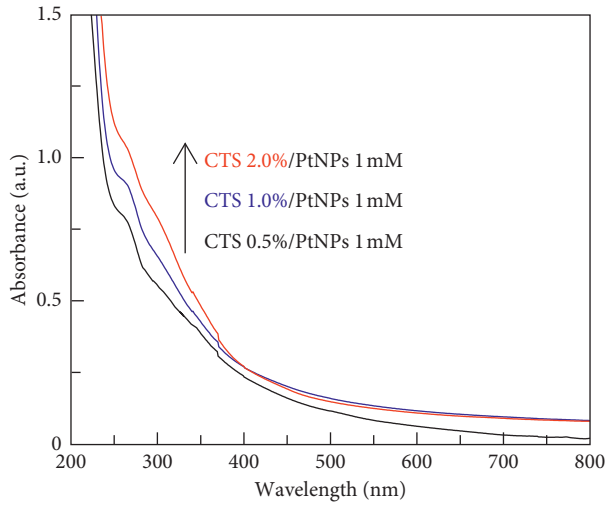

Figure 2: UV-Vis spectra of PtNPs/CTS solutions with different CTS concentrations.

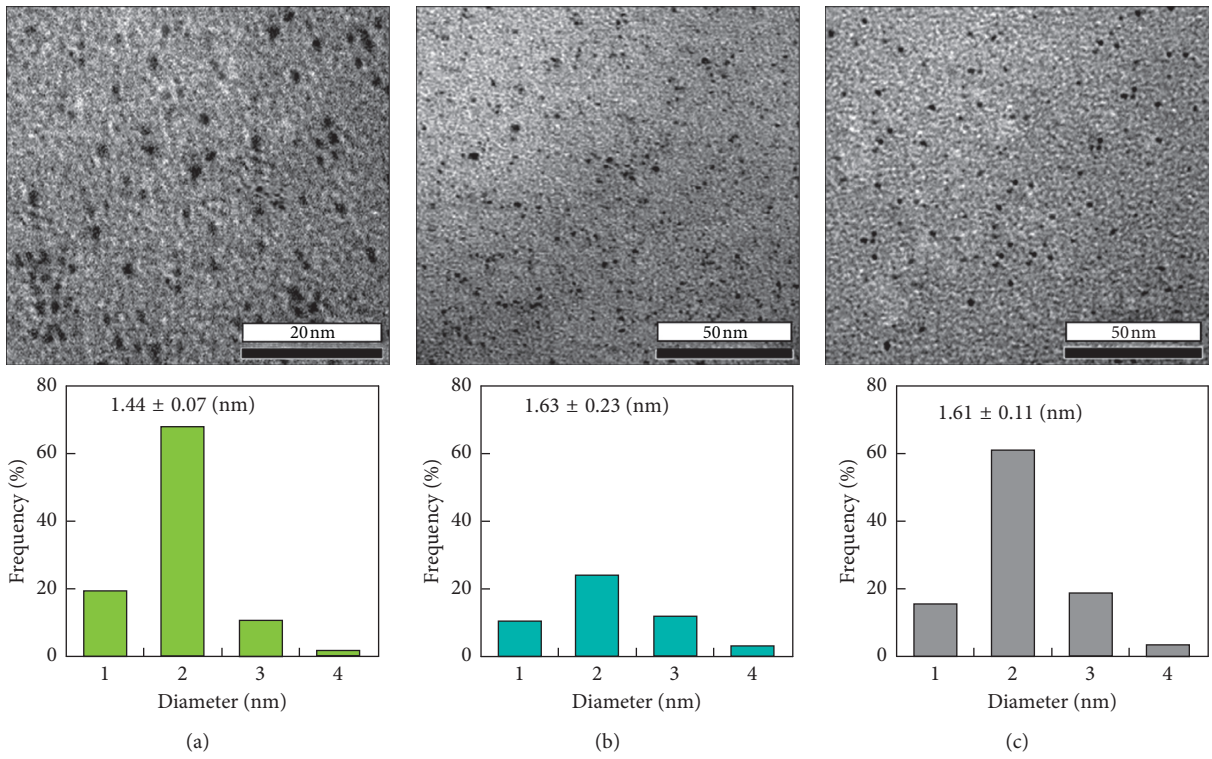

Figure 3: TEM images and size distribution of PtNPs from 1 mM PtNPs in 0.5% CTS (a), 1.0% CTS (b), and 2.0% CTS (c).

7.4 nm for the PtNPs concentrations of 3.4 and 10 mM, respectively [17, 18]. Furthermore, the size of the synthesized PtNPs (1.4–1.6 nm) was also smaller than that of the PtNPs (3.4 nm) that were synthesized by the chemical method using $NaBH_4$ as a reducing agent with the same initial concentration of 1 mM Pt^{4+} and 1% CTS as a stabilizer [5]. Moreover, the study on the synthesis of Ag and Au nanoparticles by the gamma Co-60 ray irradiation method using CTS as a stabilizer revealed that the size of Ag and Au nanoparticles was 4.6 and 9.8 nm for 1 mM Ag^{+} and Au^{3+} ions, respectively [16, 20]. Thus, it is obvious that the size of PtNPs synthesized by the gamma Co-60 ray irradiation method is smaller than that of Ag and Au nanoparticles at the same initial concentration of metal ions. The reason for this phenomenon is still not clear. Furthermore, it is interesting to note that, according to Choi et al. [6], the size of PtNPs which was synthesized by the gamma Co-60 ray irradiation using polyvinyl pyrrolidone as a stabilizer and the Pt^{4+} ions concentration of 0.2 mM could not be predicted from TEM images due to the morphology of particles was not clear. Therefore, further study of the effect of stabilizers on the morphology and size of PtNPs

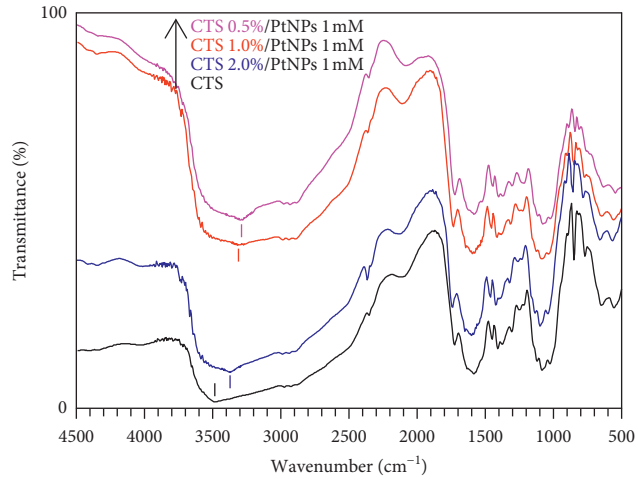

Figure 4: FT-IR spectra of CTS and PtNPs/CTS samples with different CTS concentrations.

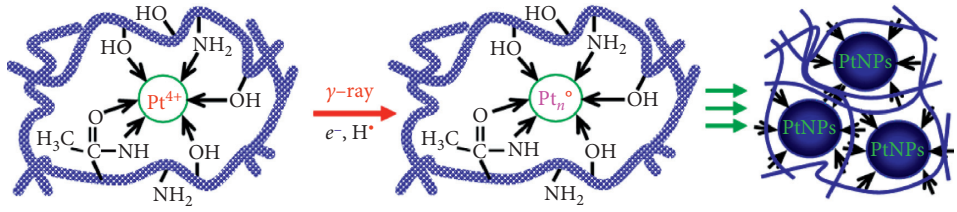

Figure 5: Schematic diagram of chitosan capped PtNPs synthesized by the gamma Co-60 ray irradiation.

synthesized by the gamma-ray irradiation method should be carried out.

The FT-IR spectra of CTS and PtNPs/CTS are shown in Figure 4. The FT-IR spectrum of the CTS possesses the main characteristic peaks that appear at 3448 cm^{-1} for O-H and N-H stretch; 2937 cm^{-1} and 2981 cm^{-1} for C-H stretch [21]; 1641 cm^{-1} for C=O stretching vibration in amide I; 1591 cm^{-1} for N-H deformation vibration in amide II; 1413 cm^{-1} and 1380 cm^{-1} for acetamide stretching and C-CH$_3$ deformation vibration of amide groups; 1126 cm^{-1} for antisymmetric stretch C-O-C and C-N stretch; and 1089 cm^{-1} and 1031 cm^{-1} for skeletal vibration of C-O stretch [21, 22]. The FT-IR spectra of PtNPs/CTS samples with different concentrations of CTS in Figure 4 are almost similar to that of CTS. However, the main difference was that the peak at 3448 cm^{-1} of CTS shifted to lower wavenumbers, particularly at 3382, 3269, and 3236 cm^{-1} for PtNPs/CTS samples with CTS concentration of 2.0, 1.0, and 0.5%, respectively. Thus, on the basis of the FT-IR spectra of PtNPs/CTS in Figure 4, it presumed that the interaction between CTS molecules and PtNPs has occurred. The obtained FT-IR spectra in this study were also consistent with that in the study of Geng et al. [21] using chitosan as a stabilizer for the synthesis of Fe nanoparticles.

Chitosan, hyaluronan, and alginate with oxygen-rich structures lead to binding them to metal nanoparticles tightly via steric and electrostatic interactions [23]. On the basis of the stabilizing interaction of polysaccharides to metal nanoparticles, a schematic diagram of chitosan capped PtNPs which were synthesized using the gamma Co-60 ray irradiation was proposed as in Figure 5. Furthermore, the spherical PtNPs with the small size (1-2 nm) were favorably synthesized using the gamma Co-60 ray irradiation. And this method has been considered as a green production method with favorable large-scale production [24, 25].

4. Conclusions

The gamma Co-60 ray irradiation has been as an effective method for synthesizing PtNPs dispersed in the CTS solution. The saturated conversion dose ($Pt^{4+} \longrightarrow Pt^0$) for the initial Pt^{4+} concentration of 1 mM was found out to be ~14 kGy. The resultant PtNPs with the small size (1.4–1.6 nm) could be potentially applied in catalyst materials and other purposes of applications as well.

Data Availability

The experimental and analytical data used to support the findings of this study are included within the article.

Conflicts of Interest

The authors declare that they have no conflicts of interest.

Acknowledgments

This research was funded by the Vietnam National Foundation for Science and Technology (NAFOSTED) under Grant no. "104.06-2017.311." The authors would like to thank

VINAGAMMA Center, VINATOM, for providing gamma Co-60 irradiation and favorable experimental conditions.

References

[1] J.-J. Du, C. Chen, Y.-L. Gan, R.-H. Zhang, C.-Y. Yang, and X.-W. Zhou, "Facile one-pot hydrothermal synthesis of Pt nanoparticles and their electrocatalytic performance," *International Journal of Hydrogen Energy*, vol. 39, no. 31, pp. 17634–17637, 2014.

[2] H. Huang, P. Hu, H. Huang, J. Chen, X. Ye, and D. Y. C. Leung, "Highly dispersed and active supported Pt nanoparticles for gaseous formaldehyde oxidation: influence of particle size," *Chemical Engineering Journal*, vol. 252, pp. 320–326, 2014.

[3] W. Yang, Y. Ma, J. Tang, and X. Yang, ""Green synthesis" of monodisperse Pt nanoparticles and their catalytic properties," *Colloids and Surfaces A: Physicochemical and Engineering Aspects*, vol. 302, no. 1–3, pp. 628–633, 2007.

[4] S. Remita, M. Mostafavi, and M. O. Delcourt, "Bimetallic Ag·Pt and Au·Pt aggregates synthesized by radiolysis," *Radiation Physics and Chemistry*, vol. 47, no. 2, pp. 275–279, 1996.

[5] M. J. Laudenslager, J. D. Schiffman, and C. L. Schauer, "Carboxymethyl chitosan as a matrix material for platinum, gold, and silver nanoparticles," *Biomacromolecules*, vol. 9, no. 10, pp. 2682–2685, 2008.

[6] S.-H. Choi, Y.-P. Zhang, A. Gopalan, K.-P. Lee, and H.-D. Kang, "Preparation of catalytically efficient precious metallic colloids by γ-irradiation and characterization," *Colloids and Surfaces A: Physicochemical and Engineering Aspects*, vol. 256, no. 2-3, pp. 165–170, 2005.

[7] D. Rao, Q. Sheng, and J. Zheng, "Preparation of flower-like Pt nanoparticles decorated chitosan-grafted graphene oxide and its electrocatalysis of hydrazine," *Sensors and Actuators B: Chemical*, vol. 236, pp. 192–200, 2016.

[8] P. L. Suryawanshi, S. P. Gumfekar, P. R. Kumar, B. B. Kale, and S. H. Sonawane, "Synthesis of ultra-small platinum nanoparticles in a continuous flow microreactor," *Colloid and Interface Science Communications*, vol. 13, pp. 6–9, 2016.

[9] D. Tongsakul, K. Wongravee, C. Thammacharoen, and S. Ekgasit, "Enhancement of the reduction efficiency of soluble starch for platinum nanoparticles synthesis," *Carbohydrate Research*, vol. 357, pp. 90–97, 2012.

[10] L. Wu, S. Shafii, M. R. Nordin, K. Y. Liew, and J. Li, "Structure determination of chitosan-stabilized Pt and Pd based bimetallic nanoparticles by X-ray photoelectron spectroscopy and transmission electron microscopy," *Materials Chemistry and Physics*, vol. 137, no. 2, pp. 493–498, 2012.

[11] S. Dehdashtian, M. B. Gholivand, M. Shamsipur, and S. Kariminia, "Construction of a sensitive and selective sensor for morphine using chitosan coated Fe_2O_3 magnetic nanoparticle as a modifier," *Materials Science and Engineering: C*, vol. 58, pp. 53–59, 2016.

[12] Y. Ma, X. Wu, and G. Zhang, "Core-shell Ag@Pt nanoparticles supported on sepiolite nanofibers for the catalytic reduction of nitrophenols in water: enhanced catalytic performance and DFT study," *Applied Catalysis B: Environmental*, vol. 205, pp. 262–270, 2017.

[13] M. Zhao, N. Zhong, and Y. Ji, "Ultra-stable colloidal porous Pt-Au-Ag nanoparticles," *Materials Letters*, vol. 191, pp. 38–41, 2017.

[14] A. Thirumurugan, P. Aswitha, C. Kiruthika, S. Nagarajan, and A. N. Christy, "Green synthesis of platinum nanoparticles using Azadirachta indica—an eco-friendly approach," *Materials Letters*, vol. 170, pp. 175–178, 2016.

[15] ASTM International, "Standard practice for use of a dichromate dosimetry system," in *Standards on Dosimetry for Radiation Processing*, ISO/ASTM 51401–2003(E), pp. 69–74, ASTM International, West Conshohocken, PA, USA, 2004.

[16] D. V. Phu, V. T. K. Lang, N. T. Kim Lan et al., "Synthesis and antimicrobial effects of colloidal silver nanoparticles in chitosan by γ-irradiation," *Journal of Experimental Nanoscience*, vol. 5, no. 2, pp. 169–179, 2010.

[17] E. Gharibshahi, E. Saion, A. Ashraf, and L. Gharibshahi, "Size-controlled and optical properties of platinum nanoparticles by gamma radiolytic synthesis," *Applied Radiation and Isotopes*, vol. 130, pp. 211–217, 2017.

[18] T. Cele, M. Maaza, and A. Gibaud, "Synthesis of platinum nanoparticles by gamma radiolysis," *MRS Advances*, vol. 3, no. 42-43, pp. 2537–2557, 2018.

[19] K. D. N. Vo, C. Kowandy, L. Dupont, X. Coqueret, and N. Q. Hien, "Radiation synthesis of chitosan stabilized gold nanoparticles comparison between e^- beam and γ irradiation," *Radiation Physics and Chemistry*, vol. 94, pp. 84–87, 2014.

[20] N. D. Nguyen, V. P. Dang, A. Q. Le, and Q. H. Nguyen, "Electron beam/γ-ray irradiation synthesis of gold nanoparticles and investigation of antioxidant activity," *Advances in Natural Sciences: Nanoscience and Nanotechnology*, vol. 5, no. 4, article 045002, 2014.

[21] B. Geng, Z. Jin, T. Li, and X. Qi, "Preparation of chitosan-stabilized Fe^0 nanoparticles for removal of hexavalent chromium in water," *Science of The Total Environment*, vol. 407, no. 18, pp. 4994–5000, 2009.

[22] J. Yang, J.-H. Yu, J. Rudi Strickler, W.-J. Chang, and S. Gunasekaran, "Nickel nanoparticle-chitosan-reduced graphene oxide-modified screen-printed electrodes for enzyme-free glucose sensing in portable microfluidic devices," *Biosensors and Bioelectronics*, vol. 47, pp. 530–538, 2013.

[23] L. Huang, M. Zhai, J. Peng, L. Xu, J. Li, and G. Wei, "Synthesis, size control and fluorescence studies of gold nanoparticles in carboxymethylated chitosan aqueous solutions," *Journal of Colloid and Interface Science*, vol. 316, no. 2, pp. 398–404, 2007.

[24] M. Chandra and P. K. Das, "Green routes to noble metal nanoparticle synthesis," *International Journal of Green Nanotechnology: Physics and Chemistry*, vol. 1, no. 1, pp. P10–P25, 2009.

[25] N. Q. Hien, D. V. Phu, N. N. Duy, and L. A. Quoc, "Radiation synthesis and characterization of hyaluronan capped gold nanoparticles," *Carbohydrate Polymers*, vol. 89, no. 2, pp. 537–541, 2012.

Hindawi
Advances in Materials Science and Engineering
Volume 2019, Article ID 1826148, 11 pages
https://doi.org/10.1155/2019/1826148

Research Article

Simultaneous Determination of Zn(II), Cd(II), Pb(II), and Cu(II) Using Differential Pulse Anodic Stripping Voltammetry at a Bismuth Film-Modified Electrode

Nguyen Mau Thanh,[1,2] Nguyen Van Hop,[1] Nguyen Dinh Luyen,[3] Nguyen Hai Phong,[1] and Tran Thanh Tam Toan[1]

[1]*University of Sciences, Hue University, 530000 Hue, Vietnam*
[2]*Faculty of Natural Sciences, Quang Binh University, 51000 Quang Binh, Vietnam*
[3]*University of Education, Hue University, 530000 Hue, Vietnam*

Correspondence should be addressed to Tran Thanh Tam Toan; tranthanhtamtoan@gmail.com

Received 6 December 2018; Accepted 4 March 2019; Published 17 April 2019

Guest Editor: Hien Duy Mai

The simultaneous electrochemical determination of Zn(II), Cd(II), Pb(II), and Cu(II) in the aqueous solution has been developed on the basis of the bismuth film glassy carbon electrode (GCE) using differential pulse anodic stripping voltammetry (DP-ASV). The bismuth film electrode (BiFE) was prepared by adding 500 ppb bismuth(III) directly to the sample solution and simultaneously depositing bismuth and the metal analytes on GCE. The optimal operational parameters, namely, accumulation potential (–1.6 V), accumulation time (110 s), pulsed amplitude (0.07 V), and scan rate (0.021 $V{\cdot}s^{-1}$), were found using a Box–Behnken design. Under the optimum conditions, a linear relationship exists between the current and the concentration of Zn(II), Cd(II), Pb(II), and Cu(II) in the range between 5.0 ppb and 110.0 ppb with the detection limits of 1.07 for Zn(II), 0.93 ppb for Cd(II), 0.65 ppb for Pb(II), and 0.94 ppb for Cu(II) calculated on the basis of a signal-to-noise ratio equal to 3 (S/N = 3). The interference experiments show that Co(II), Ni(II), and Fe(III) have a little influence on the DP-ASV signals of Zn(II), Cd(II), Pb(II), and Cu(II). In addition, a high reproducibility was indicated from small relative standard deviations (1.03%, 1.74%, 1.32%, and 4.74%) for 25 repeated measurements of 15 ppb copper, lead, cadmium, and zinc solutions. BiFE was successfully applied to determine Zn(II), Cd(II), Pb(II), and Cu(II) in river samples, and the results are in a good agreement with those determined with graphite furnace atomic absorption spectrometry (GF-AAS).

1. Introduction

Heavy metal pollution (Hg(II), Pb(II), Cd(II), and Ni(II)) has become one of the most critical environmental problems today. Unlike organic pollutants, heavy metals are non-biodegradable. They are found in industrial wastewater, and their discharge to the environment is alarming owing to their acute toxicity to aquatic and terrestrial life, including humans [1]. Of these, excessive intake of copper (over 1.0 $mg{\cdot}L^{-1}$ in drinking water) accumulates in the livers of humans and animals, which causes hemochromatosis and gastrointestinal catarrh diseases [1]. Lead is a highly toxic and cumulative poison and accumulates mainly in the bones, brain, kidneys, and muscles. Lead poisoning in humans causes severe damage to the kidneys, nervous and reproductive systems, liver, and brain [2, 3]. Cadmium (Cd) is one of the most toxic pollutants in aquatic systems. It cannot be removed easily from water systems by self-purification and could pose a serious threat to the environment and human health [4]. The longtime accumulation (30 years) of Cd through the food chain can lead to serious osteoporosis-like bone diseases [5]. Zinc, an important element for living

organisms, when exceeding the specific limits, accumulates in nature as it cannot be biodegraded. Zinc is associated with short-term "metal-fume fever," nausea, diarrhea, depression, lethargy, and neurological signs, such as seizures and ataxia [6, 7]. Therefore, the determination of heavy metals in the human environment is very necessary and important. There are several methods to determine heavy metals in water. The most widely used methods for heavy metal determination include atomic absorption spectrometry (AAS) [8], flame atomic absorption spectrometry (FAAS) [9], inductively-coupled plasma mass spectroscopy (ICP-MS) [10], graphite furnace atomic absorption spectroscopy (GF-AAS), and X-ray fluorescence [11], and they are employed currently for trace analysis of heavy metals. Among these methods, anodic stripping voltammetry approaches are an emerging and attractive method because the main advantages of this technique can be ordered as high selectivity, sensitivity, *in situ* operation, and low cost.

In 2000, a new type of electrode, the bismuth film-modified electrode (denoted as BiFE), was found as an alternative to mercury film electrodes (MFEs) [12], which are highly toxic. The significant advantage of BiFEs is that they are environmentally friendly since the toxicity of bismuth and its salts is negligible. However, the advantageous analytical properties of BiFEs in the voltammetric analysis, roughly comparable to those of MFEs, are assigned to the property of bismuth to form "fused alloys" with heavy metals, which is analogous to the amalgams that mercury form [13]. Wang et al. [12] reported that bismuth-coated carbon electrodes display an attractive stripping voltammetric performance that is similar to that of common mercury film electrodes and could be utilized to simultaneously determine Cu(II), Cd(II), and Pb(II) in aqueous solutions. Wu et al. [14] reported the simultaneous determination of Pb, Cd, and Zn using DP-ASV at a bismuth/poly(*p*-aminobenzene sulfonic acid) film electrode. Lead and cadmium in rice samples are determined by means of ASV using a bismuth film/crown ether/Nafion-modified screen-printed carbon electrode [15]. Li et al. [16] reported the simultaneous detection of ultratrace lead and cadmium by square wave stripping voltammetry with in situ depositing bismuth at the Nafion-medical stone-doped disposable electrode, and the assay results of heavy metals in wastewater with the proposed method were in a good agreement with the atomic absorption spectroscopy method. To the best of our knowledge, a few articles have attempted to study the simultaneous determination of Zn(II), Cd(II), Pb(II), and Cu(II) by BiFE.

This article demonstrates the attractive stripping voltammetric behavior of BiFE. BiFE was prepared by simultaneously accumulating bismuth and the target heavy metals (Cu, Pb, Cd, and Zn). The Box–Behnken design was conducted to optimise the operational parameters. BiFE displays well-defined, sharp, and highly reproducible stripping peaks for low (ppb) concentrations of copper, lead, cadmium, and zinc over a low background current. The simultaneous determination of copper, lead, cadmium, and zinc in real samples was also addressed.

2. Experimental

2.1. Materials. All solutions were prepared using double-distilled water. The zinc, cadmium, lead, copper, and bismuth standard stock solutions (1000 ppm Zn, Cd, Pb, and Cu or 5 (Bi) wt.% nitric acid) were obtained from Aldrich and diluted as required. An acetate buffer solution (0.10 M, pH 4.5) served as the supporting electrolyte.

2.2. Apparatus. Stripping voltammetry was performed with a CPA-HH5 Computerized Polarography Analyzer (Vietnam). A glassy carbon electrode (GCE) (3 mm diameter, BAS) served as a working electrode, with Ag/AgCl (3 M KCl) and platinum wire acting as the reference and counter electrodes, respectively. Graphite furnace atomic absorption spectroscopy (GF-AAS) was performed in ZEEnit 700P (Analytik Jena, Germany) as a reference method.

2.3. Procedure. The glassy carbon electrode was polished using 1.0 μm Al_2O_3 slurry, rinsed with ethanol/water and dried. The analytes (Zn, Cd, Pb, and Cu) were accumulated on the surface of GCE at a potential of –1.4 V (E_{acc}) for 120 s of accumulation (t_{acc}). During this step, the electrode was rotated at a constant rate of 1000 rpm. After that, the electrode rotation was ceased; then, cyclic voltammograms (CVs) were recorded from –1.5 V to +0.1 V (forward potential scan) and then from +0.1 V to –1.5 V (reverse potential scan) at a scan rate of 0.2 V·s^{-1}.

Stripping voltammetric measurements were conducted with an *in situ* accumulation of the bismuth film and target metals (Zn, Cd, Pb, and Cu). The three electrodes were immersed in a 10 mL electrochemical cell containing 0.1 M acetate buffer (pH 4.5) and an appropriate amount of bismuth. The accumulation potential at –1.4 V was applied to the carbon working electrode under stirring. After the accumulation step (120 s), stirring was stopped, and after 10 s, the voltammogram was recorded by applying a positive-going differential pulse voltammetric potential scan (with an amplitude of 50 mV and a potential step of 6 mV). The scan was terminated at 0.1 V. All experiments were carried out at room temperature.

2.4. Operational Parameters of Box–Behnken Central Design (BBD). The operational parameters were optimised by using BBD. The effect of accumulation potential (x_1), accumulation time (x_2), pulse amplitude (x_3), and scan rate (x_4) on the peak current of BiEF was studied. The number of experiments (N) required for the performance of this design is defined as $N = 2k \cdot (k-1) + C_0$, where k is the number of factors ($k = 4$) and C_0 is the number of replicates at the center point [17]. Thus, a total of 27 experiments were carried out for optimising these four variables. Each independent variable is considered at three levels: low, medium, and high, coded as –1, 0, and +1, respectively (Table 1). The center points were used to determine the error. On the basis of the experimental data, a second-order polynomial model is

Table 1: Factors in BBD and their levels.*

Level	Accumulation potential (x_1, V)	Accumulation time (x_2, s)	Pulse amplitude (x_3, V)	Scan rate (x_4, V·s^{-1})
High level (+1)	–1.0	20	0.01	0.01
Central level (0)	–1.5	100	0.05	0.02
Low level (–1)	–2.0	180	0.09	0.03

*15 ppb concentration of Zn, Cd, Pb, and Cu in 500 ppb Bi and 0.1 M acetate buffer (pH 5).

obtained. The relationship between the response and the variables could be presented as follows:

$$\begin{aligned} y = {} & b_0 + b_1 \cdot x_1 + b_2 \cdot x_2 + b_3 \cdot x_3 + b_4 \cdot x_4 + b_{11} \cdot x_{12} \\ & + b_{22} \cdot x_{22} + b_{33} \cdot x_{32} + b_{44} \cdot x_{42} + b_{12} \cdot x_1 \cdot x_2 \\ & + b_{13} \cdot x_1 \cdot x_3 + b_{14} \cdot x_1 \cdot x_4 + b_{23} \cdot x_2 \cdot x_3 + b_{24} \cdot x_2 \cdot x_4 \\ & + b_{34} \cdot x_3 \cdot x_4, \end{aligned} \tag{1}$$

where y is the predicted response value (anodic peak current, I_{pa}); x_1, x_2, x_3, and x_4 are the independent variables; b_0 is the intercept term (the mean value of response at the center points); b_1, b_2, b_3, and b_4 are the linear coefficients; b_{12}, b_{13}, and b_{14} and b_{23}, b_{24}, and b_{34} are the cross-product coefficients; and b_{11}, b_{22}, b_{33}, and b_{44} are the quadratic-term coefficients. The design and analysis of the experiment were carried out using Minitab version 16. The definition of the factors and their level values are shown in Table 1.

2.5. Sample Preparation. One milliliter of the sample solution was adjusted to pH 5 with NaOH or HCl and diluted to 5 mL with a 0.1 M acetate buffer (pH 5), and then it was placed in the cell without deaeration. Stripping voltammetric measurements were performed with an *in situ* accumulation of bismuth and the target metals (Zn, Cd, Pb, and Cu), and the accumulation was carried out for 110 s at –1.6 V, while the solution was stirred. After the solution was kept standstill for 10 s, DP-ASV was recorded. The metal analytes in the river water were determined by means of GF-AAS for the sake of comparison.

3. Results and Discussion

3.1. Effect of Bismuth Concentration. The influence of the bismuth ion concentration on the anodic current peak (I_{pa}) of the metals was studied in the range 0–1000 ppb for a solution containing 15 ppm Zn(II), Cd(II), Pb(II), and Cu(II) in a 0.1 M acetate buffer (pH 4.5) at bare GCE. Very small and distorted stripping peaks of the metal analytes are observed at bare GCE, and the signal of Zn is not obtained (Figure 1(a)). When bismuth (500 ppb) was added to the sample, distinct and undistorted stripping peaks for the analytes are achieved, indicating that bismuth is responsible for the attractive electrochemistry behavior. It is supposed that the amount of the Bi(III) ion decides the thickness of the Bi film, whereas the film thickness does not influence the peak position of any metals. Figure 1(b) presents the effect of Bi concentration on the anodic peak current. The anodic peak of cadmium increases significantly with the bismuth concentration from 0 to 400 ppb and then levels off. A similar trend is observed for Pb below 600 ppb, and the anodic peak of lead fluctuates slightly after this concentration. The copper and zinc peaks increase significantly with the bismuth concentration up to 500 ppb, and the rise becomes slight afterwards. The results suggest that the appropriate combination of sensitivity, peak sharpness, and background current (especially close to the Zn peak) was performed for Bi(III) concentration of 500 ppb.

3.2. Effect of pH. The effect of pH on the stripping peak current of Zn(II), Cd(II), Pb(II), and Cu(II) at BiFE was studied (Figure 2(a)). The optimal pH ranges are 5.0–6.0 for Zn(II) and Cd(II) and 4.0–6.0 for Pb(II) and Cu(II) (Figure 2(b)). If the acidity is higher or lower than the optimum ranges, the responses of Zn(II) and Cd(II) decrease. For Pb(II) and Cu(II) peak currents, I_{pa} decreases slightly in pH from 4.0 to 6.0 and declines significantly with the further increasing pH. The best compromise of I_{pa} could be obtained at pH 5.0–6.0. In the present study, we choose pH of 5.0 for the next experiments.

Figure 2(c) provides the linear plots of pH dependence of peak potential (E_p). The linear equations are expressed as follows:

$$\begin{aligned} E_{p,Zn} &= (-0.87 \pm 0.05) + (-0.059 \pm 0.007) \cdot \text{pH}, \\ & \qquad R^2 = 0.941,\ p < 0.001, \\ E_{p,Cd} &= (-0.62 \pm 0.02) + (-0.052 \pm 0.003) \cdot \text{pH}, \\ & \qquad R^2 = 0.984,\ p < 0.001, \\ E_{p,Pb} &= (-0.31 \pm 0.02) + (-0.060 \pm 0.003) \cdot \text{pH}, \\ & \qquad R^2 = 0.990,\ p < 0.001, \\ E_{p,Cu} &= (0.20 \pm 0.03) + (-0.054 \pm 0.004) \cdot \text{pH}, \\ & \qquad R^2 = 0.977,\ p < 0.001. \end{aligned} \tag{2}$$

The linear relationship of E_p vs. pH exhibits a high statistical significance with high determination coefficients (0.941–0.990, $p < 0.05$). The slopes of the lines are very close to the theoretical value of 0.059 for the Nerstian equation, indicating that the redoxidation involves the equal number of protons and electrons.

3.3. Effect of CV Scan Rate. The relationship between the peak current and the scan rate could provide important information about the electrochemical mechanism. Therefore, the effect of scan rate on the peak potential (E_p) and peak current (I_p) was investigated using CV, as shown in Figure 3(a). If the electrooxidation reaction is reversible, E_p is independent on v, and vice versa. As can be seen from

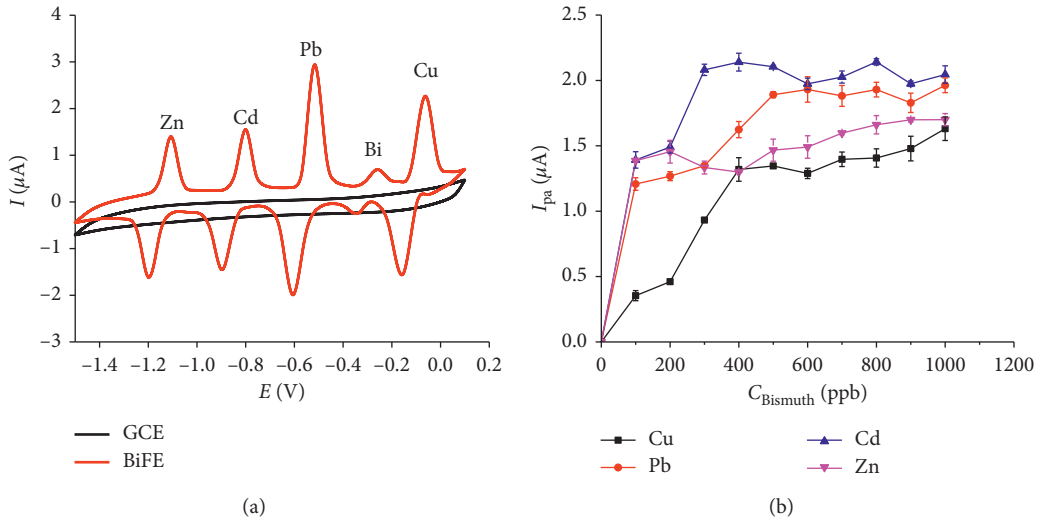

Figure 1: (a) Differential pulse stripping voltammograms of 15 ppm Zn(II), Cd(II), Pb(II), and Cu(II) at GCE without and with 500 ppb Bi(II) in 0.1 M acetate buffer (pH 4.5); (b) the influence of the bismuth ion concentration on anodic current peaks (I_{pa}) (accumulation for 120 s at −1.4 V).

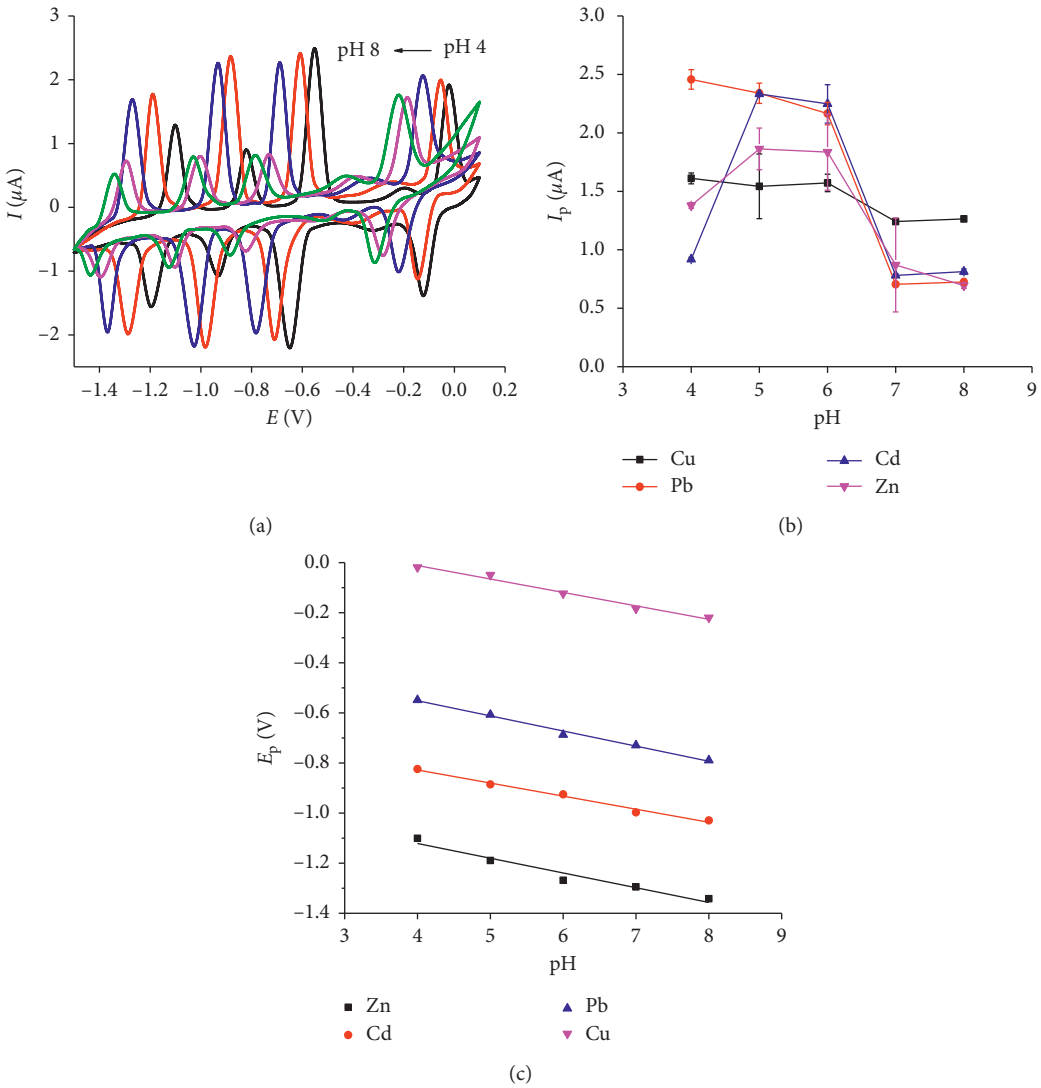

Figure 2: (a) CV curves of Zn, Cd, Pb, and Cu at different pH values (15 ppm Zn(II), Cd(II), and Pb(II), 500 ppb Bi(II) in 0.1 M acetate buffer, and accumulation for 120 s at −1.4 V); (b) pH dependence of I_p; (c) pH dependence of E_p.

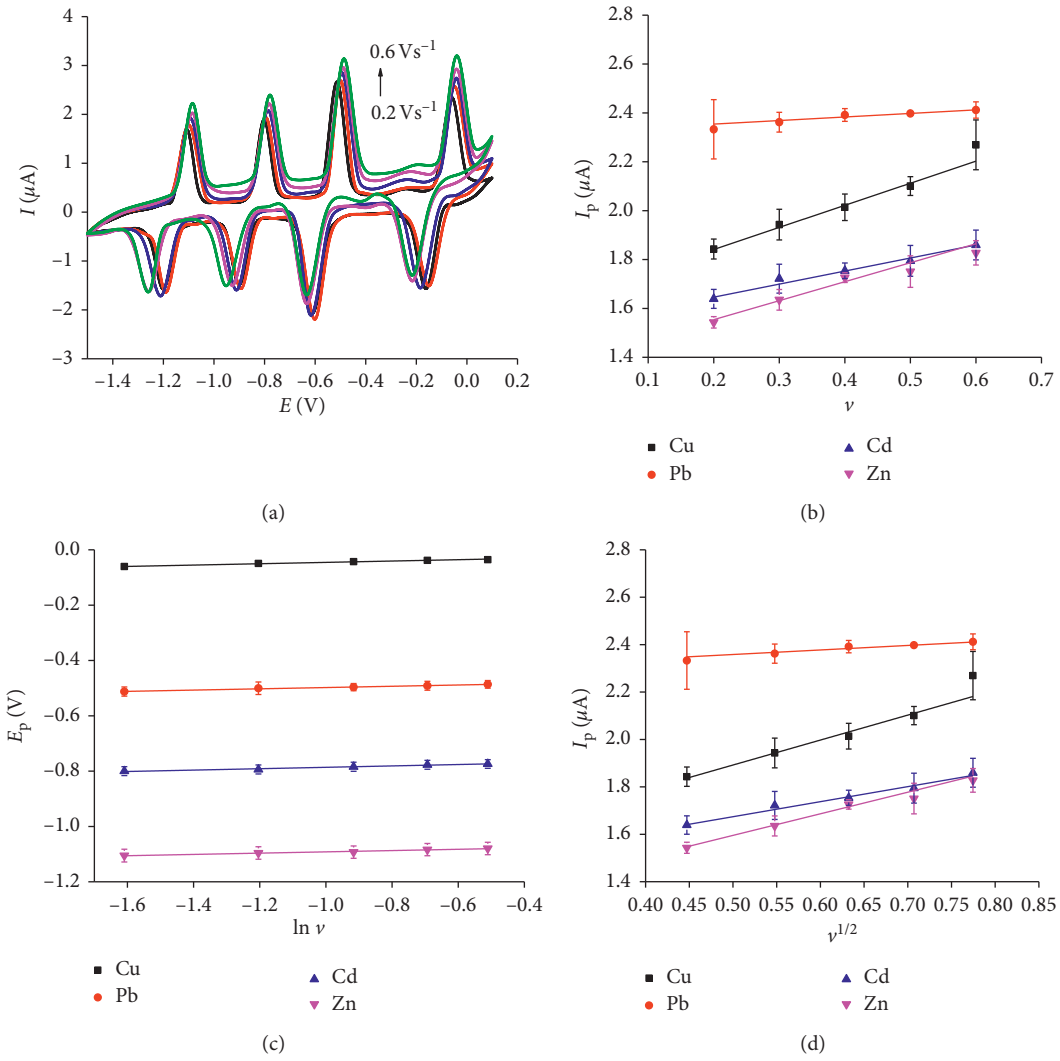

FIGURE 3: (a) CVs of analytes (Zn, Cd, Pb, and Cu) with increasing scan rate (v); (b) plot of I_{pa} vs. scan rate (v); (c) plot of E_p vs. ln v; (d) plot of I_{pa} vs. $v^{1/2}$ (conditions: 15 ppm Zn(II), Cd(II), Pb(II), and Cu(II) in 0.1 M acetate buffer (pH 5), 500 ppb Bi, and accumulation for 120 s at −1.4 V).

Figure 3(a), the anodic peak potential (E_p) shifts to a higher potential with the increase in the scan rate, and then it is suggested that the electron transfer in analyte electrooxidation is irreversible. The anodic peak current (I_{pa}) increases with the increase in the scan rate from 0.2 to 0.6 V·s^{-1}, as shown in Figure 3(b), suggesting that the electron transfer reaction involves a surface-confined process.

The relationship between the peak potential (E_{pc}) and the natural logarithm of the scan rates is described by Laviron's equation [18]:

$$E_p = E^O + \frac{RT}{\alpha nF} \ln \frac{\alpha nFk_s}{RT} + \frac{RT}{\alpha nF} \ln v, \quad (3)$$

where α is the charge transfer coefficient, k_s is the heterogeneous electron transfer rate constant of the surface-confined redox couple, n is the number of electrons transferred, v is the scan rate (V·s^{-1}), and E^0 is the formal redox potential, $T = 298$ K, $R = 8.314$ J·mol·K^{-1}, and $F = 96480$ C·mol^{-1}.

The plots of E_{pa} of the analytes versus ln v are shown in Figure 3(c). The linear regression equations are as follows:

$$E_{pa,Zn} = (-1.069 \pm 0.002) + (0.023 \pm 0.002) \cdot \ln v, \quad R^2 = 0.986, \quad (4)$$

$$E_{pa,Cd} = (-0.761 \pm 0.002) + (0.025 \pm 0.002) \cdot \ln v, \quad R^2 = 0.988, \quad (5)$$

$$E_{pa,Pb} = (-0.475 \pm 0.001) + (0.023 \pm 0.001) \cdot \ln v, \quad R^2 = 0.995, \quad (6)$$

$$E_{pa,Cu} = (-0.0210 \pm 0.0001) + (0.024 \pm 0.001) \cdot \ln \nu, \quad R^2 = 0.997. \tag{7}$$

The value of $\alpha \cdot n$ in equation (3) for Zn, Cd, Pb, and Cu can be derived from the slope of regression equations (4)–(7), and they are 1.11, 1.02, 1.11, and 1.05, respectively. The value of α is assumed to be equal to 0.5 for an irreversible system [19]. Therefore, the number of electrons transferred (n) in the electrooxidation of Zn, Cd, Pb, and Cu is 2.23, 2.05, 2.23, and 2.10, respectively. Consequently, with $n = 2$, the oxidation mechanism for Zn, Cd, Pb, and Cu could involve two electrons and two protons at pH 5. The reactions at the electrode are as follows:

$$\begin{aligned}
\mathrm{Bi(III)} + 3e &\longrightarrow \mathrm{Bi/GCE\,(BiFE)} \\
\mathrm{M(II)} + \mathrm{BiFE} + 2e &\longrightarrow \mathrm{M-(BiFE)\,(M: Cu, Pb, Cd\ and\ Zn)} \\
\mathrm{Zn-Cd-Pb-Cu-BiFE} + 2\mathrm{CH_3COOH} &\longrightarrow \mathrm{Zn(CH_3COO)_2} + \mathrm{Cd-Pb-Cu-BiFE} + 2e + 2\mathrm{H^+} \\
\mathrm{Cd-Pb-Cu-BiFE} + 2\mathrm{CH_3COOH} &\longrightarrow \mathrm{Cd(CH_3COO)_2} + \mathrm{Pb-Cu-BiFE} + 2e + 2\mathrm{H^+} \\
\mathrm{Pb-Cu-BiFE} + 2\mathrm{CH_3COOH} &\longrightarrow \mathrm{Pb(CH_3COO)_2} + \mathrm{Cu-BiFE} + 2e + 2\mathrm{H^+} \\
\mathrm{Cu-BiFE} + 3\mathrm{CH_3COOH} &\longrightarrow \mathrm{Bi(CH_3COO)_3} + \mathrm{Cu-GCE} + 3e + 3\mathrm{H^+} \\
\mathrm{Cu-BiFE} + 2\mathrm{CH_3COOH} &\longrightarrow \mathrm{Cu(CH_3COO)_2} + \mathrm{BiFE} + 2e + 2\mathrm{H^+}
\end{aligned} \tag{8}$$

In order to decide whether the electrooxidation reaction is controlled by adsorption or diffusion, the plots of peak current (I_p) against $\nu^{1/2}$ are drawn (Figure 3(d)). If the linear plot of I_p vs. $\nu^{1/2}$ crosses the origin, the process is controlled by diffusion [20]. In the range 0.2 to 0.6 V·s^{-1}, the linear regression equations of I_{pa} for Zn, Cd, Pb, and Cu oxidation versus $\nu^{1/2}$ are as follows:

$$I_{pa,Cu} = (1.37 \pm 0.07) + (1.10 \pm 0.10) \cdot \nu^{(1/2)}, \quad R^2 = 0.958, \tag{9}$$

$$I_{pa,Pb} = (2.26 \pm 0.02) + (0.19 \pm 0.04) \cdot \nu^{(1/2)}, \quad R^2 = 0.867, \tag{10}$$

$$I_{pa,Cd} = (1.35 \pm 0.03) + (0.63 \pm 0.04) \cdot \nu^{(1/2)}, \quad R^2 = 0.980, \tag{11}$$

$$I_{pa,Zn} = (1.14 \pm 0.04) + (0.91 \pm 0.06) \cdot \nu^{(1/2)}, \quad R^2 = 0.981. \tag{12}$$

Although the plots of I_p versus $\nu^{1/2}$ are linear with high determination coefficients (0.958–0.981, $p \geq 0.001$), the intercepts do not cross the origin because the 95% confidence intervals for the intercepts do not contain zero (see the intercepts of equations (9)–(12)). This means that the electrode process of analyte electrooxidation is not controlled by diffusion.

3.4. Optimising the Operational Parameters Using BBD. A total of 27 experiments consisting of 24 standard cube points and 3 center points in the cube were carried out. The design of experiments and response values (I_p: anodic stripping current) of Cu, Pb, Cd, and Zn corresponding to each run is listed in Table 2.

The analysis of the data using Minitab 16 gives the following regression equations for I_p:

$$\begin{aligned}
I_{p,Zn} &= 1.53 - 0.14 \cdot x_1 + 0.07 \cdot x_2 + 0.14 \cdot x_3 \\
&\quad + 0.06 \cdot x_4 - 0.30 \cdot x_1^2 - 0.24 \cdot x_2^2 - 0.15 \cdot x_3^2 - 0.22 \cdot x_4^2 \\
&\quad + 0.03 \cdot x_1 \cdot x_2 + 0.01 \cdot x_1 \cdot x_3 + 0.02 \cdot x_1 \cdot x_4 \\
&\quad - 0.01 \cdot x_2 \cdot x_3 - 0.02 \cdot x_2 \cdot x_4 + 0.02 \cdot x_3 \cdot x_4, \quad R^2 = 0.999, \\
I_{p,Cd} &= 2.02 - 0.16 \cdot x_1 + 0.08 \cdot x_2 + 0.17 \cdot x_3 + 0.09 \\
&\quad \cdot x_4 - 0.33 \cdot x_1^2 - 0.24 \cdot x_2^2 - 0.16 \cdot x_3^2 - 0.26 \cdot x_4^2 - 0.03 \\
&\quad \cdot x_1 \cdot x_2 - 0.02 \cdot x_1 \cdot x_3 - 0.00 \cdot x_1 \cdot x_4 - 0.01 \\
&\quad \cdot x_2 \cdot x_3 - 0.03 \cdot x_2 \cdot x_4 + 0.05 \cdot x_3 \cdot x_4, \quad R^2 = 0.998, \\
I_{p,Pb} &= 3.34 - 0.25 \cdot x_1 + 0.15 \cdot x_2 + 0.25 \cdot x_3 + 0.11 \\
&\quad \cdot x_4 - 0.51 \cdot x_1^2 - 0.42 \cdot x_2^2 - 0.24 \cdot x_3^2 - 0.40 \cdot x_4^2 + 0.01 \\
&\quad \cdot x_1 \cdot x_2 + 0.02 \cdot x_1 \cdot x_3 + 0.01 \cdot x_1 \cdot x_4 \\
&\quad + 0.02 \cdot x_2 \cdot x_3 + 0.02 \cdot x_2 \cdot x_4 - 0.01 \cdot x_3 \cdot x_4, \quad R^2 = 0.999, \\
I_{p,Cu} &= 3.33 - 0.27 \cdot x_1 + 0.13 \cdot x_2 + 0.26 \cdot x_3 + 0.13 \\
&\quad \cdot x_4 - 0.53 \cdot x_1^2 - 0.41 \cdot x_2^2 - 0.26 \cdot x_3^2 - 0.40 \cdot x_4^2 \\
&\quad + 0.01 \cdot x_1 \cdot x_2 - 0.02 \cdot x_1 \cdot x_3 - 0.00 \cdot x_1 \cdot x_4 \\
&\quad + 0.01 \cdot x_2 \cdot x_3 + 0.01 \cdot x_2 \cdot x_4 - 0.00 \cdot x_3 \cdot x_4, \quad R^2 = 0.998.
\end{aligned} \tag{13}$$

The values of the coefficient of determination are 0.999, 0.998, 0.999, and 0.998 for Zn, Cd, Pb, and Cu, respectively, indicating an excellent agreement between experimental and predicted values. The positive and negative signs in each equation imply the synergistic and antagonistic effect of the variables. Although the magnitude of the coefficients in the equations varies, their sign is the same, indicating that the

Table 2: Design matrix and responses for full factorial design.

Run	Coded variable levels				Anodic peak current, I_{pa} (μA)			
	x_1	x_2	x_3	x_4	Cu	Pb	Cd	Zn
1	0	−1	0	−1	2.291	2.294	1.332	0.918
2	+1	0	−1	0	2.053	2.079	1.233	0.789
3	−1	−1	0	0	2.543	2.531	1.510	1.104
4	0	−1	−1	0	2.297	2.305	1.336	0.909
5	+1	0	+1	0	2.513	2.596	1.531	1.101
6	0	0	−1	−1	2.254	2.317	1.401	0.980
7	−1	0	−1	0	2.524	2.612	1.483	1.076
8	0	0	−1	+1	2.532	2.562	1.488	1.059
9	+1	0	0	−1	1.991	2.066	1.181	0.788
10	0	+1	−1	0	2.554	2.560	1.577	1.090
11	+1	−1	0	0	1.988	1.999	1.241	0.770
12	+1	+1	0	0	2.250	2.307	1.326	0.959
13	0	0	0	0	3.302	3.359	2.022	1.532
14	−1	+1	0	0	2.773	2.806	1.719	1.185
15	−1	0	0	+1	2.831	2.804	1.699	1.189
16	0	−1	0	+1	2.509	2.451	1.533	1.073
17	0	+1	0	−1	2.516	2.556	1.567	1.105
18	+1	0	0	+1	2.259	2.312	1.377	0.966
19	0	+1	+1	0	3.077	3.101	1.863	1.357
20	0	−1	+1	0	2.766	2.781	1.748	1.226
21	0	0	+1	−1	2.811	2.862	1.624	1.230
22	0	0	0	0	3.358	3.332	2.022	1.537
23	−1	0	0	−1	2.554	2.587	1.485	1.099
24	0	0	+1	+1	3.082	3.057	1.893	1.407
25	0	+1	0	+1	2.783	2.775	1.667	1.179
26	−1	0	+1	0	3.046	3.064	1.871	1.356
27	0	0	0	0	3.342	3.338	2.032	1.530

impact of each variable on the intensity of the peak current has the same tendency. The tests for the significance of the regression model for the response of analytes were adjusted, and the ANOVA tests are presented in Table 3. The non-significant lack-of-fit (0.654 for Cu, 0.541 for Pb, 0.086 for Cd, and 0.132 for Zn) confirms the validity of these quadratic models in the present study. From the statistical point of view, the coefficient with the p value > 0.05 is insignificant. This means that their contribution to the peak currents is negligible, and these effects should be discarded from the model. Thus, the predictive models become as follows:

$$\begin{aligned}
I_{p,Zn} &= 1.53 - 0.14 \cdot x_1 + 0.07 \cdot x_2 + 0.14 \cdot x_3 \\
&\quad + 0.06 \cdot x_4 - 0.30 \cdot x_1^2 - 0.24 \cdot x_2^2 - 0.15 \cdot x_3^2 - 0.22 \cdot x_4^2 \\
&\quad + 0.03 \cdot x_1 \cdot x_2 + 0.02 \cdot x_1 \cdot x_4 - 0.01 \cdot x_2 \cdot x_3 - 0.02 \\
&\quad \cdot x_2 \cdot x_4 + 0.02 \cdot x_3 \cdot x_4, \quad R^2 = 0.999, \\
I_{p,Cd} &= 2.02 - 0.16 \cdot x_1 + 0.08 \cdot x_2 + 0.17 \cdot x_3 \\
&\quad + 0.09 \cdot x_4 - 0.33 \cdot x_1^2 - 0.24 \cdot x_2^2 - 0.16 \cdot x_3^2 - 0.26 \cdot x_4^2 \\
&\quad - 0.03 \cdot x_1 \cdot x_2 - 0.02 \cdot x_1 \cdot x_3 - 0.01 \cdot x_2 \cdot x_3 - 0.03 \\
&\quad \cdot x_2 \cdot x_4 + 0.05 \cdot x_3 \cdot x_4, \quad R^2 = 0.998, \\
I_{p,Pb} &= 3.34 - 0.25 \cdot x_1 + 0.15 \cdot x_2 + 0.25 \cdot x_3 \\
&\quad + 0.11 \cdot x_4 - 0.51 \cdot x_1^2 - 0.42 \cdot x_2^2 - 0.24 \cdot x_3^2 - 0.40 \cdot x_4^2, \\
&\qquad\qquad R^2 = 0.999, \\
I_{p,Cu} &= 3.33 - 0.27 \cdot x_1 + 0.13 \cdot x_2 + 0.26 \cdot x_3 + 0.13 \\
&\quad \cdot x_4 - 0.53 \cdot x_1^2 - 0.41 \cdot x_2^2 - 0.26 \cdot x_3^2 - 0.40 \cdot x_4^2, \\
&\qquad\qquad R^2 = 0.998.
\end{aligned} \tag{14}$$

For the sake of simplicity, the I_p signal of Zn was used to optimise the experimental conditions because it is the lowest of those of the four metals at the same concentration. The profile for predicted values in Minitab 16 was performed for the optimisation process. The optimisation design matrix (Figure 4) represents the maximal $I_{pa,Zn}$ (1.59 μA) at the optimal conditions: accumulation potential −1.6 V, accumulation time 110 s, pulse amplitude 0.07 V, and scan rate 0.021 V·s^{-1}. To evaluate the repeatability of the model, the experiment under optimal conditions was repeated three times, and the obtained $I_{pa,Zn}$ is 1.55, 1.57, and 1.60 μA. The one-sample t-test proves that there is no statistical difference among these values ($t(2) = 1.147$, $p = 0.37 > 0.05$). These optimal operational parameters were utilized for further experiments.

3.5. Interference Study. The interference study was performed by adding various foreign substances to a standard solution containing 15 ppb of Zn(II), Cd(II), Pb(II), and Cu(II) and 500 ppb Bi(III) in the 0.1 M acetate buffer (pH 5) at the accumulation potential of −1.6 V and accumulation time of 110 s. The ratios of interference to Zn(II), Cd(II), Pb(II), and Cu(II) for the ±5.0% signal change are 15 for Co(II), 15 for Ni(II), and 45 for Fe(III) (Tables S1–S3).

3.6. Precision and Limit of Detection (LOD). An appropriate precision is another attractive feature of bismuth electrodes. A series of 25 repetitive measurements of a solution containing 15 ppb zinc, cadmium, lead, and copper results in highly reproducible stripping peaks with a relative standard deviation of 1.74%, 1.29%, 1.07%, and 0.76%, respectively, less than 1/2 RDS_H (Table S4). Such a good precision is attributed to the reproducible film renewal accrued from the *in situ* bismuth film. Compared with the "stabilization" period required for *in situ* plating of mercury-film electrodes [21], BiFE displays a highly stable response starting with the first run.

To verify the practicality of BiFE for the simultaneous determination of Zn(II), Cd(II), Pb(II), and Cu(II), the stripping process of these four metal ions in the mixture was also investigated (Figure 5). In each measurement, the concentration of one species changes while keeping that of the others constant. It can be seen from Figure 5(a) that the peak current of Cu(II) is positively proportional to its concentration from 5 to 110 ppb when keeping the concentration of Zn(II), Cd(II), and Pb(II) constant; meanwhile, the response of Zn(II), Cd(II), and Pb(II) is practically unaltered with the increasing Cu(II) content (a slight increase in the peak heights of lead and cadmium with increasing zinc concentration is merely due to the additive signal contribution of the slightly overlapping copper peak). A similar situation is observed with Zn(II), Cd(II), and Pb(II) (Figures 5(b)–5(d)). No interference can be detected for the determination of Zn(II), Cd(II), Pb(II), or Cd(II) by the coexistence of the other three species. Therefore, it can be concluded that, in the quaternary mixtures containing Zn(II), Cd(II), Pb(II), and Cu(II), the stripping peaks of the four analytes are clearly separated from each other.

Table 3: Analysis of variance (ANOVA) for BBD.

Terms	Coefficient $I_{pa,Cu}$	p value	Coefficient $I_{pa,Pb}$	p value	Coefficient $I_{pa,Cd}$	p value	Coefficient $I_{pa,Zn}$	p value
Constant	3.33	≤0.001	3.34	≤0.001	2.03	≤0.001	1.53	≤0.001
x_1	−0.27	≤0.001	−0.25	≤0.001	−0.16	≤0.001	−0.14	≤0.001
x_2	0.13	≤0.001	0.15	≤0.001	0.08	≤0.001	0.07	≤0.001
x_3	0.26	≤0.001	0.25	≤0.001	0.17	≤0.001	0.15	≤0.001
x_4	0.13	≤0.001	0.11	≤0.001	0.09	≤0.001	0.06	≤0.001
x_1^2	−0.53	≤0.001	−0.51	≤0.001	−0.33	≤0.001	−0.30	≤0.001
x_2^2	−0.41	≤0.001	−0.42	≤0.001	−0.24	≤0.001	−0.24	≤0.001
x_3^2	−0.26	≤0.001	−0.24	≤0.001	−0.16	≤0.001	−0.15	≤0.001
x_4^2	−0.40	≤0.001	−0.40	≤0.001	−0.26	≤0.001	−0.22	≤0.001
$x_1 \cdot x_2$	0.01	0.556	0.556	0.313	−0.03	0.005	0.03	≤0.001
$x_1 \cdot x_3$	−0.02	0.270	0.270	0.056	−0.02	0.032	0.01	0.129
$x_1 \cdot x_4$	0.00	0.857	0.857	0.347	0.00	0.634	0.02	0.001
$x_2 \cdot x_3$	0.01	0.335	0.335	0.055	−0.03	0.005	−0.01	0.026
$x_2 \cdot x_4$	0.01	0.381	0.381	0.063	−0.03	0.017	−0.02	0.002
$x_3 \cdot x_4$	0.00	0.900	0.900	0.131	0.05	≤0.001	0.02	≤0.001
Lack-of-fit		0.654		0.541		0.086		0.132
Regression		≤0.001		≤0.001		≤0.001		≤0.001

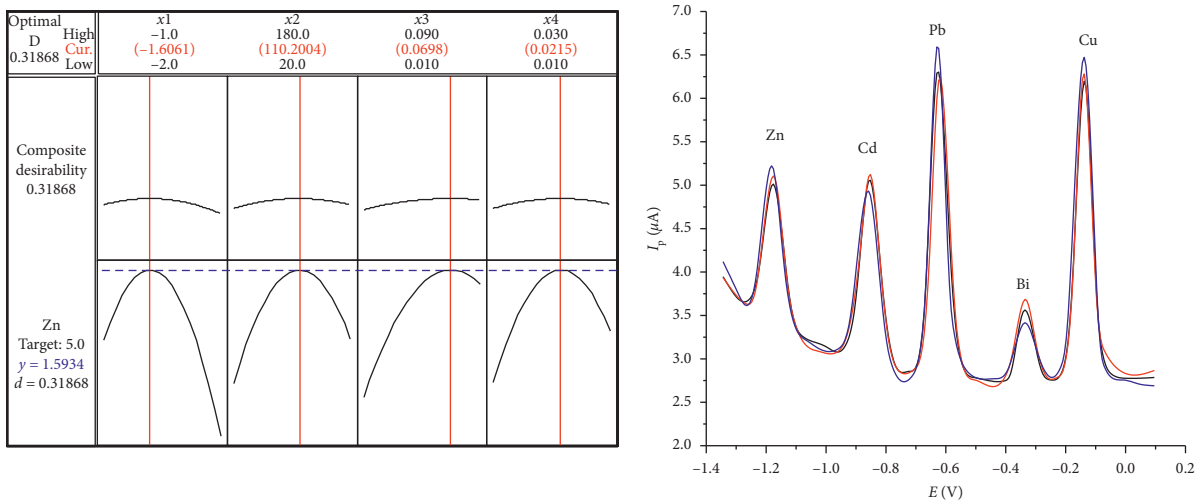

(a) (b)

Figure 4: (a) Profiles for predicated values; (b) reliability function for peak current of Zn.

The linear calibration graphs for Zn(II), Cd(II), Pb(II), and Cu(II) are as follows:

$$I_{p,Zn} = (0.58 \pm 0.03) + (0.091 \pm 0.001) \cdot C_{Zn}, \quad R^2 = 0.998,$$
$$I_{p,Cd} = (-0.57 \pm 0.05) + (0.251 \pm 0.001) \cdot C_{Cd}, \quad R^2 = 0.999,$$
$$I_{p,Pb} = (0.12 \pm 0.03) + (0.278 \pm 0.001) \cdot C_{Pb}, \quad R^2 = 0.999,$$
$$I_{p,Cu} = (-0.6 \pm 0.6) + (0.439 \pm 0.009) \cdot C_{Cu}, \quad R^2 = 0.996. \tag{15}$$

The detection limits are 1.07, 0.93, 0.65, and 0.94 ppb for Zn, Cd, Pb, and Cu, respectively ($3\sigma/b$).

The simultaneous determination of Zn, Cd, Pb, and Cu was also performed using the DP-ASV method. The electrochemical signals of Zn, Cd, Pb, and Cu were recorded simultaneously when increasing the concentration of the analytes in the 0.1 acetate buffer solution with pH = 5. Figure 6 shows the DP-ASV curves obtained for the solutions containing an equal concentration of Zn, Cd, Pb, and Cu in the range from 5 to 110 ppb. The linear regression equations between I_{pa} and corresponding concentration are as follows:

$$I_{p,Zn} = (0.6 \pm 0.1) + (0.093 \pm 0.001) \cdot C_{Zn}, \quad R^2 = 0.999,$$
$$I_{p,Cd} = (0.01 \pm 0.29) + (0.260 \pm 0.009) \cdot C_{Cd}, \quad R^2 = 0.989,$$
$$I_{p,Pb} = (3.2 \pm 0.2) + (0.232 \pm 0.005) \cdot C_{Pb}, \quad R^2 = 0.996,$$
$$I_{p,Cu} = (-1.3 \pm 0.2) + (0.456 \pm 0.005) \cdot C_{Cu}, \quad R^2 = 0.999. \tag{16}$$

In the range of 5 to 110 ppb, the values of LOD are 2.95, 1.84, 1.29, and 1.11 ppb for Zn, Cd, Pb, and Cu, respectively. It is worth noting that the values of LOD of Cu, Pb, Cd, and Zn in the simultaneous and individual determination are

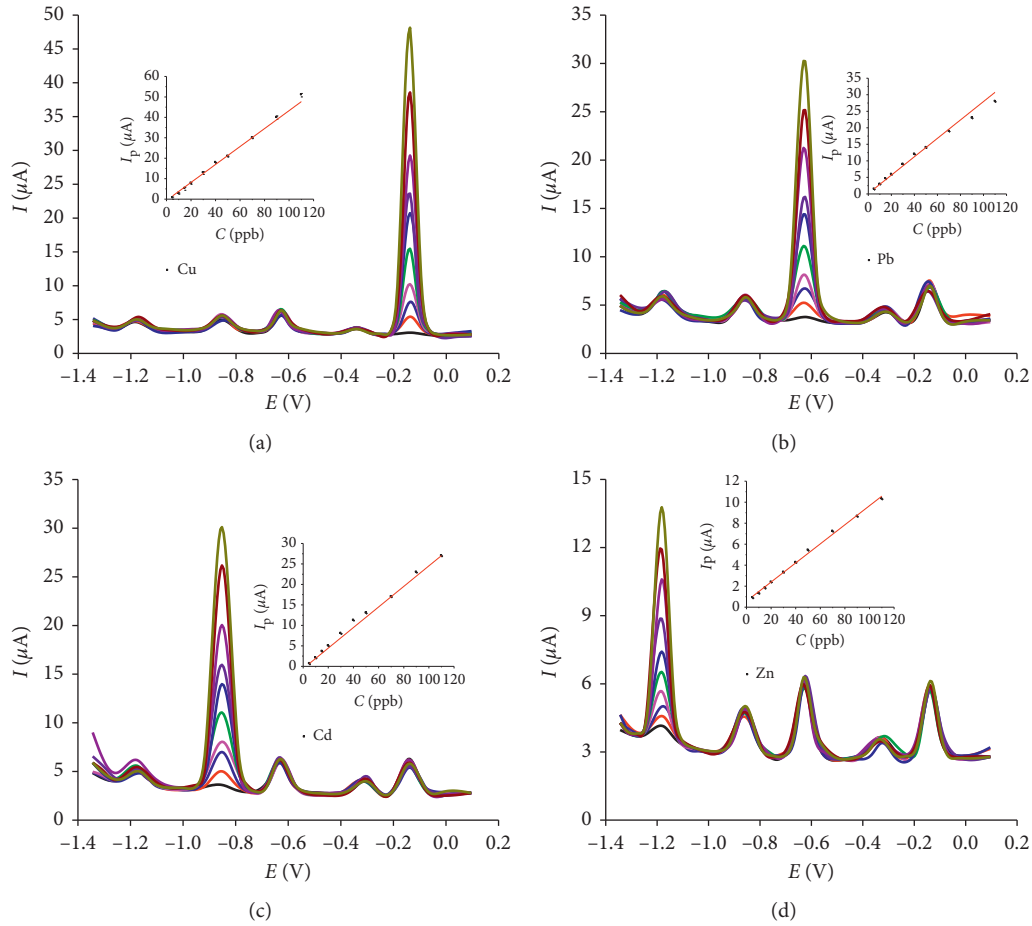

Figure 5: (a) DP-ASVs of Zn(II), Cd(II), Pb(II), and Cu(II) oxidation with different concentrations in acetate buffer (pH 5) at BiFE. (a) Zn(II), Cd(II), and Pb(II) fixed at 15 ppb; Cu(II) (from 5.0 to 110.0 ppb): 5.0, 10.0, 15.0, 20.0, 30.0, 40.0, 50.0, 70.0, 90.0, and 110.0 ppb; inset: the calibration curves of Cu(II); (b) Zn(II), Cd(II), and Cu(II) fixed at 15 ppb; inset: the calibration curves of Pb(II) (from 5.0 to 110.0 ppb); (c) Zn(II), Pb(II), and Cu(II) fixed at 15 ppb; inset: the calibration curve of Cd(II) (from 5.0 to 110.0 ppb); (d) Cd(II), Pb(II), and Cu(II) fixed at 15 ppb; inset: the calibration curve of Zn(II) (from 5.0 to 110.0 ppb). Acetate buffer: pH 5; Bi(III): 500 ppb; accumulation potential –1.6 V; accumulation time 110 s; accumulation potential –1.6 V; accumulation time 110 s; pulsed amplitude 0.07 V; scan rate 0.021 $V \cdot s^{-1}$.

very close to each other. This suggests that the simultaneous voltammetric determination of Cu, Pb, Cd, and Zn is possible at BiFE in the mixed samples without any cross interference. This linearity is also relevant for the determination of Zn, Cd, Pb, and Cu in water.

A comparison of the developed method with other voltammetric methods for Zn, Cd, Pb, and Cu determination is listed in Table 4. It could be noticed that LOD of Zn, Cd, Pb, and Cu from this method is lower or comparable with that obtained on the basis of modified electrodes in the literature. Overall, BiFE proves to be an effective electrode for the simultaneous determination of Zn, Cd, Pb, and Cu.

3.7. Practical Application. Water samples taken randomly from five rivers in Quang Binh province, Vietnam, namely, Cau Rao, Kien Giang, Nhat Le, and Son and Gianh river were used to determine the concentration of copper, lead, cadmium, and zinc using the proposed method (DP-ASV) and GF-AAS for the sake of comparison. Table 5 lists the content of Zn, Cd, Pb, and Cu in the samples determined by using these two methods. The paired t-test was used to compare the data. With the significant level $\alpha = 0.05$, the data show that the amounts of Zn, Cd, Pb, and Cu determined with the proposed method are not statistically different from those determined with GF-AAS (Cu: $t(4) = 0.291$; $p = 0.785$; Pb: $t(4) = 0.347$; $p = 0.746$; Cd: $t(4) = 0.975$; $p = 0.385$; Zn: $t(4) = 1.545$; $p = 0.197$). The recovery measurements were also performed to evaluate the accuracy of the method. The data provide good average recoveries, ranging from 92% to 105% for Cu, 91% to 102% for Pb, 96% to 108% for Cd, and 92% to 106% for Zn, suggesting that the developed method does not suffer from any significant effects of matrix interference.

4. Conclusion

In this article, the differential pulse anodic stripping voltammetry was used to determine Zn, Cd, Pb, and Cu in the rivers at a bismuth film-modified electrode. Simultaneous determination of Zn, Cd, Pb, and Cu using DP-ASV on BiFE displayed low detection limit, excellent long-time stability,

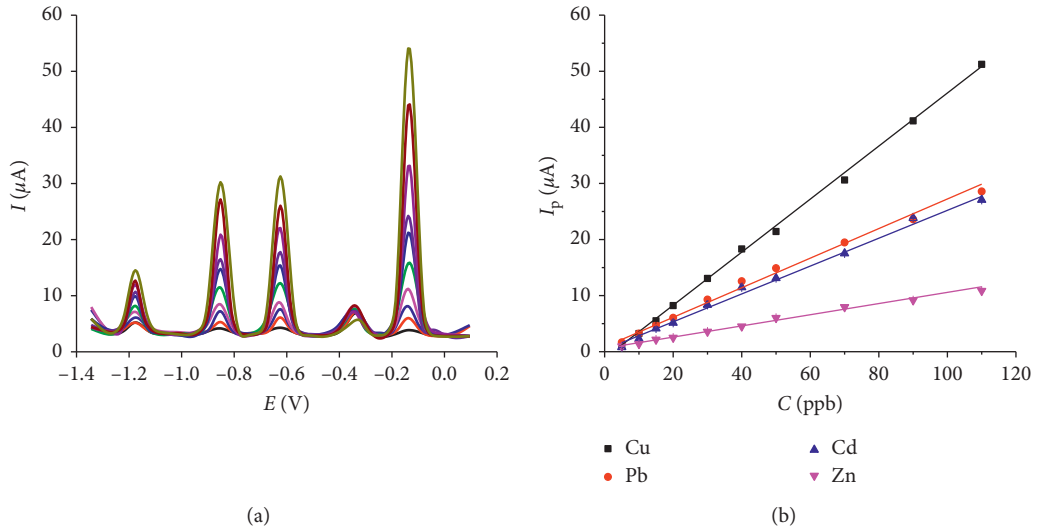

Figure 6: (a) DP-ASVs curves obtained for the oxidation of Zn(II), Cd(II), Pb(II), and Cu(II) at equal concentrations in the 0.1 acetate buffer solution (pH = 5): 5.0, 10.0, 15.0, 20.0, 30.0, 40.0, 50.0, 70.0, 90.0, and 110.0 ppb; (b) linear plots of $I_{pa,Cu}$, $I_{pa,Pb}$, $I_{pa,Cd}$, and $I_{pa,Zn}$ with their concentration (acetate buffer: pH 5; Bi(III): 500 ppb; accumulation potential –1.6 V; accumulation time 110 s; accumulation potential –1.6 V; accumulation time 110 s; pulsed amplitude 0.07 V; scan rate 0.021 $V \cdot s^{-1}$).

Table 4: Comparison of some figures of merit related to different electrodes for the determination of analytes.

Electrode	Method	LOD (ppb)				Reference
		Cu(II)	Pb(II)	Cd(II)	Zn(II)	
G/PANI/SPE	SqWASV	N/A	0.1	0.1	1.0	[22]
GCE	DP-ASV	39	16.6	9.6	14.7	[23]
Hg-Bi/SWNTs/GCE	SqWASV	N/A	1.3	0.98	2	[24]
	LSV	1.50	4.04	2.91	1.68	
Glassy carbon mercury film	DPV	1.11	1.54	2.21	1.29	[25]
	SWV	0.55	1.70	1.09	0.52	
BiFE	SqWASV	N/A	1.64	0.82	0.08	[26]
BiFE	SqWASV	N/A	0.41	0.49	—	[27]
BiFE	DP-ASV	0.94	0.65	0.93	1.07	The present work

— and N/A: not applicable.

Table 5: Concentration of Cu, Pb, Cd, and Zn determined using DP-ASV and GF-AAS for the water samples taken from the rivers.

River	DP-ASV (ppb)				GF-AAS (ppb)			
	Cu	Pb	Cd	Zn	Cu	Pb	Cd	Zn
Cau Rao river	9.1 ± 2.5	13.3 ± 1.4	2.9 ± 0.7	12.5 ± 0.5	8.7 ± 1.5	14.5 ± 3.6	3.2 ± 0.5	13.7 ± 2.8
Kien Giang river	7.2 ± 3.9	17.2 ± 7.3	3.1 ± 0.9	7.8 ± 2.8	6.5 ± 2.1	18.8 ± 4.2	2.5 ± 0.6	7.3 ± 1.8
Nhat Le river	8.6 ± 3.1	22.5 ± 3.6	3.1 ± 0.4	6.2 ± 2.6	9.4 ± 1.2	21.8 ± 3.1	3.5 ± 0.7	6.9 ± 1.5
Gianh river	5.5 ± 1.8	11.2 ± 4.4	3.1 ± 1.6	7.9 ± 1.7	5.8 ± 0.9	10.2 ± 2.7	2.6 ± 0.5	8.7 ± 1.6
Son river	4.6 ± 2.1	7.3 ± 2.1	2.9 ± 0.9	5.5 ± 1.4	4.2 ± 0.3	7.1 ± 1.2	2.1 ± 0.6	5.6 ± 1.4

Number of experiments $n = 3$.

and high reproducibility. The limits of detection were found to be 1.07, 0.93, 0.65, and 0.94 ppb for Zn, Cd, Pb, and Cu, respectively. The proposed method was successfully employed for the determination of Zn, Cd, Pb, and Cu in river water in an agreement with GF-AAS analysis.

Data Availability

The data used to support the findings of this study are available from the corresponding author upon request.

Conflicts of Interest

The authors declare that they have no conflicts of interest.

Supplementary Materials

Table S1: effect of Co(II) on the stripping peak current. Table S2: effect of Ni(II) on the stripping peak current. Table S3: effect of Fe(II) on the stripping peak current. Table S4:

repeatability of Ip according to the analyte concentration. (*Supplementary Materials*)

References

[1] R. Gündoğan, B. Acemioğlu, and M. H. Alma, "Copper(II) adsorption from aqueous solution by herbaceous peat," *Journal of Colloid and Interface Science*, vol. 269, pp. 303–309, 2004.

[2] H. Lalhruaitluanga, K. Jayaram, M. N. V. Prasad, and K. K. Kumar, "Lead(II) adsorption from aqueous solutions by raw and activated charcoals of Melocanna baccifera Roxburgh (bamboo)-A comparative study," *Journal of Hazardous Materials*, vol. 175, no. 1–3, pp. 311–318, 2010.

[3] T. K. Naiya, A. K. Bhattacharya, S. Mandal, and S. K. Das, "The sorption of lead(II) ions on rice husk ash," *Journal of Hazardous Materials*, vol. 163, no. 2-3, pp. 1254–1264, 2009.

[4] H. Wang, Y. Jia, S. Wang, H. Zhu, and X. Wu, "Bioavailability of cadmium adsorbed on various oxides minerals to wetland plant species *Phragmites australis*," *Journal of Hazardous Materials*, vol. 167, no. 1–3, pp. 641–646, 2009.

[5] J. Pan, J. A. Plant, N. Voulvoulis, C. J. Oates, and C. Ihlenfeld, "Cadmium levels in Europe: implications for human health," *Environmental Geochemistry and Health*, vol. 32, no. 1, pp. 1–12, 2010.

[6] T. A. Kurniawan, G. Y. S. Chan, W.-h. Lo, and S. Babel, "Comparisons of low-cost adsorbents for treating wastewaters laden with heavy metals," *Science of the Total Environment*, vol. 366, no. 2-3, pp. 409–426, 2006.

[7] T. A. Kurniawan, G. Y. S. Chan, W.-H. Lo, and S. Babel, "Physico-chemical treatment techniques for wastewater laden with heavy metals," *Chemical Engineering Journal*, vol. 118, no. 1-2, pp. 83–98, 2006.

[8] D. G. Biechler, "Determination of trace copper, lead, zinc, cadmium, nickel, and iron in industrial waste waters by atomic absorption spectrometry after ion exchange concentration on dowex A-1," *Analytical Chemistry*, vol. 37, no. 8, pp. 1054-1055, 1965.

[9] C. Duran, A. Gundogdu, V. N. Bulut et al., "Solid-phase extraction of Mn(II), Co(II), Ni(II), Cu(II), Cd(II) and Pb(II) ions from environmental samples by flame atomic absorption spectrometry (FAAS)," *Journal of Hazardous Materials*, vol. 146, no. 1-2, pp. 347–355, 2007.

[10] C. Huang and B. Hu, "Silica-coated magnetic nanoparticles modified with γ-mercaptopropyltrimethoxysilane for fast and selective solid phase extraction of trace amounts of Cd, Cu, Hg, and Pb in environmental and biological samples prior to their determination by inductively coupled plasma mass spectrometry," *Spectrochimica Acta Part B: Atomic Spectroscopy*, vol. 63, no. 3, pp. 437–444, 2008.

[11] L. P. Eksperiandova, A. B. Blank, and Y. N. Makarovskaya, "Analysis of waste water by x-ray fluorescence spectrometry," *X-Ray Spectrometry*, vol. 31, no. 3, pp. 259–263, 2002.

[12] J. Wang, J. Lu, S. B. Hocevar, P. A. M. Farias, and B. Ogorevc, "Bismuth-coated carbon electrodes for anodic stripping voltammetry," *Analytical Chemistry*, vol. 72, no. 14, pp. 3218–3222, 2000.

[13] A. Economou, "Bismuth-film electrodes: recent developments and potentialities for electroanalysis," *TrAC Trends in Analytical Chemistry*, vol. 24, no. 4, pp. 334–340, 2005.

[14] Y. Wu, N. B. Li, and H. Q. Luo, "Simultaneous measurement of Pb, Cd and Zn using differential pulse anodic stripping voltammetry at a bismuth/poly(p-aminobenzene sulfonic acid) film electrode," *Sensors and Actuators B: Chemical*, vol. 133, no. 2, pp. 677–681, 2008.

[15] K. Keawkim, S. Chuanuwatanakul, O. Chailapakul, and S. Motomizu, "Determination of lead and cadmium in rice samples by sequential injection/anodic stripping voltammetry using a bismuth film/crown ether/Nafion modified screen-printed carbon electrode," *Food Control*, vol. 31, no. 1, pp. 14–21, 2013.

[16] H. Li, J. Li, Z. Yang et al., "Simultaneous determination of ultratrace lead and cadmium by square wave stripping voltammetry with in situ depositing bismuth at Nafion-medical stone doped disposable electrode," *Journal of Hazardous Materials*, vol. 191, no. 1–3, pp. 26–31, 2011.

[17] Y. Zhou, J.-Z. Song, F. F.-K. Choi et al., "An experimental design approach using response surface techniques to obtain optimal liquid chromatography and mass spectrometry conditions to determine the alkaloids in Meconopsi species," *Journal of Chromatography A*, vol. 1216, no. 42, pp. 7013–7023, 2009.

[18] L. E., "General expression of the linear potential sweep voltammogram in the case of diffusionless electrochemical systems," *Electroanalysis*, vol. 101, pp. 19–28, 1979.

[19] C. Li, "Electrochemical determination of dipyridamole at a carbon paste electrode using cetyltrimethyl ammonium bromide as enhancing element," *Colloids and Surfaces B: Biointerfaces*, vol. 55, no. 1, pp. 77–83, 2007.

[20] J. Soleymani, M. Hasanzadeh, N. Shadjou et al., "A new kinetic-mechanistic approach to elucidate electrooxidation of doxorubicin hydrochloride in unprocessed human fluids using magnetic graphene based nanocomposite modified glassy carbon electrode," *Materials Science and Engineering: C*, vol. 61, pp. 638–650, 2016.

[21] T. Florence, "Anodic stripping voltammetry with a glassy carbon electrode mercury-plated in situ," *Journal of Electroanalytical Chemistry*, vol. 27, no. 2, pp. 273–281, 1970.

[22] N. Ruecha, N. Rodthongkum, D. M. Cate, J. Volckens, O. Chailapakul, and C. S. Henry, "Sensitive electrochemical sensor using a graphene-polyaniline nanocomposite for simultaneous detection of Zn(II), Cd(II), and Pb(II)," *Analytica Chimica Acta*, vol. 874, pp. 40–48, 2015.

[23] J. F. Van Staden and M. C. Matoetoe, "Simultaneous determination of copper, lead, cadmium and zinc using differential pulse anodic stripping voltammetry in a flow system," *Analytica Chimica Acta*, vol. 411, no. 1-2, pp. 201–207, 2000.

[24] R. Ouyang, Z. Zhu, C. E. Tatum, J. Q. Chambers, and Z.-L. Xue, "Simultaneous stripping detection of Zn(II), Cd(II) and Pb(II) using a bimetallic Hg-Bi/single-walled carbon nanotubes composite electrode," *Journal of Electroanalytical Chemistry*, vol. 656, no. 1-2, pp. 78–84, 2011.

[25] M. F. De Oliveira, A. A. Saczk, L. L. Okumura, A. P. Fernandes, M. De Moraes, and N. R. Stradiotto, "Simultaneous determination of zinc, copper, lead, and cadmium in fuel ethanol by anodic stripping voltammetry using a glassy carbon-mercury-film electrode," *Analytical and Bioanalytical Chemistry*, vol. 380, no. 1, pp. 135–140, 2004.

[26] R. Pauliukaitė and C. M. A. Brett, "Characterization and application of bismuth-film modified carbon film electrodes," *Electroanalysis*, vol. 17, pp. 1354–1359, 2005.

[27] G. Hwang, W. Han, S. Hong, J. Park, and S. Kang, "Determination of trace amounts of lead and cadmium using a bismuth/glassy carbon composite electrode," *Talanta*, vol. 77, no. 4, pp. 1432–1436, 2009.

Hindawi
Advances in Materials Science and Engineering
Volume 2019, Article ID 6707143, 8 pages
https://doi.org/10.1155/2019/6707143

Research Article

Evaluation of Structural Properties and Catalytic Activities in Knoevenagel Condensation Reaction of Zeolitic Imidazolate Framework-8 Synthesized under Different Conditions

Pham Dinh Du,[1] **Nguyen Viet Duy Thanh**,[2] **and Nguyen Trung Hieu**[3]

[1]*Faculty of Natural Science, Thu Dau Mot University, Thu Dau Mot 820000, Vietnam*
[2]*Center for Vocational Education and Continuing Education, Can Tho 900000, Vietnam*
[3]*Center for Scientific Research and Practice, Thu Dau Mot University, Thu Dau Mot 820000, Vietnam*

Correspondence should be addressed to Pham Dinh Du; dupd@tdmu.edu.vn

Received 27 December 2018; Accepted 21 March 2019; Published 17 April 2019

Guest Editor: Hien Duy Mai

In the present study, the zeolitic imidazolate framework-8 (ZIF-8) was synthesized at both room temperature and high temperatures. The effects of solvents, molar ratios of precursors, reaction time, and temperature on the structural properties of the as-prepared materials were investigated. Moreover, the surface morphologies of the obtained specimens were characterized using X-ray diffraction, scanning electron microscopy, Fourier-transform infrared spectroscopy, and nitrogen adsorption methods. The results show that ZIF-8 was formed in methanol and water at room temperature and in dimethylformamide (DMF) at high temperatures. Further, in methanol, the molar ratios of precursors and reaction time have negligible effects on the morphologies and structures of ZIF-8; however, in DMF, the reaction temperature has a significant influence on the microstructures of ZIF-8. The catalytic activities of the obtained materials were evaluated using the Knoevenagel condensation reaction, and ZIF-8 proves to be an excellent solid base catalyst.

1. Introduction

Zeolitic imidazolate frameworks (ZIFs) belong to the family of metal-organic frameworks (MOFs) and possess unique properties (uniform small pores and high surface area) of both zeolites and MOFs [1, 2]. In ZIFs, divalent metal cations are found to be tetrahedrally coordinated with the imidazolate anions [2, 3]. In recent years, ZIFs have attracted significant attention in gas storage and separation applications [4, 5], catalytic reactions [6], chemical processes [7, 8], and drug delivery systems [9]. ZIF-8 is one of the most studied zeolitic imidazolate frameworks due to its high chemical and thermal stabilities. In addition, ZIF-8 has a large surface area ($S_{BET} = 1630\,m^2 \cdot g^{-1}$) and high porosity ($0.636\,cm^3 \cdot g^{-1}$) [2]. In previous studies, ZIF-8 is synthesized in DMF at high temperature and pressure [2, 3]. ZIF-8 can also be synthesized in methanol at room temperature under normal pressure [2, 10–14]. In these two approaches, the solvents and temperature/pressure have a critical role in the formation of ZIF-8. However, there have not been any studies dealing with this issue.

The Knoevenagel condensation is an important reaction for the formation of carbon-carbon double bonds. The reaction is traditionally catalyzed by conventional bases such as KOH, NaOH, or amine compounds [15]. Today, many researchers have conducted this reaction with different precursors by using solid base catalysts to expand their applicability in the organic synthesis industry [16–18]. Recently, Tran et al. [19] have studied the catalytic activity of ZIF-8 by the Knoevenagel condensation reaction and advocated its feasibility as a catalyst.

In the present work, ZIF-8 was synthesized in two different routes. The effects of solvents, molar ratios of precursors, reaction time, and temperature on the structural properties of the as-prepared materials were investigated. In addition, the catalytic activities of the fabricated materials

were evaluated using the Knoevenagel condensation reaction.

2. Experimental

2.1. Synthesis and Characterization of ZIF-8. ZIF-8 was synthesized via two different routes using zinc nitrate hexahydrate ($Zn(NO_3)_2{\cdot}6H_2O$, Fisher) and 2-methylimidazole ($C_4H_6N_2$, 99%, Acros) (denoted as meIm) precursors.

(i) Process A was performed according to Zhu et al. [20]. In a typical process, 8 mmol $Zn(NO_3)_2{\cdot}6H_2O$ was dissolved in 1.4 mol methanol (CH_3OH, 99.9%, Fisher) (denoted as MeOH) (solution 1) and 64.4 mmol meIm was dissolved in 1.4 mol MeOH (solution 2). Solution 2 was then added to solution 1, and the as-prepared mixture was stirred for 8 h. Finally, the obtained ZIF-8 powder (denoted as Z-A(MeOH)) was collected using centrifugation at 3000 rpm, washed three times with MeOH, and dried overnight at 100°C.

(ii) Process B was carried out according to Bushell et al. [21]. In a typical process, 7.20 g $Zn(NO_3)_2{\cdot}6H_2O$ and 4.48 g meIm were first dissolved in 90 mL dimethylformamide (C_3H_7NO, ≥99.5%, Fisher) (denoted as DMF) and the prepared solution was then heated in a Teflon-lined steel autoclave (volume of 200 mL) for three days at 100°C. The as-produced white solid material was collected using filtration, washed in a Soxhlet apparatus for two days with MeOH, and dried at 100°C to obtain ZIF-8 (denoted Z-B(DMF)).

The effects of solvents, molar ratios of $Zn(NO_3)_2{\cdot}6H_2O$ and meIm, reaction time, and temperature on the structural properties of the as-prepared ZIF-8 samples were further studied.

Characterization. X-ray diffraction (XRD) patterns were recorded on a VNU-D8 Advance Instrument (Bruker, Germany) under-Cu Kα radiation ($\lambda = 1.5418$ Å). The N_2 adsorption/desorption isotherm measurement test was performed at 77 K in a Tristar 3000 analyzer, and before setting the dry mass, the samples were degassed at 250°C with N_2 for 5 h. Scanning electron microscopy (SEM) images were obtained using an SEM JMS-5300LV (Japan), and infrared spectra (IR) were recorded in a Jasco FT/IR-4600 spectrometer (Japan) in the range of 4000–400 cm^{-1}.

2.2. Knoevenagel Reaction. The Knoevenagel condensation reaction between benzaldehyde and ethyl cyanoacetate was carried out according to Martins et al. [18]. In the reaction, 1.07 g (10 mmol) benzaldehyde (C_6H_5CHO, 98%, Acros), 1.04 g (10 mmol) ethyl cyanoacetate ($NCCH_2CO_2C_2H_5$, 98%, Acros), and 15.42 g toluene ($C_6H_5CH_3$, 99.9%, Duksan) were added to a glass reactor and stirred at 30°C. When the temperature became stable, 0.1 g of ZIF-8 was added. After 6 h of reaction, the solution was centrifuged to remove the catalyst. The compositional analysis of the reactants and products in the liquid sample was executed using a GC-MS chromatograph (Agilent GC-MS 7890).

The conversion and the selectivity were calculated according to the following equations:

$$\text{conversion (\%)} = \frac{\text{moles of reacted benzaldehyde}}{\text{moles of initial benzaldehyde}} \times 100,$$

$$\text{selectivity (\%)} = \frac{\text{\%product of ethyl-2-cyano-3-phenylacrylate}}{\text{\%total products}} \times 100. \quad (1)$$

3. Results and Discussion

3.1. Structural Properties of Z-A(MeOH) and Z-B(DMF). Figure 1(a) exhibits the XRD patterns of ZIF-8 synthesized with process A and process B. The diffraction peak (011) at $2\theta = 7.2°$ is observed in both samples, indicating their high crystallinities [2, 10, 12, 20, 22]. However, the intensity of diffraction peaks in Z-B(DMF) is higher than that in Z-A(MeOH), and this means that Z-B(DMF) has higher symmetric planes.

The FT-IR spectra of both Z-A(MeOH) and Z-B(DMF) are displayed in Figure 1(b), and the findings are consistent with earlier reported results [19, 23, 24]. The bands at 3122 cm^{-1} and 2920 cm^{-1} are associated with the aromatic and the aliphatic C-H asymmetric stretching vibrations, respectively. The band at 1668 cm^{-1} is attributed to the C=C stretching mode, and the band at 1574 cm^{-1} is assigned to the C=N stretching mode. The bands at 1300–1460 cm^{-1} are associated with the entire ring stretching, whereas the band at 1140 cm^{-1} is formed from the aromatic C-N stretching mode. Similarly, the bands at 991 cm^{-1} and 748 cm^{-1} could be assigned to the C-N bending vibration mode and to the C-H bending mode, respectively. Moreover, the band at 690 cm^{-1} is developed due to the ring out-of-plane bending vibration of imidazolate. The sharp band at 416 cm^{-1} formed due to Zn-N stretching indicates that zinc atoms are connected to the nitrogen atoms in the 2-methylimidazolate linkers.

The surface morphologies of the materials synthesized with the two approaches are totally different. Z-A(MeOH) comprises cubic crystals, hexagonal-faceted crystals, and rhombic dodecahedrons (with an edge of ~100 nm) (Figures 2(a) and 2(b)). In contrast, Z-B(DMF) has truncated rhombic dodecahedrons with varying particle sizes of 3–20 μm (Figures 2(c) and 2(d)) [19, 22, 25]. Hence, compared with Z-A(MeOH), Z-B(DMF) yields high and sharp diffraction peaks due to its clear crystal planes and large crystal size.

In process A, the formation path of ZIF-8 depends on the reaction time [10, 11]. However, in process B, ZIF-8 was prepared in DMF at 100°C in three days; hence, a fully crystalline ZIF-8 phase was obtained.

Figure 3 displays the nitrogen adsorption/desorption isotherms of Z-A(MeOH) sample and Z-B(DMF) sample at 77 K. According to the classification of IUPAC, the isotherm curves belong to type-I, indicating that Z-A(MeOH) and Z-B(DMF) are microporous materials. The specific

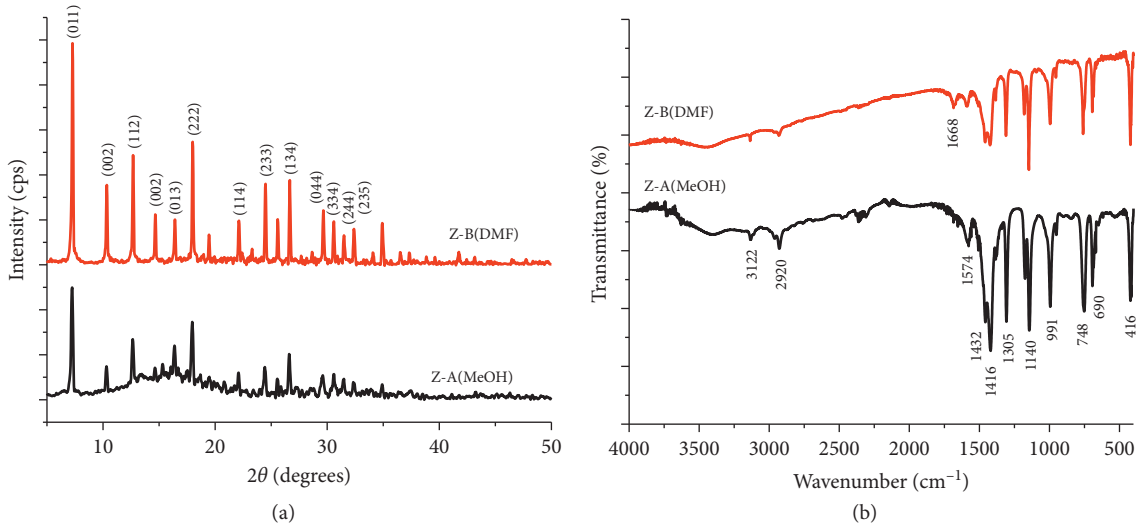

Figure 1: (a) XRD patterns and (b) FT-IR spectra of Z-A(MeOH) and Z-B(DMF) samples.

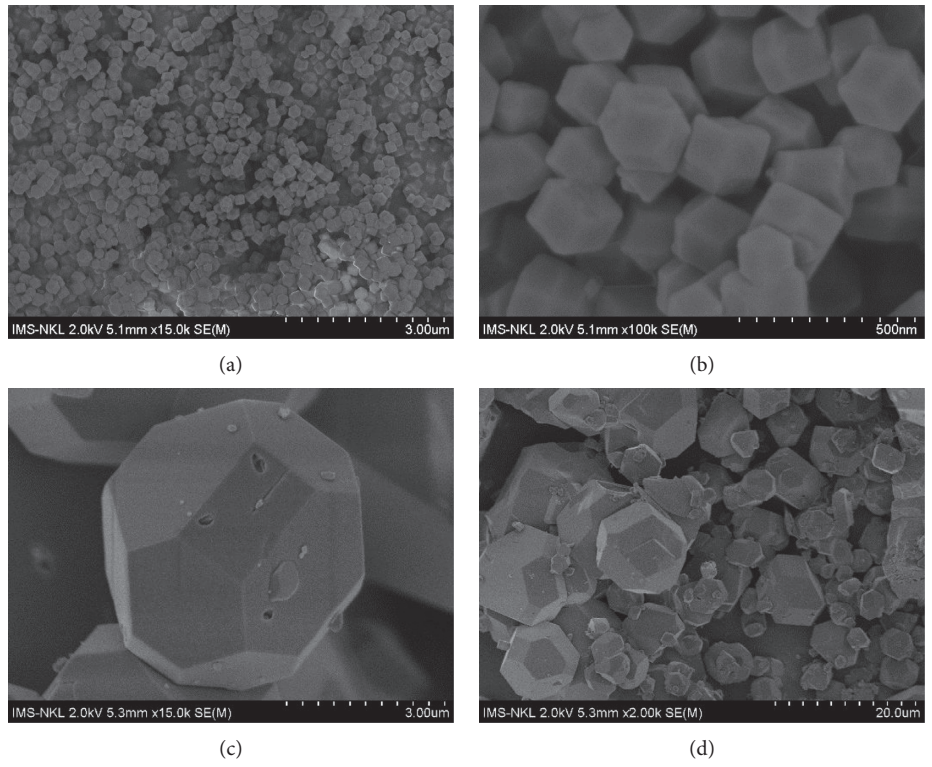

Figure 2: SEM images of Z-A(MeOH) (a, b) and Z-B(DMF) (c, d).

surface area of Z-A(MeOH) and Z-B(DMF) is 1279 $m^2 \cdot g^{-1}$ and 1415 $m^2 \cdot g^{-1}$, respectively (Table 1). These values are higher than those of ZIF-8 synthesized with other routes [23, 26].

3.2. Effects of Solvents. Solvents play an important role in the ZIF-8 synthesis. Earlier studies reported that ZIF-8 can be formed in different solvents: DMF [19, 21], methanol [2, 10–14], and water [25]. Therefore, in our experiment, the effects of different solvents (methanol, DMF, water, and toluene) on the ZIF-8 formation were investigated in detail. Table 2 describes the characteristics of ZIF-8 obtained from process A and process B with different solvents.

It is clear that toluene is an unsuitable solvent for the ZIF-8 synthesis. This can be attributed to the very small dipole moment of toluene (0.36 D) compared with that of methanol (1.69 D), water (1.85 D), and DMF (3.86 D), and the deprotonation of a meIm compound cannot occur to form a $meIm^-$ ion.

Figure 4 shows that the synthesized samples in water have characteristic diffraction peaks (at $2\theta < 30^\circ$) and

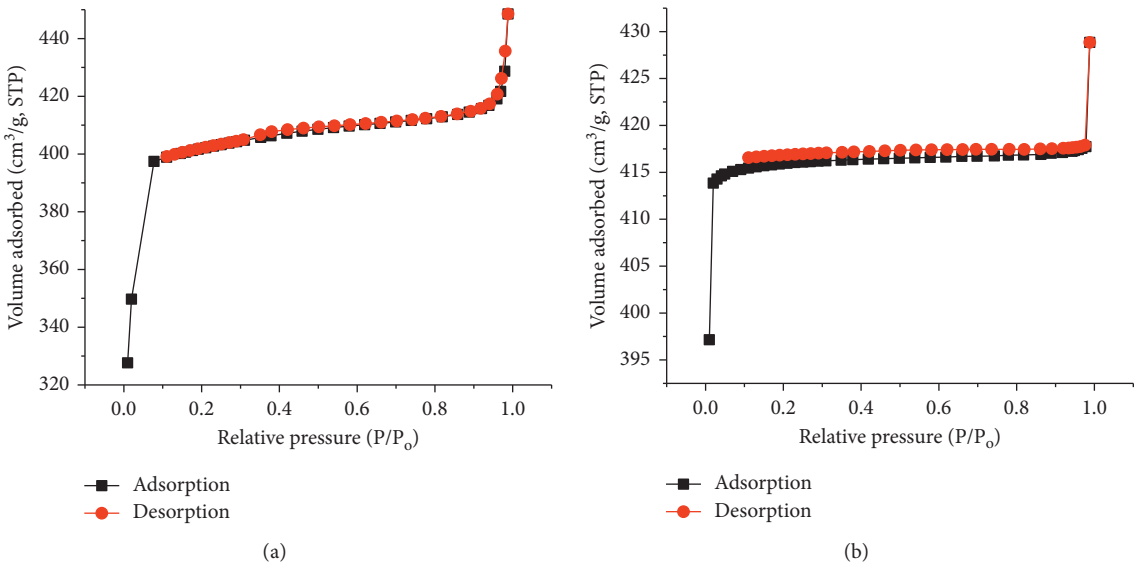

Figure 3: Nitrogen adsorption/desorption isotherms of Z-A(MeOH) sample (a) and Z-B(DMF) sample (b).

Table 1: Porous properties of ZIF-8 samples.

Sample	BET surface area ($m^2 \cdot g^{-1}$)	t-plot micropore area ($m^2 \cdot g^{-1}$)	t-plot external surface area ($m^2 \cdot g^{-1}$)	t-plot micropore volume ($cm^3 \cdot g^{-1}$)
Z-A(MeOH)	1279	1237	42	0.604
Z-B(DMF)	1415	1412	3	0.642

Table 2: Characteristics of ZIF-8 obtained in different solvents.

Solvent	Product (state, color, and abundance ratio)	
	Process A	Process B
Methanol	Solid, white, medium*	Solid, milk white, very small
DMF	Gel, white	Solid, white, medium**
Water	Solid, white, large	Solid, white, large
Toluene	Solid, gray, very small	Gel, white

*Z-A(MeOH) sample; **Z-B(DMF) sample.

characteristic vibration bands. However, in process B, the diffraction peaks at $2\theta = 31.73^\circ$, 34.4°, 36.23°, and 47.48° and the band at $492\,cm^{-1}$ indicate the existence of ZnO oxides and Zn-O bonds in ZIF-8 [26]. This can be ascribed to the hydrolysis of Zn^{2+} ions in water at high temperatures.

The morphologies of the synthesized samples in water are displayed in Figure 5. In process A, the surface morphologies of ZIF-8 are indeterminate (Figures 5(a) and 5(b)). On the contrary, the microstructures of ZIF-8 synthesized in process B consist of hexagonal cylinders and cubic crystals (Figures 5(c) and 5(d)).

The results in Table 2 indicate that the solvent exchange between the two processes did not lead to the formation of ZIF-8. This is due to large differences in the boiling temperature and dipole moment of the solvents, indicating that solvents play an important role in the synthesis of ZIF-8.

3.3. Effects of Synthesis Time and meIm/Zn Molar Ratios. Figure 6 displays the SEM images of the synthesized ZIF-8 samples at two different stirring intervals—two days and five days. Both samples have mainly hexagonal and rhombic dodecahedron crystals of a diameter of ~100 nm. Further, their very sharp diffraction peaks appear at 2θ below 10°, indicating the formation of highly crystalline materials (Figure 7(a)).

The XRD patterns of the samples synthesized at different meIm/Zn molar ratios are presented in Figure 7(b). In all cases, the amounts of $Zn(NO_3)_2 \cdot 6H_2O$ and methanol were kept constant. No conspicuous difference was noticed in the XRD peaks of the samples; however, their relative crystallinities slightly decrease as the meIm/Zn molar ratio increases from 64.4/8 to 100/8. These findings are well consistent with those reported by Zhang et al. [24].

3.4. Effects of Synthesis Temperature. The effects of reaction temperature on ZIF-8 synthesized with the process B are depicted in Figure 8. Noticeably, better cohesion of particles in the sample synthesized at 200°C reduces the intensities of diffraction peaks at larger angles. However, as the reaction temperature increases, the intensities of diffraction peaks at angles less than 10° become higher, indicating the formation of ZIF-8 with higher crystallinities.

In conclusion, the meIm/Zn molar ratios, reaction time, and temperature have an impact on the crystallinity of ZIF-8 but do not affect its crystalline structure.

3.5. Catalytic Test. The Knoevenagel condensation reaction between benzaldehyde and ethyl cyanoacetate to form ethyl-

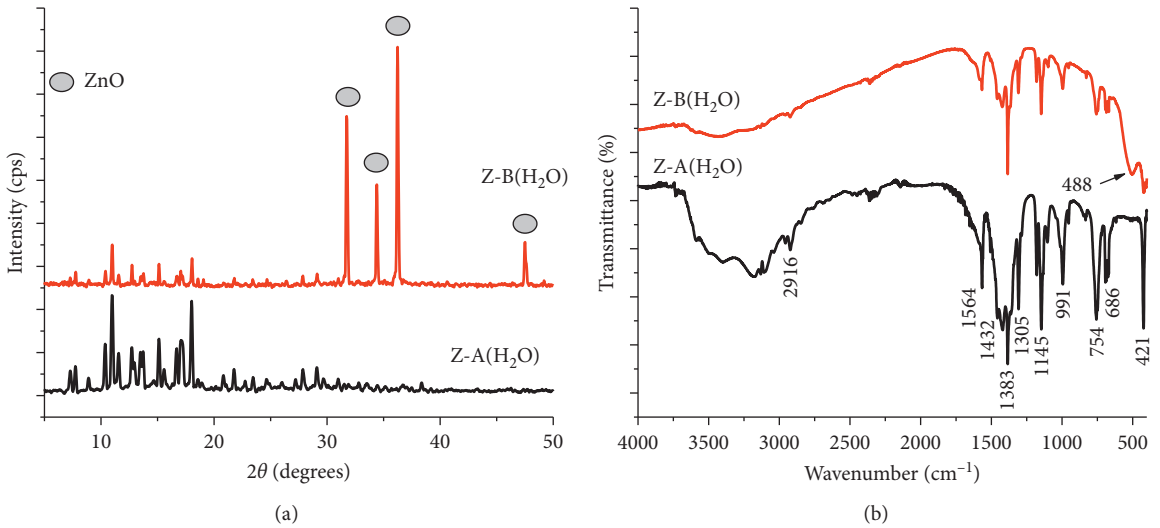

Figure 4: (a) XRD patterns and (b) FT-IR spectra of ZIF-8 synthesized in water.

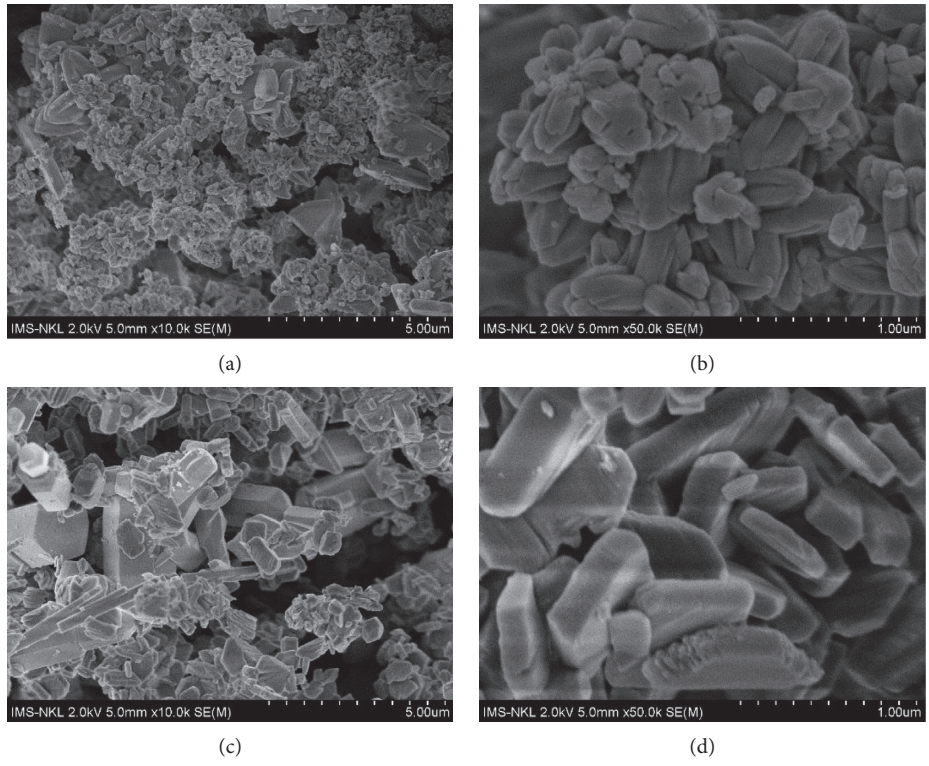

Figure 5: SEM of ZIF-8 synthesized in water: process A (a, b); process B (c, d).

2-cyano-3-phenylacrylate (Scheme 1) was used to test the catalytic activities of the synthesized ZIF-8 samples.

The effect of different ZIF-8 samples on the Knoevenagel condensation reaction is illustrated in Figure 9. Evidently, all synthesized samples exhibit excellent catalytic activities in the Knoevenagel condensation reaction (the benzaldehyde conversion in the catalytic reactions is considerably higher than that in the reactions without catalysts). Figure 9(a) shows that the conversion of benzaldehyde depends on the crystallinity of ZIF-8. The conversion is greater when the intensity of diffraction peaks at $2\theta < 10^{\circ}$ is higher (Figures 1(a), 7(a), and 8(b)). Specifically, ZIF-8 synthesized with process B at 200°C has the highest yield. In addition, the selectivity of ethyl-2-cyano-3-phenylacrylate always remains close to 100% (Figure 9(b)), indicating that the formation of benzoic acid during the catalytic reaction is negligible.

The Knoevenagel condensation reaction is commonly catalyzed by liquid or solid bases. ZIF-8 is a bifunctional catalyst composed of both acidic (Lewis acid Zn^{2+} ions) and basic sites (imidazole groups) [20]. It was noticed that the

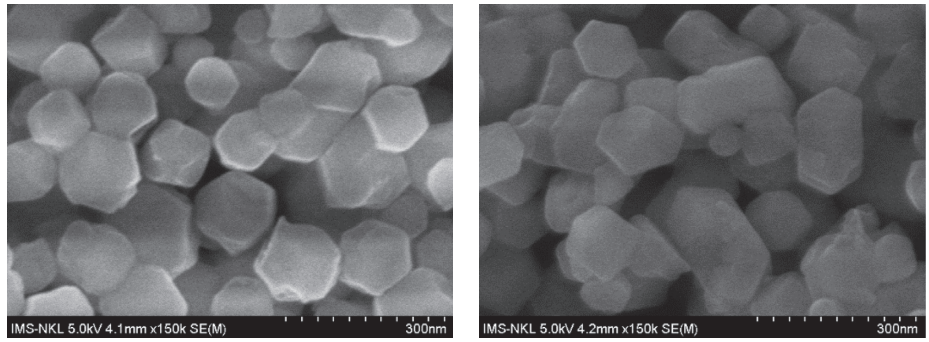

(a) (b)

Figure 6: SEM images of ZIF-8 crystals synthesized with process A as a function of synthesis time: (a) two days; (b) five days.

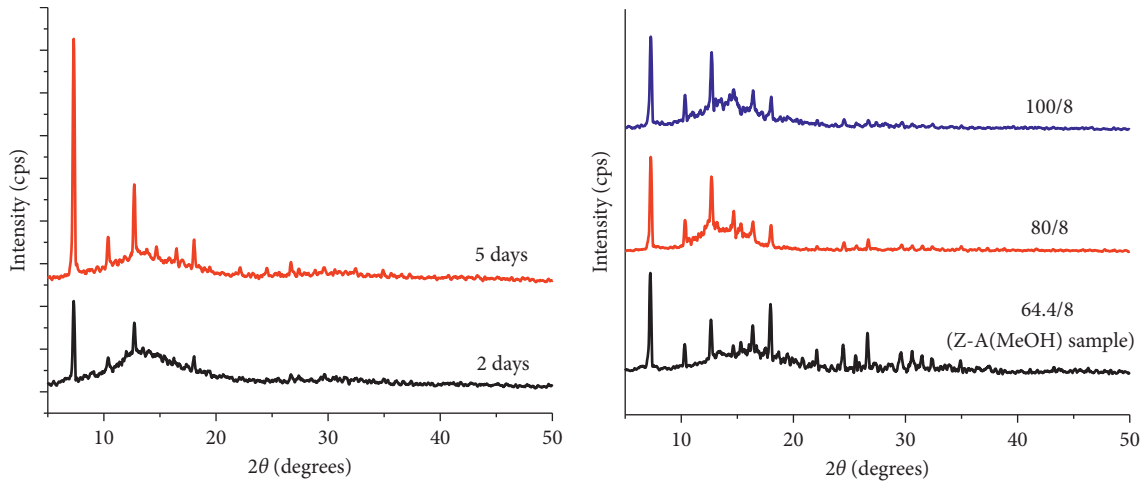

(a) (b)

Figure 7: XRD patterns of ZIF-8 crystals synthesized with process A: (a) different synthesis times; (b) different meIm/Zn molar ratios.

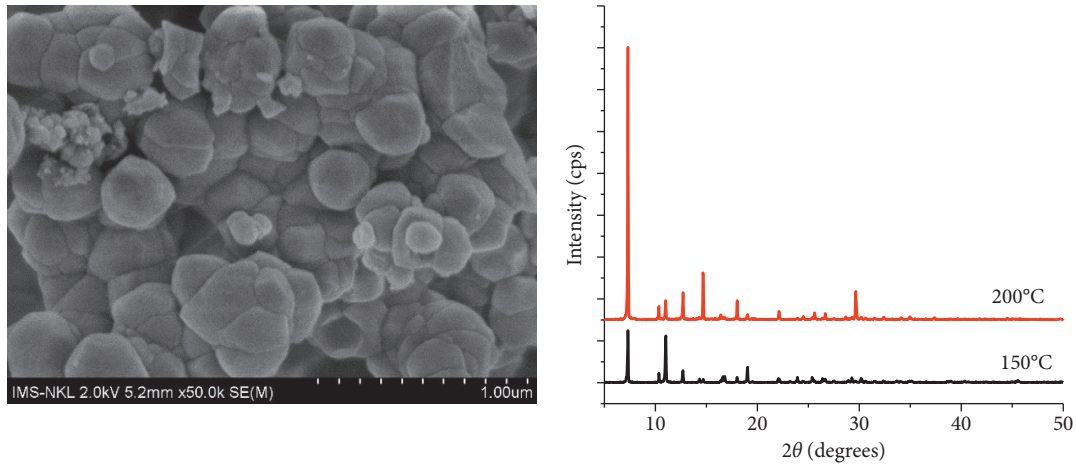

(a) (b)

Figure 8: SEM image (a) and XRD patterns (b) of ZIF-8 samples synthesized with process B at different temperatures.

catalytic activities of ZIF-8 are governed by the basic sites of imidazoles. To evaluate the durability of ZIF-8 catalyst for the Knoevenagel reaction, Tran et al. also test the leaching of the 2-methylimidazole linker [19]. They conclude that the ZIF-8 solid catalysts remain stable, and no contribution of homogeneous catalysis due to active acid species leaching

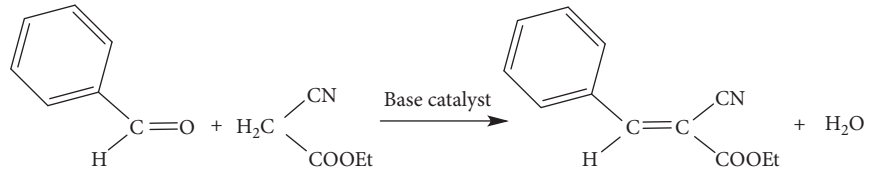

Scheme 1: Knoevenagel condensation reaction between benzaldehyde and ethyl cyanoacetate.

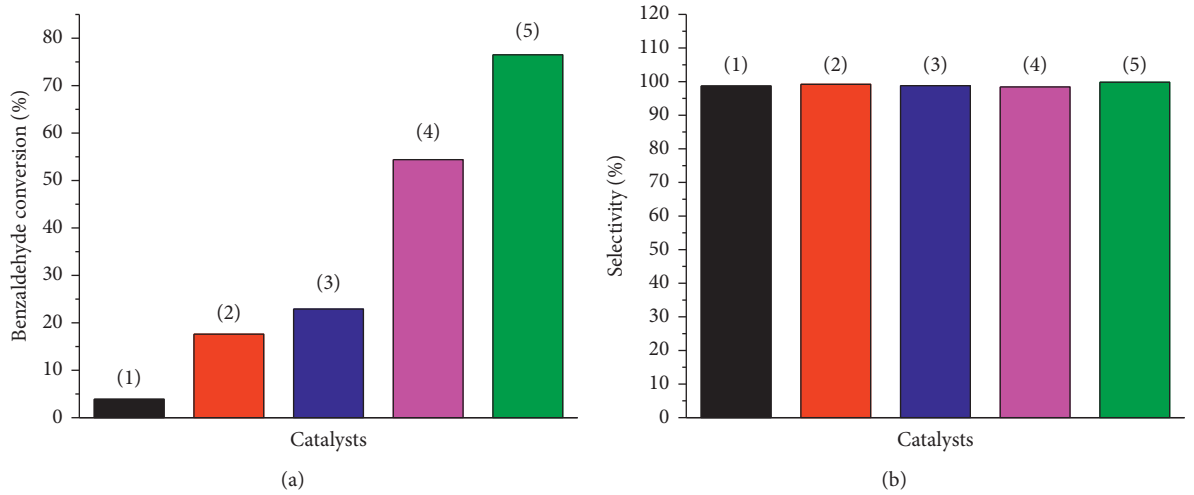

Figure 9: Effect of various ZIF-8 samples on the Knoevenagel condensation reaction: (a) benzaldehyde conversion (%); (b) ethyl-2-cyano-3-phenylacrylate selectivity ((1) without a catalyst; (2) Z-A(MeOH); (3) Z-B(DMF); (4) ZIF-8 sample synthesized with process A for five days; and (5) ZIF-8 sample synthesized with process B at 200°C).

Table 3: Effect of the different catalysts on Knoevenagel condensation.

Catalyst	Precursors	Reaction condition	Benzaldehyde conversion (%)	References
ZIF-8*	Benzaldehyde (10 mmol) and ethyl cyanoacetate (10 mmol)	30°C, 6 h, 0.1 g of the catalyst	76.5	The present work
ZIF-8	Benzaldehyde (1.9 mmol) and malononitrile (1.9 mmol)	Room temperature, 6 h, 0.02 g of the catalyst	51	[19]
MCM-41	Benzaldehyde (10 mmol) and diethyl malonate (10 mmol)	Room temperature, 24 h, 0.025 g of the catalyst	56–70	[16]
Amine-MCM-41	Benzaldehyde (10 mmol) and diethyl malonate (10 mmol)	Room temperature, 24 h, 0.025 g of the catalyst	78–92	[16]
$[CTA^+]$-Si-MCM-41	Benzaldehyde (4.8 mmol) and ethyl cyanoacetate (4.8 mmol)	30°C, 3 h, 20 mg of the catalyst	57.2	[17]

*ZIF-8 sample synthesized with process B at 200°C.

into the reaction solution is found. Thus, in the ZIF-8 sample synthesized with process B at 200°C, the Lewis acid Zn^{2+} sites may become saturated; hence, the decrease in densities of the Lewis acid sites results in more base sites from the imidazole linkers.

A comparison of the benzaldehyde conversion of the Knoevenagel condensation with different catalysts is shown in Table 3. Although the reaction conditions are different, the benzaldehyde conversion of this study is higher (76.5% compared with 51–70%) or consistent with that of previous studies (78–92%).

4. Conclusions

ZIF-8 was formed in methanol and water at room temperature and in DMF at high temperatures (100–200°C). In methanol, the reaction time and meIm/Zn molar ratio have small effects on the microstructures (uniform particles of ~100 nm diameter) of ZIF-8; however, the diffraction peaks at the angles smaller than 10° had slight variations. In contrast, ZIF-8 synthesized in DMF manifests full crystallinity with varying particle sizes (3~20 μm) with the better cohesion of particles observed at 200°C. All ZIF-8 samples

exhibit excellent catalytic activities in the Knoevenagel condensation reaction because of the base sites of imidazoles. When ZIF-8 are highly crystalline (samples synthesized in MeOH for five days and in DMF at 200°C), the activities of the base sites of imidazole prevail those of the Lewis acid sites of Zn^{2+}, resulting in a higher conversion of benzaldehyde.

Data Availability

The data used to support the findings of this study are available from the corresponding author upon request.

Conflicts of Interest

The authors declare that they have no conflicts of interest.

References

[1] H. Hayashi, A. P. Côté, H. Furukawa, M. O'Keeffe, and O. M. Yaghi, "Zeolite A imidazolate frameworks," *Nature Materials*, vol. 6, no. 7, pp. 501–506, 2007.

[2] K. S. Park, Z. Ni, A. P. Cote et al., "Exceptional chemical and thermal stability of zeolitic imidazolate frameworks," *Proceedings of the National Academy of Sciences*, vol. 103, no. 27, pp. 10186–10191, 2006.

[3] X. C. Huang, Y. Y. Lin, J. P. Zhang, and X. M. Chen, "Ligand-directed strategy for zeolite-type metal-organic frameworks: zinc(II) imidazolates with unusual zeolitic topologies," *Angewandte Chemie International Edition*, vol. 45, no. 10, pp. 1557–1559, 2006.

[4] Y. He, W. Zhou, G. Qian, and B. Chen, "Methane storage in metal-organic frameworks," *Chemical Society Reviews*, vol. 3, no. 16, pp. 5657–5678, 2014.

[5] E. Barea, C. Montoro, and J. A. R. Navarro, "Toxic gas removal-metal-organic frameworks for the capture and degradation of toxic gases and vapours," *Chemical Society Reviews*, vol. 45, no. 43, 2014.

[6] M. Hu, H. Lou, X. Yan, X. Hu, R. Feng, and M. Zhou, "In-situ fabrication of ZIF-8 decorated layered double oxides for adsorption and photocatalytic degradation of methylene blue," *Microporous and Mesoporous Materials*, vol. 271, pp. 68–72, 2018.

[7] V. Stavila, A. A. Talin, and M. D. Allendorf, "MOF-based electronic and opto-electronic devices," *Chemical Society Reviews*, vol. 43, no. 16, pp. 5994–6010, 2014.

[8] D. Q. Khieu, M. T. Thanh, T. V. Thien et al., "Synthesis and voltammetric determination of Pb(II) using a ZIF-8-based electrode," *Journal of Chemistry*, vol. 2018, Article ID 5395106, 12 pages, 2018.

[9] P. Horcajada, R. Gref, T. Baati et al., "Metal-organic frameworks in biomedicine," *Chemical Reviews*, vol. 112, no. 2, pp. 1232–1268, 2012.

[10] S. R. Venna, J. B. Jasinski, and M. A. Carreon, "Structural evolution of zeolitic imidazolate framework-8," *Journal of the American Chemical Society*, vol. 132, no. 51, pp. 18030–18033, 2010.

[11] J. Cravillon, C. A. Schröder, H. Bux, A. Rothkirch, J. Caro, and M. Wiebcke, "Formate modulated solvothermal synthesis of ZIF-8 investigated using time-resolved in situ X-ray diffraction and scanning electron microscopy," *CrystEngComm*, vol. 14, no. 2, pp. 492–498, 2012.

[12] M. Zhu, S. R. Venna, J. B. Jasinski, and M. A. Carreon, "Room-temperature synthesis of ZIF-8: the coexistence of ZnO nanoneedles," *Chemistry of Materials*, vol. 23, no. 16, pp. 3590–3592, 2011.

[13] M. T. Thanh, T. V. Thien, P. D. Du, N. P. Hung, and D. Q. Khieu, "Iron doped zeolitic imidazolate framework (Fe-ZIF-8): synthesis and photocatalytic degradation of RDB dye in Fe-ZIF-8," *Journal of Porous Materials*, vol. 25, no. 3, pp. 857–869, 2018.

[14] D. N. Ta, H. K. D. Nguyen, B. X. Trinh, Q. T. N. Le, H. N. Ta, and H. T. Nguyen, "Preparation of nano-ZIF-8 in methanol with high yield," *Canadian Journal of Chemical Engineering*, vol. 96, no. 7, pp. 1518–1531, 2018.

[15] P. Formentín, H. García, and A. Leyva, "Assessment of the suitability of imidazolium ionic liquids as reaction medium for base-catalysed reactions Case of Knoevenagel and Claisen-Schmidt reactions," *Journal of Molecular Catalysis A: Chemical*, vol. 214, no. 1, pp. 137–142, 2004.

[16] K. M. Parida and D. Rath, "Amine functionalized MCM-41: an active and reusable catalyst for Knoevenagel condensation reaction," *Journal of Molecular Catalysis A: Chemical*, vol. 310, no. 1-2, pp. 93–100, 2009.

[17] L. Martins, W. Hölderich, P. Hammer, and D. Cardoso, "Preparation of different basic Si-MCM-41 catalysts and application in the Knoevenagel and Claisen-Schmidt condensation reactions," *Journal of Catalysis*, vol. 271, no. 2, pp. 220–227, 2010.

[18] L. Martins, T. J. Bonagamba, E. R. de Azevedo, P. Bargiela, and D. Cardoso, "Surfactant containing Si-MCM-41: an efficient basic catalyst for the Knoevenagel condensation," *Applied Catalysis A: General*, vol. 312, pp. 77–85, 2006.

[19] U. P. N. Tran, K. K. A. Le, and N. T. S. Phan, "Expanding applications of metal-organic frameworks: zeolite imidazolate framework ZIF-8 as an efficient heterogeneous catalyst for the Knoevenagel reaction," *ACS Catalysis*, vol. 1, no. 2, pp. 120–127, 2011.

[20] M. Zhu, D. Srinivas, S. Bhogeswararao, P. Ratnasamy, and M. A. Carreon, "Catalytic activity of ZIF-8 in the synthesis of styrene carbonate from CO_2 and styrene oxide," *Catalysis Communications*, vol. 32, pp. 36–40, 2013.

[21] A. F. Bushell, M. P. Attfield, C. R. Mason et al., "Gas permeation parameters of mixed matrix membranes based on the polymer of intrinsic microporosity PIM-1 and the zeolitic imidazolate framework ZIF-8," *Journal of Membrane Science*, vol. 427, pp. 48–62, 2013.

[22] J. Yao, R. Chen, K. Wang, and H. Wang, "Direct synthesis of zeolitic imidazolate framework-8/chitosan composites in chitosan hydrogels," *Microporous and Mesoporous Materials*, vol. 165, pp. 200–204, 2013.

[23] X. Zhou, H. P. Zhang, G. Y. Wang, Z. G. Yao, Y. R. Tang, and S. S. Zheng, "Zeolitic imidazolate framework as efficient heterogeneous catalyst for the synthesis of ethyl methyl carbonate," *Journal of Molecular Catalysis A: Chemical*, vol. 366, pp. 43–47, 2013.

[24] Y. Zhang, Y. Jia, M. Li, and L. Hou, "Influence of the 2-methylimidazole/zinc nitrate hexahydrate molar ratio on the synthesis of zeolitic imidazolate framework-8 crystals at room temperature," *Scientific Reports*, vol. 8, no. 1, pp. 1–7, 2018.

[25] K. Kida, M. Okita, K. Fujita, S. Tanaka, and Y. Miyake, "Formation of high crystalline ZIF-8 in an aqueous solution," *CrystEngComm*, vol. 15, no. 9, p. 1794, 2013.

[26] Y. Du, R. Z. Chen, J. F. Yao, and H. T. Wang, "Facile fabrication of porous ZnO by thermal treatment of zeolitic imidazolate framework-8 and its photocatalytic activity," *Journal of Alloys and Compounds*, vol. 551, pp. 125–130, 2013.

Hindawi
Advances in Materials Science and Engineering
Volume 2019, Article ID 2710926, 13 pages
https://doi.org/10.1155/2019/2710926

Research Article

Adsorption of Arsenate from Aqueous Solution onto Modified Vietnamese Bentonite

Nguyen Le My Linh,[1] Duc Hoang Van,[1] Tran Duong,[1] Mai Xuan Tinh,[2] and Dinh Quang Khieu[2]

[1]*University of Education, Hue University, Hue 530000, Vietnam*
[2]*University of Sciences, Hue University, Hue 530000, Vietnam*

Correspondence should be addressed to Dinh Quang Khieu; dqkhieu@hueuni.edu.vn

Received 15 January 2019; Accepted 13 March 2019; Published 11 April 2019

Academic Editor: Frederic Dumur

In this study, pillared layered clays were prepared by modifying Vietnamese bentonite with polymeric Al and Fe. The obtained materials were characteristic of X-ray diffraction analysis, thermal analysis, and nitrogen adsorption/desorption isotherms. The results indicated that hydroxy-aluminum ($[Al_{13}O_4(OH)_{24}(H_2O)_{12}]^{7+}$) and poly-hydroxyl-Fe or polyoxo-Fe cations were intercalated into layers of clay, resulting in an increase of d_{001} values and of the specific surface areas compared with those of initial bentonite. Modified bentonites were employed to adsorb As(V) from aqueous solution. The adsorption of As(V) was strongly dependent on solution pH, and the maximum adsorption of modified bentonites was obtained in the pH 3.0 for Fe-bentonite and the pH 4.0 for Al-bentonite. The equilibrium adsorption study showed that the data were well fit by the Langmuir isotherm model. The maximum monolayer adsorption capacity of As(V) at 30°C derived from the Langmuir equation was 35.71 mg/g for Al-bentonite and 18.98 mg/g for Fe-bentonite. Adsorption kinetics, thermodynamics, and reusability of modified bentonites have been addressed.

1. Introduction

Arsenic is a potentially toxic metal that is said to be one of the most concerned contaminants in aquatic sources. Many approaches have been reported for the removal of arsenic including membrane dialysis, oxidation/reduction, precipitation/coprecipitation, filtration and adsorption, and ion exchange [1]. Among them, adsorption is recognized as one of the most promising method due to high efficiency and low cost. Various materials such as dolomite [2], chitosan [3], zeolites [4], organic clays [1], pillared interlayered clay [5, 6], activated carbon [7], metal oxides [8], and reduced metals [9] have been applied as adsorbents to eliminate arsenic from aqueous solutions. Many reports demonstrate that clays and modified clays have great potential to adsorb arsenic from contaminated water. Among the modified clays, pillared interlayered clays (PILCs) by means of the replacement of the exchangeable interlayer cations with Al_{13}, Fe_{13} Keggin ions have attracted extensive attention [10–12]. The surface area and pore volume of these PILCs are greatly enhanced so that they are used as effective adsorbents for arsenate removal. Ramesh et al. [5] reported that the maximum arsenate adsorption of Al/Fe-modified montmorillonite was about 21.23 mg/g (pH 3.0–6.0). Luengo et al. [6] studied the arsenate adsorption on a Fe(III)-modified montmorillonite. The authors concluded that both monomeric/polymeric Fe(III) species in the interlayer and on the external surface were responsible for arsenate adsorption. Zhao et al. [10] have proven that the adsorption capacity of the montmorillonites for As(V) was significantly promoted with increasing Al_{13} content. The experimental results showed the important role of the high positive charge of Al_{13} in the improvement of adsorption capacity of the modified montmorillonites. However, up to now, less efforts have been paid on both mechanism, kinetics, and thermodynamics of arsenate adsorption onto inorganic clay.

In the present article, the preparation of pillared layered clays by modification of bentonite with polymeric Al and Fe

and the removal of As(V) from aqueous solution were demonstrated.

2. Experimental

2.1. Materials. Bentonite was obtained from Vietnamese mining company and purified by the sedimentation combined with sonication and centrifugation. Aluminum chloride ($AlCl_3{\cdot}6H_2O$, 99%), ferric nitrate nonahydrate ($Fe(NO_3)_3{\cdot}9H_2O$, 99%), silver nitrate ($AgNO_3$, 98%), and sodium hydroxide (NaOH, 98%) were obtained from Guangzhou company, China. Stock solution of H_3AsO_4 100 mg/L was purchased from Merck. Chemical composition in mass analyzed by EDX of SiO_2; Al_2O_3; Fe_2O_3; TiO_2; MgO; CaO; K_2O; and Na_2O in mass is 69.1; 18.7; 4.4; 0.37; 4.19; 2.93; 0.25; and 0.07, respectively. The cation exchange capacity (CEC) was found to be 0.75 mmol/g.

2.2. Characterization. X-ray diffraction (XRD) patterns were obtained on D8-Advance Brucker, Germany with CuKα radiation. Thermogravimetric (TG) analysis was recorded on DTG-60H (Shimadzu) from 25 to 1000°C at a heating rate of 10°C/min under air atmosphere. Fourier transform infrared spectra (FTIR) were carried out on SHIMADZU FT-IR 8010M. Nitrogen adsorption/desorption isotherms were performed on Tri Star 3000. Before adsorption measurements, the specimen of 1.25 gram was outgassed for 5 h at 250°C. BET specific surface area was calculated from the nitrogen adsorption data with the relative pressure ranged from 0.04 to 0.25. Scanning electron microscopy (Hitachi, S-4500) was used to analyze the morphology of the obtained samples. A pH meter (Horiba, F-52) was employed for pH measurements. The point of zero charge (pH_{PZC}) of bentonite and polymeric Al/Fe-modified bentonite was calculated by the pH drift method. Arsenate was analyzed by means of atomic absorption spectroscopy (AAS, SHIMADZU-6800).

2.3. Preparation of Fe-Bentonite and Al-Bentonite. The purified bentonite was noted as B. The Fe pillaring solution, prepared from $Fe(NO_3){\cdot}9H_2O$ and NaOH with OH^-/Fe^{3+} molar ratio of 0.3 was stirred for 2 h and then aged in 24 h at ambient temperature. The mixture of B (1.0 g) and 100 mL of deionized water was vigorously stirred for 1 h. After that, the Fe pillaring solution was added slowly into the suspension containing the bentonite (the ratio of 10 mmol Fe/g dry bentonite); the mixture was stirred for 24 h at room temperature. The solid was separated by centrifugation and dried at 100°C for 10 h. The obtained polymeric Fe-modified bentonite was denoted as Fe-B. The Al pillaring solution was prepared by adding 0.1 M NaOH to 0.1 M $AlCl_3$ solution with vigorous stirring to obtain the $[OH^-]/[Al^{3+}]$ molar ratio of 2.4. Then, the pillaring solution was vigorously stirred for 7 h at 70°C and aged for 24 h at ambient temperature. After the aging process, the solution was slowly dropped under vigorous stirring to bentonite suspension for 24 h (24 mmol Al/g of dry bentonite). The final solid was obtained by filtration and washed with distilled water until free of chlorides (using the $AgNO_3$ test). The solid was dried at 100°C for 10 h. The obtained polymeric Al-modified bentonite was denoted as Al-B.

2.4. Adsorption Studies. Batch adsorption experiments were performed in 100 mL flask. 0.05 g of modified bentonite was added into the 100 mL flasks containing 50 mL solution with various concentrations of As(V). The pH solution was adjusted to the desired value by adding amounts of 0.01 M NaOH or 0.01 M HCl, and the bottles were shaken by magnetic stirrer for 4 h to attain equilibrium. The adsorbent was separated by centrifugation. Then, the concentration of As(V) was analyzed by the AAS method. Blank control tests were carried out for the sake of comparison.

The adsorption capacity of arsenate was calculated by using the following equation:

$$q_t = \frac{C_o - C_t}{m} \cdot V, \tag{1}$$

where q_t is the adsorption capacity of arsenate at time t, C_o (mg/L) is the initial arsenate concentration, C_t (mg/L) is the concentration of arsenate at time t, V (L) is the volume of arsenate solution used, and m (g) is the mass of the adsorbent used.

The effect of pH on arsenic adsorption was investigated in the pH ranges from 2 to 9 at ambient temperature.

For kinetic experiments, 0.2 g of adsorbent was added to 250 mL of known initial concentration in the pH = 3.0 (for the Fe-B sample) or pH = 4.0 (for the Al-B sample), and the mixture was stirred at an identical stirring speed of 600 rpm. At given time intervals, about 5 mL of solution was withdrawn and then centrifuged, and the equilibrium concentrations of the adsorbate were analyzed by the AAS method. The adsorption kinetics experiments were conducted at 10°C, 20°C, 30°C, and 40°C.

3. Results and Discussion

3.1. Characterization of the Adsorbents. The XRD patterns of B, Fe-B, and Al-B samples are shown in Figure 1.

The XRD patterns of B, Fe-B, and Al-B samples are shown in Figure 1. The basal spacing (d_{001}) of B is 1.44 nm while the recorded basal spacings were 1.48 nm for the Fe-B and 1.78 nm for the Al-B. Changes in the basal spacing depended on the charge, size, and hydration behavior of the ion or molecule that was located in the interlayer and on interactions between it and the phyllosilicate layers [12]. For the Fe-B sample, a slight increase in d_{001} has contributed to the presence of polymeric species of iron within the interlayer. In addition, from Figure 1, there was no characteristics reflections peaks of phases α, β–FeOOH, Fe_2O_3, and Fe_3O_4, showing that the iron oxides and hydroxides were not formed in Fe-bentonite sample. It was possible that iron oxides and hydroxides were forming very fine particles absorbed onto bentonite that could not be detected by XRD to destroy a part of crystal structure of bentonite, which was reflected in the decrease of intensity of d_{001} peak. The interlayer spacing distance of Al-B was 1.74 nm; this was a proof for the successful intercalation of hydroxyaluminum polycation into the

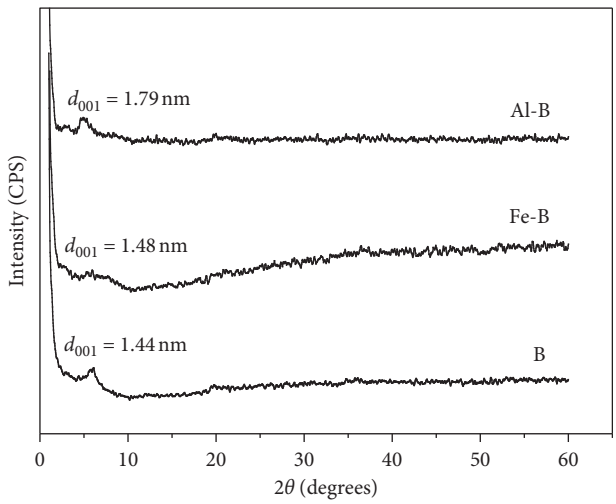

Figure 1: XRD patterns of B, Fe-B, and Al-B.

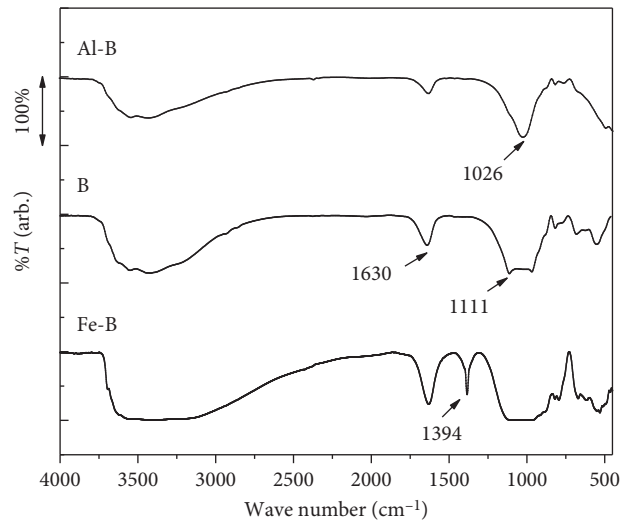

Figure 2: FTIR spectra of B, Fe-B, and Al-B.

bentonite layers. According to Hao et al. [13], the size of hydroxyaluminum polycation ($[AlO_4Al_{12}(OH)_{24}(OH_2)_{12}]^{7+}$) was of about 0.9 nm, and the basal spacing (d_{001}) of bentonite was 0.96 nm, so if there was an intercalation of ion Keggin Al_{13} into the interlayer space of bentonite, the basal spacing (d_{001}) of bentonite would be about of 1.86 nm. Other authors [14, 15] have observed that Al_{13} pillared bentonite gave basal spacings between 17 and 18 Å. This was explained by Qin et al. [11] that the value of d_{001} could not attain 1.86 nm probably due to the delamination of bentonite.

The FTIR spectra of the samples are depicted in Figure 2.

The peak at 3549 cm^{-1} of B sample was assigned to Al-Fe-OH vibration [16], the peak at 3414 cm^{-1} contributed to Fe-Fe-OH vibration [16] and HO-H vibration of the adsorbed water, and the peak at 1638 cm^{-1} was due to the deformation band (δ(O-H)) of physically adsorbed water. The peak at 1111 cm^{-1} was assigned to Si-O vibration in tetrahedral. If the amount of iron (Fe) in clays was high, this peak would shift to the higher position. According to other reports [1, 11, 17], this peak was in the range of 1033–1041 cm^{-1}, indicating that bentonite was iron-rich clay. The peak at 964 cm^{-1} was corresponded to Si-OH vibration [18], the peak at 816 cm^{-1} was because of the deformation vibration of Fe-Fe-OH [16], and the peak at 675 cm^{-1} was attributed to Al-Fe-OH vibration [19].

FT-IR spectra of the Fe-B and Al-B show that some characteristic bands of the initial bentonite were changed. Peak related to the δ(O-H) deformation shifted from 1638 cm^{-1} (B) to 1630 cm^{-1} (Fe-B) and to 1636 cm^{-1} (Al-B) with lower intensity. This could be due to the decrease of the H_2O content with replacing of the intercalated Fe/Al polycations. For Al-B, the peak at 3441 cm^{-1} and the intensity was higher than that of B (3414 cm^{-1}). The former was contributed to the O-H stretching vibration in hydroxyl-Al cations while the latter was corresponded to the hydroxyl groups in water-water hydrogen bands [17]. The band of Si-O vibration shifted from 1111 to 1026 cm^{-1} attributing to the strong interactions of the hydroxyl Al and bentonite layers. The FTIR results were in accordance with those of XRD.

TG and DTA curves of B, Fe-B, and Al-B samples are presented in Figure 3.

TG and DTA curves of B, Fe-B, and Al-B samples are presented in Figure 3. There were three main mass losses in the TG curve for the sample without modification. The first one below 200°C was due to physical water adsorption. The second mass loss being broadened from 200 to 600°C could be assigned to the interlayer water in bentonite structure. The third mass loss in the range of the temperatures over 600°C corresponding to the DTA peak 778°C was contributed to the dehydroxylation of bentonite layers. The TG curves of Fe-B and Al-B samples were similar than that of B sample. The mass loss in the range of 20–200°C (Loss 1) was assigned to physically adsorbed water. This period of the Al-B sample corresponding to the DTA endothermic peak 75°C was also attributed to the dehydration of oligomer Al cations [20], and the value was 14.1% which was higher than that of the unmodified one (3.5%). The mass loss in the range of 200–400°C (Loss 2) was contributed to the dehydration of bentonite layers and the decomposition of hydroxyl groups in polymeric Fe/Al cations. The second mass loss of Fe-B and Al-B samples at 200–400°C was 11.2% and 9.9%, respectively, which was higher than that of the B sample (8.1%). The mass loss above 600°C (Loss 3) was due to the decomposition of hydroxyl groups in the octahedron layer of bentonite.

The nitrogen adsorption and desorption isotherms of B, Fe-B, and Al-B materials are shown in Figure 4.

The nitrogen adsorption/desorption isotherms of the samples were all of type III according to IUPAC classification which indicated that the samples possessed mesoporous structure. The shape of hysteresis loops around from 0.4 to 0.9 of relative pressure was attributed to the slit-shaped pores, and their sizes are not well proportioned [4]. Table 1 lists the textural properties of all the samples. The BET surface area of pure bentonite was 114.44 m^2/g, but it increased to 146.07 m^2/g (Fe-B) and 170.13 m^2/g (Al-B) after modification. This is probably due to the increase of micropore volume (0.057 cm^3/g) and micropore surface area

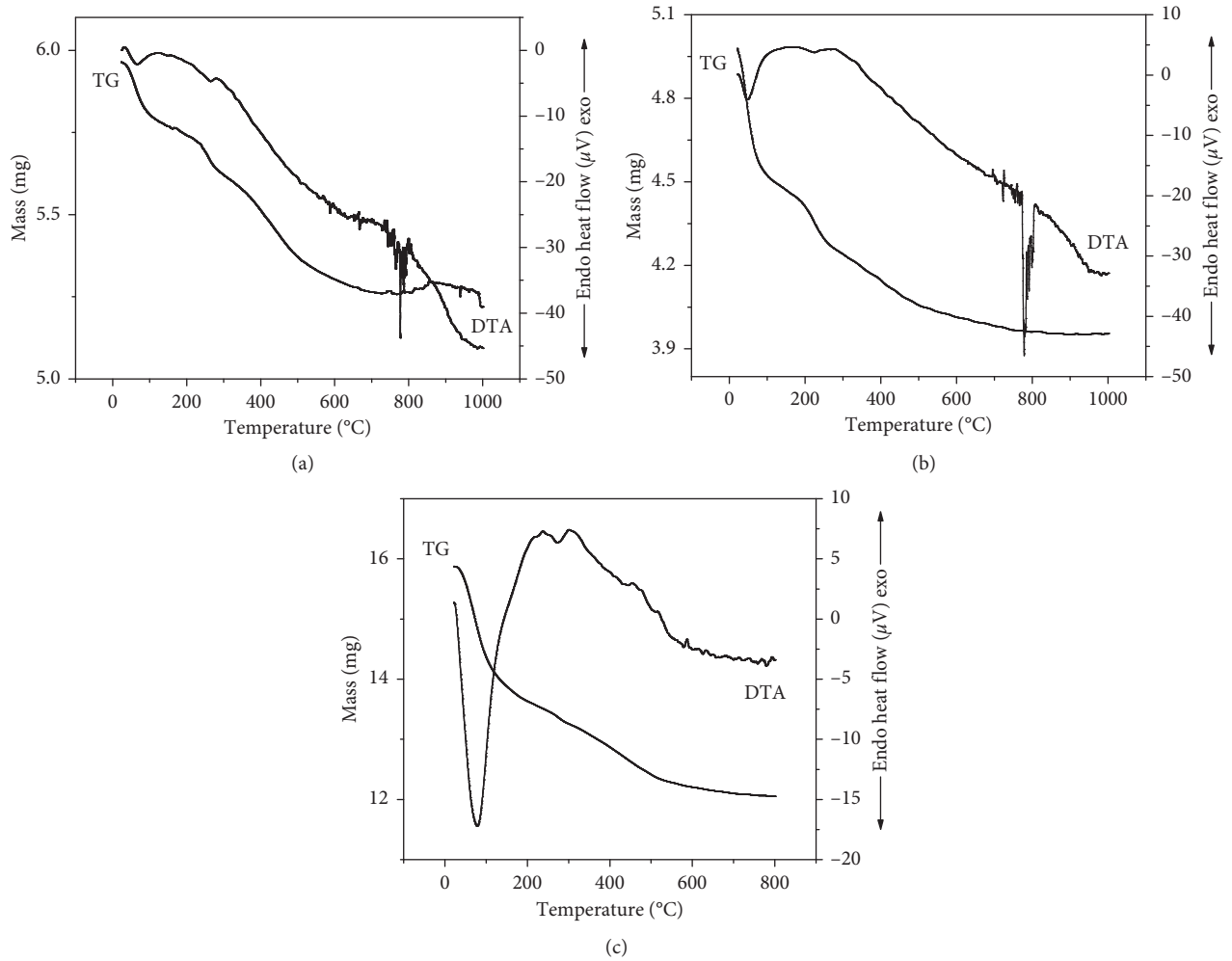

Figure 3: TG and DTA curves of B (a), Fe-B (b), and Al-B (c).

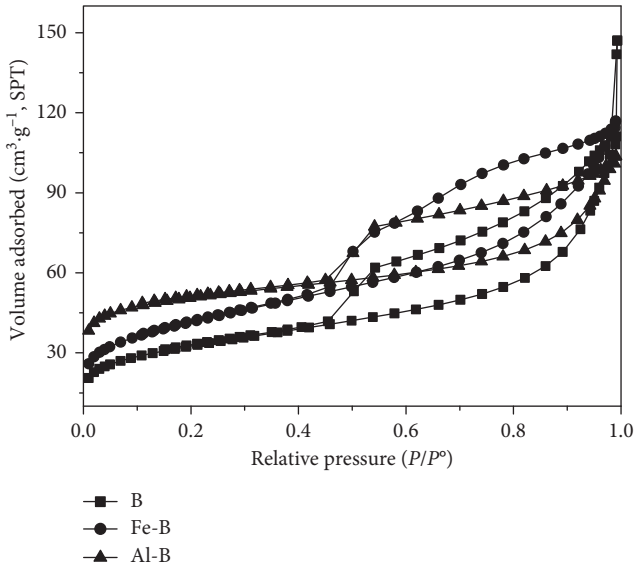

Figure 4: N_2 adsorption/desorption isotherms of B, Fe-B, and Al-B.

Table 1: Textural parameters of B, Fe-B, and Al-B samples.

Adsorbent	S_{BET} (m^2/g)	S_{micro} (m^2/g)	S_{ext} (m^2/g)	V_{micro} (cm^3/g)	V_{total} (cm^3/g)
B	114.44	44.72	69.72	0.020	0.187
Fe-B	146.07	41.03	105.04	0.018	0.159
Al-B	170.13	119.61	50.52	0.057	0.111

($119.61\ m^2/g$) in the interlayer spaces of the modified bentonite. This result was similar to the report of Ramesh et al. [5]. Before inserting polymeric Al into interlayer spaces of bentonite, these spaces were full of hydrated cations. The arrangement of these cations created the spaces between them, favoring the absorption of nitrogen. When intercalating polymeric Al into the bentonite, there were more pores in the interlayer space of bentonite favoring the absorption of nitrogen, so the micropore surface area of Al-B sample increased. According to the other authors [21, 22], the cation charge in the spaces of bentonite strongly affected the absorption of nitrogen. The decrease of external areas of

Al-B sample was explained by the increase of the number of micropores.

3.2. Adsorption Studies

3.2.1. Effect of pH. The pH effect on the arsenate adsorption capacity of polymeric Al/Fe-modified bentonite is shown in Figure 5.

It was found that the best adsorption of As(V) onto modified bentonite was in the range of pH 2.0–4.0. When increasing pH from 4.0 to 9.0, the amount of arsenate adsorbed (q_e) decreased. The point of zero charge (pH_{PZC}) of Fe-B and Al-B samples was, respectively, found to be 3.1 and 4.8 (Figure 6). At $pH < pH_{PZC}$, the modified bentonite surface was positively charged, so it favored for the adsorption of arsenic species in the form of $H_2AsO_4^-$ anions by electrostatic interaction. However, at a $pH > pH_{PZC}$, the modified surface was negatively charged, causing a repulsion force between the As(V) anions and bentonite surface. In addition, the hydroxyl ions and arsenate species could compete for adsorption at high pH causing a reduction in As(V) adsorption. Experimental results showed that As(V) had a maximum adsorption at pH 3.0 for Fe-B sample and pH 4.0 for the Al-B sample. Therefore, pH 3.0 and pH 4.0 were selected for further experiments, respectively, for Fe-B and Al-B samples.

In order to get more understanding of mechanism for arsenate absorption onto modified bentonite, the As(V) absorption at different pH was carried out. The pH values before and after the absorption are shown in Table 2.

From Table 2, it can be observed that the values of the pH for all of cases in the adsorption experiment changed. The pH values decreased after the arsenate absorption onto Fe-B. This could be explained by the reaction between the absorption sites $Fe\text{-}OH_{(surface)}$ and $H_3AsO_{4(solution)}$, creating the surface complexes such as the following:

$$Fe\text{-}OH_{(surface)} + H_3AsO_{4(solution)} \rightleftarrows Fe\text{-}HAsO_4^- + H_{(solution)}^+ + H_2O \quad (2)$$

The liberation of H^+ ions decreased pH of the solution.

The pH increased after the As(V) absorption onto Al-B sample due to the following reaction:

$$(Fe/Al) - OH_{(surface)} + H_2AsO_{4(solution)}^- \rightleftarrows (Fe/Al) - H_2AsO_{4(surface)} + OH_{(solution)}^- \quad (3)$$

The liberation of OH^- ions increased pH of the solution.

So, in this pH range, the main adsorption mechanisms could be considered as the electrostatic interactions and ion exchange.

FTIR spectra of Fe-B before and after the As(V) absorption are depicted in Figure 7.

Figure 7 shows a band in the range of 3500–3700 cm^{-1}, related to the stretching vibration of the structural hydroxyls group (AlAlOH, AlMgOH) [5]; a strong band at 3563 cm^{-1} related to the O-H stretching vibration of the silanol (Si-OH) groups and HO-H vibration of the water adsorbed silica surface [5]. The adsorption band at 1635 cm^{-1} was due to the deformation band (δ(O-H)) of physisorbed water [17]. After As(V) adsorption, these peaks were also observed with decreased intensity. This should be assigned to the direct interactions between arsenate anions and Fe-OH and Al-OH groups at corners of bentonite layers to create Fe-O-As(V) or Al-O-As(V) bonds which decreased intensity of these peaks. In addition, a new peak with low intensity was observed at 879 cm^{-1} corresponding to As-O vibration in $HAsO_4^{2-}$ anion, indicating that there was the As(V) adsorption onto Fe-B.

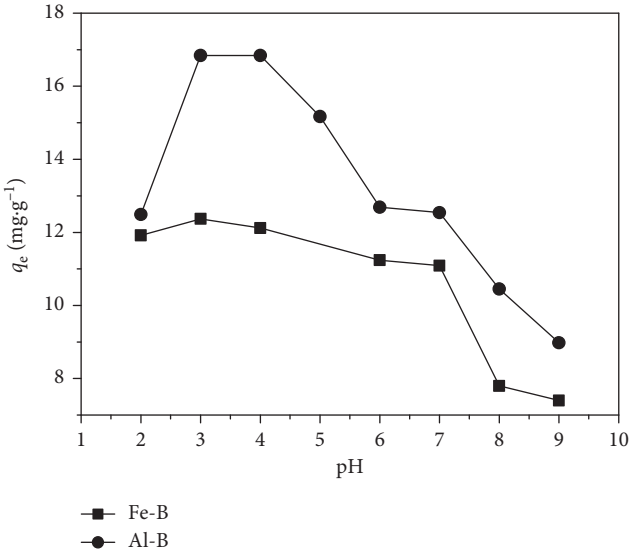

Figure 5: Effect of pH on the adsorption capacity of As(V) onto Fe-B sample ($C_{o(As)} = 12.98$ mg/L) and Al-B sample ($C_{o(As)} = 16.84$ mg/L) ($T = 303$ K, $m = 0.05$ g, $t = 4$ h).

The SEM images of Fe-B, Fe-B after the As(V) adsorption, Al-B, and Al-B after the As(V) adsorption are shown in Figure 8.

The morphology of modified bentonite changed clearly by the As(V) adsorption. The morphology of Fe-B included plates with diameter of several μm, around of which particles of small sizes were located. This morphology might facilitate for As(V) to adsorb onto modified bentonite. After As(V) adsorption, the lamellar structure of the Fe-B was left and a large number of flakes appeared. This indicated that there was a change in distance between the clay particles after arsenate adsorption. In addition, the small-size particles around the clay plates disappeared, suggesting that small clusters of Fe(III) oxides and hydroxides were also adsorption sites on surfaces. The morphology of Al-B sample consisted of the aggregate of smectites with irregular shape and partly a mass of flake shape. After arsenate adsorption, the modified clay surface was changed to an aggregated morphology, and there were several clusters around the clay plates. This indicated that the As(V) adsorption had a strong influence on the structure and morphology of modified bentonites.

3.2.2. Adsorption Kinetics. Experimental kinetic data were evaluated by using pseudo-first-order and pseudo-second-order kinetic models. The pseudo-first-order kinetic model in linear form is presented in the following equation:

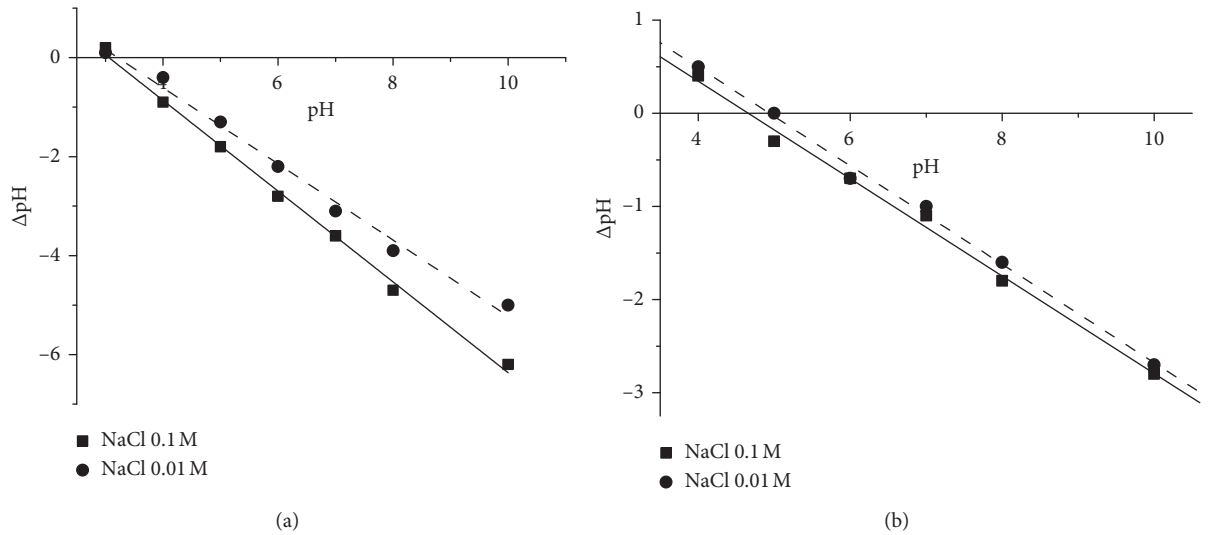

Figure 6: Point of zero charge plots of Fe-B (a) and Al-B (b).

Table 2: pH of As(V) solution before and after the arsenate absorption onto Fe-B ($C_{o(As)} = 12.98$ mg/L) and Al-B ($C_{o(As)} = 16.84$ mg/L) ($T = 303$ K, $m = 0.05$ g).

pH before the arsenate absorption	2.0	3.0	4.0	5.0	6.0	7.0	8.0	9.0
pH after the arsenate absorption onto Fe-B	2.0	2.9	3.3	—	4.0	4.8	7.0	7.2
pH after the arsenate absorption onto Al-B	2.7	3.7	5.4	5.8	6.4	7.9	8.1	9.4

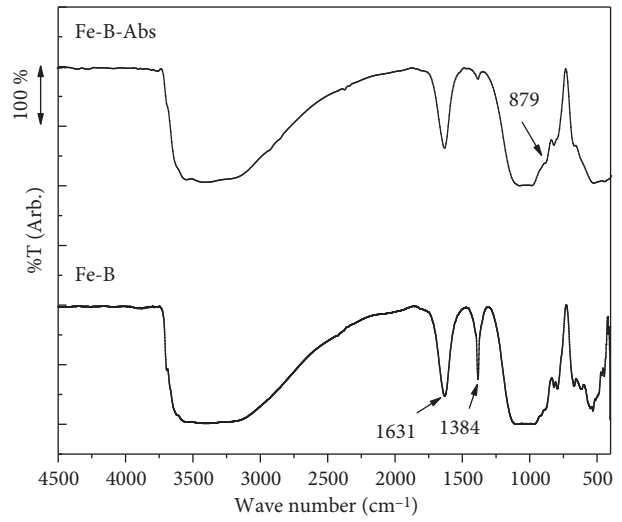

Figure 7: FT-IR spectra of Fe-B before and after the As(V) adsorption.

$$\ln(q_e - q_t) = \ln q_e - k_1 \cdot t, \tag{4}$$

where q_e and q_t are the adsorption capacity at equilibrium and at time t (mg/g) and k_1 is the pseudo-first-order rate constant (min^{-1}).

The pseudo-second-order kinetic model is given by [23, 24]

$$\frac{t}{q_t} = \frac{1}{k_2 q_e^2} + \frac{1}{q_e} \cdot t, \tag{5}$$

where k_2 is the equilibrium rate constant of pseudo-second-order kinetic model (g/mol·min).

The goodness of fit for the compatible model is assessed based on determination coefficient R^2 for the regression equation.

The plots of pseudo-first-order and pseudo-second-order kinetic models are illustrated in Figures 9 and 10, respectively. Their parameters are summarized in Table 3. The high determination coefficients (>0.92) as well as the calculated q_e values close to the experimental ones indicated that pseudo-second-order kinetic model was more suitable for the description of the adsorption kinetics of arsenate on modified bentonite (Table 3). This implied that the adsorption process could be chemisorption [23, 24]. The values of q_e at different temperatures for Al-B were greater than those for Fe-B, indicating that the adsorption capacity of Al-B is larger than that of Fe-B. The average diameter of $H_2AsO_4^-$ ions was about 3.5 Å, meanwhile the pore diameter of studied materials was about 26–220 Å, so arsenate ions were easy to move inside the mesopores of materials without being obstructed the geometry.

Table 3 shows that the value of k_2 increased with increasing temperature for both two samples (Fe-B: $0.353.10^{-3}$–$7.301.10^{-3}$ g/mg·min; Al-B: $2.8.10^{-3}$–$5.8.10^{-3}$ g/mg·min).

The activation energy can be computed by using the Arrhenius equation:

$$\ln k_2 = -\frac{E_a}{RT} + \ln A, \tag{6}$$

where A is the Arrhenius constant (g/mg·min), E_a the activation energy of adsorption (kJ/mol), R is the gas constant (8.314 J/mol·K), and T is the absolute temperature (K). The activation energy (E_a) was obtained from the slope of the linear plot of ln k_2 versus $1/T$ (Figure 11(a)).

Besides calculating the activation energy, the Gibbs energy $\Delta G^{\#}$, enthalpy $\Delta H^{\#}$, and entropy $\Delta S^{\#}$ of the activation

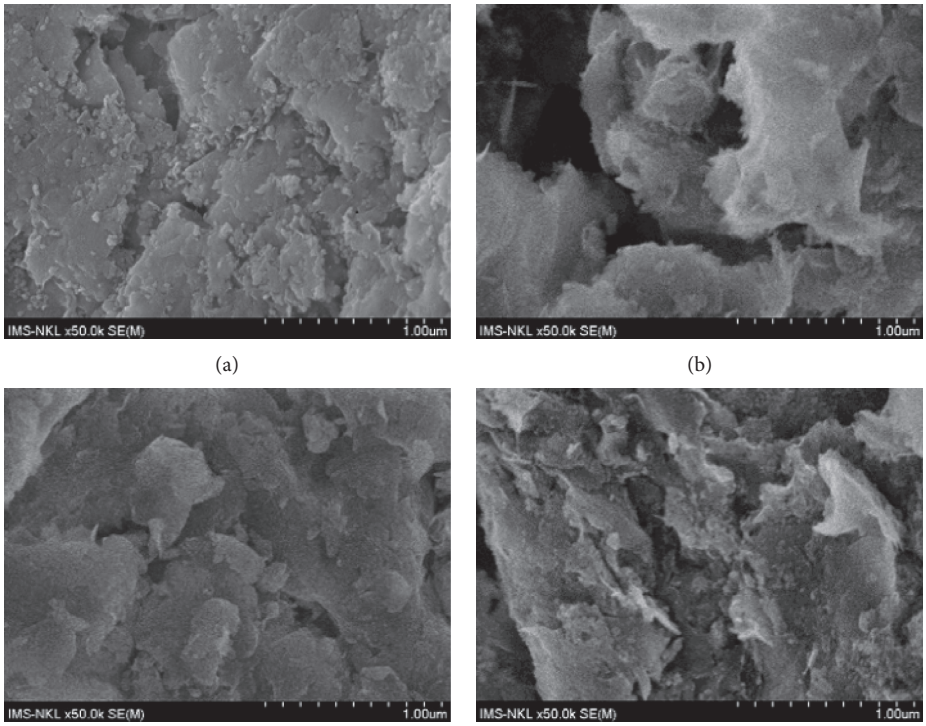

Figure 8: SEM images of Fe-B (a), Fe-B after the As(V) adsorption (b), Al-B (c), and Al-B after the As(V) adsorption (d).

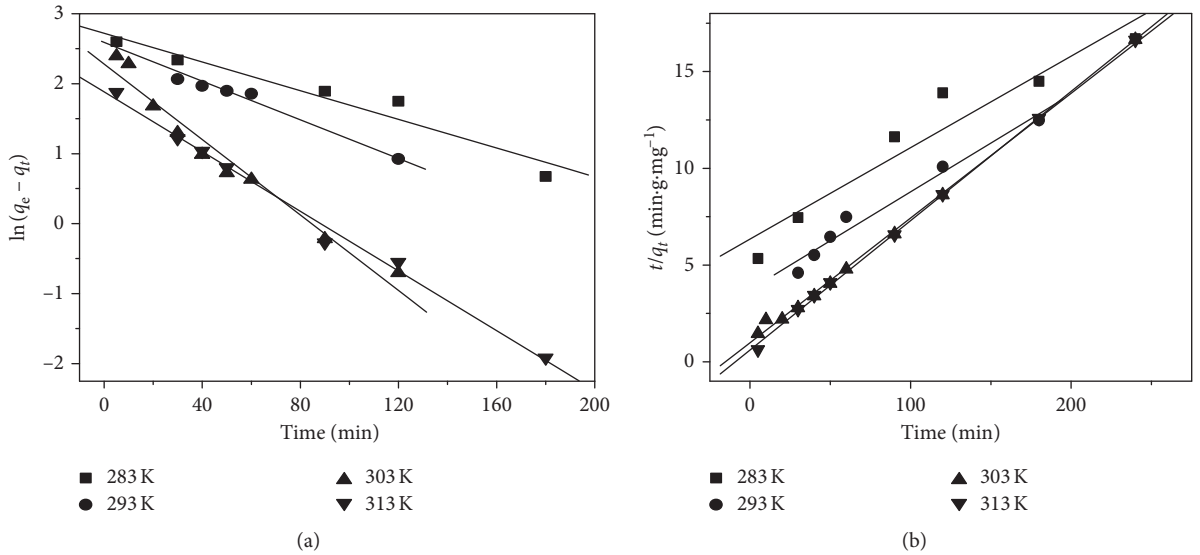

Figure 9: The pseudo-first-order kinetic model (a) and pseudo-second-order kinetic model (b) of As(V) adsorption by Fe-B at different temperatures.

for As(V) adsorption kinetics can be computed by using the Eyring equation [25]:

$$\ln \frac{k_2}{T} = \ln\left(\frac{k_b}{h}\right) - \frac{\Delta G^{\#}}{R \cdot T} = -\frac{\Delta H^{\#}}{R} \cdot \frac{1}{T} + \left[\ln\left(\frac{k_b}{h}\right) + \frac{\Delta S^{\#}}{R}\right], \quad (7)$$

where k_b (1.3807×10^{-23} J/K) is the Boltzmann constant, h (6.621×10^{-34} J·s) is the Planck constant, $\Delta G^{\#}$ is the Gibbs energy of activation, $\Delta H^{\#}$ is the activation enthalpy, and $\Delta S^{\#}$ is the activation entropy.

The linear plot of $\ln(k/T)$ versus $1/T$ gives a straight line. The activation parameters could be derived from the slope and intercepts of these lines (Figure 11(b)).

The values of the activation energy were found to be 80.29 kJ/mol and 41.90 kJ/mol for the arsenate adsorption onto Fe-B and Al-B, respectively (Table 4). The magnitude of activation energy can give information on whether the

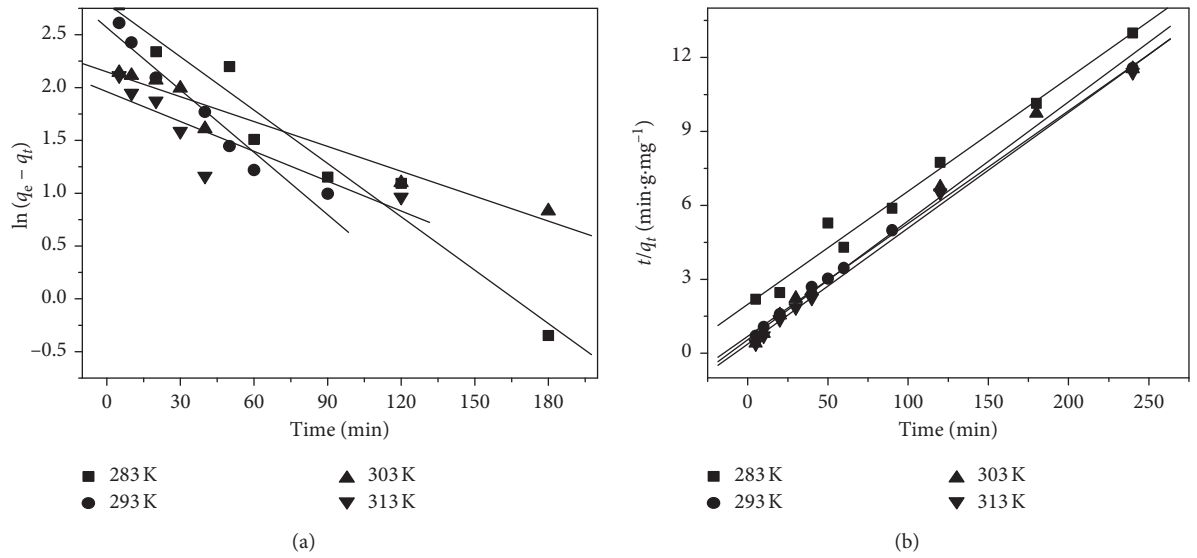

Figure 10: The pseudo-first-order kinetic model (a) and pseudo-second-order kinetic model (b) of As(V) adsorption by Al-B at different temperatures.

Table 3: Parameters of pseudo-first-order and pseudo-second-order kinetic model of As(V) adsorption by Fe-B and Al-B at different temperatures.

Adsorbent	T (K)	q_e (experimental) (mg/g)	First-order kinetic model			Second-order kinetic model		
			k_1 (min^{-1})	q_e (cal) (mg/g)	R^2	k_2 (g/mg·min)	q_e (cal) (mg/g)	R^2
Fe-B	283	14.38	0.010	15.19	0.942	0.35×10^{-3}	21.14	0.924
	293	14.42	0.013	12.44	0.977	0.68×10^{-3}	19.80	0.973
	303	14.42	0.027	9.80	0.962	4.20×10^{-3}	15.53	0.999
	313	14.44	0.021	6.57	0.992	7.30×10^{-3}	14.97	0.998
Al-B	283	18.47	1.6×10^{-3}	16.35	0.956	1.0×10^{-3}	22.22	0.984
	293	20.75	1.9×10^{-3}	13.01	0.948	2.9×10^{-3}	22.22	0.998
	303	20.80	7.0×10^{-3}	8.56	0.949	4.2×10^{-3}	20.83	0.992
	313	21.05	9.0×10^{-3}	7.09	0.752	5.8×10^{-3}	21.28	0.996

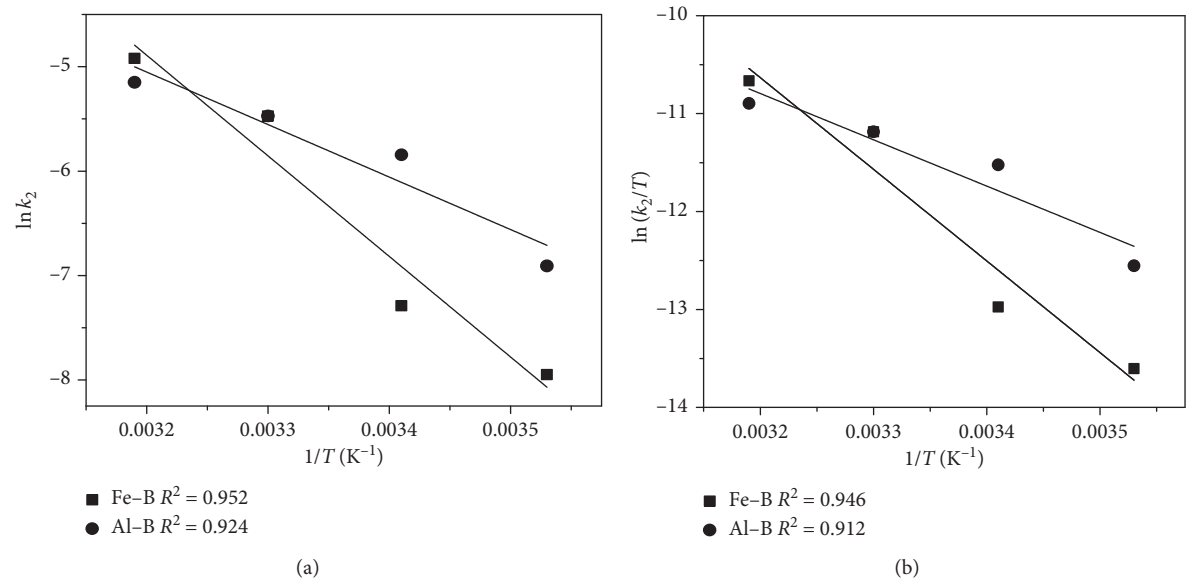

Figure 11: (a) Arrhenius plots and (b) Eyring plots of As(V) adsorption onto Fe-B and Al-B.

Table 4: Activation energy and activation parameters of adsorption process.

T (K)	E_a (kJ/mol)	$\Delta H^{\#}$ (kJ/mol)	$\Delta S^{\#}$ (kJ/mol.K)	$\Delta G^{\#}$ (kJ/mol)
Fe-B				
283	80.29	77.82	−0.037	88.41
293				88.79
303				89.16
313				89.53
Al-B				
	41.90	39.32	−0.162	85.16
				86.78
				88.40
				90.02

adsorption process is physical or chemical. Ramesh et al. [5] reported that the activation energy of physisorption was normally not more than 42 kJ/mol. Hence, the values of activation energy were found in this study suggesting that the adsorption of As(V) on Fe-B was a chemical adsorption. The smaller E_a for the adsorption of As(V) on Al-B was due to the formation of weak chemical bond between absorbent and adsorbate. According to the literature, the rate constant increased when decreasing the value of activation energy or increasing the frequency factor A. The calculated A values were found to be 1.8×10^{-11} and 80821 for the adsorption of As(V) on Fe-B and on Al-B, respectively. These results were interesting due to showing "the compensation effect" in heterogeneous adsorption.

The free energy of activation ($\Delta G^{\#}$), activation enthalpy ($\Delta H^{\#}$), and activation entropy ($\Delta S^{\#}$) are listed in Table 4. The positive value of $\Delta H^{\#}$ for both samples confirmed an endothermic process. The magnitude and sign of $\Delta S^{\#}$ can give an indication of whether the adsorption reaction is an associative or dissociative mechanism [25]. The high negative values of $\Delta S^{\#}$ manifested that the As(V) adsorption process was an associative mechanism. This was additional evidence for the analysis of adsorption mechanism as described in Section 3.2.1. The large positive values of $\Delta G^{\#}$ inferred that the adsorption reactions required energy to convert the reactants into products [26].

3.2.3. Adsorption Isotherms. Equilibrium studies were carried out to obtain the adsorption capacity of modified bentonite at different temperatures. Two adsorption isotherms, namely, the Langmuir [23] and the Freundlich [23] isotherms were employed to analyze the adsorption data. The linear form of Langmuir isotherm is given by

$$\frac{C_e}{q_e} = \frac{C_e}{q_m} + \frac{1}{K_L \cdot q_m}, \tag{8}$$

where q_e is the equilibrium adsorption capacity (mg/g), C_e is the equilibrium arsenate concentration in solution (mg/L), q_m is the monolayer adsorption capacity of the adsorbent (mg/g), and K_L is the Langmuir constant (L/mg) which is related to the energy of adsorption, respectively. q_m and K_L can be computed from the intercept and slope of the linear plot, with C_e/q_e versus C_e.

In addition, a separation factor, R_L (also equilibrium parameter), is defined by the following equation:

$$R_L = \frac{1}{1 + K_L C_i}, \tag{9}$$

where C_i (mg/L) is the initial dye concentration and K_L (L/mg) is the Langmuir constant. The value of R_L indicates the shape of the isotherms to be either unfavorable ($R_L > 1$), linear ($R_L = 1$), favorable ($0 < R_L < 1$), or irreversible ($R_L = 0$).

The Freundlich isotherm was applied to the adsorption on a heterogeneous surface with uniform energy. The linear form of this model can be expressed as follows:

$$\ln q_e = \ln K_F + \frac{1}{n} \cdot \ln C_e, \tag{10}$$

where q_e and C_e are the equilibrium adsorption capacity (mg/g) and equilibrium concentration in liquid phases (mg/L), respectively. K_F and n are the Freundlich constants which are related to adsorption capacity and intensity, respectively. The linear plot with $\ln q_e$ versus $\ln C_e$ can provide the values of K_F and n from the slope and intercepts.

The plots for he Langmuir and Freundlich isotherm models are shown in Figures 12 and 13.

As seen from Table 5, the high values of R^2 for the Langmuir isotherm model ($R^2 > 0.920$), as compared with those for the Freundlich isotherm model ($R^2 < 0.875$) and the values of R_L in the range 0 and 1 inferred that As(V) adsorption onto the modified bentonite was favorable for the Langmuir model. Based on the maximum monolayer adsorption capacity of the adsorbent q_m (mg/g), specific area of modified bentonite can computed by the following expression:

$$S = \frac{q_{max}^{As}}{M_{As}} \cdot N_A \cdot \sigma_{As}, \tag{11}$$

where q_{max}^{As} is the Langmuir monolayer adsorption capacity, M_{As} is the molar masse of As, N_A is Avogadro number, and σ_{As} is the surface area of AsO_4^{3-} ($\sigma_{As} = \pi \cdot r^2$, $r = 1.7$ Å).

Specific surface area of modified bentonite was calculated at the temperature of 283 K as follows:

$$\begin{aligned} S(\text{Fe} - \text{B}) &= \left(\frac{17.76}{75}\right) \times 6.03 \times 10^{23} \times 3.14 \times (1.7)^2 \times \left(10^{-10}\right)^2 \\ &= 12.96\ \text{m}^2/\text{g}, \\ S(\text{Al} - \text{B}) &= \left(\frac{29.41}{75}\right) \times 6.03 \times 10^{23} \times 3.14 \times (1.7)^2 \times \left(10^{-10}\right)^2 \\ &= 21.46\ \text{m}^2/\text{g}. \end{aligned} \tag{12}$$

The effective surface area values of the studied samples were less than S_{BET} of Fe-B (146.07 m^2/g) and Al-B (170.13 m^2/g), indicating that the As(V) absorption onto studied materials only occurred at the outer surfaces and in the large pores of bentonite particles.

The maximum As(V) adsorption capacities (q_m) computed from the Langmuir model at 303 K were 18.98 mg/g for Fe-B and 35.71 mg/g for Al-B. As can be seen from Table 6, the adsorption capacity for arsenate

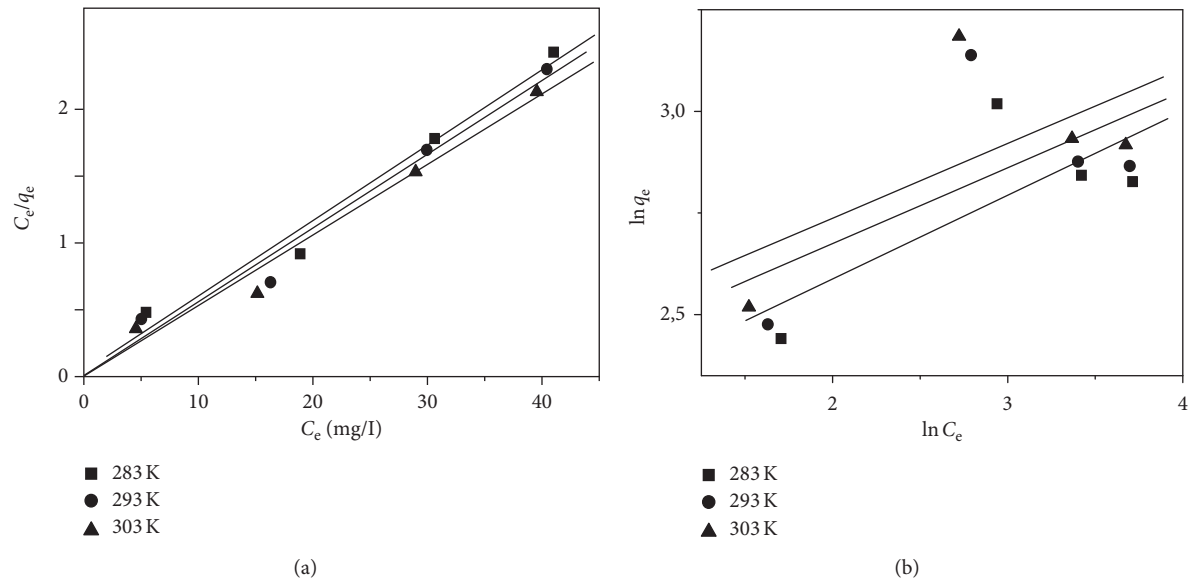

Figure 12: Plots of Langmuir (a) and Freundlich (b) isotherms in linear form for the adsorption of As(V) onto Fe-B at several temperatures.

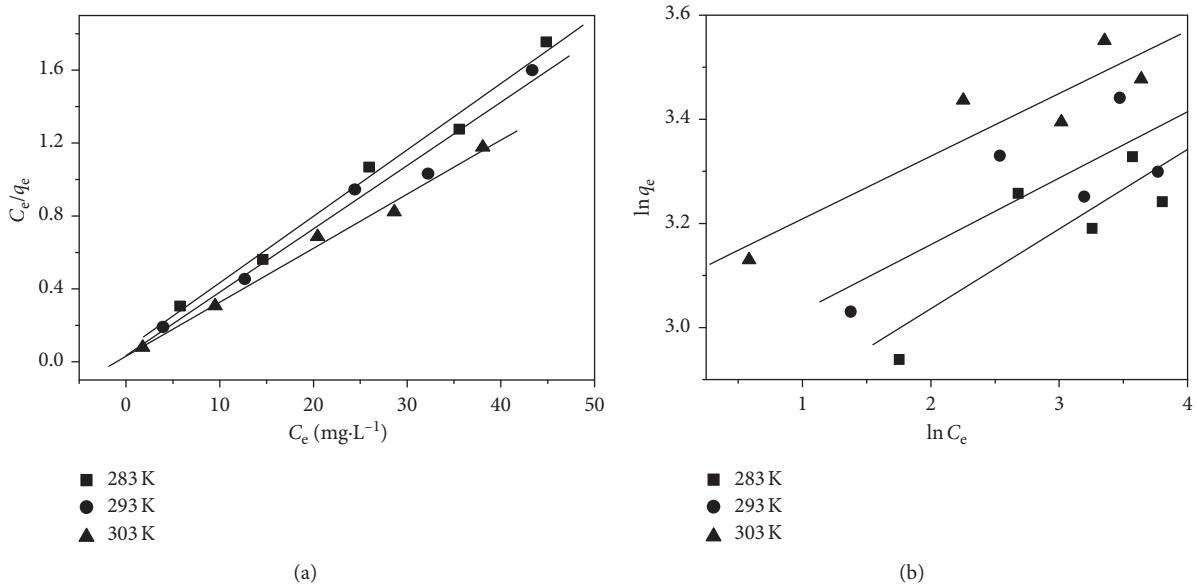

Figure 13: Plots of Langmuir (a) and Freundlich (b) isotherms in linear form for the adsorption of As(V) onto Al-B at several temperatures.

Table 5: The parameters of isotherm models in linear form for the adsorption of As(V) onto modified bentonite.

T (K)	Langmuir model				Freundlich model		
	q_{max} (mg/g)	K_L (L/mg)	R^2	R_L	K_F (mg/g)	n	R^2
Fe-B							
283	17.76	1.08	0.976	0.016–0.053	8.81	4.86	0.561
293	18.05	5.18	0.972	0.003–0.011	9.99	5.36	0.391
303	18.98	7.87	0.976	0.002–0.007	10.69	5.44	0.405
Al-B							
283	29.41	0.32	0.984	0.046–0.111	21.477	7.41	0.795
293	32.59	0.41	0.970	0.037–0.090	16.912	6.10	0.779
303	35.71	0.70	0.984	0.022–0.055	14.069	5.29	0.875

Table 6: Comparison of adsorption capacity with other adsorbents.

Adsorbent	Arsenate adsorption capacity (mg/g)	References
SMB3	0.288	[1]
Polymeric Al/Fe-modified montmorillonite	21.233	[5]
Al_{13}-Mont	5.008	[10]
C-Fe-M	8.85	[27]
Fe-M	15.15	[27]
Al-B	35.71	Present study
Fe-B	18.98	Present study

adsorption onto studied materials was greater than those for other adsorbents reported. Therefore, the modified bentonite showed a good capability for eliminating arsenate from aqueous solution down to part per billion levels, making the present modified bentonite to be used commercially in future for adsorbing arsenate from aquatic sources contaminated with arsenic.

3.2.4. Calculation of Thermodynamic Parameters. Gibb's free energy (ΔG°), entropy change (ΔS°), and enthalpy change (ΔH°) have been obtained from the following expressions [28]:

$$\Delta G^\circ = -RT \ln K_L, \tag{13}$$

where K_L is the Langmuir constant:

$$\ln K_L = -\frac{\Delta G^\circ}{RT} = -\frac{\Delta H^\circ}{RT} + \frac{\Delta S^\circ}{R}. \tag{14}$$

The values of ΔH° and ΔS° were computed from the slope and intercept of the plot, with $\ln K_L$ versus $1/T$ in Figure 14. The thermodynamic parameters for the As(V) adsorption are presented in Table 7.

For the both cases, the obtained ΔH° values were positive, which manifested the endothermic nature of arsenate adsorption onto modified bentonite. The positive value of ΔS° indicated the entropy of the system increased during the adsorption. This result suggested that the arsenate adsorption onto modified bentonite was promoted by entropy than by enthalpy. The mechanism of the As(V) adsorption onto modified bentonites might be ion exchange, so the large value of entropy was corresponded to greater randomness. The values of ΔG° were negative for both samples indicating the spontaneous adsorption in the investigated temperature range, and the decrease of ΔG° values with increasing temperature inferred that the adsorption became more favorable at higher temperature.

3.3. Reusability. In the reusability test, 0.5 g of used modified bentonites saturated with As(V) (initial Al-B or initial Fe-B) was added into thirty milliliters of 0.01 M HCl solution. The mixture was shaken at a temperature of 30°C using a magnetic stirrer for 24 h. The solids were centrifuged, rinsed for several times with distilled water, dried at 100°C, and investigated for As(V) adsorption capacity at the first run.

Figure 15 represents the reusability of modified bentonite. The adsorption capacity of the adsorbents decreased gradually during the repeated absorption/desorption operations. The adsorption capacity of Al-B decreased from 21.05 mg/g for initial adsorbent to 14.66 mg/g for third cycle. The adsorption capacity for Fe-B decreased from 14.44 mg/g for initial adsorbent to 9.98 mg/g for third cycle.

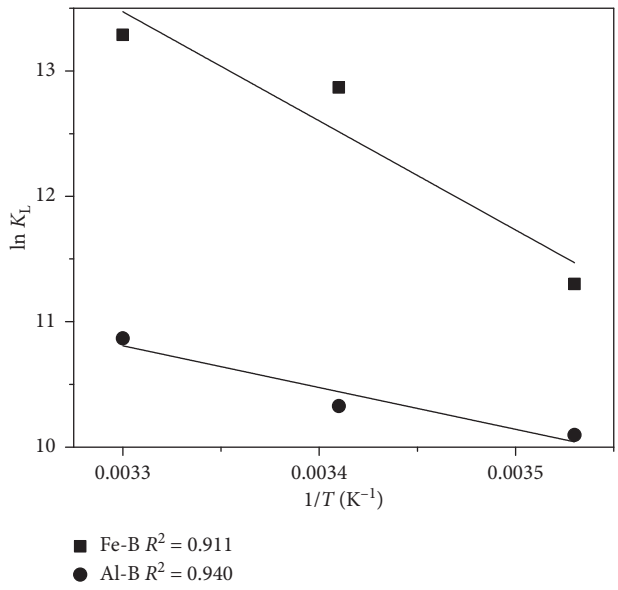

Figure 14: Plot $\ln K_L$ versus $1/T$ for the determination of thermodynamic parameters.

Table 7: Thermodynamic parameters for the As(V) adsorption onto Fe-B and Al-B materials.

Adsorbent	ΔG° (kJ/mol)			ΔH°	ΔS°
	283 K	293 K	303 K	(kJ/mol)	(kJ/mol.K)
Fe-B	−26.59	−31.35	−33.47	71.23	0.347
Al-B	−23.76	−25.16	−27.38	27.34	0.180

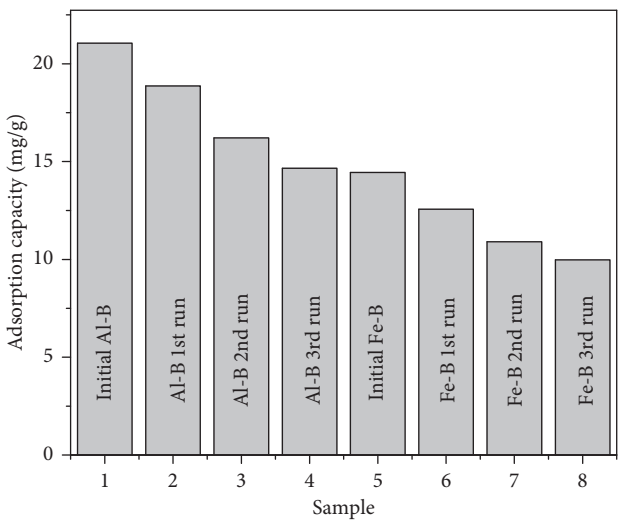

Figure 15: The dependence of adsorption capacity through the reuse of adsorbent ($C_{o(As)}$ = 24.66 mg/L, T = 303 K, m = 0.05 g, t = 4 h).

The adsorption capacity was reduced by 30.4% for Al-B and by 30.9% for Fe-B after four uses. The results showed that the polymeric Al and polymeric Fe bentonite were good reusable adsorbents in removal of arsenate ions from aqueous solution.

4. Conclusions

In this study, the polymeric Al- and Fe-modified bentonites were applied to remove arsenate ions from aqueous solution. The pseudo-second-order kinetic model fit well with the arsenate adsorption kinetic data for the two modified bentonites. The maximum monolayer adsorption capacities of As(V) at 303 K derived from the Langmuir model were 35.71 mg/g for Al-bentonite and 18.98 mg/g for Fe-bentonite, which were higher than that compared to other adsorbents reported previously. The negative values of ΔG° implied the spontaneity while the positive values of ΔH° and ΔS° indicated the endothermic nature and increase in randomness of the process taking place, respectively. The activation energies for the Fe-modified bentonite and Al-modified bentonite were found to be 80.29 and 41.90 kJ/mol, respectively. The modified bentonites can be regenerated and used effectively after four uses for adsorbing arsenate from aqueous solution.

Data Availability

The data used to support the findings of this study are available from the corresponding author upon request.

Conflicts of Interest

The authors declare that they have no conflicts of interest.

References

[1] J. Su, H.-G. Huang, X.-Y. Jin, X.-Q. Lu, and Z.-L. Chen, "Synthesis, characterization and kinetic of a surfactant-modified bentonite used to remove As(III) and As(V) from aqueous solution," *Journal of Hazardous Materials*, vol. 185, no. 1, pp. 63–70, 2011.

[2] Y. Salameh, N. Al-Lagtah, M. N. M. Ahmad, S. J. Allen, and G. M. Walker, "Kinetic and thermodynamic investigations on arsenic adsorption onto dolomitic sorbents," *Chemical Engineering Journal*, vol. 160, no. 2, pp. 440–446, 2010.

[3] K. C. M. Kwok, L. F. Koong, T. Al Ansari, and G. McKay, "Adsorption/desorption of arsenite and arsenate on chitosan and nanochitosan," *Environmental Science and Pollution Research*, vol. 25, no. 15, pp. 14734–14742, 2018.

[4] P. Chutia, S. Kato, T. Kojima, and S. Satokawa, "Arsenic adsorption from aqueous solution on synthetic zeolites," *Journal of Hazardous Materials*, vol. 162, no. 1, pp. 440–447, 2009.

[5] A. Ramesh, H. Hasegawa, T. Maki, and K. Ueda, "Adsorption of inorganic and organic arsenic from aqueous solutions by polymeric Al/Fe modified montmorillonite," *Separation and Purification Technology*, vol. 56, no. 1, pp. 90–100, 2007.

[6] C. Luengo, V. Puccia, and M. Avena, "Arsenate adsorption and desorption kinetics on a Fe(III)-modified montmorillonite," *Journal of Hazardous Materials*, vol. 186, no. 2-3, pp. 1713–1719, 2011.

[7] D. Borah, S. Satokawa, S. Kato, and T. Kojima, "Sorption of As(V) from aqueous solution using acid modified carbon black," *Journal of Hazardous Materials*, vol. 162, no. 2-3, pp. 1269–1277, 2009.

[8] M. Jang, S.-H. Min, T.-H. Kim, and J. K. Park, "Removal of arsenite and arsenate using hydrous ferric oxide incorporated into naturally occurring porous diatomite," *Environmental Science & Technology*, vol. 40, no. 5, pp. 1636–1643, 2006.

[9] S. Bang, G. Korfiatis, and X. Meng, "Removal of arsenic from water by zero-valent iron," *Journal of Hazardous Materials*, vol. 121, no. 1–3, pp. 61–67, 2005.

[10] S. Zhao, C. Feng, X. Huang, B. Li, J. Niu, and Z. Shen, "Role of uniform pore structure and high positive charges in the arsenate adsorption performance of Al13-modified montmorillonite," *Journal of Hazardous Materials*, vol. 203-204, pp. 317–325, 2012.

[11] Z. Qin, P. Yuan, J. Zhu, H. He, D. Liu, and S. Yang, "Influences of thermal pretreatment temperature and solvent on the organosilane modification of Al_{13}-intercalated/Al-pillared montmorillonite," *Applied Clay Science*, vol. 50, no. 4, pp. 546–553, 2010.

[12] L. Borgnino, M. J. Avena, and C. P. De Pauli, "Synthesis and characterization of Fe(III)-montmorillonites for phosphate adsorption," *Colloids and Surfaces A: Physicochemical and Engineering Aspects*, vol. 341, no. 1-3, pp. 46–52, 2009.

[13] Y.-F. Hao, L.-G. Yan, H.-Q. Yu et al., "Comparative study on adsorption of basic and acid dyes by hydroxy-aluminum pillared bentonite," *Journal of Molecular Liquids*, vol. 199, pp. 202–207, 2014.

[14] F. Bertella and S. B. C. Pergher, "Pillaring of bentonite clay with Al and Co," *Microporous and Mesoporous Materials*, vol. 201, pp. 116–123, 2015.

[15] M. Altunlu and S. Yapar, "Effect of OH^-/Al^{3+} and Al^{3+}/clay ratios on the adsorption properties of Al-pillared bentonites," *Colloids and Surfaces A: Physicochemical and Engineering Aspects*, vol. 306, no. 1–3, pp. 88–94, 2007.

[16] R. L. Frost and J. T. Kloprogge, "Vibrational spectroscopy of ferruginous smectite and nontronite," *Spectrochimica Acta Part A: Molecular and Biomolecular Spectroscopy*, vol. 56, no. 11, pp. 2177–2189, 2000.

[17] W. Xue, H. He, J. Zhu, and P. Yuan, "FTIR investigation of CTAB-Al-montmorillonite complexes," *Spectrochimica Acta Part A: Molecular and Biomolecular Spectroscopy*, vol. 67, no. 3-4, pp. 1030–1036, 2007.

[18] B. A. Goodman, J. D. Russell, and A. R. Frasera, "A MÖssbauer and I.R. Spectroscopic study of the structure of nontronite," *Clays and Clay Minerals*, vol. 24, no. 2, pp. 53–59, 1976.

[19] J. D. Russel and A. R. Fraser, "Infrared methods," in *Clay Mineralogy, Spectroscopic and Chemical Determinative Methods*, M. J. Wilson, Ed., pp. 11–67, Chapman & Hall, London, UK, 1994.

[20] M. E. R. J. Jalil, R. S. Vieira, D. Azevedo, M. Baschini, and K. Sapag, "Improvement in the adsorption of thiabendazole by using aluminum pillared clays," *Applied Clay Science*, vol. 71, pp. 55–63, 2013.

[21] H. Faghihian and M. H. Mohammadi, "Surface properties of pillared acid-activated bentonite as catalyst for selective production of linear alkylbenzene," *Applied Surface Science*, vol. 264, pp. 492–499, 2013.

[22] H. Khalaf, O. Bouras, and V. Perrichon, "Synthesis and characterization of Al-pillared and cationic surfactant modified Al-pillared Algerian bentonite," *Microporous Materials*, vol. 8, no. 3-4, pp. 141–150, 1997.

[23] M. E. Pena, G. P. Korfiatis, M. Patel, L. Lippincott, and X. Meng, "Adsorption of As(V) and As(III) by nanocrystalline titanium dioxide," *Water Research*, vol. 39, no. 11, pp. 2327–2337, 2005.

[24] M. Toor and B. Jin, "Adsorption characteristics, isotherm, kinetics, and diffusion of modified natural bentonite for removing diazo dye," *Chemical Engineering Journal*, vol. 187, pp. 79–88, 2012.

[25] K. A. Krishnan and T. S. Anirudhan, "Uptake of heavy metals in batch systems by sulfurized steam activated carbon prepared from sugarcane bagasse pith," *Industrial & Engineering Chemistry Research*, vol. 41, no. 20, pp. 5085–5093, 2002.

[26] H. T. M. Thanh, T. T. T. Phuong, P. L. T. Hang, T. T. T. Toan, T. X. Mau, and D. Q. Khieu, "Comparative study of Pb(II) adsorption onto MIL–101 and Fe–MIL–101 from aqueous solutions," *Journal of Environmental Chemical Engineering*, vol. 6, no. 4, pp. 4093–4102, 2018.

[27] X. Ren, Z. Zhang, H. Luo et al., "Adsorption of arsenic on modified montmorillonite," *Applied Clay Science*, vol. 97-98, pp. 17–23, 2014.

[28] A. Özcan, Ç. Ömeroğlu, Y. Erdoğan, and A. S. Özcan, "Modification of bentonite with a cationic surfactant: an adsorption study of textile dye Reactive Blue 19," *Journal of Hazardous Materials*, vol. 140, no. 1-2, pp. 173–179, 2007.

Hindawi
Advances in Materials Science and Engineering
Volume 2019, Article ID 5719651, 9 pages
https://doi.org/10.1155/2019/5719651

Research Article

Simultaneous Determination of Amlodipine, Hydrochlorothiazide, and Valsartan in Pharmaceutical Products by a Combination of Full Spectrum Measurement and Kalman Filter Algorithm

Nguyen Thi Quynh Trang,[1,2] Nguyen Van Hop,[1] Nguyen Dang Giang Chau,[1] and Thuc Binh Tran[1]

[1]*University of Sciences, Hue University, Hue 530000, Vietnam*
[2]*Faculty of Environmental Sciences, Saigon University, Ho Chi Minh City 700000, Vietnam*

Correspondence should be addressed to Thuc Binh Tran; ttbinh@hueuni.edu.vn

Received 13 November 2018; Accepted 6 March 2019; Published 1 April 2019

Guest Editor: Hien Duy Mai

In this work, a new solution has been found for selecting the approximate initial value of concentration (by means of the classical least squares) and variance (calculated by the Horwitz equation) for the Kalman filter algorithm. With this solution, the Kalman method is less error-prone and has a better repeatability than the least squares method when using the full spectrum. A protocol for simultaneous determination of amlodipine (AML), hydrochlorothiazide (HYD), and valsartan (VAL) in pharmaceutical products was developed based on the spectrophotometry-chemometric method using full spectrum measurement in combination with the Kalman filter algorithm written in Microsoft Excel 2016 and Visual Basic for Applications (VBA). The method was validated on the Exforge HCT tablets with good repeatability (RSD) (varied from 2.2% to 2.3% ($n = 3$) for all the three studied compounds) and good recovery (90.0%–94.0% for AML, 90.3%–94.5% for HYD, and 98.5%–103.1% for VAL ($n = 3$)). The results were in good agreement with the measurements achieved from the high-performance liquid chromatography (HPLC) method.

1. Introduction

In the development history of analytical chemistry, chemometrics has been used and applied successfully for identification and quantification of a mixture in different matrices, particularly in pharmaceutical samples. The commonly used chemometric methods could be named as partial least squares (PLS), classical least squares (CLS), principal component regression (PCR), artificial neural networks (ANNs), derivative spectrum, and Kalman filter.

Generally, each method has its own advantages and disadvantages. CLS [1] uses all the spectrum data to form a system of m equations and n unknowns ($m > n$), in which the transformation matrix basing on least squares principle yields acceptable results in terms of relative errors. However, if the input data contain many noises (or errors) and/or there are reactions between analytical compounds causing photometric effects to the absorbance, then this CLS method fails to reduce the noises and consequently large number of errors is expected. Meanwhile, the ANN method [1] requires long time for network formation and a number of algorithms. Therefore, to build a suitable model, each potential model developed needs to be tested until the optimal network structure is defined.

The derivative spectrum method [1, 2], in the meantime, is inapplicable when the sample contains components of overlapping or similar absorbance spectrum since it is difficult to find the suitable wavelength and their derivative spectrum still has maximum absorbance overlapping.

The Kalman filter method is able to remove maximally the noise effects, therefore, limiting the measurement errors. This method in combination with spectrophotometry was applied to analyze mixtures of metal ions and components in multicomponent pharmaceutical dosages [3, 4]. In the previous works [5–8], equations for calculating employing Kalman filter algorithm were given. However, the method for selection of initial values including initial concentrations and initial variances for the Kalman filter still has not been dealt with. Based on the pretests (data not shown), it could be addressed that the calculated results strongly depend on the method to select the initial guesses for the Kalman filter. If the selected initial guesses of concentration ($C_{\text{est}}(0)$) and variance ($P_{\text{est}}(0)$) are not suitable or selected concentration is too different from the real value, then it would cause divergent result or big errors. In general, until now, there has not been a comprehensive solution for selection of initial guesses for the Kalman filter.

From the mentioned gaps above, the three main objectives of this study are (i) to find a suitable method to define the initial guesses for the Kalman filter algorithm, (ii) to build a software based on the Kalman filter algorithm and spectrophotometry (called the Kalman method from now on) to determine simultaneously components in a mixture, (iii) to apply the developed Kalman method for simultaneous determination of the compounds with overlapping absorbance spectra in a multicomponent pharmaceutical product, specifically in this study were amlodipine, hydrochlorothiazide, and valsartan in Exforge HCT tablet.

2. Materials and Methods

2.1. Chemicals and Reagents. All the three target compounds AML (100.43%), VAL (98.38%), and HYD (99.55%) were purchased from Vietnamese Drug Quality Control Center.

Stock solutions of 1000 μg/mL and working solutions of 50 μg/mL, 25 μg/mL, 10 μg/mL, and 5 μg/mL of each compound were prepared in methanol (Merck, USA).

The commercial pharmaceutical product Exforge HCT tablet contains the labelled ingredients as follows: AML 10 mg, VAL 160 mg, and HYD 12.5 mg; batch number: BK917; manufactured date: 09/2016; expired date: 08/2018; registered number VN-19287-15; manufactured at Novartis Farmaceutica S.A. Ronda Santa Maria 158, 08210 Barberà del Vallès, Barcelona, Spain.

2.2. Sample Preparation. The drug sample was prepared following the method of Galande [9]: 20 tablets were balanced to calculate the average tablet weight ($\overline{M}$), which were then finely milled and homogenized. Take m grams, in accordance with one tablet weight (theoretically, mass of AML is 10 mg, of HYD is 12.5 mg, and of VAL is 160 mg), into a 250 mL glass bottle with cap, 50 mL of methanol was added, and the bottle was shaked well before applying ultrasonic extraction for 30 min. The solution was then filtered into a 100 mL volumetric flask and filled up with methanol. The obtained solution was diluted 100 times before measurement by using a V-630 UV/Vis Spectrometer JASCO (Japan).

Accordingly, an average mass of one tablet was $\overline{M} = 4.1252$ g.

Mass of an individual compound in a tablet was calculated as follows:

$$x = \frac{C \cdot V \cdot K \cdot \overline{M}}{m \cdot 1000} \text{ (mg/tablet)}, \tag{1}$$

where $\overline{M}$ is the average mass of one tablet (g), m is the mass of the weighted sample (g), C is the concentration of the target compound (μg/mL), V is the initial volume (100 mL), and K is the dilution factor ($K = 100$).

Accordingly, when $m = \overline{M}$, we have

$$x = C \cdot 10 \text{ (mg/tablet)}. \tag{2}$$

2.3. Kalman Filter Method. The Kalman filter is a linear parameter estimation technique. In analytical chemistry, it is used to estimate the concentrations of components in a mixture from the absorbance spectra. The initial state of concentration (at the first wavelength) is required. The next concentration state will be estimated based on the initial one. Basically, the model consists of two equations as follows:

The equation to describe the chemical system:

$$C_{(k)} = C_{(k-1)} + w_{(k)}. \tag{3}$$

And the other to describe the measurement process:

$$A_{(k)} = e_{(k)} C_{(k)} + \nu_{(k)}, \tag{4}$$

where $C_{(k)}$ is a vector of state concentrations at point k (which is the wavelength), $w_{(k)}$ is the vector of noise contribution to the system model at point k, $A_{(k)}$ is the measurement at point k, $\varepsilon_{(k)}$ is the state transition matrix, and $\nu_{(k)}$ is the corresponding measurement noise.

The Kalman filter algorithm applied in this study for multicomponent spectrophotometry analysis consists of the following equations:

(i) State (concentration) estimate extrapolation:

$$C_{\text{pri}(k)} = C_{\text{est}(k-1)}. \tag{5}$$

(ii) Error covariance extrapolation:

$$P_{\text{pri}(k)} = P_{\text{est}(k-1)}. \tag{6}$$

(iii) Kalman gain:

$$K_{(k)} = P_{\text{pri}(k)} e^{T}_{(k)} \left(e_{(k)} P_{\text{pri}(k)} e^{T}_{(k)} + R_{(k)} \right)^{-1}. \tag{7}$$

(iv) State estimate updation:

$$C_{\text{est}(k)} = C_{\text{pri}(k)} + K_{(k)} \left(A_{(k)} - e_{(k)} C_{\text{pri}(k)} \right). \tag{8}$$

(v) Error covariance updation:

$$P_{\text{est}(k)} = \left[\text{INV} - \varepsilon_{(k)} K_{(k)} \right] P_{\text{pri}(k)}. \tag{9}$$

The above calculation steps are performed from the first wavelength to the last wavelength. Finally, the calculation program will produce the result: the concentration of each

constituent in the system and the covariance of the error. This variance is usually the smallest at the last wavelength [5–8].

2.4. Method Validation

2.4.1. Relative Error (RE %). The relative error was calculated as follows [10, 11]:

$$\mathrm{RE}\,(\%) = \frac{C - C_0}{C_0} \cdot 100, \tag{10}$$

where C is the measured concentration (μg/mL) and C_0 is the known concentration (standard solution) (μg/mL).

2.4.2. Repeatability. Repeatability was assessed via the relative standard deviation (RSD) value [10, 11]:

$$\mathrm{RSD}\,(\%) = \frac{S \cdot 100}{\overline{x}}, \tag{11}$$

where S is the standard deviation and is the mean concentration after n times of measurement (μg/mL).

For internal laboratory quality control, the method repeatability was approved if the obtained RSDs were lower than a half of the RSD value calculated from the Horwitz function [9–11]:

$$\mathrm{RSD}_{\mathrm{Horwitz}} = 2^{(1-0.5\cdot \lg C)}. \tag{12}$$

2.4.3. Method Recovery. Method recovery was calculated based on the spiked samples as follows [10, 11]:

$$\mathrm{Rev}\,(\%) = \frac{C_{\mathrm{T}} - C_{\mathrm{a}}}{a} \cdot 100, \tag{13}$$

where a is the spike concentration (μg/mL), C_{T} is the measured concentration after spiking (μg/mL), and C_{a} is the measured concentration before spiking (μg/mL).

2.5. Analytical Procedure. The analytical procedure is shown in Figure 1.

The three main analytical steps are shown as follows:

Step 1. Prepare the standard solutions or samples

Step 2. Measure molecular absorbance spectra, data were recorded as .txt or .dat files

Step 3. Extract the files to the computer and run the developed Kalman-Excel program to calculate the specific concentration

3. Results

3.1. Absorbance Spectra of Standard Solutions. Absorbance spectra of four solutions, namely, AML 5 μg/mL, HYD 5 μg/mL, VAL 5 μg/mL, and mixture of AML 5 μg/mL, HYD 5 μg/mL, and VAL 5 μg/mL in methanol at the wavelength range 230–340 nm were scanned and are shown in Figure 2.

As shown in Figure 2, absorbance spectra of AML, HYD, and VAL in ethanol overlapped between 230 nm and 340 nm wavelength, causing difficulty in simultaneously determination of these compounds in mixture. This problem, however, could be solved smoothly using a combination of spectrophotometry and chemometrics.

Within the wavelengths from 230 nm to 340 nm at 0.5 nm intervals, the measured absorbance spectrum of the standard mixture was almost fit with the theory spectrum (estimated from the additive property of absorbance); therefore, absorbance of mixture containing AML, HYD, and VAL had additive property. In other words, it was able to use full spectrum for simultaneous determination of AML, HYD, and VAL by using the combination of spectrophotometry and chemometric method.

3.2. Selection of Initial Guesses to Start the Kalman Filter. As mentioned above, the main challenge to use the Kalman filter is to choose a proper method to identify the initial guesses. A wrong selection would cause an improper calculation. In a mixture containing different substances, the initial guesses are the estimated concentrations in accordance with specific variances of individual substances. Based on the previous studies, there have been two solutions to select the initial guesses:

Group 1. Random selection of initial guesses, which means the values of concentration (C) could be randomly assigned, such as 0 or 0.5 μg/mL; and of variance (P) could be 1, etc. [5, 8].

Group 2. Assumption of initial guesses, which means either (i) C and P values are subjectively selected based on personal experience and the properties of the samples, (ii) some preliminary experiments are conducted to define the initial C and P values [1, 5], or (iii) Beer–Lambert's law is applied at some selected wavelengths to calculate the initial C value (for individual substances in the mixture) by solving linear equation systems, while the variance P is calculated based on a specific guideline for statistical errors in analytical chemistry (i.e., applying Horwitz equation to calculate relative standard deviation (RSD), accordingly the standard deviation and variance at that concentration are defined) [5, 7, 10, 12].

In general, so far there have been no comprehensive method to select suitable initial guesses (C and P values) for the Kalman filter algorithm, raising a challenge for the analytical chemists who want to apply the Kalman filter in their studies. In this study, we investigated three different methods to select the initial C and P values, specifically based on the selection of group 1, group 2, and the proposed selection method of this study.

3.3. Random Selection of Initial Guesses. In this method, $C_{\mathrm{est}(0)}$ and $P_{\mathrm{est}(0)}$ values could be randomly selected [11]; therefore, this study chose 0.3 μg/mL for $C_{\mathrm{est}(0)}$ and 1 for $P_{\mathrm{est}(0)}$. The $C_{\mathrm{est}(0)}$ value of 0.3 μg/mL was delivered from the

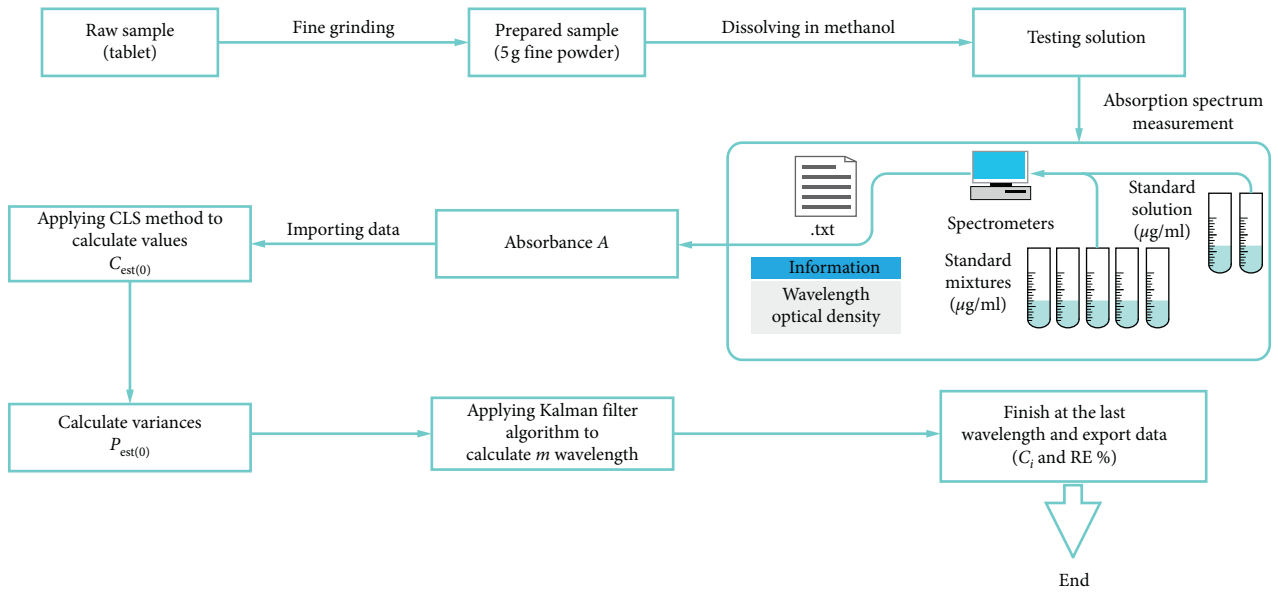

Figure 1: Analytical scheme.

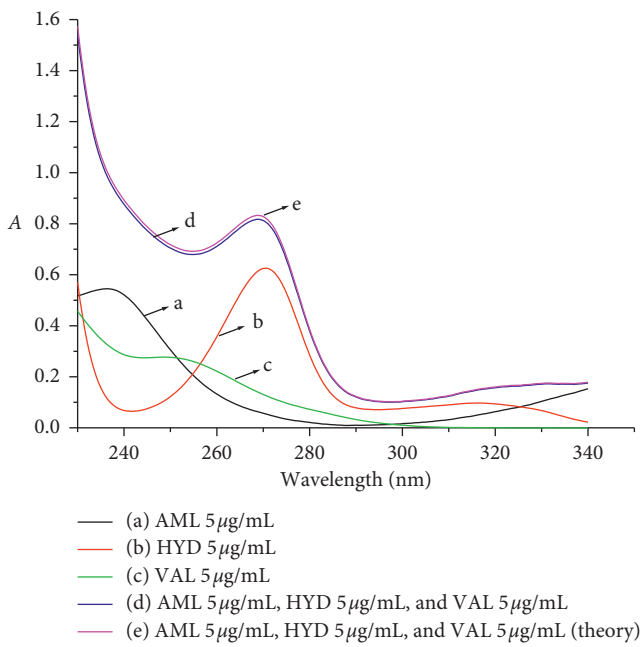

Figure 2: Measured absorbance spectra of the standards AML 5 μg/mL (a), HYD 5 μg/mL (b), VAL 5 μg/mL (c), and mixture of AML 5 μg/mL, HYD 5 μg/mL, and VAL 5 μg/mL (d) in methanol. The theory spectrum is demonstrated as (e).

common limit of detection (LOD) value of spectrophotometry of about 0.1 μg/mL, of which the limit of quantification would be around 0.3 μg/mL.

Apply the Kalman method for monospectral data and a mixture (AML, HYD, and VAL) of three substances (in the range of 220 nm–340 nm), and the results are shown in Table 1.

The results in Table 1 demonstrated that, in the cases of AML and HYD of mixture H1, when C_0 was close to the selected concentration (0.3 μg/mL), this method provided acceptable relative error (RE) values (20% for AML and −6%

Table 1: Quantification results of AML, HYD, and VAL in a mixture using the Kalman filter with a random selection of initial guesses method.

	Mixture	H1	H2	H3	H4
AML	C_o (μg/mL)	0.250	0.500	1.000	5.000
	C (μg/mL)	0.300	0.300	0.300	0.304
	RE (%)	20	−40	−70	−94
HYD	C_o (μg/mL)	0.325	0.650	1.300	5.000
	C (μg/mL)	0.307	0.304	0.302	0,299
	RE (%)	−6	−53	−77	−94
VAL	C_o (μg/mL)	4.000	8.000	16.000	5.000
	C (μg/mL)	0.301	0.300	0.300	0.299
	RE (%)	−93	−97	−98	−94

C_o: concentration in the standard solution; C: calculated concentration.

for HYD). Otherwise it brought big measurement errors with RE values fluctuated from 40% to 98% for all the target compounds in all the rest investigated mixtures. The cause of this result could be interpreted that the applied Kalman filter considered the random selected concentration of 0.3 μg/mL belonged to another distribution with a certain real value, which was different with this current distribution in accordance with the real values of the studied compounds (1.00 to 9.00 μg/mL). In other words, when the initial concentration is too different from its real value, the Kalman filter using the random selection method for initial guesses will not result in convergence but divergence, causing unacceptable statistical errors.

In short, the initial guesses ($C_{est(0)}$ and $P_{est(0)}$) selected in random is not suitable if the selected concentration is too different from the real value, which would cause divergent result or big errors.

3.4. Assumption of Initial Guesses. This assumption was applied in some previous studies [5, 7], in which a series of

preliminary experiments were conducted with different initial guesses ($C_{est(0)}$ and $P_{est(0)}$) to identify the suitable initial concentration and variance for the Kalman filter. Moreover, there were studies suggested automatically carrying out the preliminary experiments (employing self-written computer programs); however, the calculation speed was generally slow, which required some repeated calculations to select proper $C_{est(0)}$ and $P_{est(0)}$ values [1, 5].

In this study, two different solutions were tested for an assumption of $C_{est(0)}$ and $P_{est(0)}$ values (in mixtures containing 2 or 3 compounds):

Solution 1. Based on the equation systems of 2 (or 3) unknowns (concentrations) at 2 (or 3) adjacent wavelengths (this is the equation showing the relationship between absorbance and concentration in a mixture with absorption coefficient (α) calculated from the individual spectrum of the studied compound), concentration of each compound will be calculated which then used as $C_{est(0)}$ for the Kalman filter. Meanwhile, the $P_{est(0)}$ value was randomly selected, for instance by 1. The results are shown in Table 2.

Solution 2. Select 0.3 μg/mL as $C_{est(0)}$ for each compound in a mixture. The initial variance $P_{est(0)}$ was calculated based on the Horwitz equation, which resulted in a value of 0.003 in accordance with a concentration $C = 0.3\,\mu\text{g/mL} = 3 \cdot 10^{-7}$ [13]. The results are shown in Table 2.

Apply the Kalman method for monospectral data and a mixture of two substances (in the range of 220 nm–340 nm), and the results are shown in Tables 2 and 3.

Solution 1 provided big relative errors (RE % fluctuating from 14% to 82%, except for the case of AML in mixtures H2 and H4, Table 2). This *Solution 1* required complicated steps and depended on the two initial wavelengths selected to solve the equation system, which helped us to define the initial concentration. On the contrary, the application on real samples was strongly affected by the matrix, causing big errors.

In *Solution 2,* although a different approach was applied to define the initial variance (employing the Horwitz equation), the Kalman filter in this stage brought big errors (RE % varying from 7% to 97%).

In short, the above two tested methods to identify initial guesses by either random selection or assumption failed to bring an acceptable result (judged via relative errors). The only exception resulted when the initial concentration selected was close to the real value of concentration in the mixture. It was, therefore, necessary to find a new approach in identifying the initial concentration approximately to the actual value of the analyzed compound in the mixture.

3.5. Selection of Approximate Initial Guesses. Based on the literature review and laboratory experiments for a mixture containing 3 substances, a new method to select initial guesses was proposed, specifically:

(i) Apply the classical least squares method to solve the system of m linear equations with n unknowns (in which m was the number of wavelengths selected to scan the absorption spectrum of the mixture and n was the number of compounds in the mixture), followed by the Gaussian elimination method to solve a system of n linear equations with n unknowns for concentrations of compounds in the mixture. The resulting concentrations of the compounds in the mixture were selected as initial concentrations.

(ii) Apply the Horwitz equation to estimate the variance corresponding to the concentration of each compound in the mixture, which was considered as the initial variance $P_{est(0)}$. The calculation of initial variance $P_{est(0)}$ corresponding to the initial concentration $C_{est(0)}$ was as follows:

From equation (11),

$$\text{RSD}_{\text{Horwitz}}(\%) = \frac{S}{C_{est(0)}} \cdot 100, \tag{14}$$

$$\Rightarrow S = \frac{\left[\text{RSD}_{\text{Horwitz}} \cdot C_{est(0)}\right]}{100}. \tag{15}$$

Table 2: Quantification results of AML, HYD, and VAL in a mixture using the Kalman filter with the assumption of initial guesses method (Solution 1).

	Mixture	H1	H2	H3	H4
AML	C_o (μg/mL)	0.250	0.500	1.000	5.000
	C (μg/mL)	1.731	0.478	0.530	5.032
	RE (%)	−30.8	−4.5	−47	0.6
HYD	C_o (μg/mL)	0.325	0.650	1.300	5.000
	C (μg/mL)	2.794	0.495	1.610	5.910
	RE (%)	−14.0	−23.8	23.85	18.2
VAL	C_o (μg/mL)	4.000	8.000	16.000	5.000
	C (μg/mL)	4.796	11.053	29.067	3.949
	RE (%)	19.9	38.2	81.7	−21.03

C_o: concentration in the standard solution; C: calculated concentration.

Table 3: Quantification results of AML, HYD, and VAL in a mixture using the Kalman filter with the assumption of initial guesses method (Solution 2).

	Mixture	H1	H2	H3	H4
AML	C_o (μg/mL)	0.250	0.50	1.00	5.00
	C (μg/mL)	0.300	0.300	0.282	0.477
	RE (%)	20.0	−40.0	−71.8	−90.5
HYD	C_o (μg/mL)	0.325	0.650	1.300	5.000
	C (μg/mL)	0.301	0.304	0.368	0.443
	RE (%)	−7.4	−53.2	−71.7	−91.1
VAL	C_o (μg/mL)	4.00	8.00	16.00	5.00
	C (μg/mL)	0.319	0.454	0.542	0.289
	RE (%)	−92.0	−94.3	−96.6	−94.2

C_o: concentration in the standard solution; C: calculated concentration.

In which $RSD_{Horwitz}$ was calculated as (12) and $C_{est(0)}$ represented by fractions.

$$RSD_{Horwitz}(\%) = 2^{(1-0.5\lg C_{est(0)})}. \quad (16)$$

Finally,

$$S^2 = P_{est(0)}. \quad (17)$$

Noticeably, when conducting repeated measures in a laboratory, if the repeatability (represented via RSD value) smaller or equal to a half of the theory RSD value delivered from the Horwitz equation ($RSD \leq 1/2\ RSD_{Horwitz}$), then the method repeatability is acceptable [10]. Accordingly, the initial variance corresponding to the initial concentration $C_{est(0)}$ would be a quarter of the $P_{est(0)}$ value calculated from (13).

The overall experiment was conducted as follows: apply the CLS method to define $C_{est(0)}$ values of AML, HYD, and VAL from the spectrum data—which were the absorbance values of individual compound and mixture solutions measured from 230 nm–340 nm wavelength. From the result of $C_{est(0)}$, calculate the specific $P_{est(0)}$ values of AML, HYD, and VAL. Finally, provide $C_{est(0)}$ and $P_{est(0)}$ to the designed computer program using the Kalman filter to get the results, as shown in Table 4.

The output data provided the concentrations close to the actual values. In other words, this developed method showed good results with small relative errors ($RE \leq 4$ %), compared to the two previous methods—using random selection and assumption of initial guesses.

To ensure the applicability of the developed method using selection of approximate initial guesses to identify the initial guesses for the Kalman filter, it is necessary to validate the method in both standard solutions and real samples (pharmaceutical products).

3.6. Relative Errors of the Method. To check the performance of the method, four different mixtures (AML/HYD/VAL, μg/mL) of the three target compounds were prepared, including H1: 0.250/0.325/4.000; H2: 0.50/0.65/8.00; H3: 1.00/1.30/16.00; and H4: 5.00/5.00/5.00. The absorbance spectrum of the prepared mixtures was scanned from 230 nm to 340 nm wavelength. The Kalman-Excel program was then applied to calculate the concentration of each compound in order to identify RE values. The results are shown in Table 5.

Under different mixtures, the obtained RE values of AML measurements varied from 0.4 to 2.2%, of HYD from −1.5 to 1.3%, and of VAL from −3.6 to 0.8% (Table 5). These low RE values demonstrated the high similarity of the standard concentrations and the measured concentrations of the three studied compounds. In other words, the developed method has good trueness.

3.7. Method Repeatability for Laboratory-Prepared Samples. The similar experiment as described in Section 3.1 was conducted, in which each mixture was prepared and analyzed in triplicate. Method repeatability was assessed based on the comparison between the calculated RSD values and 1/2 $RSD_{Horwitz}$. The results are shown in Table 6.

Table 4: Quantification results of AML, HYD, and VAL in a mixture using the Kalman filter with the selection of the approximate initial guesses method.

	Mixture	H1	H2	H3	H4
AML	C_o (μg/mL)	0.250	0.500	1.000	5.000
	C (μg/mL)	0.253	0.511	1.016	4.981
	RE (%)	1.2	2.2	1.6	0.4
HYD	C_o (μg/mL)	0.325	0.650	1.300	5.000
	C (μg/mL)	0.320	0.646	1.290	5.064
	RE (%)	−1.5	−0.6	−0.8	1.3
VAL	C_o (μg/mL)	4.000	8.000	16.000	5.000
	C (μg/mL)	3.99	8.06	16.05	4.821
	RE (%)	−0.2	0.8	0.3	−3.6

C_o: concentration in the standard solution; C: calculated concentration.

The results in Table 6 show that the RSD value for both AML and VAL measurements ($n = 3$) in 4 different mixtures was 0.4%, for HYD fluctuated from 0.3 to 0.5%. For internal laboratory quality control, the method repeatability was approved if the obtained RSD was lower than a half of the RSD value calculated from the Horwitz function [10]. Accordingly, this developed method has good repeatability.

3.8. Method Repeatability and Trueness for Pharmaceutical Samples

3.8.1. Repeatability. The repeatability of the procedure to simultaneously determine AML, HYD, and VAL in the pharmaceutical sample (Exforge HCT tablets, $n = 3$) is described in Section 2.4.2. Accordingly, the final masses of AML, HYD, and VAL per tablet after preparation were 10.00 mg, 12.50 mg, and 160.00 mg, which were considered as the expected contents. The developed Kalman-Excel program was used for calculating the concentrations of each target compounds. The results of content of target substances and repeatability are shown in Table 7.

Average mass of AML per tablet was 9.61 mg with the RSD value of 2.3% (the expected mass was 10 mg, $RSD_{Horwitz}$ was 8%), of HYD was 11.63 mg with RSD value of 2.2% (the expected mass was 12.50 mg, $RSD_{Horwitz}$ was 5.5%), and of VAL was 169.17 mg with RSD value of 2.2% (the expected mass was 160.00 mg, $RSD_{Horwitz}$ was 5.3%). Apparently, all of the RSD values were lower then the corresponded $RSD_{Horwitz}$, implying that the developed method was successfully applied to analyze simultaneously AML, HYD, and VAL in pharmaceutical product.

3.8.2. Trueness. To assess the trueness, in this study, two different approaches were considered, which were (i) define method recovery and (ii) compare the results with the ones analyzed by a validated method: high-performance liquid chromatography (HPLC).

Table 5: Measured concentrations of AML, HYD, and VAL in the standard mixtures with corresponding RE values.

Mixture	AML			HYD			VAL		
	$C_{0,AML}$ (μg/mL)	C_{AML} (μg/mL)	RE (%)	$C_{0,HYD}$ (μg/mL)	C_{HYD} (μg/mL)	RE (%)	$C_{0,VAL}$ (μg/mL)	C_{VAL} (μg/mL)	RE (%)
H1	0.250	0.253	1.2	0.325	0.320	−1.5	4.000	3.990	−0.2
H2	0.500	0.511	2.2	0.650	0.646	−0.6	8.000	8.060	0.8
H3	1.000	1.016	1.6	1.300	1.290	−0.8	16.000	16.050	0.3
H4	5.000	4.981	0.4	5.000	5.064	1.3	5.000	4.8210	−3.6

C_o: concentration in the standard solution; C: calculated concentration; RE: relative error (Section 2.1).

Table 6: Method repeatability.

Mixture		AML			HYD			VAL		
		Rep 1	Rep 2	Rep 3	Rep 1	Rep 2	Rep 3	Rep 1	Rep 2	Rep 3
H1	C (μg/mL)	0.253	0.252	0.254	0.320	0.320	0.321	3.990	3.980	4.010
	C_{mean} (μg/mL)		0.253			0.320			3.993	
	RSD_{mea} (%)		0.4			0.3			0.4	
	1/2 $RSD_{Horwitz}$ (%)		9.9			9.5			6.5	
H2	C (μg/mL)	0.511	0.510	0.514	0.646	0.645	0.650	8.060	8.044	8.109
	C_{mean} (μg/mL)		0.5120			0.647			8.071	
	RSD_{mea} (%)		0.4			0.5			0.4	
	1/2 $RSD_{Horwitz}$ (%)		6.3			8.6			5.9	
H3	C (μg/mL)	1.016	1.013	1.020	1.290	1.286	1.296	16.050	15.994	16.114
	C_{mean} (μg/mL)		1.016			1.291			16.053	
	RSD_{mea} (%)		0.4			0.4			0.4	
	1/2 $RSD_{Horwitz}$ (%)		8.0			7.7			5.3	
H4	C (μg/mL)	4.981	4.971	5.008	5.064	5.054	5.089	4.821	4.811	4.844
	C_{mean} (μg/mL)		4.987			5.069			4.825	
	RSD_{mea} (%)		0.4			0.4			0.4	
	1/2 $RSD_{Horwitz}$ (%)		6.3			6.3			6.3	

RSD_{mea}: RSD calculated from standard mixture measurement.

Table 7: Measured concentrations of AML, HYD, and VAL in Exforge HCT tablets employing the developed Kalman-Excel program.

Replicate samples	AML		HYD		VAL	
	C_{AML} (mg/mL)	Mass per tablet (mg)	C_{HYD} (mg/mL)	Mass per tablet (mg)	C_{VAL} (mg/mL)	Mass per tablet (mg)
B1	0.965	9.65	1.168	11.68	16.997	169.97
B2	0.980	9.80	1.186	11.86	17.249	172.49
B3	0.937	9.37	1.134	11.34	16.506	165.06
C_{mean} (mg/mL)	0.961	9.61	1.163	11.630	16.917	169.170
S	0.022	0.22	0.026	0.26	0.378	3.78
RSD %	2.3	2.3	2.2	2.2	2.2	2.2
1/2 $RSD_{Horwitz}$ (%)	8		5.5		5.3	

(1) Method Recovery. Three replicate samples (B1, B2, and B3) were prepared from Exforge HCT tablets. Different spiked levels of AML, HYD, and VAL were added (Table 4). The absorbance spectrum was scanned from 230 to 340 nm wavelength (0.5 nm step), followed by data computing and concentration calculating by the developed Kalman-Excel program. The results of method recovery are shown in Table 8.

The average recoveries of AML, HYD, and VAL were 92.9%, 93.3%, and 101.8%, respectively (Table 8). According to AOAC, for the measured concentration from 1 ppm to 10 ppm, the required recovery should fluctuate from 80% to 110% [1]. Based on this, the developed method performed good trueness for all the analyzed substances, suggesting that the excipients caused almost no effects to the analytical results.

(2) Method Trueness Assessment Based on Comparison with HPLC Analytical Measurement. Exforge HCT tablets were sent to the Drug, Cosmetic and Food Quality control Center of Thua Thien Hue Province for analysis using the HPLC method. AML was analyzed following Vietnam Pharmacopoeia IV guideline, USP 38 was used for VAL and HYD analysis.

Student's t-test [13, 14] was used to compare the analytical results of the two methods. The result of comparing mean values of two methods is shown in Table 9.

Table 9 shows that all the t_{exp} values were smaller than the corresponding t (0.05; f) of the three target compounds, demonstrating that the analytical results obtained from the developed Kalman–Excel method were in agreement with the ones obtained from HPLC measurements.

Table 8: Method recovery for Exforge HCT tablet samples.

Replicate samples	AML			HYD			VAL		
	C_{spike} (μg/mL)	C_{mea} (μg/mL)	REV (%)	C_{spike} (μg/mL)	C_{mea} (μg/mL)	REV (%)	C_{spike} (μg/mL)	C_{mea} (μg/mL)	REV (%)
B1	0	0.965		0	1.168		0	16.997	
	0.25	1.200	94.0	0.30	1.451	94.3	4.0	21.112	102.9
	0.50	1.415	90.0	0.60	1.710	90.3	8.0	24.876	98.5
B2	0	0.980		0	1.186		0	17.249	
	0.25	1.214	93.6	0.30	1.469	94.3	4.0	21.363	102.9
	0.50	1.450	94.0	0.60	1.753	94.5	8.0	25.497	103.1
B3	0	0.937		0	1.134		0	16.506	
	0.25	1.171	93.6	0.30	1.416	94.0	4.0	20.603	102.4
	0.50	1.397	92.0	0.60	1.689	92.5	8.0	24.567	100.8
REV_{mean} (%)		92.9			93.3			101.8	

Table 9: Comparison of AML, HYD, and VAL contents in Exforge HCT tablet measured ($n = 3$) by using the developed method and HPLC method.

	AML		HYD		VAL	
	Kalman	HPLC	Kalman	HPLC	Kalman	HPLC
X_{mean} (mg/tablet, $n = 3$)	9.61	9.51	11.66	11.63	169.17	167.66
S (mg/tablet. $n = 3$)	0.22	0.09	0.26	0.19	3.78	1.24
$F_{exp}/F(0.05; 2; 2)$	5.30/19		1.9/19		9.32/19	
Sp	0.16		0.34		0.10	
$t_{exp}/t(0.05; f)$	0.53/4.3		0.06/4.3		0.71/4.30	
P	0.65		0.96		0.55	

Kalman: the Kalman-Excel program combined with spectrophotometry method; F_{exp}: the experimental variance of the corresponding method; $F(0.05; 2; 2)$: F distribution at alpha 0.05 and the respective degrees of freedom of numerator and denominator; S_p: pooled variance; t_{exp}: experimental t value; $t(0.05; f = 4)$: t value at alpha 0.05 and 4 degrees of freedom.

4. Conclusions

In this work, a new solution has been found for the first time, selecting the approximate initial value of the concentration (by means of the classical least squares) and variance (calculated by using the Horwitz equation) for the Kalman filter algorithm. This new solution allows convenient application of the chemometric-spectrophotometric method using the Kalman filter algorithm (Kalman method) to simultaneously determine two or three substances in their mixture with an UV-Vis absorption spectrophotometer. The Kalman method is less error-prone and has a better repeatability than the least squares method when using the full spectrum.

A computer program that uses the Visual Basic for Applications programming language written on the basis of Microsoft software Excel 2016 based on the Kalman filter algorithm has been written, which allows quick and convenient calculation when applied on practical testing of pharmaceutical products in laboratories.

First, the process of simultaneous analysis of three active ingredients, i.e., amlodipine, hydrochlorothiazide, and valsartan, was established in multicomponent pharmaceutical formulation by the Kalman method using full spectrum without any separation technique. The process exhibited good repeatability and trueness for all the three analyzed compounds with RSD <2.5% ($n = 3$), recovery varied from 93 to 102%, and the received analytical results were identical with ones of HPLC method. The process was not only simple to implement but also reduced the cost of analysis compared to the standard method of high-performance liquid chromatography (HPLC).

Data Availability

The data used to support the finding of this study are available from the corresponding author upon request.

Conflicts of Interest

The authors declare that they have no conflicts of interest.

References

[1] N. Miller James and J. C. Miller, *Statistics and Chemometrics for Analytical Chemistry*, Pearson Education Limited, Harlow, UK, 5th edition, 2005.

[2] T. G. Dobre, G. Jose, and S. Marcano, *Chemical Engineering: Modelling, Simulation and Similitude*, John Wiley and Sons Ltd., Chichester, UK, 2007.

[3] H. N. Hassan, B. N. Barsoum, and I. Habib, "Simultaneous Sepctrophotometric determination of rutin, quercetin and ascorbic acid in drugs using a Kalman Filter approach," *Journal of Pharmaceutical and Biomedical Analysis*, vol. 20, no. 1-2, pp. 315–320, 1999.

[4] L. Shi, Z. Li, Z. Xu, Z. Pan, and L. Wang, "Simultaneous analysis of Co(II), Ni(II), Cu(II), Zn(II) and Cd(II) by

spectrophotometry and the Kalman filter," *Journal of Chemometrics*, vol. 5, no. 3, pp. 193–199, 1991.

[5] S. C. Rutan and S. D. Brown, "Adaptive Kalman Filtering Used to compensate for model errors in multicomponent methods," *Analytica Chimica Acta*, vol. 160, pp. 99–119, 1984.

[6] D. D. Gerow and S. C. Rutan, "Background correction for fluorescence detection in thin-layer chromatography using factor analysis and the adaptive Kalman filter," *Analytical Chemistry*, vol. 60, no. 9, pp. 847–852, 1988.

[7] H. C. Smit, "The use of Kalman filtering and correlation techniques in analytical calibration procedures," *Journal of Research of the National Bureau of Standards*, vol. 90, no. 6, pp. 441–450, 1985.

[8] E. A. Wan and R. Merwe Van der, "The unscented Kalman filter for nonlinear estimation," in *Proceedings of Symposium 2000 on Adaptive Systems for Signal Processing, Communication and Control (AS-SPCC)*, Lake Louise, Alberta, Canada, 2000.

[9] V. R. Galande, K. G. Baheti, S. Indraksha, and M. H. Dehghan, "Estimation of amlodipine besylat, valsartan and hydrochlorothiazide in bulk mixture and tablet by UV spectrophotometry," *Indian Journal of Pharmaceutical Sciences*, vol. 74, no. 1, pp. 18–23, 2012.

[10] AOAC International, *AOAC® Guidelines for Single Laboratory Validation of Chemical Methods for Dietary Supplements and Botanicals*, AOAC International, Gaithersburg, MD, USA, 2012.

[11] R. G. Brereton, *Chemometrics: Data Analysis for the Laboratory and Chemical Plant*, John Wiley & Sons Ltd., Chichester, UK, 2003.

[12] M. Thompson and P. J. Lowthian, "A Horwitz-like function describes precision in a proficiency test," *Analyst*, vol. 120, no. 2, pp. 271-272, 1995.

[13] I. Taverniers, M. De Loose, and E. Van Bockstaele, "Trends in quality in the analytical laboratory. II. Analytical method validation and quality assurance," *TrAC Trends in Analytical Chemistry*, vol. 23, no. 8, pp. 535–552, 2004.

[14] L. C. Brown, *Statistics for Environmental Engineers*, Lewis Publishers, Boca Raton, FL, USA, 2002.

Hindawi
Advances in Materials Science and Engineering
Volume 2019, Article ID 8781013, 8 pages
https://doi.org/10.1155/2019/8781013

Research Article

Study on Preparation of Water-Soluble Chitosan with Varying Molecular Weights and Its Antioxidant Activity

Dang Xuan Du and Bui Xuan Vuong

Faculty of Pedagogy in Natural Sciences, Sai Gon University, 273 An Duong Vuong Street, Ho Chi Minh City 700000, Vietnam

Correspondence should be addressed to Dang Xuan Du; dangxuandu@sgu.edu.vn

Received 2 January 2019; Accepted 13 February 2019; Published 20 March 2019

Guest Editor: Hien Duy Mai

The preparation of water-soluble chitosan (WSC) with various molecular weights by gamma Co-60 irradiation of chitosan solution (5%) in the presence of hydrogen peroxide (1%) combined with acetylated reaction was carried out. The average molecular weight (M_w) of chitosan was measured by gel permeation chromatography (GPC). The chemical structure and the crystallinity of chitosan and WSC were characterized by Fourier-transform infrared (FT-IR) spectroscopy and X-ray diffraction (XRD), respectively. The antioxidant activity of WSC and chitosan was investigated using the free radical 2,2′-azino-bis (3-ethylbenzothiazoline-6-sulphonic acid) ($ABTS^{\bullet+}$). Obtained results showed that chitosan with M_w of 18–90 kDa could be efficiently prepared by this technique in the dose range from 10 to 24.5 kGy. After the acetylated process, the resulting WSC possesses good solubility in a wide pH level of 2–12, and WSC with low molecular weight exhibited significantly higher antioxidant activity than the one with high molecular weight. In detail, the antioxidant activity was 14.7%, 70.5%, 84.2%, 89.4%, and 97.5% for WSC samples prepared from chitosan with M_w of 140.2 kDa, 91.4 kDa, 51.2 kDa, 35.3 kDa, and 18.1 kDa, respectively, at the same reaction time of 90 min. Moreover, the antioxidant activity of WSC was higher than that of chitosan. Thus, WSC prepared by gamma Co-60 irradiation and acetylated process can be potentially applied as a natural antioxidant agent.

1. Introduction

Antioxidant is construed as any substance that inhibits oxidation or reactions promoted by oxygen, peroxides, or free radicals. Nowadays, synthetic antioxidants such as *t*-butylhydroquinone, propyl gallate, butylated hydroxytoluene and butylated hydroxyanisole have been diversely utilized to counteract the deterioration of stored food and preserve cosmetics [1]. However, the application of synthetic antioxidants requites a strict adherence in utilized dose due to its possibly harmful side effects to the human health. Hence, study on extraction and application of antioxidants from natural origin to alternative to synthetic antioxidants was very necessary [2–4].

Chitosan is a natural polymer which has structure of polysaccharide consisting of *N*-glucosamine and *N*-acetyl-glucosamine units linked by β-1,4 glycoside. This polymer has been widely applied in many fields owing to its unique properties such as biocompatibility, biodegradability, non-toxicity, antibacterial, antifungal, and antitumor. Moreover, chitosan also has the ability to stimulate disease resistance and heal the wound quickly [5]. However, a significant drawback of chitosan is it is soluble only in diluted-acid media. This cause restricted applications of chitosan, and therefore, modification of chitosan with the aim of enhancing its solubility has attracted a great deal of research attention [3, 6]. Recently, studies on chitosan modified with resultant products as natural antioxidants were carried out [2, 7–9]. However, these studies have only focused on preparation of low molecular weight chitosan or oligomers due to their easy solubility in water and high antioxidant activity [10]. In addition, the antioxidant activity of high molecular weight chitosan [8] and chitosan derivatives [11] has also been investigated. Generally, the lower the molecular weight of the chitosan, the higher the solubility obtained [9]. This means that, chitosan with low molecular

weight had a merit in applied ability due to soluble potency. However, if molecular weight was too low, like chitosan oligomer, it was also able to be a demerit in case of utilizing as a stabilizer to prepare metal nanoparticles; then, a high molecular weight of polymers had a better stability. Consequently, the preparation of water-soluble chitosan with molecular weight that was higher than chitosan oligomers for adding information and extending application was a necessary study.

The chitosan with varying molecular weight could be prepared from initial chitosan by a variety of techniques. Among them, gamma irradiation and hydrogen peroxide have some merits such as environment-friendly and being suitable for production of high-purity products and industrial manufacturing [12]. Furthermore, the simultaneous combination of gamma irradiation and hydrogen peroxide could efficiently degrade chitosan and reduce required dose owing to synergistic effect [13].

In this study, chitosan with varying molecular weight was prepared by hydrogen peroxide and gamma irradiation of chitosan solution containing hydrogen peroxide. Then, degraded chitosan has been acetylated by acetic anhydride to prepare water-soluble chitosan. The structure and solubility of resultant water-soluble chitosan have been investigated. Moreover, the antioxidant activity of water-soluble chitosan with varying molecular weight has also been evaluated.

2. Materials and Methods

2.1. Materials. Chitosan derived from shrimp shell with a weight average molecular weight (M_w) of 140.1 kDa and degree of deacetylation (DD%) of 91.3% was supplied by a company in Vung Tau province, Vietnam. Hydrogen peroxide (30%) was purchased from Merck, Germany. 2,2′-azino-bis (3-ethylbenzothiazoline-6-sulphonic acid) (ABTS) was supplied by Biobasic, Canada. The other chemicals such as NaOH, NH_4OH (25%), lactic acid, and ethyl alcohol were of reagent grade.

2.2. Preparation of Chitosan with Varying Molecular Weights. In this study, the degradation of chitosan was carried out in two steps. In the first step, initial chitosan (CTS_0) was degraded in the swollen state by using 1% hydrogen peroxide with the ratio of chitosan/H_2O_2 of 1/10 (w/v) for 24 h. The obtained product (CTS_1) was washed by distilled water and then dried naturally. In the second step, CTS_1 was dissolved in 3% lactic acid and stirred for 2 h. An amount of hydrogen peroxide was added in the mixture to create solution with concentration of chitosan, lactic acid, and H_2O_2 to be 5%, 2.5%, and 1% (w/v), respectively. Finally, this resulting mixture was irradiated by gamma SVST Co-60/B source with a dose rate of 1.33 kGy/h in the range of dose up to 24.5 kGy. The obtained chitosan at the different doses of this irradiated process, CTS_2 (3.5 kGy), CTS_3 (10.5 kGy), and CTS_4 (24.5 kGy), has been filtered by a stainless steel mesh and neutralized by 5% NH_4OH (v/v). Ethyl alcohol was added in solution during stirring to precipitate chitosan. This precipitant was filtered and washed several times with alcohol and then dried in a force air oven at 60°C. The samples of dried chitosan were ground into powder for GPC measurement and preparation of water-soluble chitosan.

2.3. Preparation of Water-Soluble Chitosan. The chitosan samples from CTS_0 to CTS_4 were dissolved in lactic acid to create 150 mL solution with chitosan concentration of 5%. 40.5 mL ethyl alcohol and 4.5 mL anhydride acetic were added in solution. Then, the solution was stirred for 2 h and kept at ambient temperature overnight for acetylated process. The solutions after reaction were filtered, precipitated, washed, and dried. The dried chitosan samples were also ground into powder for FT-IR, XRD measurements, and antioxidant activity investigations.

2.4. Characterization. The M_w of chitosan samples was determined by using a GPC (LC-20AB Shimadzu, Japan) using an ultra-hydrogel column model 250 of Waters (USA) and detector RI-10A. The calibration of column was carried out by using pullulan with M_w of 780–3,80,000 Da. The mobile phase was buffer solution 0.25 M CH_3COOH/0.25 M CH_3COONa with a flow rate of 1 mL/min [14] and temperature at 30°C. The concentration of chitosan sample was ca. 0.1% (w/v).

IR spectra were taken on an FT-IR 8400S spectrometer (Shimadzu, Japan) using KBr pellets. The DD% was calculated based on FT-IR spectra according to the following equation [15]:

$$\mathrm{DD\%} = 100 - \left[\frac{\left((A_{1320}/A_{1420}) - 0.3822\right)}{0.03133}\right], \quad (1)$$

where A_{1320} and A_{1420} are the absorbances of chitosan at 1320 and 1420 cm^{-1}, respectively.

X-ray diffraction (XRD) measurements of WSC were carried out on an X'Pert Pro X-ray diffractometer (PANalytical, Netherlands) and used a CuK_α target at 45 kV-40 mA with a scattering range (2θ) of 5°–40°.

The water solubility of WSC was estimated based on the solution transmittance at 600 nm that was recorded on a UV-vis spectrophotometer (V630, Jassco, Japan) against 0.5% WSC solution (w/v) using a quartz cell with an optimal path length of 1 cm [16].

2.5. Antioxidant Assay. Antioxidant assay was carried out by dissolving 2,2-azino-bis (3-ethylbenzothiazoline-6-sunphonic acid) (ATBS) in water to create the solution with a concentration of 7.4 mM. Next, 2 mL ATBS solution was mixed with 2 mL $K_2S_2O_8$ with a concentration of 2.6 mM to obtain the free radical cation $ATBS^{\bullet+}$. This $ATBS^{\bullet+}$ solution was kept in the dark for 24 h. Then, the $ATBS^{\bullet+}$ solution was diluted by water to receive an optical density (OD) of 1 ± 0.1 at a wavelength of 734 nm, after which the solution was also diluted with water for the control. For investigating antioxidant activity, the WSC samples with concentration of 0.2% were mixed with 0.1% acetic acid [9]. About 0.6 mL of solution sample was added into the cuvette that contained 1 mL of $ABTS^{\bullet+}$ solution.

Added otherwise by 0.6 mL distilled water into a cuvette that contained 1 mL $ABTS^{\bullet+}$ solution, we could receive a control sample. The OD of the samples was measured over time by using a UV-vis spectrophotometer at a max absorbance wavelength of 734 nm [17]. The efficiency of free radical scavenging was calculated by the following equation:

$$\text{Efficiency}(\%) = 100 \times \left(\frac{OD_{AC} - OD_{AS}}{OD_{AC}}\right), \quad (2)$$

where OD_{AC} is the OD of the control sample ($ABTS^{\bullet+}$ and water without WSC) and OD_{AS} is the OD of the solution containing $ABTS^{\bullet+}$ and WSC [17, 18].

2.6. Determination of Reducing Power. In order to clarify the rule of antioxidant activity in another way, the reducing power of WSC was also determined based on the ferricyanide method [19]. The WSC sample was diluted to create solution with 0.3% concentration (w/v). 1 mL of this solution was added to 2.5 mL of phosphate buffer (200 mM, pH = 6.6) and then 2.5 mL of potassium ferricyanide. This mixture was incubated for 20 min at 50°C in a water bath. Next, 2.5 mL of 10% trichloroacetic acid was added and then centrifuged at 3000 rpm for 10 min. 5 mL of upper layer solution was mixed with 1.0 mL of 0.1% ferric chloride and water. The obtained solution was measured for absorbance at 700 nm. The higher the absorbance, the stronger the reducing power obtained.

3. Results and Discussion

3.1. Preparation of Chitosan of Different Molecular Weights. According to the previous studies, the degradation of chitosan in the heterogeneous state in the presence of hydrogen peroxide solution is quite efficient [9, 20]. However, if the concentration of hydrogen peroxide was at the high level, the main chain structure of chitosan may be changed [20]. The way around this situation is the choice of 1% H_2O_2 [9, 13]. In addition, the degradation of chitosan in the heterogeneous state was almost supposed that it occurred in the amorphous region, and as a result, the reduction of molar mass of chitosan is only reached to a certain extent. Reasoning further along this line, the degradation of chitosan at crystal regions regularly occurs in the homogeneous state, i.e., in solution. For this study, the degradation of chitosan in the heterogeneous state and homogeneous state was performed in two steps in turn.

As shown in Table 1, the degradation of chitosan by 1% hydrogen peroxide is fairly efficient. Moreover, the DD of chitosan was almost unchanged. According to Qin et al. [20], the structure of the degraded chitosan with a M_w less than 50 kDa that was obtained by the high concentration of hydrogen peroxide as well as the long degradation time had been remarkably changed. Hence, the H_2O_2 concentration of 1% was chosen to prevent the change of the structure of chitosan. Moreover, the obtained chitosan with a molecular weight of 91 kDa was suitable for preparation of WSC with varying molecular weight. Since M_w was lower than 10 kDa, chitosan was in the form of an oligomer that may be soluble in water [9]; then, the acetylation of chitosan for its improvement of solubility was unnecessary.

Table 1: Degradation of chitosan in the swollen state (first step) and in solution (second step).

		First step (1% H_2O_2)	Second step (1% H_2O_2 and γ-ray)		
	CTS_0	CTS_1	3.5 kGy CTS_2	10.5 kGy CTS_3	24.5 kGy CTS_4
M_w (kDa)	140.1	91.7	51.7	35.1	18.6
DD (%)	91.1	91.3	90.3	91.0	89.5

The further degradation of chitosan was carried out in solution by combination of H_2O_2 and gamma irradiation. The results showed that M_w of obtained chitosan at the different doses of 3.5 kGy, 10.5 kGy, and 24.5 kGy were 51.7 kDa, 35.1 kDa, and 18.6 kDa, respectively. Meanwhile, the DD of resulting chitosan samples was hardly different. This outcome indicated that at only 1% concentration of H_2O_2 combined with gamma ray, the reduction of molar mass is very efficient even when the applied dose is quite low, less than 25 kGy. Nguyen et al. [9] and Nguyen et al. [13] degraded chitosan by simultaneously combining H_2O_2 and gamma ray; as a result, they obtained chitosan oligomers at the low dose, about 12 kGy with 1% concentration of H_2O_2 used. Although these reductions were further than those in our study, the degree of M_w degradation (%) is almost the same owing to the fact that initial chitosan in those studies has different molecular weights as well as origin (i.e., crab shell in their studies and shrimp shell in this study). However, the degree of M_w reduction (%) in their studies and in this study is almost the same owing to the fact that initial chitosan in those studies was different in molecular weight as well as origin (from crab shell in their studies and shrimp shell in this study). The phenomenon of the increase in degraded efficiency with the presence of H_2O_2 was suggested through synergistic effect [13]. Accordingly, the hydroxyl radicals formed through the radiolysis of water and H_2O_2 are mainly responsible for degradation of chitosan:

$$\begin{aligned} H_2O &\xrightarrow{h\nu} H_2, H_2O_2, e_{aq}^{-}, H^{\bullet}, {}^{\bullet}OH, H_3O^{+} \\ H_2O_2 &\xrightarrow{h\nu} 2\,{}^{\bullet}OH \end{aligned} \quad (3)$$

Additionally formation of hydroxyl radicals, e_{aq}^{-} and $H^{\bullet}$ can react with H_2O_2 during irradiation:

$$\begin{aligned} H^{\bullet} + H_2O_2 &\xrightarrow{h\nu} H_2O + {}^{\bullet}OH \\ e_{aq}^{-} + H_2O_2 &\xrightarrow{h\nu} OH^{-} + {}^{\bullet}OH \end{aligned} \quad (4)$$

Hydroxyl radicals plays a significant role as a powerful oxidative agent, reacting with chitosan chain by abstraction of hydrogen atoms linked with carbon to form carbohydrate radicals (Figure 1) that can then cause the direct breakage of the glycosidic linkage by rearrangement [21]. The obtained chitosan samples with varying molecular weight and DD of ~90% then were utilized for preparation of WSC through *N*-acetylation process.

3.2. Preparation of Water-Soluble Chitosan. The chitosan samples with different molar masses CTS_0, CTS_1, CTS_2, CTS_3, and CTS_4 were *N*-acetylated by acetic anhydride to

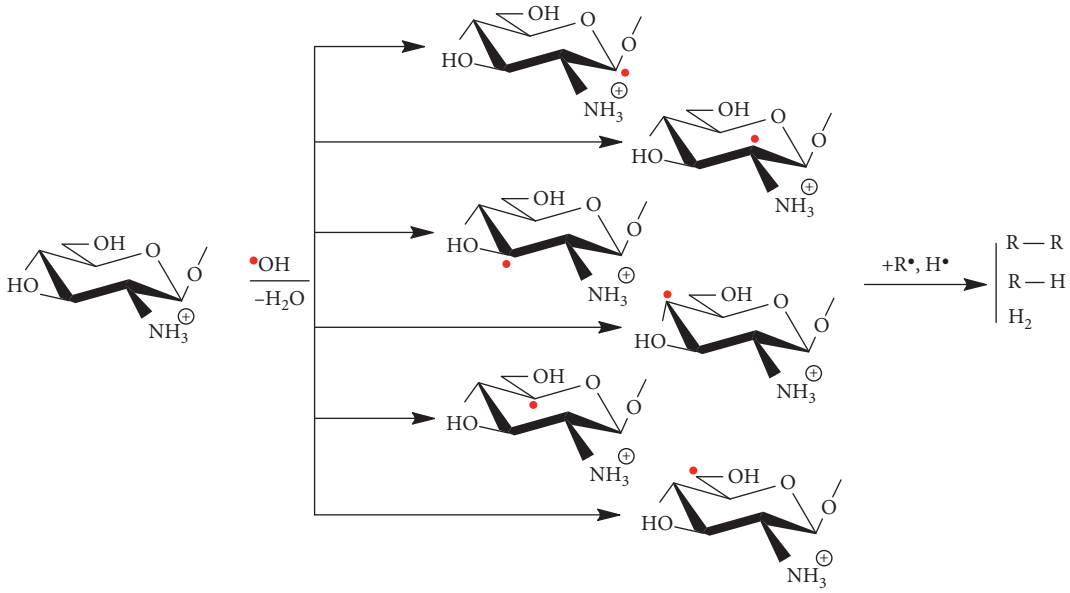

Figure 1: The mechanism of abstraction of hydrogen by hydroxyl radical [21] in the degradation of chitosan.

create WSC samples denoted by WSC_0, WSC_1, WSC_2, WSC_3, and WSC_4, respectively. Unlike chitosan insoluble in water before reaction, all WSC samples shown in Figure 2 had good solubility in water despite different soluble time periods (Table 2). The transmittance (T) of all WSC samples was more than 98%. This means that water solubility of CTS was remarkably improved by virtue of *N*-acetylated process. Furthermore, these WSC samples also were soluble in the slightly alkaline media (pH of 7–12) regardless of its different molecular weights (data not showed). According to the results previously published by Lu et al. [6], the impact of molecular weight of WSC on solubility in water and in alkali media was ineffective and effective, respectively. In terms of the solubility in water, we have the similar result. For the alkaline media, the higher molecular weight of WSC has the lower solubility obtained [6]. However, all WSC samples in our study were soluble in weakly alkaline media. It may be due to the fact that the range of molecular weight in our study is far lower compared to that of their study. The WSC samples with $M_w > 180$ kDa in their study were slightly soluble in pH > 9 media. In our study, all WSC samples were prepared from chitosan with M_w less than 140 kDa, and therefore, they accounted for good solubility in dilute alkaline media. Feng et al. [3] also studied solubility of *N*-acetylated chitosan with DD~50%, prepared by acetylation of chitosan degraded by cellulase enzyme. They reported that the only *N*-acetylated chitosan with low M_w (<18 kDa) has a high solubility and retained over a wide pH range. The solubility of the others ($M_w > 18$ kDa) in the alkaline decreased with increasing M_w. Unlike the results of Feng et al., WSC prepared in our study has a high solubility in over a wide pH range despite the M_W from 18 to 140 kDa. Apart from the molecular weight, the solubility of chitosan depends on the other factors such as intermolecular interactions (van der Walls forces), intermolecular interaction forces, the degree of acetylation, and initial soluble media [2, 3].

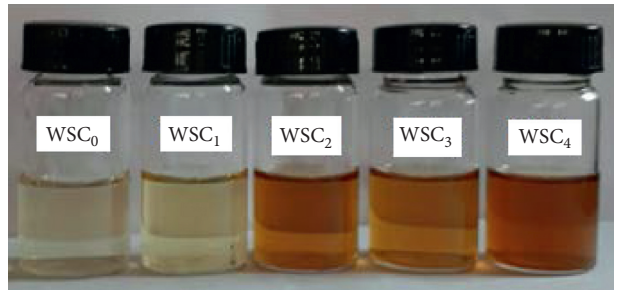

Figure 2: WSC samples dissolved in water at 25°C with the concentration 0.5% (w/v).

Table 2: DD and soluble time of WSC samples and CTS_4.

Samples	DD (%)	Soluble time at 25°C (h)	T (%)
WSC_0	56.3	2.5	99.93
WSC_1	57.7	2.0	99.95
WSC_2	52.3	2.0	99.97
WSC_3	49.2	1.5	99.98
WSC_4	48.7	1.5	99.98

The FT-IR spectra of the WSC samples as well as CTS_0 (initial chitosan) and CTS_1 (degraded by only H_2O_2) are shown in Figure 3. The broad band around 3427 cm^{-1} is assigned to O–H and N–H bond stretching. The band at 1159–895 cm^{-1} is assigned to the special absorption peaks of β (1–4) glycoside bond, which is characteristic of polysaccharide structure of chitosan [22]. The peaks at 1072 and 1028 cm^{-1} are assigned to stretching vibration of C–O and stretching of the C–O–C in the glucopyranose ring, respectively. Peaks at 1320 and 1420 cm^{-1} are assigned to the absorbance of C–N of CH_3CONH (amid III) and symmetrical deformation of CH_2 as well as CH_3. The peaks at 1650 cm^{-1} and 1597 cm^{-1} are, respectively, concerned to stretching vibration of amide I and amide II groups [3]. The

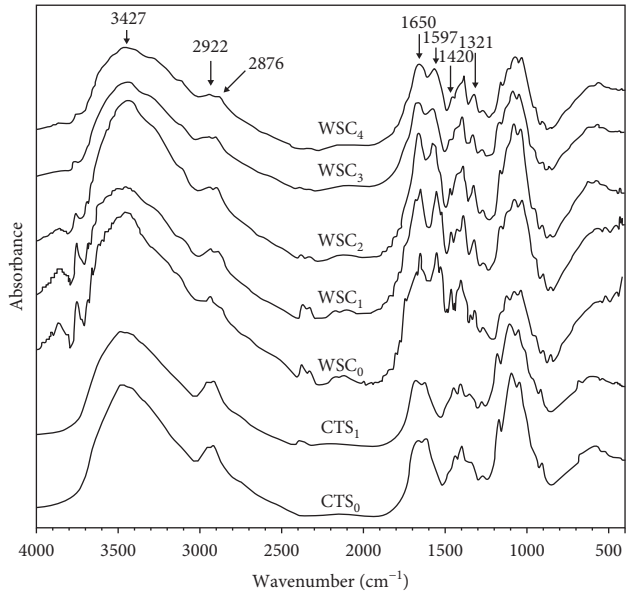

Figure 3: FT-IR spectra of the initial chitosan (CTS_0), only H_2O_2-degraded chitosan (CTS_1), and WSC samples prepared from CTS_0 (WSC_0), CTS_1 (WSC_1), and degraded chitosan at doses of 3.5 kGy (WSC_2), 10.5 kGy (WSC_3), and 24.5 kGy (WSC_4).

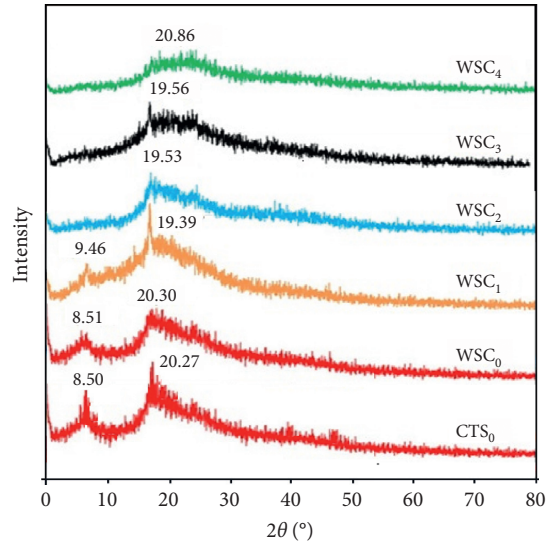

Figure 4: XRD patterns of CTS_0 and the WSC samples.

C–H stretching of methyl and methane were assigned at 2922 and 2876, respectively. In terms of mainly chemical structure, CTS_1 is hardly different from CTS_0. This accounts for unchanged DD (Table 1). Compared to initial chitosan (CTS_0) and CTS_1, the principle functional groups of WSC were still present after *N*-acetylation. This implied that the main polysaccharide chain structure remained after degradation and *N*-acetylation. However, there is change of absorbance at some bands. Especially, the peaks at 1650 and 1597 cm^{-1} owing to $-CONH_2$ stretching vibration were significantly enhanced. This revealed that the acetylated reaction mainly occurred at the amino group of chitosan [15]. On the contrary, the absorbance at 2922 and 2876 cm^{-1} due to C–H stretching of methyl and methane were quite weakened. It indicated that *N*-acetylation reaction impacts on inter-macromolecular hydrogen bonds and interchain hydrogen bonds. This is due to of water solubility by virtue of reduced crystallinity of chitosan [6].

The X-ray diffraction (XRD) patterns of WSC and initial chitosan (CTS_0) are shown in Figure 4. In the XRD pattern of CTS_0, a broad peak of 2θ around 20° and another peak around 9° were assigned to the diffraction of the plane of the crystal region in the chitosan structure. This pattern refers to as the L-2 polymorph of chitosan [9, 23]. As can be seen in Figure 4, the diffraction intensity of peaks in WSC patterns is weaker than that of in CTS_0—even disappearance at 2θ around 9°. These results showed that *N*-acetylation and degradation caused the destruction of the crystallinity of chitosan. Consequently, the lower degree of crystallinity of WSC obtained from these processes induced the higher solubility attained in aqueous media. This is similar to the previous reports [6, 13]. For the WSC_1, the higher intensity can be observed at 2θ around 20° compared to WSC_0 and CTS_0. This result may be due to the fact that the first step of degradation by only H_2O_2 mainly occurs at the amorphous region. Accordingly, the obtained chitosan has relatively higher crystallinity similar to the outcome previously reported by Qin et al. [20].

3.3. Antioxidative Activity Assay. Free radicals containing reactive oxygen species are unstable agents. They react readily with other groups or substances in body, causing cell damage. Thus, one of the most effective defense mechanisms of the body against diseases is removal of free radicals by using antioxidants. In this study, the antioxidant activity of WSC was investigated by free-radical scavenging of $ABTS^{\bullet+}$. As can be seen in Figure 5, initial ABTS solution was transparent, whereas the color of $ABTS^{\bullet+}$ solution was dark green (Figure 5(a)). The color of $ABTS^{\bullet+}$ in aqueous solution was green. When $ABTS^{\bullet+}$ solution was added into WSC solution, a variation in color occurred. The color of $ABTS^{\bullet+}$ solution in the presence of WSC was decreased. Moreover, the $ABTS^{\bullet+}$ samples in WSC_3 and WSC_4 were almost colorless (Figure 5(b)). It proved that WSC scavenged $ABTS^{\bullet+}$. As a result, the green color of $ABTS^{\bullet+}$ solution in the presence of WSC was weaker than that of $ABTS^{\bullet+}$ without WSC. The higher the molecular weight of WSC was, the lower the free-radical scavenging activity attained. The efficiency of antioxidant activity is one of the parameters using to evaluate free-radical scavenging activity of WSC. In this study, the efficiency of antioxidant activity was calculated by equation (2) [9]. It was obvious that the efficiency of antioxidant activity of WSC samples increased in a time-dependent manner, and this parameter also increased versus the decrease of molecular weight (Figure 6). In particular, the WSC_4 sample with the lowest molecular weight exhibited the highest efficiency of antioxidant activity, attained 92% after only 10 min and 98% after 90 min (Figure 6). Besides, the efficiency of antioxidant activity of the WSC_0 sample was entirely lower than that of CTS_4 sample and the others. The reason may be due to the

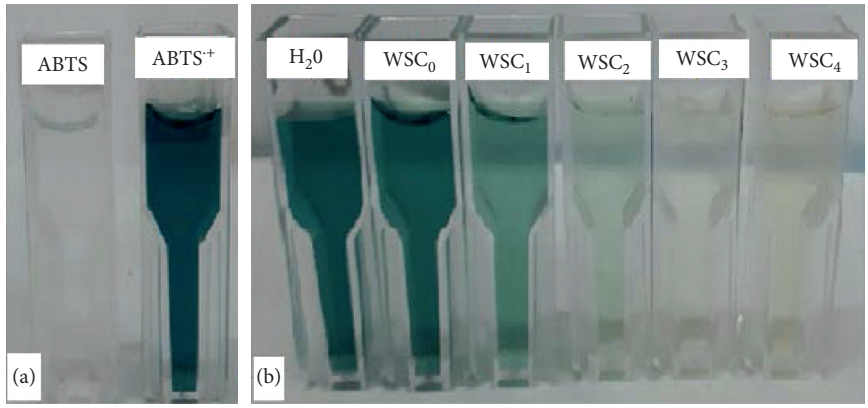

Figure 5: ABTS and $ABTS^{\bullet+}$ solution (a) and $ABTS^{\bullet+}$ with the presence of WSC and H_2O (b).

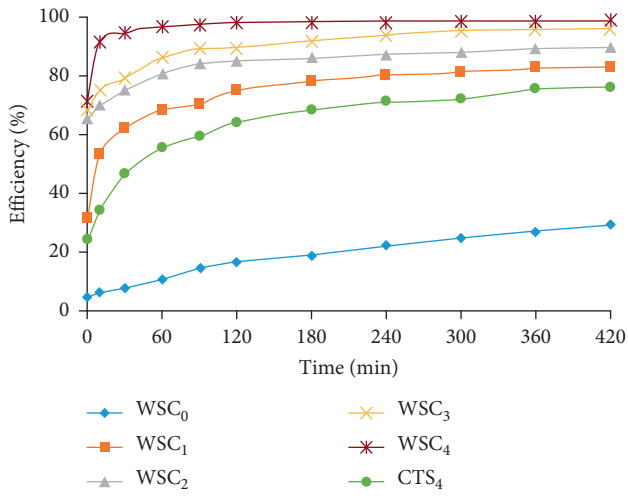

Figure 6: Efficiency of antioxidant activity of WSC and CTS_4 with reaction time.

significant difference of M_w. Feng et al. [3] also reported that the antioxidant activity of WSC with M_w of 281.0 and 1.8 kDa was significantly different. The WSC with M_w of 281 kDa has a relatively low antioxidant activity. Whereas, the other with M_w of 1.8 kD had a quite high antioxidant activity approximated with α-tocopherol [3]. The antioxidant activity of a compound was also suggested in various mechanisms such as prevention of chain initiation, decomposition of peroxides, biding of transition metal ion catalysts, radical scavenging, and reductive capacity [3].

Nguyen et al. [9] reported the preparation of water-soluble oligochitosan and its antioxidant activity. Results showed that water-soluble oligochitosan mainly prepared by degradation of chitosan using hydrogen peroxide and gamma irradiation at low dose <25 kGy. The obtained oligochitosan with M_w of 35.29 kDa, 7.03 kDa, and 4.07 kDa had the scavenge percentage against $ATBS^{\bullet+}$ radical in 90 min of 69.6%, 84.5%, and 99.2%, respectively. In terms of the rule of efficiency of antioxidant activity versus molecular weight of chitosan, their study was consistent with our study. However, the difference is that the M_w of oligochitosan in their study was lower compared to that in our study despite the same efficiency of antioxidant activity (more than 90%) and good solubility. Chitosan with low molecular weight such as oligochitosan (M_w less than 10 kDa) in studies reported by Je et al. [2], Feng et al. [3], and Nguyen et al. [9] generally had a good antioxidant activity. However, its antimicrobial property was less than that of chitosan with medium molecular weight (M_w~10–100 kDa). In addition, in the case of chitosan using as a stabilizer for synthesis of metal nanoparticles, a high M_w has a better stability. In our study, WSC with a molecular weight of 18–90 kDa has good solubility in water so that it has suitably potential to be used as a stabilizer or an antioxidant substance. The other point is the difference of the method for preparation of water-soluble chitosan. In our method, apart from degradation by hydrogen peroxide and gamma Co-60 irradiation like the method in Nguyen et al. [9], chitosan also was acetylated to increase solubility and M_w was kept constant at medium molecular weight. Therefore, in terms of this approach, the obtained chitosan has good solubility and high antioxidant activity at the relatively higher molecular weight.

In terms of reason for antioxidant activity, many authors mentioned in their studies [3, 9, 24] that the hydroxyl and amino groups in chitosan molecules play important roles in free-radical scavenging activity. According to these authors, the more activated the hydroxyl and amino group are, the more the antioxidant activity. The hydroxyl and amino group could be activated in case intramolecular hydrogen bond and van der Waals forces reduced sharply. In our study, acetylated process destroyed crystallinity of chitosan as mentioned above. This may significantly decline intramolecular hydrogen bond. As a result, hydroxyl and amino groups could be more mobile. They facilitate effective reactions with $ABTS^{\bullet+}$ radical [11]. In addition, the residual hydroxyl groups in polysaccharides can react with radicals via a H abstraction. In a similar way, the residual free amino groups can absorb a hydrogen ion to form ammonium groups, which in turn react with radicals through an addition reaction [25].

The reducing capacity of a substance may be construed as a significant indicator of its potential antioxidant activity [26]. The substances with good reducing capacity are

Table 3: OD of solution determined by reducing power of WSC samples and CTS_4.

Samples	WSC_0	WSC_1	WSC_2	WSC_3	WSC_4	CTS_4
OD	0.03	0.20	0.36	0.44	0.47	0.12

electron donors. They can easily react with free radicals to convert them to more stable states and terminate radical chain reactions [2]. As shown in Table 3, the reducing power of WSC samples increased with the decrease of M_w. It is obvious that reducing power of CST_4 and WSC samples was in good agreement with the efficiency of antioxidant activity. The stronger the reducing power of WSC, the higher the efficiency of antioxidant activity attained. Besides, reducing power of CTS_4 was also more than WSC_0 but less than the others. It implicated that WSC has generally given a higher reducing power than chitosan. However, in this case, CTS_4 having a higher reducing power than WSC_0 may be due to the limit of M_w [8, 10, 27]. In WSC_0 with the higher M_w, the structure chain was twisted making a mobile degree of amino and hydroxyl groups with decreasing vigour. It could be accounted for a negligible reducing power of WSC_0. Rao et al. [26] studied irradiation of chitosan-glucose mixture and antioxidant activity of the resultant Maillard products. They reported that the mixture irradiated at high dose had a high reducing power. They also suggested that the intermediate reduction compounds of Maillard reaction products broke the radical chain by donation of a hydrogen atom [26].

4. Conclusions

Water-soluble chitosan (WSC) with M_w in the range of 18–140 kDa was successfully prepared by combination of degradation and acetylation in which the gamma Co-60 irradiation and hydrogen peroxide were used to adjust the molecular weight. The solubility and antioxidant activity of the obtained WSC were significantly enhanced. All WSC samples showed good solubility in water with the transmittance more than 98%. The WSC_4 sample exhibited the highest efficiency of antioxidant activity, attained 92% after only 10 min and 98% after 90 min. Owing to the water solubility and high efficiency of antioxidant activity, WSC can be potentially used for various purposes of applications, especially as an effective antioxidant or a stabilizer in synthesizing metal nanoparticles.

Data Availability

The data used to support the findings of this study are included within the article.

Conflicts of Interest

The authors declare that they have no conflicts of interest.

Acknowledgments

The authors would like to thank Professor Q. H. Nguyen (VINAGAMMA Center, Vietnam) for reading this manuscript.

References

[1] A. Wanita and K. Lorenz, "Antioxidant potential of 5-*n*-pentadecylresorsinol," *Journal of Food Processing and Preservation*, vol. 20, no. 5, pp. 417–429, 1996.

[2] J.-Y. Je, P.-J. Park, and S.-K. Kim, "Radical scavenging activity of hetero-chitooligosaccharides," *European Food Research and Technology*, vol. 219, no. 1, pp. 60–65, 2004.

[3] T. Feng, Y. Du, J. Li, Y. Wei, and P. Yao, "Antioxidant activity of half *N*-acetylated water-soluble chitosan in vitro," *European Food Research and Technology*, vol. 225, no. 1, pp. 133–138, 2007.

[4] C. Schyvens, "Food additives: antioxidant," *Encyclopedia of Food Safety*, vol. 2, pp. 455–458, 2014.

[5] T. Dai, M. Tanaka, Y.-Y. Huang, and M. R. Hamblin, "Chitosan preparations for wounds and burns: antimicrobial and wound-healing effects," *Expert Review of Anti-infective Therapy*, vol. 9, no. 7, pp. 857–879, 2011.

[6] S. Lu, X. Song, D. Cao, Y. Chen, and K. Yao, "Preparation of water-soluble chitosan," *Journal of Applied Polymer Science*, vol. 91, no. 6, pp. 3497–3503, 2004.

[7] P.-J. Chien, F. Sheu, W.-T. Huang, and M.-S. Su, "Effect of molecular weight of chitosans on their antioxidative activities in apple juice," *Food Chemistry*, vol. 102, no. 4, pp. 1192–1198, 2007.

[8] A. Wan, Q. Xu, Y. Sun, and H. Li, "Antioxidant activity of high molecular weight chitosan and N,O-quaternized chitosans," *Journal of Agricultural and Food Chemistry*, vol. 61, no. 28, pp. 6921–6928, 2013.

[9] N. T. Nguyen, D. Q. Hoang, N. D. Nguyen, Q. H. Nguyen, and D. H. Nguyen, "Preparation, characterization, and antioxidant activity of water-soluble oligochitosan," *Green Processing and Synthesis*, vol. 6, no. 5, pp. 461–468, 2017.

[10] T. Laokuldilok, T. Potivas, N. Kanha et al., "Physicochemical, antioxidant, and antimicrobial properties of chitooligosaccharides produced using three different enzyme treatments," *Food Bioscience*, vol. 18, pp. 28–33, 2017.

[11] H.-Y. Lin and C.-C. Chou, "Antioxidative activities of water-soluble disaccharide chitosan derivatives," *Food Research International*, vol. 37, no. 9, pp. 883–889, 2004.

[12] N. D. Nguyen, V. P. Dang, T. A. Nguyen, and Q. H. Nguyen, "Synergistic degradation to prepare oligochitosan by γ-irradiation of chitosan solution in the presence of hydrogen peroxide," *Radiation Physics and Chemistry*, vol. 80, no. 7, pp. 848–853, 2011.

[13] Q. H. Nguyen, V. P. Dang, N. D. Nguyen, and T. K. L. Nguyen, "Degradation of chitosan in solution by gamma irradiation in the presence of hydrogen peroxide," *Carbohydrate Polymers*, vol. 87, no. 1, pp. 935–938, 2012.

[14] J. Z. Knaul, M. R. Kasaai, V. T. Bui, and K. A. Creber, "Characterization of deacetylated chitosan and chitosan molecular weight review," *Canadian Journal of Chemistry*, vol. 76, no. 11, pp. 1699–1706, 1998.

[15] J. Brugnerotto, J. Lizardi, F. M. Goycoolea, W. Argüelles-Monal, J. Desbrières, and M. Rinaudo, "An infrared investigation in relation with chitin and chitosan characterization," *Polymer*, vol. 42, no. 8, pp. 3569–3580, 2001.

[16] M. Fan, Q. Hu, and K. Shen, "Preparation and structure of chitosan soluble in wide pH range," *Carbohydrate Polymers*, vol. 78, no. 1, pp. 66–71, 2009.

[17] R. Re, N. Pellegrini, A. Proteggente, A. Pannala, M. Yang, and C. Rice-Evans, "Antioxidant activity applying an improved ABTS radical cation decolorization assay," *Free Radical Biology and Medicine*, vol. 26, no. 9-10, pp. 1231–1237, 1999.

[18] K. Thaipong, U. Boonprakob, K. Crosby, L. Cisneros-Zevallos, and D. Hawkins Byrne, "Comparison of ABTS, DPPH, FRAP, and ORAC assays for estimating antioxidant activity from guava fruit extracts," *Journal of Food Composition and Analysis*, vol. 19, no. 6-7, pp. 669–675, 2006.

[19] G.-C. Yen and P.-D. Duh, "Antioxidative properties of methanolic extracts from peanut hulls," *Journal of the American Oil Chemists' Society*, vol. 70, no. 4, pp. 383–386, 1993.

[20] C. Q. Qin, Y. M. Du, and L. Xiao, "Effect of hydrogen peroxide treatment on the molecular weight and structure of chitosan," *Polymer Degradation and Stability*, vol. 76, no. 2, pp. 211–218, 2002.

[21] P. Ulanski and C. von Sonntag, "OH-Radical-induced chain scission of chitosan in the absence and presence of dioxygen," *Journal of the Chemical Society, Perkin Transactions*, vol. 2, no. 10, pp. 2022–2028, 2000.

[22] L. Wei, Q. Li, W. Tan, F. Dong, F. Luan, and Z. Guo, "Synthesis, characterization, and the antioxidant activity of double quaternized chitosan derivatives," *Molecules*, vol. 22, no. 3, p. 501, 2017.

[23] C. H. Hsu, S. K. Chen, W. Y. Chen, M. L. Tsai, and R. H. Chen, "Effect of the characters of chitosans used regeneration conditions on the yield and physicochemical characteristics of regenerated products," *International Journal of Molecular Sciences*, vol. 16, no. 12, pp. 8621–8634, 2015.

[24] Y. Yang, R. Shu, J. Shao, G. Xu, and X. Gu, "Radical scavenging activity of chitooligosaccharide with different molecular weights," *European Food Research and Technology*, vol. 222, no. 1-2, pp. 36–40, 2006.

[25] W. Xie, P. Xu, and Q. Liu, "Antioxidant activity of water-soluble chitosan derivatives," *Bioorganic & Medicinal Chemistry Letters*, vol. 11, no. 13, pp. 1699–1701, 2001.

[26] M. S. Rao, S. P. Chawla, R. Chander, and A. Sharma, "Antioxidant potential of Maillard reaction products formed by irradiation of chitosan-glucose solution," *Carbohydrate Polymers*, vol. 83, no. 2, pp. 714–719, 2011.

[27] K. W. Kim and R. L. Thomas, "Antioxidative activity of chitosans with varying molecular weights," *Food Chemistry*, vol. 101, no. 1, pp. 308–313, 2007.

Hindawi
Advances in Materials Science and Engineering
Volume 2019, Article ID 8573451, 15 pages
https://doi.org/10.1155/2019/8573451

Research Article

Aminopropyl Functionalised MCM-41: Synthesis and Application for Adsorption of Pb(II) and Cd(II)

Pham Dinh Du,[1] **Nguyen Trung Hieu**,[2] **Thuy Chau To**,[1] **Long Giang Bach**,[3] **Mai Xuan Tinh**,[4] **Tran Xuan Mau**,[4] **and Dinh Quang Khieu**[4]

[1]*Faculty of Natural Science, Thu Dau Mot University, Thu Dau Mot 590000, Vietnam*
[2]*Center for Scientific Research and Practice, Thu Dau Mot University, Thu Dau Mot 590000, Vietnam*
[3]*NTT Institute of High Technology, Nguyen Tat Thanh University, Ho Chi Minh City 700000, Vietnam*
[4]*University of Sciences, Hue University, Hue 530000, Vietnam*

Correspondence should be addressed to Dinh Quang Khieu; dqkhieu@hueuni.edu.vn

Received 21 November 2018; Accepted 4 February 2019; Published 19 February 2019

Academic Editor: Peter Majewski

This paper shows a comparison of porous properties of aminopropyl-MCM-41 materials functionalised via the direct and indirect methods. The obtained materials were characterised using X-ray powder diffraction (XRD), transmission electron microscopy (TEM), thermogravimetric analysis-differential scanning calorimeter (TGA-DSC), adsorption/desorption isotherms of nitrogen, and Fourier-transfer infrared (FT-IR) spectroscopy. The results showed that the direct method provided the aminopropyl-MCM-41 material with well-ordered pores and high surface areas but with a lower quantity of grafted 3-aminopropyltriethoxysilane than the indirect method. To remove the organic template in the indirect method, solvent extraction with HCl/C_2H_5OH and calcination at 500°C were used, and the former gave a higher quantity of grafted 3-aminopropyltriethoxysilane in the resulting aminopropyl-MCM-41 materials. The experimental data were applied to the isotherm models of adsorption including Langmuir, Freundlich, Redlich–Peterson, and Sips either in the linear or nonlinear form. In order to avoid the bias of the determination coefficient and the error function method, the paired-samples *t*-test as an alternative method was first proposed to look for the most appropriate adsorption isotherms. The maximum adsorption capacity of Cd(II) and Pb(II) was 14.08 $mg \cdot g^{-1}$ and 64.21 $mg \cdot g^{-1}$, respectively. The mechanism of complexation and isoelectric interaction was suggested to explain the adsorption of Pb(II) and Cd(II) from aqueous solutions on aminopropyl functionalised MCM-41 in the range of pH from 2 to 9.

1. Introduction

Lead and cadmium are potentially toxic metals released to the environment because of its wide use in many industrial applications such as metallurgy, storage battery, printing, pigments, electronics, photographic materials, and petroleum refining industry [1]. Aquatic wastewater polluted with lead and cadmium has endangered the environment and human health. The adverse effects of their toxicity include impaired blood synthesis, hypertension, severe stomach ache, brain functions and kidney damage [2], and serious osteoporosis-like bone disease [3]. A great deal of interest in the research of removing potentially toxic metals such as lead, cadmium, nickel, and mercury from industrial effluents has focused on using the adsorption approach among different other conventional removal methods [4–6]. The adsorbents have widely used to be natural and synthesised materials with large porosity and high adsorptive site density and surface area. Among porous materials, MCM-41 (Mobil Composition of Matter No. 41) is a mesoporous material with a hierarchical structure from a family of silicate that was first developed by researchers at Mobil Oil Corporation [7], and MCM-41 has received great interest because it possesses a highly ordered hexagonal structure and large specific surface area [8, 9]. Recently, the preparation of organic-inorganic hybrid silicon materials has drawn many

researchers' attention [10–12]. Surface modification by organic functional groups can improve the physical and chemical properties of the silica surface of MCM-41 and extends the practical applications of the material in catalysts [13–17] and adsorption [18, 19]. Amino groups can be included by postsynthesis grafting or by co-condensation during the synthesis [10, 11, 13–19]. In postsynthesis grafting, a precalcined mesoporous silica, partially rehydrated to generate surface hydroxyls, reacts with an appropriate alkoxysiloxane, whereas cocondensation involves the addition of both tetraethyl orthosilicate (TEOS) and a functionalised siloxane $(MeO)_3$-Si-X to the synthesis mixture.

Several models including kinetics [20], isotherm [21–28], and diffusion ones [20] have widely employed to interpret the adsorption processes. The fitting of the experimental data to these models have been carried out by various error functions such as the correlation coefficient (r), coefficient of determination (r^2), nonlinear Chi-square (χ^2) test analyses, relative standard deviation [2, 24–29], Akaike's information criterion (AIC) [30], sum of the squares of errors (SSE), hybrid fractional error function (HYBRID), Mardquardt's percent standard deviation (MPSD), average relative error (ARE), and sum of the absolute errors (SAE) [31] to find out which one is the best fit. There are two approaches to choose the model: (i) compare the test value: the smaller the χ^2 or AIC value, the more compatible the model is or the more the value of R or R^2 goes to unite the best and (ii) address the question statistically and get answer in terms of probabilities. For the former, the question seems to be easy. However, the problem is how to evaluate which model is compatible when both test values are approximately the same, nor does it mention how big or small the test value is to except. This might lead to misunderstand the adsorption mechanism. For the latter, the answer is based on the statistical hypothesis testing. First, set the significant level (alpha) and if p value is less than this alpha, the alternative mode fits the data significantly better than the null hypothesis model. Otherwise, accept the simpler (null) model. To the best of our knowledge, very few studies use statistical evaluation to consider the differences between the two models.

In this paper, 3-aminopropyltriethoxysilyl functionalised MCM-41 materials (denoted as aminopropyl-MCM-41) were prepared via direct and postsynthesis grafting. For the former method, aminopropyl-MCM-41 was prepared by means of direct co-condensation of 3-aminopropyltriethoxysilane and tetraethyl orthosilicate. For the latter, the amino groups were grafted to parent MCM-41 materials in which the template was removed using acid/ethanol extraction or calcination. The physical chemistry of the obtained materials was discussed. The resultant 3-aminopropyltriethoxysilane-modified MCM-41 was used as an adsorbent to remove ionic Pb(II) and Cd(II) from aqueous solutions. The isotherm models including Langmuir, Freundlich, Redlich–Peterson, and Sips in the linear and nonlinear forms were applied to describe the experimental data. In this paper, the method of paired-samples t-test was proposed to assess the compatibility of the adsorption isotherm models on the statistical perspective.

2. Experimental

2.1. Preparation of MCM-41 and Aminopropyl-MCM-41. Tetraethyl orthosilicate ($Si(OC_2H_5)_4$, TEOS, Merck), cetyltrimethylammonium bromide ($C_{19}H_{42}BrN$, CTAB, Merck), and 3-aminopropyltriethoxysilane ($H_2N(CH_2)_3Si(OC_2H_5)_3$, APTES, Merck) were used as a silica source, template, and functionalizing agent, respectively. Aminopropyl-MCM-41 was prepared via direct and postsynthesis grafting. For the direct synthesis, 0.5 g of CTAB, 480 mL of distilled water, and 7 mL of 2 M NaOH were mixed at 80°C for 30 minutes. Then, 9.4 g of TEOS was added to the resulting mixture under strong stirring for 30 minutes. Next, APTES with a molar ratio of TEOS/APTES = 5 was added under vigorous stirring for 1.5 hours [17]. The obtained solids were filtered. A complete removal of the organic template could be conducted in a solvent of acid/ethanol (a mixture of ethanol (100 mL) and concentrated HCl (1 mL, 36% in weight)) for 1 hour. The samples were denoted as direct-NH_2-MCM-41.

In the postsynthesis, first, the MCM-41 material was synthesised as mentioned above but without APTES. The CTAB template was removed from as-synthesised MCM-41 by calcination at 500°C for 6 hours to obtain a material denoted as calcined MCM-41. The other way to remove CTAB was the acid/ethanol extraction (1 gram of as-synthesised MCM-41 was added to 200 mL of a mixture HCl/C_2H_5OH (the ratio of 1 mL of HCl 36% in 100 mL of C_2H_5OH) and stirred at room temperature for 5 minutes) to obtain a material denoted as extracted MCM-41. Then, 0.78 mL of APTES was added to 1 gram of extracted MCM-41 in 60 mL of toluene under magnetic stirring and refluxing for 8 hours at 110°C. The samples were washed many times with distilled water (until the rinse reaches the neutral medium) and denoted as post-NH_2-extracted MCM-41. In a similar manner, calcined MCM-41 was hydrated for 2 hours in a desiccator containing a saturated NaCl solution at the bottom before functionalisation. This sample was denoted as post-NH_2-calcined MCM-41.

2.2. Characterisation of Materials. X-ray diffraction (XRD) patterns were recorded on VNU-D8 Advance Instrument (Bruker, Germany) using Cu Kα radiation ($\lambda = 1.5418$ Å). The N_2 adsorption/desorption isotherm measurements were performed at 77 K using TriStar 3000 Micromeritics. The samples were degassed at 200°C with N_2 for 2 hours before setting the dry mass and data collection. Specific surface areas were calculated using the Brunauer–Emmett–Teller (BET) model. Pore size distributions were calculated using the BJH model on the desorption branch. The thermal behaviour of the samples was conducted using thermal analysis-differential scanning calorimeter (TG-DSC) on Labsys TG/DSC SETARAM. The transmission electron microscopy (TEM) micrographs were obtained using JEOL JEM-2100 operating at 80 kV. Infrared spectra (IR) were recorded on an FT-IR spectrometer using IR-Prestige-21 (Shimadzu) in the KBr matrix in the range 4000–400 cm^{-1}.

2.3. Determination of the Point of Zero Charge. The point of zero charge (pH_{PZC}) of the aminopropyl functionalised MCM-41 materials was determined by the solid addition method [24, 32]. 25 mL of 0.1 M NaCl was added to a series of 50 mL Erlenmeyer flasks. The initial pH (pH_i) of the solution was adjusted, ranging from 2 to 12 by adding either 0.1 M HCl or 0.1 M NaOH solution. Then, 0.01 g of the post-NH_2-extracted MCM-41 sample was added to each flask, and the mixture was shaken for 48 hours. Then, the final pH (pH_f) of the solution was measured. The plot represents the relation between the difference of the final and initial pH value ($\Delta pH = pH_f - pH_i$), and pH_i was drawn; the point of intersection of the curve with the abscissa, at which $\Delta pH = 0$, provided pH_{PZC}. This process is performed similarly for the 0.01 M NaCl, 0.1 M KCl, and 0.01 M KCl solutions.

2.4. Adsorption Experiments. The adsorption of Pb(II) and Cd(II) ions on the aminopropyl functionalised MCM-41 material was performed in an Erlenmeyer flask (volume 100 mL): 0.01 g synthetic materials were added to a 50 mL of Pb(II) (or Cd(II)) solution, the pH value of which was adjusted with the 0.1 M HCl or 0.1 M NaOH solution; the mixture was then shaken for 4 hours. Finally, the solution was centrifuged to remove the adsorbent, and the concentration of Pb(II) or Cd(II) was determined using atomic absorption spectroscopy (AAS) by Shimadzu AA-6800 (Singapore). The removal efficiency of Pb(II) and Cd(II) was accessed.

The adsorption isotherm of Pb(II) and Cd(II) in the aqueous solution of aminopropyl-MCM-41 was studies at room temperature ($27 \pm 2^{\circ}C$). 0.05 g of aminopropyl-MCM-41 was added to the Erlenmeyer flasks containing 50 mL of the Pb(II) or Cd(II) ion of various concentrations, and the mixture was shaken for 4 hours to reach equilibrium adsorption. Then, the liquid was used to determine the remaining amount of Pb(II) or Cd(II) after removing the solid by centrifuge.

The amount of the metal ion adsorbed at equilibrium (q_e) was calculated according to the following equation:

$$q_e = \frac{(C_0 - C_e) \cdot V}{m} \left(\text{mg} \cdot \text{g}^{-1}\right), \tag{1}$$

where C_0 and C_e ($\text{mg} \cdot \text{L}^{-1}$) are the Pb(II) or Cd(II) ion concentrations at the initial and equilibrium time, respectively, and V (L) and m (g) are the volume of the Pb(II) or Cd(II) solutions and the mass of aminopropyl-MCM-41 used, respectively.

The removal efficiency (H) of metal ions was calculated according to the following equation:

$$H = \frac{(C_0 - C_e)}{C_0} (\%). \tag{2}$$

In this work, the two-parameter equations, namely, Langmuir isotherm and Freundlich isotherm, and three-parameter equations, i.e., Redlich–Peterson isotherm and Sips isotherm, were used to analyse the adsorption equilibrium data.

The Langmuir isotherm equation [20, 21, 23, 33] is as follows:

$$q_e = q_m \cdot \frac{K_L \cdot C_e}{1 + K_L \cdot C_e}, \tag{3}$$

where q_m is the maximum monolayer adsorption capacity of adsorbent ($\text{mg} \cdot \text{g}^{-1}$) and K_L is the Langmuir constant ($\text{L} \cdot \text{mg}^{-1}$). The other parameters have been described before.

Different linear forms of the Langmuir isotherm are shown in Table 1.

The Freundlich isotherm is expressed by the following empirical equation [20, 21, 23, 33]:

$$q_e = K_F \cdot C_e^{1/n}, \tag{4}$$

where n is the heterogeneity factor and K_F is the Freundlich constant ($\text{mg}^{(1-1/n)} \cdot \text{L}^{1/n} \cdot \text{g}^{-1}$). n and K_F are dependent on temperature: n indicates the extent of the adsorption, and K_F expresses the degree of nonlinearity between the solution concentration and the adsorption. If n is greater than 1, the adsorption process is favorable [20, 33].

The linear form of the Freundlich equation is

$$\ln q_e = \ln K_F + \frac{1}{n} \cdot \ln C_e. \tag{5}$$

The Redlich–Peterson isotherm equation [22, 23, 33] is as follows:

$$q_e = \frac{K_R \cdot C_e}{1 + a_R \cdot C_e^{b_R}}, \tag{6}$$

where K_R ($\text{L} \cdot \text{g}^{-1}$) and a_R ($\text{L}^{b_R} \cdot \text{mg}^{(b_R - 1)}$) are the Redlich–Peterson isotherm constants and b_R is the exponent with a value between 0 and 1.

A linear form of the Redlich–Peterson equation is

$$\ln\left(K_R \cdot \frac{C_e}{q_e} - 1\right) = b_R \cdot \ln C_e + \ln a_R. \tag{7}$$

According to the Freundlich model (equation (4)), the adsorbed amount increases with the adsorbate concentration. This is the problem of the Freundlich model. Therefore, Sips proposed an equation similar to the Freundlich equation, but it has a finite limit when the concentration is sufficiently high [22, 33]:

$$q_e = q_{mS} \cdot \frac{K_{S1} \cdot C_e^{1/n_S}}{1 + K_{S1} \cdot C_e^{1/n_S}}, \tag{8}$$

where q_{mS} is the Sips maximum adsorption capacity ($\text{mg} \cdot \text{g}^{-1}$), K_{S1} is the Sips equilibrium constant ($\text{L}^{1/n_S} \cdot \text{mg}^{((1/n_S)-1)}$), and n_S is a constant.

The Sips isotherm can be represented as

$$q_e = \frac{K_{S2} \cdot C_e^{b_S}}{1 + a_S \cdot C_e^{b_S}}, \tag{9}$$

where K_{S2} ($\text{mg}^{(1-b_S)} \cdot \text{L}^{b_S} \cdot \text{g}^{-1}$) and a_S ($\text{L}^{b_S} \cdot \text{mg}^{(b_S - 1)}$) are the Sips isotherm constants and b_S is the Sips model exponent.

The linear form of Sips equation can be described as

$$\frac{1}{q_e} = \frac{1}{K_{S2}} \cdot \frac{1}{C_e^{b_S}} + \frac{a_S}{K_{S2}}. \tag{10}$$

The Sips and Redlich–Peterson equations contain three unknown parameters, and they are impossible to obtain

Table 1: Linear form equations of the Langmuir isotherm model.

Isotherm	Linear form	Plot	Reference
Langmuir 1	$1/q_e = (1/(K_L \cdot q_m)) \cdot (1/C_e) + (1/q_m)$	$(1/q_e)$ vs. $(1/C_e)$	[21, 25–28, 33]
Langmuir 2	$C_e/q_e = (1/q_m) \cdot C_e + (1/(K_L \cdot q_m))$	(C_e/q_e) vs. C_e	[20, 21, 25–28, 33]
Langmuir 3	$q_e = -(1/K_L) \cdot (q_e/C_e) + q_m$	q_e vs. (q_e/C_e)	[21, 25–28, 33]
Langmuir 4	$q_e/C_e = -K_L \cdot q_e + K_L \cdot q_m$	(q_e/C_e) vs. q_e	[21, 25–28, 33]
Langmuir 5	$1/C_e = K_L \cdot q_m \cdot (1/q_e) - K_L$	$(1/C_e)$ vs. $(1/q_e)$	[21]

simply by linearisation. Therefore, a minimisation procedure using the Solver function of Microsoft Excel was carried out to maximise the determination coefficient of $\ln(K_R \cdot (C_e/q_e) - 1)$ vs. $\ln C_e$ and $1/q_e$ vs. $1/C_e^{b_S}$. After maximising the R^2 value, the isotherm parameters were determined using the linear regression equation.

3. Results and Discussion

3.1. Characterisation of Aminopropyl Functionalised MCM-41. Figure 1(a) presents the X-ray diffraction patterns of MCM-41 and the aminopropyl-MCM-41. All the samples had a single intensive reflection at the 2θ angle around 2° as is the case for typical MCM-41 materials, and this reflection is generally related to a regular pore size and an ordered pore arrangement [34]. This suggests that the mesoporous structure remained intact after amine modification. However, the intensity of peak (100) characterised for the mesostructure decreased as APTES was grafted to the silica framework. The direct-NH_2-MCM-41 sample still remained a higher hexagonal mesoporous structure since the (100), (110), and (200) reflections were still observed. The low intensity of (100) reflection implied a poorly ordered structure of the postsynthesis samples.

The efficiency of the incorporation of APTES into the silica framework can be studied using TG-DSC (Figure 1(b)). For the as-synthesised MCM-41 samples, a large weight loss (16.3%) in several steps corresponding to the exothermic peak in DSC at around 250°C before levelling off at around 600°C was observed. Since DSC only had an exothermic peak, the removal of the template appeared to take place through oxidative decomposition rather than evaporation (desorption). For aminopropyl-MCM-41, the endothermic peak at around 100°C can be attributed to the desorption of water from the channels of the material. The second weight loss between 300 and 600°C, together with exothermic peaks corresponds to the decomposition/oxidation of aminopropyl residues. The third weight loss around 600–800°C, which could be observed for all the samples, should relate to the release of water formed during condensation of silanols in the silica framework. It was found that post-NH_2-calcined MCM-41 and post-NH_2-extracted MCM-41 showed similar patterns of thermal decomposition with sharp exothermic peaks while the direct-NH_2-MCM-41 sample showed a relatively broaden exothermic peak. This evidence suggested an inconsistent incorporation of APTES into the silica framework in the direct-NH_2-MCM-41 material. It is assumed that the weight loss over 250°C was attributed to aminopropyl loading. The amine content of direct-NH_2-MCM-41, post-NH_2-calcined MCM-41, and post-NH_2-extracted MCM-41 are 10.5%, 12.8%, and 17.5%, respectively. Then, although the direct-NH_2-MCM-41 sample possessed higher mesoporous ordering, it had lower aminopropyl loading in comparison with those of postsynthesis. The highest aminopropyl loading in post-NH_2-extracted MCM-41 was possible because the surface of the silica framework in which the template was removed by solvent extraction contains a larger amount of silanol groups, as mentioned in a previous paper [19].

The existence of the amino group is further confirmed by IR spectra. The FT-IR spectra of the MCM-41 and aminopropyl-MCM-41 samples are shown in Figure 2. The sharp absorption band at 3100–3600 cm^{-1} is attributed to the stretching of O-H on the surface silanol groups with the hydrogen bond and the remaining adsorbed water molecules. The absorption bands at 2920 cm^{-1} and 2850 cm^{-1} are ascribed to the asymmetric stretching and symmetric stretching of (–CH_2–), respectively, while the absorption at 1460 cm^{-1} is attributed to the bending of the (–CH_2–) group. The absorption bands at 1051 cm^{-1} and 800 cm^{-1} are due to Si-O-Si and Si-O stretching vibrations, respectively. The band at 954 cm^{-1} is assigned to the Si-OH stretching. The adsorption band at 1635 cm^{-1} is due to the deformation vibrations of adsorbed water molecules (δ_{H-O-H}). The presence of the N-H bending vibration at 690 cm^{-1} and –NH_2 symmetric bending vibration at 1532 cm^{-1}, which are absent in neat MCM-41, indicates the successful inclusion of organic amine onto the silica surface [10, 17, 18].

Figure 3 shows the TEM observation of calcined MCM-41, extracted MCM-41, and aminopropyl-MCM-41 grafted via the direct and indirect process. It can be seen that the calcined MCM-41 and extracted MCM-41 samples consist of nanospherical particles of around two hundred nanometres. There are nanobubbles in the extracted MCM-41 sample. These bubbles inside the nanospherical particles possibly formed during the extraction process. The acidic solvent might corrode unstable silica inside the nanoparticles producing sub-nanobubbles. Grafting APTES into the MCM-41 framework by the direct process provided the morphology with some inclusions that possibly formed through the condensation of APTES outside the MCM-41 nanoparticles, while no inclusions and smooth surface were observed in the post-NH_2-calcined MCM-41 or post-NH_2-extracted MCM-41 samples. The inconsistent condensation of 3-aminopropyltriethoxysilane including self-condensation and condensation with the silanol group of the silica framework in direct-NH_2-MCM-41 explained why the DSC profile had a broad exothermic peak compared with that of postaminopropyl-MCM-41.

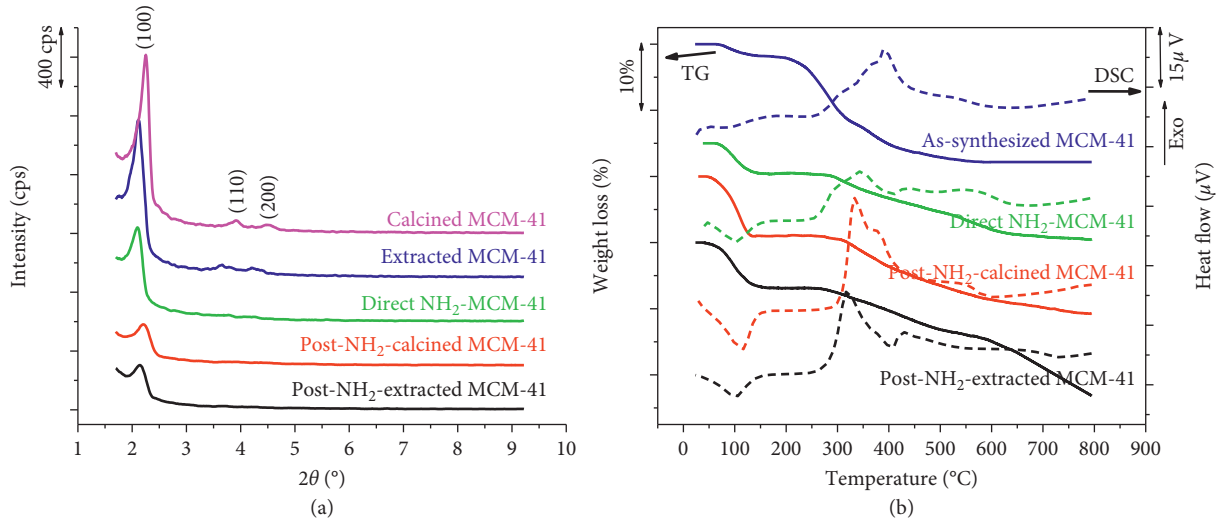

Figure 1: (a) XRD patterns of MCM-41 and aminopropyl-MCM-41; (b) TG-DSC profiles of as-synthesised MCM-41 and aminopropyl-MCM-41.

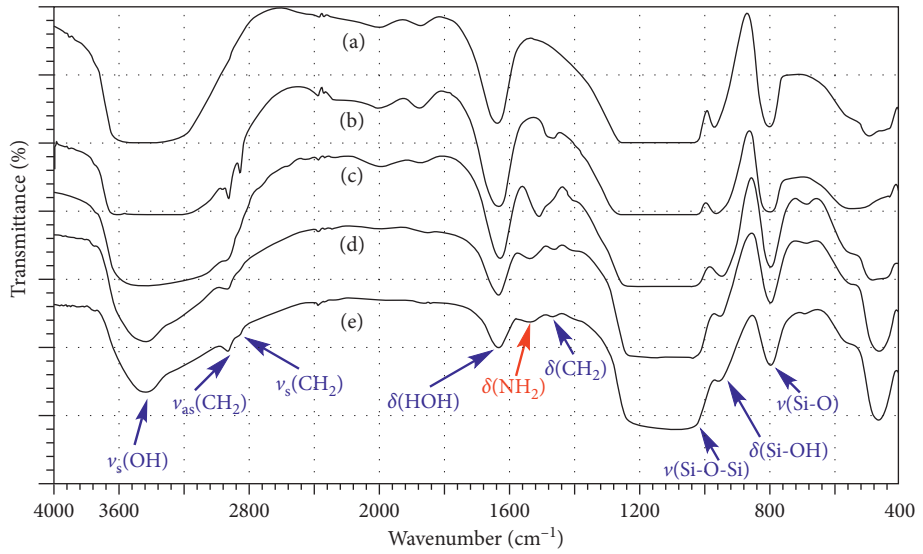

Figure 2: The FT-IR spectra: (a) calcined MCM-41; (b) extracted MCM-41; (c) direct-NH_2-MCM-41; (d) post-NH_2-calcined MCM-41; (e) post-NH_2-extracted MCM-41.

Figure 4 shows the nitrogen adsorption/desorption isotherms of MCM-41 and aminopropyl-MCM-41. Calcined MCM-41 and extracted MCM-41 showed practically the same porous properties. Direct-NH_2-MCM-41 and MCM-41 exhibited the sharp condensation capillaries around a relative pressure of 0.35 and characteristic-type IV isotherms. This shows that MCM-41 and direct-NH_2-MCM-41 had a hexagonal mesoporous structure with a narrow pore size distribution (the inset of Figures 4(a)–4(c)). This finding is consistent with that of the XRD study discussed in Section 3.1. A hysteresis of the H_3 type at $P/P_o > 0.9$ was observed for both samples prepared by postsynthesis (Figures 4(d) and 4(e)). This is due to nitrogen condensation and evaporation in the interparticle space. The distribution of the functional group on the surface of the pore wall of the materials prepared via postsynthesis was not uniform, and the organic groups could block the mesopores leading to the decrease of the surface area and broad pore distribution (Table 2 and the inset of Figures 4(d) and 4(e)).

One of the most important properties of a solid material is the point of zero charge (pH_{PZC}). When a solid material is in a solution with pH lower than pH_{PZC}, the material surface has a positive charge by adsorption of H^+ ions from the aqueous solution, leading to a positive variation of the solution pH ($\Delta pH > 0$). On the contrary, if the solid material is in a solution with pH greater than pH_{PZC}, the material surface has a negative charge by adsorption of OH^- ions, leading to a negative variation of the solution pH ($\Delta pH < 0$). Thus, the pH value, at which the material surface has a zero charge, $\Delta pH = 0$, is the point of zero charge. The point of

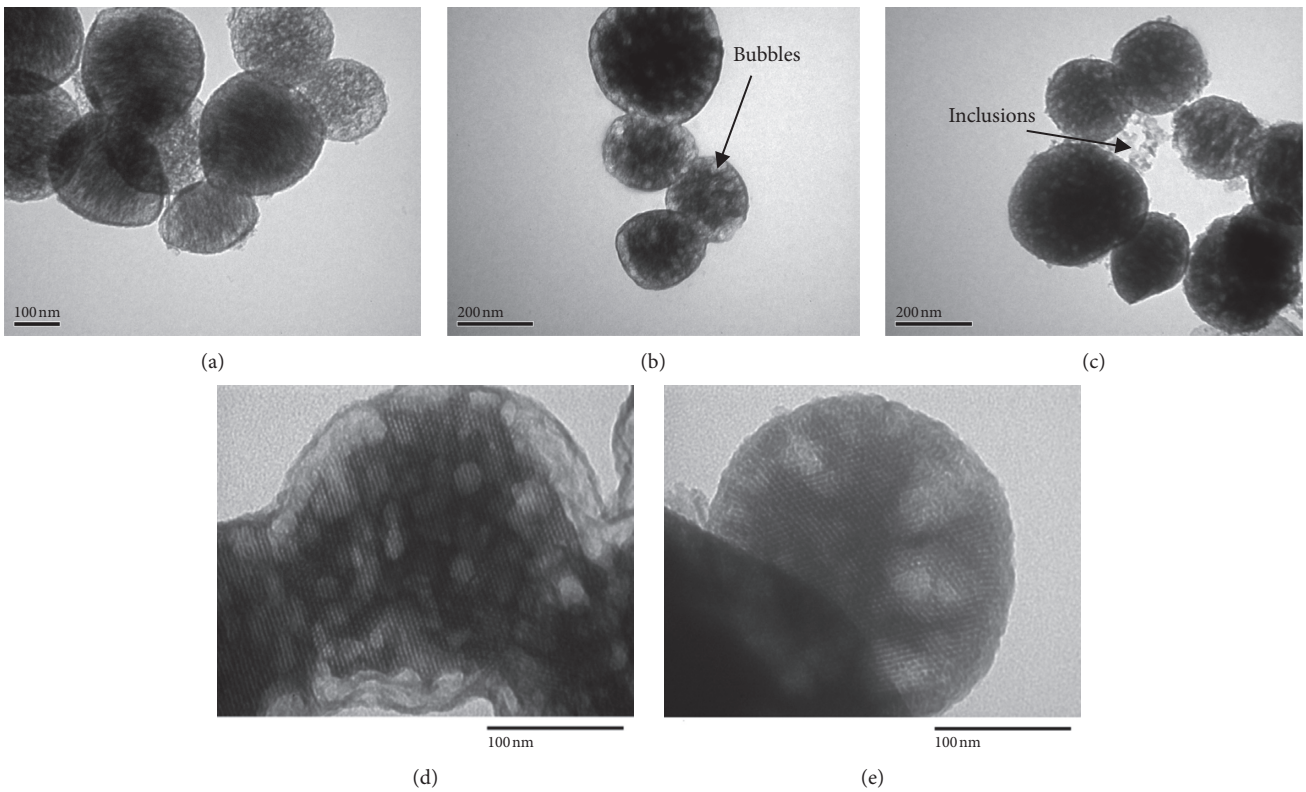

Figure 3: TEM images of MCM-41 and aminopropyl functionalised MCM-41: (a) calcined MCM-41; (b) extracted MCM-41; (c) direct-NH_2-MCM-41; (d) post-NH_2-calcined MCM-41; (e) post-NH_2-extracted MCM-41.

zero charge determination can be performed in a neutral environment or a neutral electrolyte solution. In this study, the NaCl and KCl solutions at two different concentrations (0.1 M and 0.01 M) were used.

The point of zero charge of the aminopropyl-MCM-41 material was 7.5 and 8.1 in the 0.1 M and 0.01 M NaCl solution, respectively (Figure 5(a)). Similarly, for the 0.1 M and 0.01 M KCl solution, the point of zero charge of the aminopropyl-MCM-41 material was 7.6 and 7.7, respectively (Figure 5(b)). It is evident that pH_{PZC} of the aminopropyl-MCM-41 material was independent of the concentration of the studied electrolytes. The average value of pH_{PZC} of the aminopropyl-MCM-41 material is 7.73 ± 0.11, which is similar to the pH_{PZC} of the base solid materials already published [35]. Qin et al. [36] announced that the point of zero charge of the aminopropyl-MCM-41 material was 9.5 measured using the zeta potential. This difference is probably due to the nature of the two measurement methods and the nature of the NH_2-MCM-41 products.

3.2. Adsorption Studies

3.2.1. Choosing Adsorbent. The synthesised MCM-41 materials were used to adsorb Pb(II) and Cd(II) from aqueous solutions. As can be seen from Figure 6, calcined MCM-41 and extracted MCM-41 had a very low removal efficiency for Pb(II) (<20%) (Figure 6(a)) and for Cd(II) (around 7%) (Figure 6(b)). When MCM-41 was functionalised with 3-aminopropyl, it had a significantly higher removal efficiency, especially when the postsynthesis was used. For the Pb(II) adsorption, post-NH_2-extracted MCM-41 was more effective than post-NH_2-calcined MCM-41 with more than 90% efficiency as opposed to around 70%, respectively. A similar pattern of adsorption on post-NH_2-extracted MCM-41 and post-NH_2-calcined MCM-41 is seen for Cd(II) but at a much lower efficiency (20%) for both the materials. This shows that the amino group was successfully grafted to the silica wall of MCM-41. Based on these findings, post-NH_2-extracted MCM-41 was chosen to evaluate the adsorption capacity of the material in the further study.

3.2.2. Effect of pH. In order to find the dependence of the removal efficiency of the synthesised materials on the acidity of the reaction mixture, a range of pH from 2 to 9 was studied. It is clear that the removal efficiency tends to increase with the solution pH (Figure 7). At pH less than 3.5, the removal efficiency of Pb(II) and Cd(II) on aminopropyl-MCM-41 was negligible; it increased significantly in the next range of pH from 3 to 4, followed by a relatively low rise. Pb(II) was adsorbed more than Cd(II) at every pH. At pH 6, the former attained an efficiency of 65% and the latter 40%. Interestingly, Cd(II) exhibited an unusual pattern when pH continued to rise: the efficiency stayed nearly stable until pH 7 and then increased slightly at pH 8 and surged abruptly, reaching the value equal to that of Pb(II) at 65% at pH 9. Here, the adsorption behaviour of Pb(II) and Cd(II) is

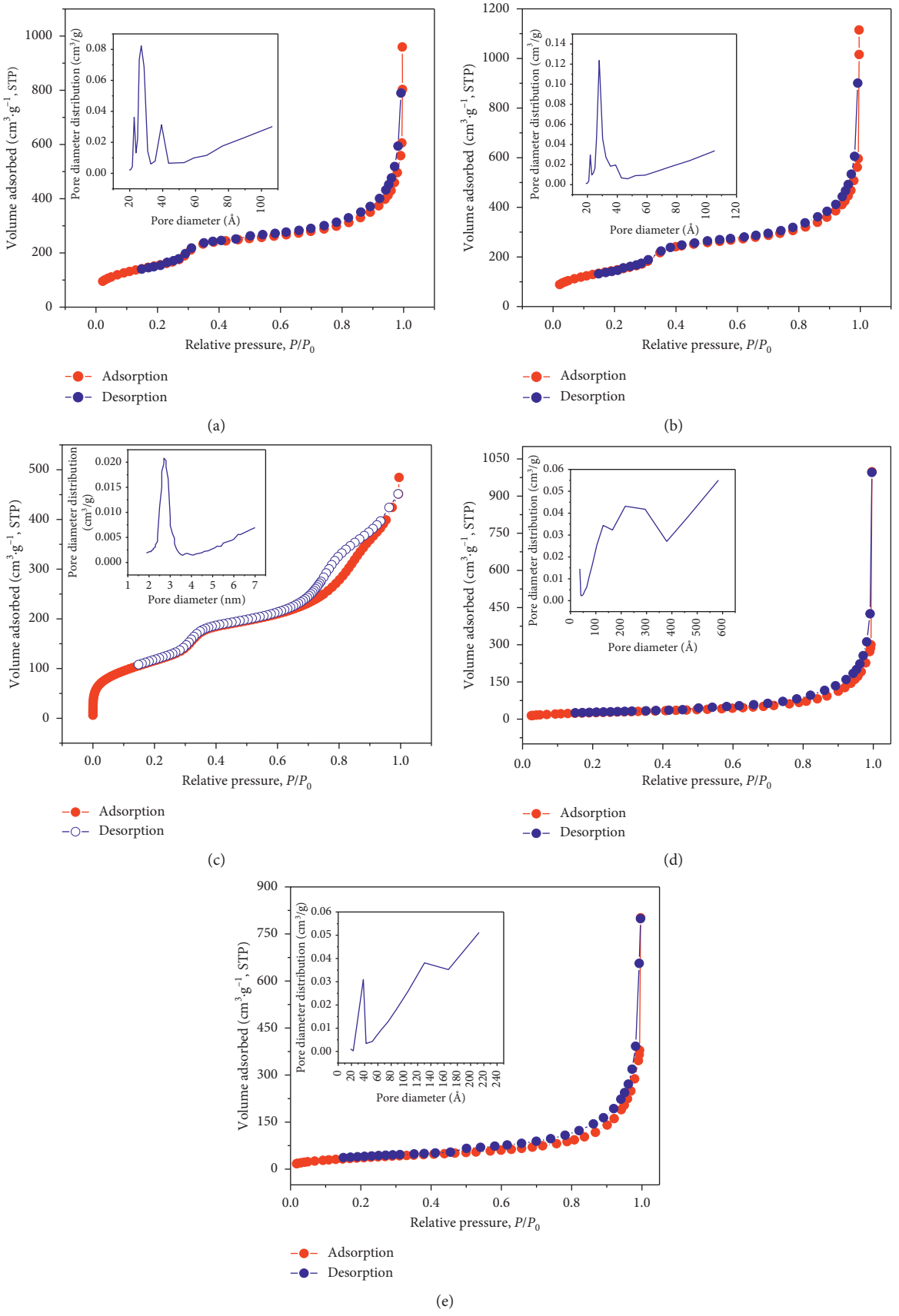

FIGURE 4: Isotherms of nitrogen adsorption/desorption and pore distribution (inset) of MCM-41 and aminopropyl-MCM-41: (a) calcined MCM-41; (b) extracted MCM-41; (c) direct-NH_2-MCM-41; (d) post-NH_2-calcined MCM-41; (e) post-NH_2-extracted MCM-41.

Table 2: Porous properties of MCM-41 and aminopropyl-MCM-41.

Samples	$d_{(100)}$ (Å)	a_0* (Å)	d_{pore} (Å)	t_w** (Å)	S_{BET} ($m^2 \cdot g^{-1}$)	V_{pore} ($cm^3 \cdot g^{-1}$)
Calcined MCM-41	39.3	45.4	27.0	18.4	564	1.53
Extracted MCM-41	42.5	49.1	27.9	21.2	538	1.76
Direct-NH_2-MCM-41	42.1	48.6	27.0	21.6	427	0.77
Post-NH_2-calcined MCM-41	—	—	—	—	97	1.54
Post-NH_2-extracted MCM-41	—	—	—	—	137	1.01

*$a_0 = 2 \cdot (d_{(100)}/\sqrt{3})$; **$t_w = a_0 - d_{pore}$; — N/A.

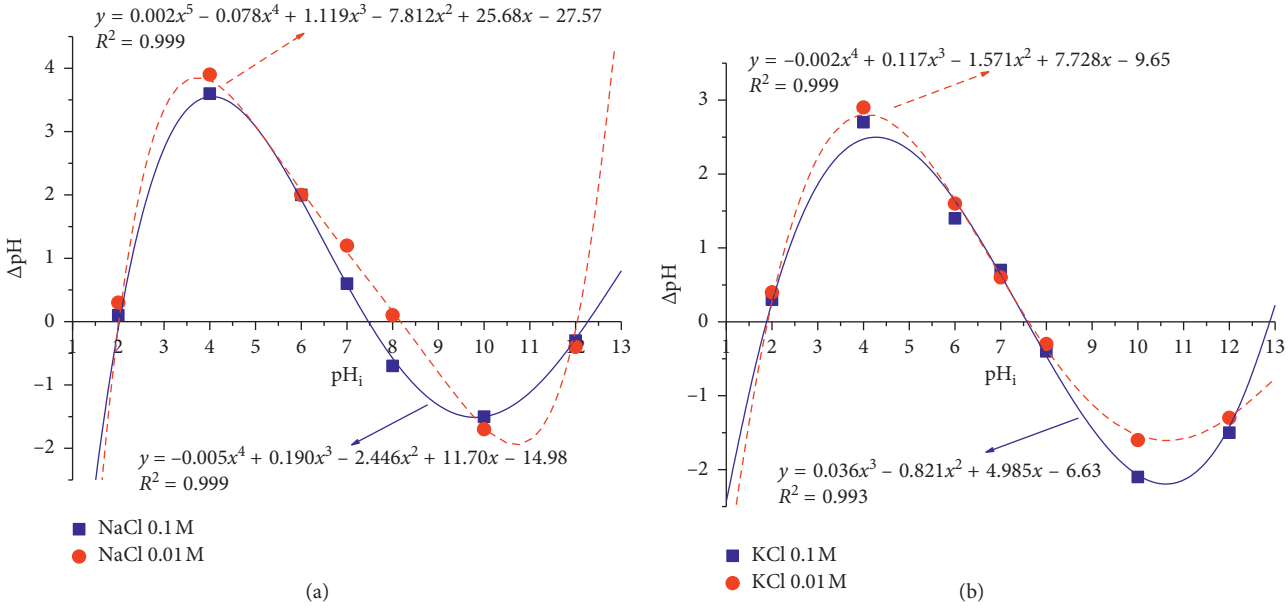

Figure 5: Point of zero charge of the aminopropyl-MCM-41 material in different solutions: (a) NaCl; (b) KCl.

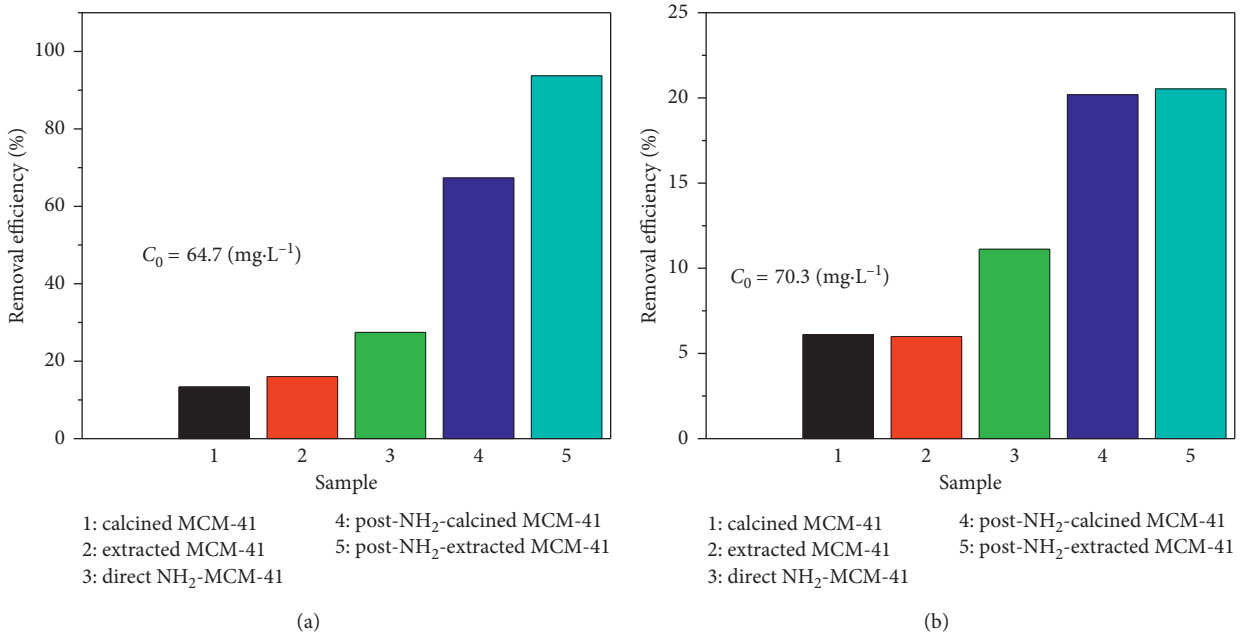

Figure 6: Removal efficiency of heavy metal ions of MCM-41 and aminopropyl-MCM-41: (a) Pb(II); (b) Cd(II) (adsorption condition: $V = 50$ mL, $m = 0.05$ g, room temperature).

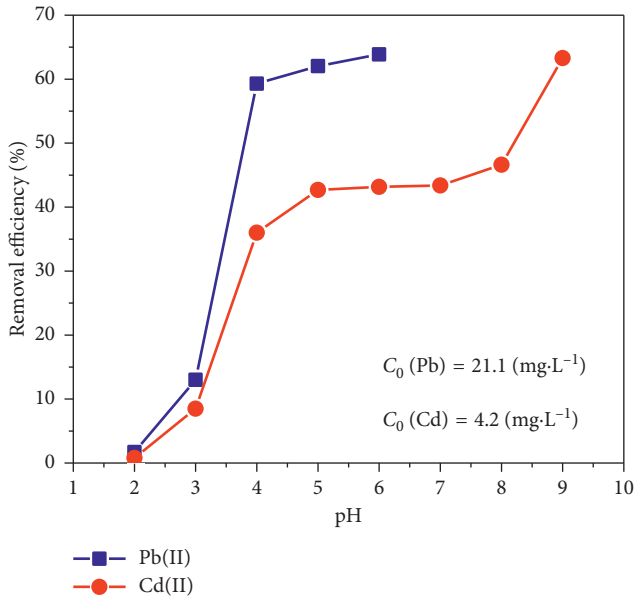

Figure 7: Removal efficiency of Pb(II) and Cd(II) ions on post-NH_2-extracted MCM-41 at various pH values (adsorption condition: $V = 50$ mL, $m = 0.01$ g, room temperature).

similar to that studied by Heidari et al. [18] on the effect of pH on the adsorption of Pb(II), Cd(II), and Ni(II) on aminopropyl-MCM-41 in the pH range from 1.5 to 5. At pH greater than 6, they proposed that Pb(II) ions precipitated due to a large amount of OH^- ions in the solution when the concentration of the studied ions was very high (50 mg·L^{-1}). In our study, the highest pH was 6 for Pb(II) and 9 for Cd(II) with a much lower concentration of metal ions (21.1 mg·L^{-1} for Pb(II) and 4.2 mg·L^{-1} for Cd(II)). In our studied pH range, the metal ions did not precipitate.

The adsorption of Pb(II) and Cd(II) on aminopropyl-MCM-41 in the aqueous solution may occur with the coordination mechanism ($[Me(NH_2)_2]^{2+}$ form, Me is the Pb or Cd ion), as suggested by Benhamou et al. [37]. Besides, the attraction mechanism of the opposite charge between the metal ion and the material surface also takes place. At pH < 5, Pb(II) and Cd(II) ions exist mainly in the Pb^{2+} and Cd^{2+} form. In this pH range, the surface of the aminopropyl-MCM-41 material also has a positive charge (the point of zero charge for the material is ~7.73). At low pH (pH = 2–4), the electrostatic repulsion between Pb^{2+} or Cd^{2+} and the positively charged surface of the material dominates. The adsorption occurs only due to complexation, and this complexation cannot take place significantly because there is also a competition of the H^+ ion in the acidic solution. As a result, the removal efficiency is low. In the case of 4 < pH < 6, both the complexation and attraction are dominant as the medium is less acidic with a smaller amount of the H^+ ion and less positive material surface, and accordingly, the removal efficiency rises rapidly reaching a high stable value. At pH from 6 to 8, the material surface becomes more or less neutral, and therefore, the adsorption by attraction halts and the efficiency stays practically constant. Further increase of pH makes the surface of the aminopropyl-MCM-41 material become negative, and ionic Cd(II) primarily exists in the $Cd(OH)^+$ form. Thus, the removal efficiency increases significantly again.

3.2.3. Adsorption Isotherms. To eliminate errors caused by experimental point [30], typically 4 to 7 experimental points are needed [18, 20, 25, 26, 30, 38, 39]. In this study, 27 experimental points were investigated. The results of the linear regression of the isotherm models, namely, Langmuir, Freundlich, Redlich–Peterson, and Sips, for Pb(II) and Cd(II) adsorption on aminopropyl-MCM-41 are presented in Figure 8 and Table 3.

As a rule, the more the R^2 is closer to unity, the more is the model compatible with the experimental data. It is clear from Table 3 that the Langmuir 2 and Redlich–Peterson isotherms fit the experimental data of the adsorption of Pb(II) and Cd(II) the most with $R^2 = 0.999$.

However, the selection of model based on the value of R^2 is also biased. For example, in the case of Langmuir 2 and Freundlich equations, if only the linear form is concerned as published in many papers [19, 25–28, 33], where the authors concluded that the Langmuir 2 equation is more appropriate than the Freundlich equation because of its high R^2 value. Meanwhile, the Redlich–Peterson equation also has a relatively high coefficient R^2.

Recently, many researchers have published their results of nonlinear forms of isotherm equations [18, 21, 25–28]. In this study, the nonlinear forms were also used to compare with the linear forms.

The parameters of the isotherm equations determined with the nonlinear regression method were calculated using the Solver function in Microsoft Excel. In this method, an error function is necessary to match the experimental data in the form of nonlinear isotherm equations. The parameter values are optimised based on the smallest value of this error function. Various error functions have been proposed [21, 23, 33]. In these studies, the error function in the following equation was used [40]:

$$\mathrm{RMSR} = \sqrt{\frac{1}{N} \cdot \sum_{i=1}^{n} \left(q_{e,\exp} - q_{e,\mathrm{cal}}\right)^2}, \tag{11}$$

where RMSR is the root mean squared residual, $q_{e,\exp}$ (mg·g^{-1}) is the experimental equilibrium adsorption capacity, $q_{e,\mathrm{cal}}$ (mg·g^{-1}) is the calculated equilibrium adsorption capacity, and N is the number of experiments.

The experimental points and the nonlinear regression lines of the adsorption of Pb(II) and Cd(II) ions on aminopropyl-MCM-41 for the models to be compared are shown in Figure 9. The parameters of the models are presented in Table 4.

Table 4 shows that the nonlinear isotherm equations of Langmuir, Redlich–Peterson, and Sips both described quite well the Pb(II) or Cd(II) adsorption on aminopropyl-MCM-41 because the RMSR were small and approximately equal together. Comparisons of R^2 in Table 3 with the RMSR error function in Table 4 also show an inconsistence. It is that the

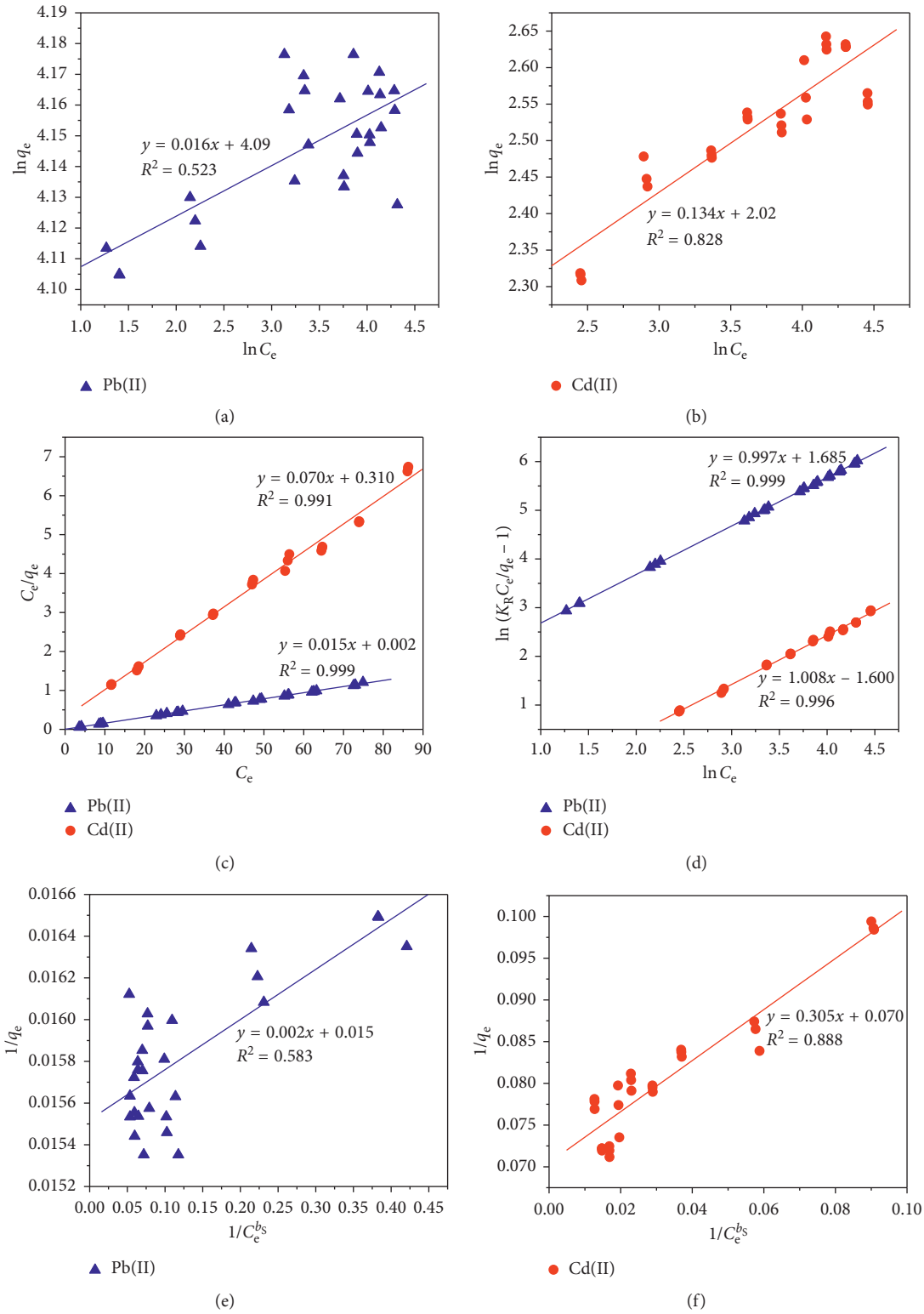

Figure 8: Plots of isotherm equations in a linear form for Pb(II) and Cd(II) adsorption on aminopropyl-MCM-41: (a, b) Freundlich; (c) Langmuir 2; (d) Redlich–Peterson; (e, f) Sips's model (adsorption condition: $V = 50$ mL, $m = 0.05$ g, room temperature).

R^2 value of the Sips equation was very low, while the RMSR of the one in the nonlinear form was very small. This is also evidence of a limitation using the value of error functions to assess model compatibility.

The majority of works published on assessing the compatibility of the model are based on the value of the error function. If the error function value of the model is the smallest, the model is the most compatible. It is also

Table 3: Parameters of the isotherm equations determined by using the linear form of Pb(II) and Cd(II) adsorption on aminopropyl-MCM-41.

Ion	Isotherm (linear form)	q_m (mg·g^{-1})	K_L, K_F, K_R, or K_{S2}	a_R or a_S	n, b_R, or b_S	R^2
Pb(II)	Langmuir 1	66.66	5.00	—	—	0.574
	Langmuir 2	66.66	7.50	—	—	**0.999**
	Langmuir 3	63.99	4.67	—	—	0.552
	Langmuir 4	64.64	2.57	—	—	0.552
	Langmuir 5	64.56	2.64	—	—	0.574
	Freundlich	—	59.73	—	62.50	0.523
	Redlich–Peterson	—	341.86	5.39	0.99	**0.999**
	Sips	—	500.00	7.50	0.68	0.583
Cd(II)	Langmuir 1	14.28	0.21	—	—	0.888
	Langmuir 2	14.28	0.22	—	—	**0.991**
	Langmuir 3	14.13	0.22	—	—	0.815
	Langmuir 4	14.54	0.18	—	—	0.815
	Langmuir 5	14.40	0.19	—	—	0.888
	Freundlich	—	7.58	—	7.46	0.828
	Redlich–Peterson	—	2.96	0.20	1.00	**0.996**
	Sips	—	3.27	0.22	0.97	0.888

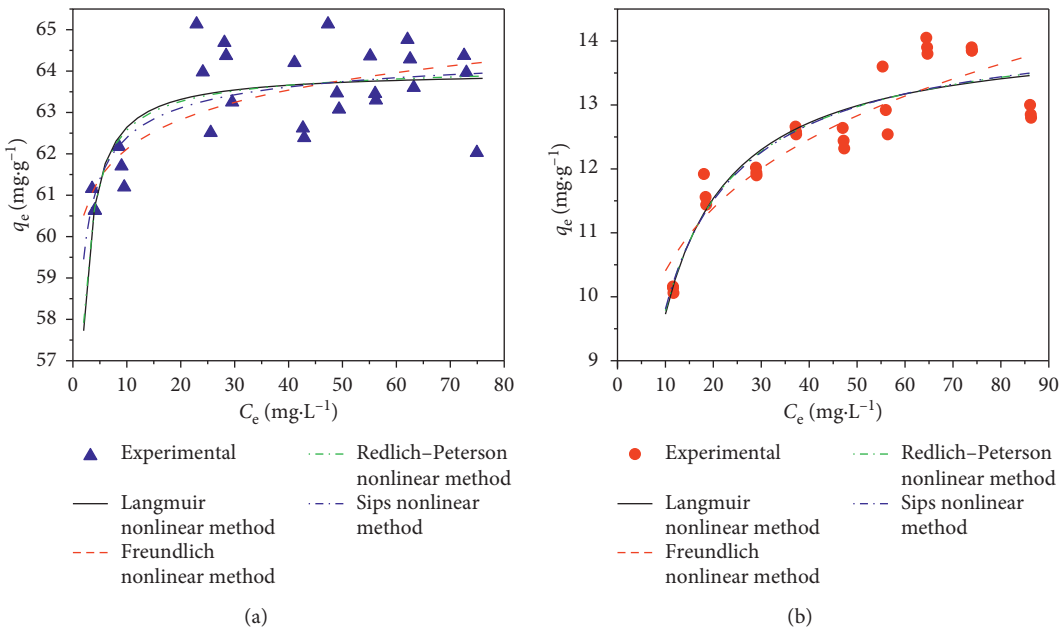

Figure 9: Adsorption isotherms determined using the nonlinear method for the adsorption of metal ions onto aminopropyl-MCM-41: (a) Pb(II); (b) Cd(II) (adsorption condition: $V = 50$ mL, $m = 0.05$ g, room temperature).

unreasonable because the difference is probably due to random errors. There have never been works that had made a statistical error function to indicate a certain error value. If the value of the error calculation results is larger or smaller than this value, the model accepted to be compatible with experimental data. So, how to know which models are described equally well with experimental data? All proposed error functions [21, 23, 31, 33] do not solve the problem because the error functions are not statistical functions. Thus, it needs to seek an error function that has a statistically normal distribution function to solve this problem.

The general principles of the evaluation model can be interpreted as follows: a set of adsorption capacity data from experimental equilibrium ($q_{e,exp}$) via a certain model will change a set value $q_{e,cal}$, as illustrated in Figure 10.

The model is the most appropriate if the difference between $q_{e,exp}$ and $q_{e,cal}$ is smallest. All error functions are based on this principle [21, 23, 31, 33]. On this basis, we believe that the most appropriate model is the one to create the $q_{e,cal}$ values that have the same sampling distribution as the $q_{e,exp}$ values, or in the other words, the average capacity calculated from the model is the closest to the average experimental capacity. We used the paired-samples t-test for

Table 4: Regression parameters of the different nonlinear isotherm models for the adsorption of Pb(II) and Cd(II) on aminopropyl-MCM-41.

Ion	Isotherm (nonlinear form)	q_m (mg·g^{-1})	K_L, K_F, K_R, or K_{S2}	a_R or a_S	n, b_R, or b_S	RMSR
Pb(II)	Langmuir	64.00	4.59	—	—	0.877
	Freundlich	—	59.82	—	61.28	0.924
	Redlich–Peterson	—	322.15	5.06	0.99	0.876
	Sips	—	499.98	7.71	0.52	0.876
Cd(II)	Langmuir	14.17	0.21	—	—	0.440
	Freundlich	—	7.71	—	7.68	0.490
	Redlich–Peterson	—	3.37	0.25	0.98	0.440
	Sips	—	3.94	0.27	0.88	0.439

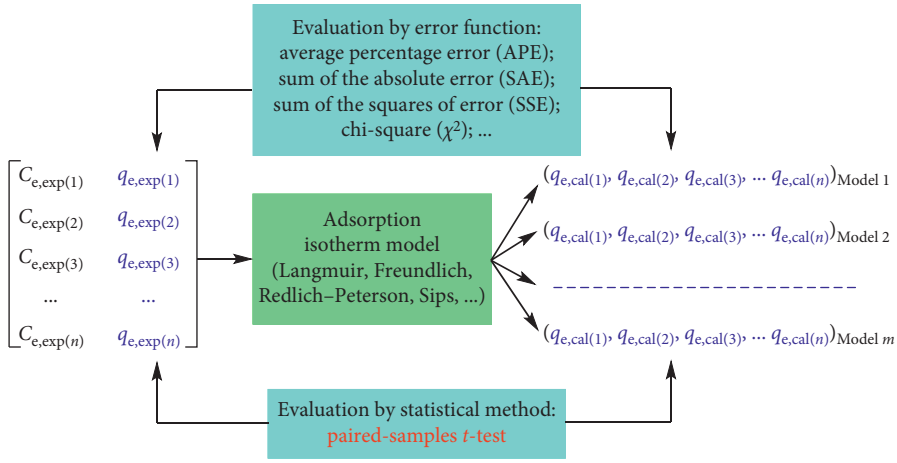

Figure 10: Idea of the statistical evaluation of the adsorption isotherm model.

this assessment. The value of the statistical t-test is calculated according to Field as follows [41]:

$$t = \frac{\sum d}{\sqrt{\left(N \cdot \left(\sum d^2\right) - \left(\sum d\right)^2\right)/(N-1)}}, \quad (12)$$

where d is the difference of the compared pairs ($d = q_{e,exp} - q_{e,cal}$) and N is the total number of pairs.

To apply this comparison, the sequence of $q_{e,cal}$ and $q_{e,exp}$ should meet the testing hypotheses: (i) dependent assumption: the values of $q_{e,cal}$ and $q_{e,exp}$ combine pairs together because they are calculated from starting values of $q_{e,exp}$, and this assumption is satisfied; (ii) normally distributed assumption, it mean difference scores are normally distributed in the population, or there is a large sample size (approximately 30): in this case, because of the large sample size ($N = 27$), the condition is satisfied [41]; and (iii) dependent variable assumption is at least the variable interval: this condition is also satisfied.

H_0 hypothesis: the average value of $q_{e,cal}$ is not different from the average value of $q_{e,exp}$. This means that the model gives a goodness description of the experimental data.

In software, such as Microsoft Excel or SPSS, the statistical values of t are transferred to corresponding probability values of p. p is the probability at which people can trust that the H_0 hypothesis is correct. For statistical comparisons, the level of significance α must be set first. This level is optional and often chosen at 0.05, 0.01, or 0.001 to evaluate the difference between the two compared quantities. In this study, the comparative expectation of the two number sequences is the same, so we selected $\alpha = 0.95$. This means that we are 95% confident that the H_0 hypothesis is true. If $p > 0.95$ then H_0 is accepted, and therefore, the average value of $q_{e,cal}$ is not different from that of $q_{e,exp}$ at the statistically significant level $\alpha = 0.95$, or the model is accepted. Conversely, if $p < 0.95$, then the H_0 hypothesis is rejected, and the model is not accepted.

The data are analysed with the paired-samples t-test at $\alpha = 0.95$ using the SPSS-17 software (Statistical Package for the Social Sciences). For the adsorption of Pb(II), 6 equations had $p < 0.95$, indicating that there was a statistically significant difference in the equilibrium adsorption capacity values given by the equation and the experimental data; 6 remaining equations, Langmuir 3, Langmuir 5, Langmuir nonlinear, Freundlich nonlinear, Redlich–Peterson nonlinear, and Sips nonlinear had $p > 0.95$ (Table 5) and should not have the statistically significant differences between the mean values of $q_{e,cal}$ and $q_{e,exp}$. Therefore, these 6 equations appropriately describe the experimental data at $\alpha = 0.95$.

Similarly, the results of the paired-samples t-test for adsorption of Cd(II) showed that four equations in the nonlinear forms, namely, Redlich–Peterson, Sips, Langmuir,

Table 5: Results of the paired-samples t-test analysis of adsorption of Pb(II) and Cd(II) on aminopropyl-MCM-41.

For adsorption of Pb(II)			For adsorption of Cd(II)		
Isotherm	*t*	*p*	*Isotherm*	*t*	*p*
Langmuir (nonlinear)	0.001	**1.000**	Redlich–Peterson (nonlinear)	0.001	**1.000**
Freundlich (nonlinear)	0.001	**1.000**	Sips (nonlinear)	0.001	**1.000**
Redlich–Peterson (nonlinear)	−0.014	**0.989**	Langmuir (nonlinear)	0.002	**0.999**
Sips (nonlinear)	−0.014	**0.989**	Freundlich (nonlinear)	−0.007	**0.994**
Langmuir 3	0.013	**0.989**	Langmuir 3	0.095	0.925
Langmuir 5	0.061	**0.952**	Redlich–Peterson (linear)	0.101	0.920
Langmuir 4	−0.139	0.891	Langmuir 5	−0.221	0.827
Redlich–Peterson (linear)	−0.848	0.404	Freundlich (linear)	0.299	0.767
Freundlich (linear)	0.896	0.379	Langmuir 4	−0.463	0.647
Langmuir 1	−15.632	<0.001	Sips (linear)	−0.781	0.442
Langmuir 2	−15.921	<0.001	Langmuir 1	−1.179	0.249
Sips (linear)	−13.671	<0.001	Langmuir 2	−1.641	0.113

Table 6: A comparison of Pb(II) and Cd(II) adsorption capacity of aminopropyl-MCM-41 with some other published adsorbents.

Adsorbent	Adsorption capacity ($mg \cdot g^{-1}$)		References
	Pb(II)	Cd(II)	
Aminopropyl-MCM-41	64.21	14.08	The present work
NH_2-MCM-41	57.7	18.2	[18]
Amino-modified silica aerogel	45.45	35.71	[42]
Amino-functionalized magnetite/kaolin clay	86.1	22.1	[43]
Silicalite-I-NH_2	43.5	—	[44]
MCM-48-NH_2	75.2	—	[44]
MCM-48-SH	31.2	—	[44]
Soil amendment	—	7.47–17.67	[45]
Dithizone-modified bagasse	37.20	—	[46]
Chromium-doped nickel nanometal oxide	1.7914	5.243	[47]

and Freundlich, had $p > 0.95$, revealing that these models are the appropriate description for the experimental data at $\alpha = 0.95$.

Hence, in terms of statistics, the four nonlinear models, namely, Langmuir, Freundlich, Redlich–Peterson, and Sips, most appropriately described the adsorption data of Pb(II) and Cd(II) on aminopropyl-MCM-41. This also confirms that nonlinear equations have matched the results more than linear equations in this study. This result is consistent with that of other works [25–28].

The maximum adsorption capacity of the aminopropyl-MCM-41 material calculated from the various compatibility equations (Langmuir 3, Langmuir 5, Langmuir model in the nonlinear form, Freundlich in the nonlinear form, Redlich–Peterson in the nonlinear form, and Sips in the nonlinear form for the adsorption of Pb(II); and Langmuir in the nonlinear form, Freundlich in the nonlinear form, Redlich–Peterson nonlinear, and Sips in the nonlinear form for the adsorption of Cd(II)) was 64.21 $mg \cdot g^{-1}$ ($N = 5$, SE = 0.21) for Pb(II) and 14.08 $mg \cdot g^{-1}$ ($N = 3$, SE = 0.33) for Cd(II). The small standard error proves the correctness of the paired-samples t-test method.

The adsorption capacity in this work was compared with the results reported previously [18, 42–47]. A comparison was listed in Table 6. It could be noticed that the adsorption capacity was higher or comparable within previous papers. The aminopropyl-MCM-41 exhibited better than some of the adsorbent based on MCM-48, silicalite-1, or chromium-doped nickel nanometal oxide but failed to some others.

4. Conclusions

A comparison of physicochemical characteristics of aminopropyl-MCM-41 prepared via direct and postsynthesis was performed. The aminopropyl-MCM-41 material prepared by means of the direct process exhibits good porous properties but low aminopropyl loading compared with the samples prepared via postsynthesis. Parent MCM-41 remarkably affects the physicochemical properties of resulting aminopropyl-MCM-41. The extracted MCM-41 material gave higher aminopropyl loading and better porous properties than the calcined MCM-41 counterpart, and therefore, it provided a high adsorption capacity for Pb(II) and Cd(II) at 64.21 $mg \cdot g^{-1}$ and 14.08 $mg \cdot g^{-1}$, respectively. The paired-samples t-test could eliminate the part-sided assessment based on the minimum value of the error function. According to our knowledge, this is the first study applying the statistical test to assess the compatibility of the isothermal models in terms of theory as well as practice.

Data Availability

The data used to support the findings of this study are available from the corresponding author upon request.

Conflicts of Interest

The authors declare that they have no conflicts of interest.

References

[1] A. T. Paulino, L. B. Santos, and J. Nozaki, "Removal of Pb^{2+}, Cu^{2+}, and Fe^{3+} from battery manufacture wastewater by chitosan produced from silkworm chrysalides as a low-cost adsorbent," *Reactive and Functional Polymer*, vol. 62, no. 2, pp. 634–642, 2008.

[2] Agency for Toxic Substances and Disease Registry, *Toxicological Profile for Polycyclic Aromatic Hydrocarbons*, U.S. Department of Health & Human Services, Public Health Service, Agency for Toxic Substances and Disease Registry, Washington, DC, USA, 1999.

[3] J. Pan, J. A. Plant, N. Voulvoulis, C. J. Oates, and C. Ihlenfeld, "Cadmium levels in Europe: implications for human health," *Environmental Geochemistry and Health*, vol. 32, no. 1, pp. 1–12, 2010.

[4] H. J. Mansoorian, A. H. Mahvi, and A. J. Jafari, "Removal of lead and zinc from battery industry wastewater using electrocoagulation process: influence of direct and alternating current by using iron and stainless steel rod electrodes," *Separation and Purification Technology*, vol. 135, pp. 165–175, 2014.

[5] T. Mahmood, M. T. Saddique, A. Naeem, S. Mustafa, B. Dilara, and Z. A. Raza, "Cation exchange removal of Cd from aqueous solution by NiO," *Journal of Hazardous Materials*, vol. 185, no. 2-3, pp. 824–828, 2011.

[6] N. Pont, V. Salvadó, and C. Fontàs, "Selective transport and removal of Cd from chloride solutions by polymer inclusion membranes," *Journal of Membrane Science*, vol. 318, no. 1-2, pp. 340–345, 2008.

[7] C. T. Kresge and W. J. Roth, "The discovery of mesoporous molecular sieves from the twenty year perspective," *Chemical Society Reviews*, vol. 42, no. 9, pp. 3663–3670, 2013.

[8] R. Köhn, D. Paneva, M. Dimitrov et al., "Studies on the state of iron oxide nanoparticles in MCM-41 and MCM-48 silica materials," *Microporous and Mesoporous Materials*, vol. 63, no. 1–3, pp. 125–137, 2003.

[9] L. C. Juang, C. C. Wang, and C. K. Lee, "Adsorption of basic dyes onto MCM-41," *Chemosphere*, vol. 64, no. 11, pp. 1920–1928, 2006.

[10] M. Anbia and M. Lashgari, "Synthesis of amino-modified ordered mesoporous silica as a new nano sorbent for the removal of chlorophenols from aqueous media," *Chemical Engineering Journal*, vol. 150, no. 2-3, pp. 555–560, 2009.

[11] G. L. Athens, R. M. Shayib, and B. F. Chmelka, "Functionalization of mesostructured inorganic-organic and porous inorganic materials," *Current Opinion in Colloid and Interface Science*, vol. 14, no. 4, pp. 281–292, 2009.

[12] A. Deryło-Marczewska, M. Zienkiewicz-Strzałka, K. Skrzypczyńska, A. Świątkowski, and K. Kuśmierek, "Evaluation of the SBA-15 materials ability to accumulation of 4-chlorophenol on carbon paste electrode," *Adsorption*, vol. 22, no. 4–6, pp. 801–812, 2016.

[13] A. Arencibia, J. Aguado, and J. M. Arsuaga, "Regeneration of thiol-functionalized mesostructured silica adsorbents of mercury," *Applied Surface Science*, vol. 256, no. 17, pp. 5453–5457, 2010.

[14] H. Sepehrian, S. Waqif-Husain, and M. Ghannadi-Maragheh, "Development of thiol-functionalized mesoporous silicate MCM-41 as a modified sorbent and its use in chromatographic separation of metal ions from aqueous nuclear waste," *Chromatographia*, vol. 70, no. 1-2, pp. 277–280, 2009.

[15] T. M. Suzuki, T. Nakamura, K. Fukumoto, M. Yamamoto, Y. Akimoto, and K. Yano, "Direct synthesis of amino-functionalized monodispersed mesoporous silica spheres and their catalytic activity for nitroaldol condensation," *Journal of Molecular Catalysis A: Chemical*, vol. 280, no. 1-2, pp. 224–232, 2008.

[16] S. Wu, F. Li, R. Xu, S. Wei, and G. Li, "Synthesis of thiol-functionalized MCM-41 mesoporous silicas and its application in Cu(II), Pb(II), Ag(I), and Cr(III) removal," *Journal of Nanoparticle Research*, vol. 12, no. 6, pp. 2111–2124, 2010.

[17] K. M. Parida and D. Rath, "Amine functionalized MCM-41: an active and reusable catalyst for Knoevenagel condensation reaction," *Journal of Molecular Catalysis A: Chemical*, vol. 310, no. 1-2, pp. 93–100, 2009.

[18] A. Heidari, H. Younesi, and Z. Mehraban, "Removal of Ni(II), Cd(II), and Pb(II) from a ternary aqueous solution by amino functionalized mesoporous and nano mesoporous silica," *Chemical Engineering Journal*, vol. 153, no. 1–3, pp. 70–79, 2009.

[19] J. Aguado, J. M. Arsuaga, A. Arencibia, M. Lindo, and V. Gascón, "Aqueous heavy metals removal by adsorption on amine-functionalized mesoporous silica," *Journal of Hazardous Materials*, vol. 163, no. 1, pp. 213–221, 2009.

[20] B. H. Hameed, A. A. Ahmad, and N. Aziz, "Isotherms, kinetics and thermodynamics of acid dye adsorption on activated palm ash," *Chemical Engineering Journal*, vol. 133, no. 1–3, pp. 195–203, 2007.

[21] O. Hamdaoui and E. Naffrechoux, "Modeling of adsorption isotherms of phenol and chlorophenols onto granular activated carbon. Part I. Two-parameter models and equations allowing determination of thermodynamic parameters," *Journal of Hazardous Material*, vol. 147, no. 1-2, pp. 381–394, 2007.

[22] O. Hamdaoui and E. Naffrechoux, "Modeling of adsorption isotherms of phenol and chlorophenols onto granular activated carbon. Part II. Models with more than two parameters," *Journal of Hazardous Materials*, vol. 147, no. 1-2, pp. 401–411, 2007.

[23] S. J. Allen, Q. Gan, R. Matthews, and P. A. Johnson, "Comparison of optimised isotherm models for basic dye adsorption by kudzu," *Bioresource Technology*, vol. 88, no. 2, pp. 143–152, 2003.

[24] A. Kumar, B. Prasad, and I. M. Mishra, "Adsorptive removal of acrylonitrile by commercial grade activated carbon: kinetics, equilibrium and thermodynamics," *Journal of Hazardous Materials*, vol. 152, no. 2, pp. 589–600, 2008.

[25] K. V. Kumar and S. Sivanesan, "Comparison of linear and non-linear method in estimating the sorption isotherm parameters for safranin onto activated carbon," *Journal of Hazardous Materials*, vol. 123, no. 1–3, pp. 288–292, 2005.

[26] K. V. Kumar and S. Sivanesan, "Prediction of optimum sorption isotherm: comparison of linear and non-linear method," *Journal of Hazardous Materials*, vol. 126, no. 1–3, pp. 198–201, 2005.

[27] K. Vasanth Kumar and S. Sivanesan, "Isotherms for Malachite Green onto rubber wood (*Hevea brasiliensis*) sawdust: comparison of linear and non-linear methods," *Dyes and Pigments*, vol. 72, no. 1, pp. 124–129, 2007.

[28] K. Vasanth Kumar and S. Sivanesan, "Sorption isotherm for safranin onto rice husk: comparison of linear and non-linear methods," *Dyes and Pigments*, vol. 72, no. 1, pp. 130–133, 2007.

[29] Y. S. Ho, W. T. Chiu, and C. C. Wang, "Regression analysis for the sorption isotherms of basic dyes on sugarcane dust," *Bioresource Technology*, vol. 96, no. 11, pp. 1285–1291, 2005.

[30] M. I. El-Khaiary and G. F. Malash, "Common data analysis errors in batch adsorption studies," *Hydrometallurgy*, vol. 105, no. 3-4, pp. 314–320, 2011.

[31] Y. C. Wong, Y. S. Szeto, W. H. Cheung, and G. McKay, "Adsorption of acid dyes on chitosan—equilibrium isotherm analyses," *Process Biochemistry*, vol. 39, no. 6, pp. 695–704, 2004.

[32] B. H. Dang Son, V. Quang Mai, D. Xuan Du, N. Hai Phong, and D. Quang Khieu, "A study on astrazon black AFDL dye adsorption onto Vietnamese diatomite," *Journal of Chemistry*, vol. 2016, Article ID 8685437, 11 pages, 2016.

[33] K. Y. Foo and B. H. Hameed, "Insights into the modeling of adsorption isotherm systems," *Chemical Engineering Journal*, vol. 156, no. 1, pp. 2–10, 2010.

[34] A. Ortlam, J. Rathouský, G. Schulz-Ekloff, and A. Zukal, "MCM-41 as-synthesized and calcined materials: temporal development of X-ray reflection intensity and pore volume," *Microporous Materials*, vol. 6, no. 4, pp. 171–180, 1996.

[35] M. Kosmulski, "pH-dependent surface charging and points of zero charge II. Update," *Journal of Colloid and Interface Science*, vol. 275, no. 1, pp. 214–224, 2004.

[36] Q. Qin, J. Ma, and K. Liu, "Adsorption of anionic dyes on ammonium-functionalized MCM-41," *Journal of Hazardous Materials*, vol. 162, no. 1, pp. 133–139, 2009.

[37] A. Benhamou, M. Baudu, Z. Derriche, and J. P. Basly, "Aqueous heavy metals removal on amine-functionalized Si-MCM-41 and Si-MCM-48," *Journal of Hazardous Materials*, vol. 171, no. 1–3, pp. 1001–1008, 2009.

[38] N. D. V. Quyen, T. N. Tuyen, D. Q. Khieu et al., "Lead ions removal from aqueous solution using modified carbon nanotubes," *Bulletin of Materials Science*, vol. 41, p. 6, 2018.

[39] N. T. V. Hoan, N. T. A. Thu, H. Van Duc, N. D. Cuong, D. Q. Khieu, and V. Vo, "Fe_3O_4/reduced graphene oxide nanocomposite: synthesis and its application for toxic metal ion removal," *Journal of Chemistry*, vol. 2016, Article ID 2418172, 10 pages, 2016.

[40] K. P. Singh, N. Basant, A. Malik, and G. Jain, "Modeling the performance of 'up-flow anaerobic sludge blanket' reactor based wastewater treatment plant using linear and nonlinear approaches—a case study," *Analytica Chimica Acta*, vol. 658, no. 1, pp. 1–11, 2010.

[41] A. Field, *Discovering Statistics Using SPSS*, SAGE Publishing, Thousand Oaks, CA, USA, 2010.

[42] H. Faghihian, H. Nourmoradi, and M. Shokouhi, "Performance of silica aerogels modified with amino functional groups in Pb(II) and Cd(II) removal from aqueous solutions," *Polish Journal of Chemical Technology*, vol. 14, no. 1, pp. 50–56, 2012.

[43] L. Qin, L. Yan, J. Chen, T. Liu, H. Yu, and B. Du, "Enhanced removal of Pb^{2+}, Cu^{2+}, and Cd^{2+} by amino-functionalized magnetite/kaolin clay," *Industrial & Engineering Chemistry Research*, vol. 55, no. 27, pp. 7344–7354, 2016.

[44] A. A. Malhis, S. H. Arar, M. K. Fayyad, and H. A. Hodali, "Amino- and thiol-modified microporous silicalite-1 and mesoporous MCM-48 materials as potential effective adsorbents for Pb(II) in polluted aquatic systems," *Adsorption Science & Technology*, vol. 36, no. 1-2, pp. 270–286, 2018.

[45] S. Li, M. Wang, Z. Zhao, C. Ma, and S. Chen, "Adsorption and desorption of Cd by soil amendment: mechanisms and environmental implications in Field-Soil remediation," *Sustainability*, vol. 10, no. 7, p. 2337, 2018.

[46] R. Shiralipour and T. Hamoule, "Removal of Pb(II) from contaminated water by bagasse adsorbent modified with dithizone," *Jundishapur Journal of Health Sciences*, vol. 10, no. 3, p. e62360, 2018.

[47] Y. V. S. Sai Krishna, G. Sandhya, and R. Ravichandra Babu, "Removal of heavy metals Pb(II), Cd(II) and Cu(II) from waste waters using synthesized chromium doped nickel oxide nano particles," *Bulletin of the Chemical Society of Ethiopia*, vol. 32, no. 2, pp. 225–238, 2018.